Multimodal Implantable Bioelectronics

Thesis by

Jiahong Li

In Partial Fulfillment of the Requirements for

the degree of

Doctor of Philosophy

CALIFORNIA INSTITUTE OF TECHNOLOGY

Pasadena, California

2026

(Defended March 25, 2026)

© 2026

Jiahong Li
ORCID: 0000-0001-7938-9589

ACKNOWLEDGEMENTS

I would like to express my deepest appreciation to all those who have contributed to the completion of this thesis. This journey would not have been possible without the invaluable support and encouragement I have received throughout this process.

First, I would like to express my sincere gratitude to my advisor, Wei Gao, for his unwavering support, mentorship, and patience throughout this journey. His guidance has profoundly shaped both the direction of this research and my development as a scholar. I am especially grateful for his insight, encouragement, and trust, which have allowed me to explore ideas with independence while maintaining a clear sense of direction.

I would also like to extend my gratitude to the members of my thesis committee, Prof. Anqi Zhang, Prof. Yaser Abu-Mostafa, and Prof. Axel Scherer, for their constructive feedback, insightful suggestions, and for generously dedicating their time and expertise to the evaluation of this research.

I am deeply grateful to my family for their unconditional love, support, and understanding throughout this journey. Their constant encouragement has been a source of strength during both challenging and rewarding moments.

I am also grateful to my colleagues and friends for their support, encouragement, and the many meaningful discussions along the way. Their companionship and shared experiences have made this journey both enjoyable and memorable.

Lastly, I would also like to acknowledge California Institute of Technology for providing the intellectually stimulating environment as well as invaluable resources and facilities essential to this work. It has been a privilege to carry out this research here.

I remain deeply grateful to all who have contributed to and supported me throughout this journey.

ABSTRACT

Advances in bioelectronic technologies are transforming healthcare by enabling continuous monitoring and active modulation of physiological functions. However, conventional electronic materials are mechanically mismatched with soft biological tissues, which can lead to poor conformal contact, unstable signal acquisition, and adverse biological responses during long-term operation. This dissertation addresses these challenges through the development of multimodal bioelectronic systems that integrate soft materials, scalable fabrication strategies, and closed-loop therapeutic functionalities for next-generation health monitoring and intervention.

First, scalable fabrication strategies are developed to construct flexible and multimodal sensing platforms capable of detecting diverse physiological and environmental signals. Inkjet-printed sensor arrays incorporating nanomaterial-based electrochemical and physical sensors enable simultaneous measurement of temperature, pressure, and chemical biomarkers with high sensitivity and spatial resolution. These sensing systems can be integrated onto soft electronic skins and robotic platforms to provide real-time physicochemical perception in complex environments.

Second, conformal bioelectronic interfaces are engineered to enable stable, long-term interactions with biological tissues. By tailoring material properties and device architectures, these interfaces achieve improved mechanical compatibility with soft tissues, facilitating reliable in vivo signal acquisition and stimulation while minimizing interfacial stress and biological reactions.

Finally, closed-loop bioelectronic systems are developed that combine continuous biosensing with responsive therapeutic stimulation. Integrated platforms capable of monitoring metabolic signals and triggering neuromodulation demonstrate the potential for automated therapeutic regulation. These systems highlight the feasibility of real-time physiological monitoring coupled with intelligent intervention.

Together, the materials, device architectures, and system-level strategies presented in this dissertation establish a framework for scalable, conformal, and multifunctional bioelectronics. These technologies provide new opportunities for wearable and implantable systems capable of continuous health monitoring, autonomous therapy, and advanced human–machine interfaces.

PUBLISHED CONTENT AND CONTRIBUTIONS

1. Yu, Y.; Li, J.; Solomon, S.; Min, J.; Tu, J.; Guo, W.; Xu, C.; Song, Y.; Gao, W. All-printed soft human-machine interface for robotic physiochemical sensing. *Science Robotics* **7** eabn0495(2022). https://doi.org/10.1126/scirobotics.abn0495

Methodology: Y.Y., J.L., and S.A.S. Investigation: Y.Y., J.L., S.A.S., J.M., J.T., W.G., C.X., and Y.S. Writing—original draft: W.G., Y.Y., J.L., and S.A.S.

2. Li, J.; Fan, K.; Ma, X.; Wang, C.; Min, J.; Chen, Y.; Song, Y.; Xu, Y.; Gao, W. Strain-insensitive wet-tissue-adhesive biphasic bioelectronics for physicochemical monitoring and adaptive therapy. *Nature Materials*, Accepted

J.L. and W.G. initiated the concept and designed the studies. J.L., K.F., X.M., C.W., J.M., Y.C., Y.S., and Y.X. performed materials preparation, characterization, validation and sample analysis. W.G. and J.L. co-wrote the paper. All authors contributed to the data analysis and provided the feedback on the paper.

3. Li, J.; Qu, J.; Gao, W. Tissue-bioelectronics interfaces. *Chemical Society Reviews*, Accepted

J. L., J. Q. and W.G. prepared the manuscript and the figures.

TABLE OF CONTENTS

Acknowledgements……...iii
Abstract ……iv
Published Content and Contributions…….....v
Table of Contents……. vi
List of Illustrations and/or Tables……vii
Abbreviations……viii
Chapter 1: Introduction 1
1.1 Introduction 2
1.2 Interfacial Mechanisms 3
1.2.1 Physical Interactions 4
1.2.2 Covalent Interactions 7
1.2.3 Biological Interactions 10
1.3 Principles for Conformal Interface on Irregular Surfaces 12
1.3.1 Principles of Structure Engineering for Conformal Interfaces ... 12
1.3.2 Principles of Materials Development for Conformal Interfaces. 16
1.4 Fabrication Strategies for Bioelectronics Interfaces 19
1.4.1 Microfabrication Methods 21
1.4.2 Printing Methods 23
1.4.3 In vivo Printing 27
1.4.4 Combination Strategies 30
1.5 Applications in Sensing and Modulation 31
1.5.1 Physiological Signal Monitoring 32
1.5.2 Multimodal Disease Management 37
1.5.3 Closed-loop Strategies 39
1.6 Strategies for Biocompatibility Optimization 41
1.6.1 Mechanical Adjustment 41
1.6.2 Chemical Modification 42
1.6.3 Bioactive Modification 44
1.6.4 Drug-releasing surfaces 45
Bibliography of Chapter 1 47
Chapter 2: All-printed Soft Human-machine Interface for Robotic Physicochemical Sensing 70
2.1 Introduction 71
2.2 Design of the Human-machine Interactive E-skins 74
2.3 Fabrication and characterization of the fully inkjet-printed multimodal sensor arrays 74
2.4 Evaluation of E-skin-H for AI-assisted Human-machine Interaction.. 80
2.5 Evaluation of the M-Bot in Human-interactive Robotic Physicochemical Sensing 82
2.6 Evaluation of an E-skin-R–enabled M-Boat for Autonomous Source

Tracking 83
2.7 Discussion 86
2.8 Materials and Methods 87
Bibliography of Chapter 2 95
Appendix A 101
Chapter 3: Strain-insensitive Wet-tissue-adhesive Biphasic Bioelectronics for Physicochemical Monitoring and Adaptive Therapy 158
3.1 Introduction 159
3.2 Mechanical and Electromechanical Characterizations of ElHyX 162
3.3 Strain-insensitive Bioelectrical and Biomolecular Sensors 166
3.4 In vivo Evaluation of ElHyX for Physicochemical Sensing and Neural Stimulation 169
3.5 Closed-loop Blood Glucose Regulation in Diabetic Rat 172
3.6 Conclusions 175
3.6 Methods 175
Bibliography of Chapter 3 184
Appendix B 188
Bibliography of Appendix B 226
Chapter 4: Outlook and Conclusion 228

LIST OF ILLUSTRATIONS AND/OR TABLES

Figure Number *Page*

1-1. Interaction on tissue-bioelectronics interface 4

1-2. Representative structural engineering models and strategies for conformal tissue–bioelectronics interfaces 14

1-3. Representative material development principles and material types... 18

1-4. Representative microfabrication strategies for flexible and in vivo bioelectronic interfaces 20

1-5. Representative printing methods applicable to flexible interface fabrication 24

1-6. Representative tissue-interfaced bioelectronic platforms for physiological monitoring 34

1-7. Representative tissue-interfaced bioelectronic platforms for therapeutic intervention 36

1-8. Architecture of integrated closed-loop soft bioelectronic systems 40

1-9. Strategies for mitigating foreign-body responses at tissue–bioelectronic interfaces 47

2-1. Artificial intelligence (AI)-powered multimodal sensing robotic system (M-Bot) based on a fully-printed soft human-machine interface 73

2-2. Characterization of the fully inkjet-printed multimodal sensor arrays on the e-skin-R 75

2-3. Evaluation of the e-skin-H for AI-assisted human-machine interaction 79

2-4. Evaluation of the M-Bot in human-interactive robotic physicochemical sensing 82

2-5. Evaluation of the-skin-R in an autonomous multimodal sensing robotic boat (M-Boat) 85

A-1. Schematic and fabrication procedure of e-skin-R 111

A-2. Characterization of drop-on-demand inkjet printing with custom-designed inks 111
A-3. Characterizations of inkjet-printed nanostructured patterns for M-Bot 113
A-4. Simulation of the hydrogel-based solid-phase hazard analyte sampling and sensing 114
A-5. Characterizations of the IPCEs 115
A-6. Evaluation of the M-Bot chemical sensing using hydrogels with enlarged size 116
A-7. Evaluation of the M-Bot chemical sensing with increased sensor density 117
A-8. Characterization of the printed AgNWs/N-PDMS tactile sensors 118
A-9. Characterization of the printed AgNWs/N-PDMS tactile sensors 119
A-10. The algorithm used for automatic baseline correction of the DPV voltammograms 120
A-11. In situ regeneration of the hydrogel-loaded Pt-graphene TNT sensors 121
A-12. Characterization of the printed MOF-808/Au electrodes 122
A-13. Evaluation of the MOF-808/Au electrode for high-concentration OP analysis 123
A-14. The selectivity of Pt-graphene and MOF-808/Au electrodes over OP and TNT 124
A-15. The selectivity of TNT and OP sensors over other nitro compounds 125
A-16. The continuous and reversible TNT and OP sensing with the printed TNT and OP sensors 126
A-17. Schematic of the modification procedure of the printed CNT electrode for SARS-CoV-2 S1 sensing 127
A-18. Evaluation of the stability of antibody immobilization 128
A-19. Selectivity of the SARS-CoV-2 S1 sensor over other viral proteins 129

A-20. Selectivity of the SARS-CoV-2 biosensor for dry-phase protein detection 130
A-21. Characterization of printed carbon-based temperature sensor toward real-time temperature sensing and calibration 131
A-22. Performance of the printed sensor arrays under mechanical deformation 132
A-23. Stability of the hydrogel 133
A-24. Influence of the contact pressure on the electrochemical sensor performance 134
A-25. Interference of the contact pressure on SARS-CoV-2 S1 sensor performance 135
A-26. Fabrication and characterization of the soft and stretchable e-skin-H 136
A-27. Gesture classification confusion matrix obtained with different machine learning algorithms 137
A-28. Evaluation of the e-skin-H on different body parts for AI-assisted human-machine interaction 138
A-29. Evaluation of the e-skin-H from gestures with different degrees 139
A-30. sEMG and root mean square (RMS) data process for robotic hand control 140
A-31. SHAP decision plots based on the arm sEMG dataset with respect to a KNN classification model 141
A-32. A SHAP heatmap that clusters each point's SHAP value by its respective gesture classification 142
A-33. Evaluation of the laser proximity sensor in robotic operation 143
A-34. Human-interactive robotic control for object touching and on-site TNT detection 144
A-35. Multiplexed simultaneous physicochemical sensor analysis using the printed sensor array 145
A-36. Human-machine interactive robotic operation for object grasping ... 146

A-37. The tactile responses of the e-skin-R on a cylindrical object..... 147
A-38. The OP sensing responses of the e-skin-R on a cylindrical object 148
A-39. Schematic illustration and component list of the electronic system of the M-Boat 149
A-40. Characterization of the operation of the M-Boat..... 150
A-41. Simulation comparison of the searching algorithms for M-Boat autonomous source locating 151
A-42. Evaluation of the M-Boat for autonomous source tracking..... 152
A-43. Evaluation of the M-Boat in seawater 153
A-44. Influence of ionic strength and pH on sensor performance 154
3-1. Overview of the soft, strain-insensitive elastomer-hydrogel biphasic multifunctional platform (ElHyX) for multimodal implantable bioelectronics 161
3-2. Mechanical and electromechanical characterizations of ElHyX 165
3-3. Characterization of strain-insensitive ElHyX physical and chemical sensors 168
3-4. In vivo characterization of ElHyX-based implantable electronics 169
3-5. In vivo evaluation of ElHyX-based closed-loop blood glucose regulation in diabetic rats..... 174
B-1. Schematic of ElHyX electrodes..... 189
B-2. Fabrication process of ElHyX-based device 190
B-3. Direck ink writing using customized inks..... 191
B-4. Quantitative evaluation of interfacial adhesion between the elastomer and hydrogel layers of the ElHyX platform 192
B-5. Schematic and SEM image of SBS-(EGaIn/SBS)-SBS trilayer structure..... 193
B-6. Electrical stability of encapsulated EGaIn–SBS composite under physiological conditions 194
B-7. Mechanical properties of ElHyX components 195
B-8. Activation of EGaIn-SBS 196

B-9. Fabrication process of Graphite-PB-SBS ink 197
B-10. Demonstration of additional chemical sensing capabilities using functional fillers 198
B-11. In vivo validation of ElHyX-based pH and uric acid sensors 199
B-12. DIW patterned functional composites 200
B-13. Printing resolution of EGaIn-SBS composite ink 201
B-14. SEM characterization of electrode materials 202
B-15. On-body ECG measurement under tensile strain 203
B-16. On-body ECG monitoring using conventional conductive composites 204
B-17. Optimization and evaluation of the electrochemical performance of the composite electrode 205
B-18. Evaluation of strain-insensitive electrochemical performance 206
B-19. Evaluation of the stability and selectivity of ElHyX-based glucose sensor 207
B-20. In vitro demonstration of adhesion on collagen sheet and stretchability of ElHyX-based electrochemical sensor 208
B-21. Photograph of in vivo animal tests 209
B-22. In vivo glucose sensor calibration 210
B-23. 6-hour continuous monitoring of heart rate and glucose levels using ElHyX electrode 211
B-24. In vivo multi-cycle dynamic glucose sensing using ElHyX-based sensor 212
B-25. Long-term stability of PU-encapsulated ElHyX devices 213
B-26. Histological and immunological evaluation of tissue response to implanted ElHyX device 214
B-27. System integration of a fully implantable wireless ElHyX-based bioelectronic platform 215
B-28. Power consumption of the wireless ElHyX system 216
B-29. In vivo evaluation of wireless ElHyX system 217

B-30. Heart rate response of a diabetic rat to IP saline injection 218
B-31. Closed-loop control logic for glucose regulation based on dual-parameter feedback 219
B-32. In vivo optimization of VNS parameters 220
B-33. In vivo demonstration of closed-loop glucose regulation in diabetic rats using the ElHyX-based system 210

Table Number *Page*

A-1. Ink composition and characterizations 155
A-2. Accuracy breakdown per feature with and without one channel removed 156
A-3. Accuracy breakdown based on five features with one and two channels 157
B-1. Composition and characterization of SBS composite inks 222
B-2. Key materials and functionality metrics of the state-of-the-art implantable bioelectronic platforms 223
B-3. Comparison of representative hydrogel–device and hydrogel–tissue integration strategies 224

ABBREVIATIONS

μ-ILEDs - microscale inorganic light-emitting diodes

3D - Three dimensional

AbC - Capture antibody

ADC - Analog-to-digital converter

AESBS - acrylyl-opening epoxidized poly(styrene-butadiene-styrene)

AFE - Analog front-end

AI - Artificial intelligence

Ag/AgCl - Silver/Silver Chloride

AgNWs - Silver nanowires

AJP - Aerosol jet printing

BLE - Bluetooth low energy

BSA - Bovine serum albumin

CD - Cluster of Differentiation

CE - Counter electrode

CLIP - Continuous liquid interface production

CNT - Carbon nanotube

COVID-19 - Coronavirus disease 2019

CPU - Central processing unit

CVD - Chemical vapor deposition

CVs - Cyclic voltammograms

Cy3 - Cyanine-3

DA - Dopaminergic

DAL - Dry adhesive layer

DIW - Direct ink writing

DLP - Digital light processing

DMDs - Digital micromirror devices

DMF - N,N′-dimethylformamide

DPBS - Dulbecco's phosphate-buffered saline

DPV - Differential pulse voltammetry

ECG - Electrocardiogram

ECM - Extracellular-matrix

EDC - 1-ethyl-3-(3-dimethylamonipropyl)carbodiimide

EDS - Energy-dispersive spectroscopy

EEG - Electroencephalogram

EGaIn - Eutectic gallium–indium

EMG – Electromyogram

EOG – Electrooculography

ES - Electrical stimulation

ESBS - epoxidized poly(styrene-butadiene-styrene)

e-skin - Electronic skin

eVNS - Efferent vagus nerve stimulation

FBR - Foreign-body response

FDA - Food and Drug Administration

FITC - Fluorescein isothiocyanate

FTIR - Fourier transform infrared

GD - Gradient descent

GelMA - Gelatin Methacrylate

GO - Graphene oxide

GPIO - General-purpose input/output

H3BTC - 1,3,5-benzenetricarboxylic acid

HDF - Human dermal fibroblasts

H&E - Hematoxylin and eosin

HPF - High-pass filter

H-SW - H-bridge software

IgG - Human immunoglobulin G

IM - Interpolated map

In-Amp - Instrumentation amplifier

IP - Intraperitoneal

IPA - Isopropyl alcohol

IPCEs - Inkjet-printed carbon electrodes

KNN - K-nearest neighbors

LEDs - Light-emitting diodes

LPS - Laser proximity sensor

M-Boat - Multimodal sensing robotic boat

M-Bot - Multimodal sensing robotic system

MD - Max direction

MEAs - Microelectrode arrays

MES - 2-(N-morpholino)ethanesulfonic acid hydrate

MOF - Metal-organic framework

MoS_2 - Molybdenum disulfide

MS - Maximum slope

MUA - Multiplexer

nDPV - Negative differential pulse voltammetry

NHS - N-hydroxysuccinimide

NIR - Near-infrared

NMP - 1-methyl-2-pyrrolidinone

N-PDMS - Nanotextured polydimethylsiloxane

OPs – Organophosphates

PAA - Poly(pyromellitic dianhydride-co-4,4′-oxydianiline) amic acid

PAAc - Poly(acrylic acid)

PANI - Polyaniline

PB - Prussian blue

PBS - Phosphate-buffered saline

PCB - Printed circuit board

PDMS - Polydimethylsiloxane

PEG - Poly(ethylene glycol)

PEGDA - Poly(ethylene glycol) diacrylate

PH - Peak height

PI – Polyimide

PPI - Pixels per inch

PU - Polyurethane

PVA - Poly(vinyl alcohol)

PVD - Physical vapor deposition

PWM - Pulse width modulation

PZT - Lead zirconate titanate

RD - Random direction

RE - Reference electrode

RMS - Root mean square

RO - Retro-orbital

S1 - Spike 1 protein

SARS-CoV-2 - Severe acute respiratory syndrome coronavirus 2

SBS - Poly(styrene–butadiene–styrene)

SEBS - Poly(styrene–ethylene–butylene–styrene)

SEM - Scanning electron microscopy

sEMG - Surface electromyography

SHAP - Shapley additive explanation

SIS - Poly(styrene–isoprene–styrene)

SLA – Stereolithography

SNR - Signal-to-noise ratio

SPI - Serial peripheral interface

SPU - Signal processing unit

STD - Standard deviation

Sulfo-NHS - N-hydroxysulfosuccinimide sodium salt

PA - Peak average

PE - Peak energy

T - Temperature

TNT - Trinitrotoluene

TPP - Two-photon polymerization

TPU - Thermoplastic polyurethanes

VNS - Vagus nerve stimulation

WE - Working electrode

wf-UMP - Wearable flexible ultrasound microneedle patch

Chapter 1

INTRODUCTION

Materials from this chapter appear in "Li, J.; Qu, J.; Gao, W. Tissue-bioelectronics interfaces. *Chemical Society Reviews*, Accepted"

1.1 Introduction

Driven by the rising cost of inpatient treatment, the growing prevalence of chronic diseases, and aging populations that demand long-term and accessible care, healthcare systems are increasingly shifting away from centralized, reactive care and toward more distributed, prevention-oriented monitoring[1,2]. Advances in wearable and implantable bioelectronics enable both continuous monitoring that allow early detection of health abnormalities and sustained therapeutic modulation[3–8]. The effective ness of these technologies depend on the tissue–bioelectronics interface; thus, establishing a stable and conformal interface is vital for accurate biosignal acquisition and consistent therapeutic performance.

A major challenge arises from the pronounced mechanical mismatch between conventional rigid bioelectronic devices and soft, irregularly shaped biological tissues. This mismatch induces interfacial stresses and motion-induced damage, which, together with biochemical incompatibility, can lead to tissue inflammation, fibrotic encapsulation, and premature device failure.[9–12]. Importantly, mechanical compliance at the device level alone does not guarantee functional stability, as both biosignal acquisition and therapeutic stimulation essentially rely on efficient coupling across the tissue–device interface[13–15].

To address these challenges, extensive efforts have been devoted to optimizing both device architectures and material compositions. Structural design strategies provide mechanical compliance by allowing rigid components to deform with the surrounding tissue[16,17], while the soft and biologically compatible materials further enhance mechanical compatibility and interfacial stability[18–20]. Notably, device architecture and material composition are often intrinsically coupled, jointly governing interfacial stress distribution and contact mechanics. These approaches have substantially improved the robustness and longevity of tissue–device integration. However, interfacial stability is not a static outcome of material softness or structural compliance; rather it is a dynamic process shaped by mechanical loading, biochemical exposure, and biological remodeling over time.

Achieving robust tissue integration therefore requires a comprehensive understanding of the interfacial interactions that govern contact, adhesion, and long-term stability at the tissue–device boundary. These interactions can be broadly categorized into physical, chemical, and biological mechanisms. Physical forces govern initial contact and conformability, chemical interaction—particularly covalent bonding—enhance interfacial toughness, and biological responses ultimately determine chronic biocompatibility. Understanding how these mechanisms operate across length and time scales is essential for designing interfaces that preserve both functional performance and tissue health.

In this chapter, we summarize the fundamental interfacial mechanisms that govern tissue–device coupling. Adopting a mechanism-driven perspective, we then discuss key principles underlying structural designs and material innovations. We further review recent fabrication strategies enabling soft, conformal, and multifunctional bioelectronics, followed by representative applications in sensing, stimulation, and therapeutic systems. Finally, we outline emerging opportunities and remaining challenges that will shape the next generation of tissue–bioelectronics interfaces. Collectively, this chapter provides an integrated framework for understanding and engineering robust tissue–bioelectronics integration.

1.2 Interfacial mechanisms

At the device–tissue boundary, bioelectronic performance is governed by a set of interfacial mechanisms that determine how interfaces form, stabilize, and evolve over time. These mechanisms control device conformability, adhesion, signal coupling, and long-term biocompatibility. Here we categorize interfacial interactions into three principal classes: physical interactions (e.g., van der Waals forces and capillary effects)[15,21], chemical interactions dominated by covalent bonding between device surfaces and tissue components[22], and biological interactions mediated by cell adhesion and immune signaling[23]. Together, these mechanisms define how effectively a device conforms to, anchors within, and communicates with surrounding tissues. An overview of these interaction types is provided in **Fig. 1-1**. By outlining these foundational processes, we establish a conceptual framework for the rational design of stable and long-lasting device–tissue interfaces.

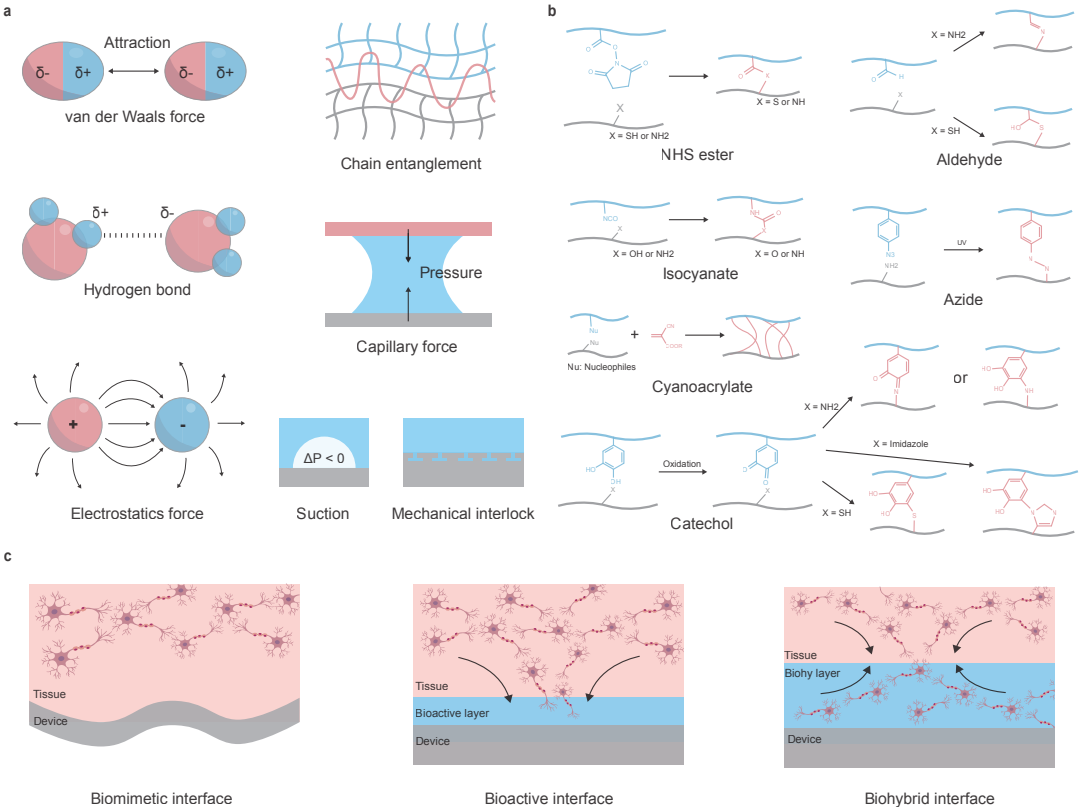

Fig. 1-1 Interaction on tissue-bioelectronics interface. (a) Physical interactions. (b) Covalent interactions. (c) Biological interactions.

1.2.1 Physical interactions

Physical interactions govern the formation of initial contact and conformal coupling between bioelectronic devices and soft biological tissues, spanning length scales from molecular-level surface forces to macroscopic structural engagement (**Fig. 1-1a**). At the microscale, weak noncovalent interactions, including van der Waals forces and hydrogen bonding, contribute to intimate surface contact and adhesion[21,24]. At larger length scales, capillary forces arising from interfacial fluids, as well as geometric and mechanical interlocking enabled by device architecture or tissue microtopography, can also enhance interfacial adhesion and load transfer[15,25]. Collectively, these physical interactions play a central role in minimizing

interfacial gaps, achieving conformability, and stabilizing tissue–device interface under physiological deformation.

Van der Waals interactions

Van der Waals interactions arise from dipole-dipole interactions between adjacent matter and are ubiquitous when materials are brought into close proximity. Although individually weak (~0.5–5 kJ mol^{-1})[26], their collective contribution can yield appreciable interfacial adhesion when conformal contact maximizes effective contact area, particularly in ultrathin and mechanically compliant devices. Skin-like electronic systems have demonstrated robust adhesion to the skin replying solely on van der Waals interactions, enabled by intimate conformal contact that maximizes the effective interfacial area and by their ultralight weight. Such epidermal electronic systems support high-fidelity recording of electrophysiological signals such as electrocardiogram (ECG), electroencephalogram (EEG), and electromyogram (EMG), as well as multimodal sensing of temperature, strain, and optical signals[21]. Importantly, van der Waals–mediated interfaces can support not only passive sensing but also the reliable operation of active electronic components such as transistors on soft and dynamic tissues. For example, stretchable electronic membranes incorporating molybdenum disulfide (MoS_2) nanosheet–based exhibit enhanced resistance to motion-induced artifacts compared with conventional gel-based Ag/AgCl electrodes, yielding improved signal-to-noise ratios under dynamic skin deformation[27].

Hydrogen bonds

Hydrogen bonding arises from directional interactions between hydrogen donors and electronegative acceptors in neighboring molecules and is particularly prevalent at tissue–device interfaces due to the abundance of hydrogen-bonding functional groups in proteins. Weak hydrogen bonds (≈10–40 kJ mol^{-1}) undergo rapid exchange and contribute limited interfacial stability in aqueous environments, where water molecules readily compete for bonding sites[28]. In contrast, stronger and more directional hydrogen bonds, such as those formed between carboxyl groups and amino acid residues (≈71–85 kJ mol^{-1})[28], can provide

a basis for more stable interfacial adhesion. When present at high density, hydrogen bonds enable efficient load sharing and continuous bond reformation at the tissue interface, collectively yielding strong and fatigue-resistant adhesion under wet and dynamic conditions[29]. Consequently, hydrogen-bond–based tissue adhesion strategies are widely employed in hydrogel-based tissue adhesives[24,29–32].

Electrostatic interactions

Electrostatic interactions arises from Coulombic interaction between oppositely charged species and are common at tissue–device interfaces due to the abundance of charged functional groups in biological tissues[33]. Several studies have demonstrated strong tissue adhesion mediated by electrostatic interactions[34,35]. However, electrostatic interactions are often screened by dissolved ions in physiological environments, which substantially limits their contributions in long-term adhesion when used in isolation.

Chain entanglement

Chain entanglement provides a noncovalent yet mechanically robust mechanism for tissue adhesion through interpenetration and topological constraints of long polymer chains at an interface. The process typically involves diffusion of polymer chains or monomers into the tissue surface, followed by network formation and solidification that locks the matrix in place. Chain entanglement-based adhesion is particularly effectively at overcoming interfacial hydration layers and accommodating irregular and rough tissue surfaces, and is therefore widely adopted in many glue-like tissue adhesive systems[36–38].

Capillary adhesion

Capillary adhesion, governed by liquid-mediated capillary forces that develop at two solid interfaces through meniscus formation in the presence of a thin fluid layer, is frequently exploited to stabilize and fix bioelectronic devices, as internal organs are intrinsically hydrated. Under thin-film approximation, the capillary pressure scales inversely with the interfacial separation and depends on the combined wettability of the two surfaces[39,40]:

$$\Delta P = \frac{\gamma(\cos\theta_1 + \cos\theta_2)}{h} \quad (1.1)$$

where γ is the surface tension of the liquid, θ_1 and θ_2 are the contact angles on the two surfaces, and h is the interfacial gap thickness. Because the surface tension of biological fluids and tissue wettability are largely fixed under physiological conditions, engineering strategies that reduce the device contact angle and minimize the thickness of the interfacial hydration layer are effective routes to enhance capillary adhesion. The resulting adhesion energy generated by capillary forces typically falls in the range of ~10–100 mJ m^{-2}, making this mechanism particularly well suited for thin, flexible implantable electronic systems[15,41–43].

Mechanical fixation

Mechanical fixation stabilizes tissue–device interfaces through geometric interlocking, friction, or physical confinement, and is inherently insensitive to surface chemistry, hydration layers, or ionic environments. Representative strategies include sutures, staples, barbs and microneedles provide robust fixation under large deformation and dynamic loading, but often induce tissue damage. Less invasive approaches, including suction-based attachment and mechanical interlocking structures, have been explored to stabilize devices under wet conditions[44–46]. However, their broader application to bioelectronics remains limited, due to the complex mechanical and biological characteristics of living tissues.

1.2.2 Covalent interactions

Covalent interactions establish strong linkages between bioelectronic devices and biological tissues, with bond dissociation energies typically in the range of ~100–800 kJ mol^{-1}[22], substantially exceeding those of noncovalent physical interactions (**Fig. 1-1b**). Owing to their short interaction range, covalent bonds require intimate molecular contact and precise chemical complementarity between functional groups on device surfaces and reactive moieties within tissue constituents. In physiological environments, blood and interstitial fluids present on the tissue surface may foul device surfaces or compete with tissue functional

groups, thereby compromising effective covalent bonding[22]. To overcome these challenges, covalent interactions are typically combined with strategies that disrupt interfacial hydration layers and with physical interactions that promote rapid conformal coupling and molecular proximity between devices and soft tissues[30,34,37]. Within this framework, a range of covalent chemistries has been developed to enable tissue–device bonding by targeting functional groups common to both bioelectronic materials and biological tissues.

N-hydroxysuccinimide esters

N-hydroxysuccinimide (NHS) esters are among the most widely used chemistries for protein modification and bioconjugation[47]. This reactivity has been adapted for hydrogel-based adhesive systems, in which NHS ester groups incorporated into polymer networks form covalent bonds with tissue amine- and thiol-containing groups on tissue under physiological conditions[30,38,48]. In addition to mediating tissue bonding, NHS esters are frequently employed as crosslinkers to generate covalently bonded polymer networks, producing bulk adhesive matrices that form the basis of several commercial medical glues[49,50]. Despite their versatility, NHS esters are susceptible to hydrolysis, which poses challenges for long-term storage and reduces bonding efficiency in persistently wet conditions.

Aldehydes

Aldehyde-based chemistries have also been extensively explored as reactive platforms for covalent tissue adhesion owing to their ability to form Schiff base linkages with amine groups on biological tissues and to induce covalent crosslinking within polymer matrices[51,52]. This dual functionality underlies the design of commercially available medical glues in which glutaraldehyde-induced crosslinking generates a robust bulk adhesive matrix while anchoring to tissue surfaces[53]. However, Schiff base bonds are dynamic and relatively low in bond stability[54], and residual aldehyde species can raise concerns regarding cytotoxicity and long-term biocompatibility.

Cyanoacrylates

Cyanoacrylates represent one of the most widely used classes of chemical adhesives, owing to their rapid bonding kinetics and strong adhesion. In fact, household "super glue" formulations are based on cyanoacrylate chemistry. Cyanoacrylate adhesion relies on anionic polymerization that is initiated by trace amounts of moisture, amines or other nucleophilic species present on surfaces, leading to rapid in situ polymerization and the formation of solid polymer networks that anchor to the substrate at the interface[55,56]. Short-chain cyanoacrylates, such as methyl and ethyl cyanoacrylate, exhibit extremely rapid polymerization kinetics and release substantial heat during curing. In wet biological environments, these monomers often react prematurely with interfacial water, limiting effective bonding to underlying tissue surfaces. To overcome these challenges, commercial medical glues employ cyanoacrylate monomers with longer alkyl side chains to deliberately moderate polymerization kinetics and improve handling and biocompatibility in physiological environments[57–59]. Nonetheless, the relatively fast degradation of cyanoacrylate-based adhesives generally restricts their use to short-term applications[60].

Catechol

Catechol-based chemistries, inspired by mussel adhesion, have been widely exploited in biomimetic adhesive systems[61–63]. Catecholic moieties support multimodal adhesion by enabling physical interactions, such as hydrogen bonding and π–π interactions, as well as multiple covalent reaction pathways with nucleophilic groups on tissue components[64]. When oxidized to quinones, carbonyl groups can form Schiff base linkage with amines, while benzene ring can form covalent interaction with amines, thiols and imidazole[65]. While catechol offer versatile and strong tissue adhesion, its susceptibility to uncontrolled oxidation and self-crosslinking complicates regulation of quinone reactivity, posing challenges for practical and reproducible long-term applications.

Other functional groups

Other reactive functional groups, such as isocyanates, and aryl azides, have also been explored for covalent tissue adhesion, owing to their strong electrophilicity and ability to

react with nucleophilic groups on biological tissues[66,67]. However, these chemistries remain relatively underutilized in tissue–bioelectronics applications, owing to concerns related to cytotoxicity, nonspecific reactivity, limited stability in wet physiological environments, and practical challenges such as the need for additional activation steps or specialized reaction conditions, which complicate their use in clinical settings.

1.2.3 Biological interactions

Biological interactions govern the long-term fate of bioelectronic devices by mediating dynamic and reciprocal processes between implanted materials and living tissues at the tissue–device interface (**Fig. 1-1c**). Unlike physical and chemical interactions that primarily determine initial contact and adhesion, biological interactions operate over extended time scales and shape chronic biocompatibility by regulating immune recognition, cellular behavior, and tissue remodeling at the cellular and molecular levels. While foreign body reactions—characterized by macrophage activation, foreign body giant cell formation, and fibrotic encapsulation—represent a prominent and often adverse biological response to implanted devices[68], biological interactions extend beyond these defensive processes to include adaptive and integrative responses such as cell adhesion, migration, differentiation, and functional tissue integration[23]. Collectively, biological interactions determine whether bioelectronic interfaces are merely tolerated, actively isolated, or ultimately integrated with host tissues.

Passive interfaces

Passive interfaces aim to improve long-term tissue compatibility by minimizing biological perturbation at the tissue–device interface. These strategies rely primarily on biomimetic mechanical and structural design principles, including soft materials, miniaturized dimensions, and tissue-matched geometries, to reduce mechanical mismatch and foreign-body recognition following implantation. By limiting the magnitude of injury, micromotion-induced stress, and abnormal force transfer, passive interfaces can attenuate immune activation and delay the onset of chronic inflammatory responses[69,70]. Ultra-thin polymer–

metal–polymer architectures exemplify this approach, as their extremely low bending stiffness enables close mechanical matching with soft tissues and has yielded encouraging performance in long-term implantation studies[71–73]. More recently, hydrogel-based electronics have attracted increasing attention, as their intrinsically soft, hydrated, and viscoelastic nature closely resembles that of biological tissues, further promoting mechanical compatibility and interfacial stability[74–76].

Bioactive interfaces

Bioactive interfaces refer to engineered tissue–device interfaces that actively interact with and regulate the biological microenvironment through biochemical functionalities. By incorporating bioactive cues, such as extracellular matrix proteins, adhesion molecules, and growth factors, these interfaces are designed to modulate host responses such as immune activation, inflammation, and tissue remodeling, rather than relying solely on passive mechanical accommodation[77–79]. In addition to immunomodulation, bioactive interfaces can enhance selective adhesion of target cells by presenting specific biochemical signals that promote controlled cell–material interactions[78,80]. Through these mechanisms, bioactive strategies can influence macrophage polarization, suppress fibrotic capsule formation, and enhance cell adhesion at the interface, thereby improving long-term functional stability and signal fidelity of implanted bioelectronic devices.

Biohybrid interfaces

Biohybrid interfaces represent a more integrative strategy in which living biological components—such as cells or tissues—directly with electronic systems to establish dynamic, bidirectional interactions[23]. By leveraging the inherent adaptability of living tissues, biohybrid interfaces offer unique opportunities for achieving long-term functional integration and adaptive performance. For example, the use of a sciatic nerve fragment as a biohybrid electrode has enabled stable long-term neural recordings with minimal foreign body response following chronic implantation[81,82]. Similarly, cell-seeded electrodes have shown improved performance in neural recording and neural regeneration by using living

cellular components to promote tissue integration and functional coupling at the interface[83–85]. However, a key limitation of biohybrid approaches is the extended time—often weeks to months—required stable physiological interactions with host tissues, which remains a barrier to rapid functional deployment[23].

1.3 Principles for conformal interface on irregular surfaces

While the interfacial mechanisms discussed above elucidate how tissue–device interactions arise at the molecular, cellular, and tissue levels, effective bioelectronic integration ultimately requires precise control over physical contact between devices and complex biological surfaces. The stability of such conformal interfaces is governed by the interfacial adhesion strength and the mechanical rigidity of the device. Whereas strategies to enhance adhesion strength were addressed in Section 2, this section focuses on fundamental design principles for reducing device rigidity to enable conformal contact.

Here, we highlight two fundamental design strategies: structural engineering, which enables devices to geometrically adapt to tissue curvature and motion[17], and materials development, which utilizes intrinsic material properties to match tissue softness, stretchability, and physiological environments[18,19]. Together, these principles establish a unifying framework for designing bioelectronic interfaces capable of maintaining robust and durable contact with irregular biological surfaces in both wearable and implantable applications.

1.3.1 Principles of structure engineering for conformal interfaces

Structural engineering in bioelectronic interfaces refers to the deliberate design of device geometry, architecture, and layout to tailor effective mechanical behavior beyond intrinsic material properties. Among the relevant mechanical parameters, bending stiffness is a primary determinant of structural flexibility. For a rectangular thin-film or beam with width b and thickness h, the bending stiffness (D) is given by[86]:

$$D = E\frac{bh^3}{12} \tag{1.2}$$

where E is the Yong's modulus of the material. The cubic dependence on thickness highlights the dominant role of thickness reduction in enhancing structural flexibility. Consequently, many structural strategies for flexible bioelectronics promote bending-dominated deformation.

A representative example is the use of serpentine geometries, which transform axial deformation into bending and rotation of curved segments, thereby substantially reducing effective stiffness and material strain[87]. Under bending-dominated conditions, curved-beam mechanics suggests that the effective stiffness (k_{eff}) scales as[88–90]:

$$k_{eff} \sim \frac{EI}{R^2 L} \sim \frac{Ehw^3}{\theta R^3} \tag{1.3}$$

where I is the second moment of area, R is the radius of curvature, and L is the arc length, h is beam thickness, w is width, and θ is the central angle. This scaling highlights the importance of large radium-to-width ratios in enabling high conformability and stretchability without excessive strain.

Since biological tissues exhibit highly irregular, multiscale surface geometries, achieving conformal interfaces requires devices to be sufficiently flexible such that interfacial adhesion can overcome structural stiffness. As a simplest model, consider a rectangular thin film with Young's modulus E, thickness h, and total length $2L$, conformally wrapped around a cylindrical substrate of radius R **(Fig. 1-2a)**, the required adhesion energy in unit area (γ) can be expressed as[15]:

$$\gamma \geq \frac{Eh^3}{24R^2} \tag{1.4}$$

For a representative material (E ≈ 3 GPa) conforming to a cylinder (R ≈ 1 cm) via capillary interaction ($\gamma \approx 10$ mJ m^{-2}), the film thickness must be below ~20 μm.

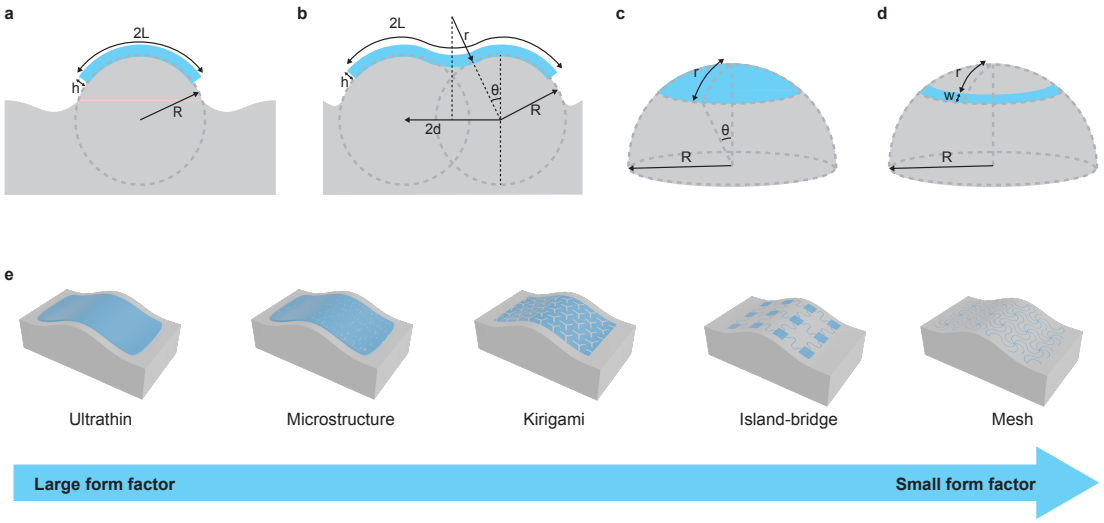

Fig. 1-2 Representative structural engineering models and strategies for conformal tissue–bioelectronics interfaces. (a-d) Representative conformal bioelectronic–tissue interface geometries. a, Rectangular thin film conforming to a cylindrical substrate. b, Rectangular thin film adhered to partially overlapped cylinders. c, Circular thin film conforming to a hemispherical substrate. d, Circular strip conforming to a hemispherical substrate. (e) Representative structural engineering strategies.

To model more complex geometries such as brain gyri, a pair of partially overlapping cylinders connected by a smooth arc can be considered (**Fig. 1-2b**). In this case, conformal adhesion requires the film thickness h to satisfy[15]:

$$\frac{R\sin\theta}{d-R\sin\theta}+\frac{dR\cos\theta}{(d-R\sin\theta)^2}-\left(\frac{24\gamma R^2}{Eh^3}\right)\left(1-\frac{d}{R\sin\theta}+\frac{d\theta\cos\theta}{R\sin^2\theta}\right)=0 \qquad (1.5)$$

with

$$\theta=\sin^{-1}\left(\frac{d}{R+r}\right) \qquad (1.6)$$

Using human cortical parameters (R ≈ 6.14 mm, d ≈ 5.93 mm, r ≈ 1.72 mm), the required thickness decreases to ~4.9 μm under capillary adhesion[15].

While cylindrical surfaces are developable and can, in principle, be conformally wrapped by thin films without inducing in-plane strain, many organs—such as the brain, heart, and stomach—exhibit non-developable geometries. For a planar circular thin film of radius r placed on a hemispherical surface of radius R (**Fig. 1-2c**), the circumferential mismatch between the film and substrate inevitably induces out-of-plane deformations such as wrinkling or buckling. However, when the contact area is sufficiently small ($\theta \ll 1$), this mismatch becomes negligible and conformal contact can be achieved.

An alternative solution for non-developable surface is to replace continuous films with narrow strip geometries (**Fig. 1-2d**). In this case, the required adhesion energy can be expressed as[15]:

$$\gamma = \frac{EI}{R^2} + \frac{w^2 Eh}{24r^2}\left(1 - \sqrt{1 - \frac{r^2}{R^2}}\right)^2 \tag{1.7}$$

where *w* is the strip width. Thin and narrow strips dramatically reduce the adhesion energy required to achieve conformal contact with non-developable surfaces, making capillary adhesion sufficient even on complex surfaces[15].

Taken together, these analyses show that achieving conformal interfaces with biological tissues fundamentally requires devices to be both thin and spatially small. Thickness reduction minimizes bending stiffness through its cubic scaling, thereby lowering the energetic penalty associated with bending. Simultaneously, reducing the lateral dimensions limits geometric mismatch, allowing modest adhesion energies to overcome the residual mechanical resistance.

Guided by these principles, a range of structural designs have been developed to enable conformal interfaces between bioelectronics and biological tissues (**Fig. 1-2e**). Ultrathin structures, with thicknesses on the order of tens of micrometers or less, substantially reduce bending stiffness and allow relatively adhesion provided by van der Waals interactions or capillary forces to be sufficient for achieving conformal interfaces with biological

tissues[3,21,27,91]. Microstructure engineering enhances conformability by introducing local mechanical compliance, in particular, micro-scale features such as microwrinkles and microcracks enable thin films to accommodate large deformations and complex surface curvatures by redistributing strain and reducing effective stiffness without sacrificing material integrity[92–95]. Kirigami-inspired designs introduce programmable cuts into thin films that transform in-plane stretching and compression into out-of-plane rotation, bending, and buckling of discrete structural units, enabling bioelectronics to accommodate large deformations and complex, non-developable surface curvatures while maintaining mechanical integrity and functional continuity[96–98]. Island-bridge designs connect rigid functional components with highly compliant interconnects, preserving high electronic performance while enabling mechanical adaptability[99–101]. Mesh electrodes further minimizing bending stiffness and volumetric footprint, enabling intimate mechanical coupling with soft and dynamic biological tissues[15,78,102–104]. Although increasingly minimal form factors improve mechanical flexibility and interfacial conformability, they often trade off component density and fabrication complexity.

1.3.2 Principles of materials development for conformal interfaces

Materials development provides a complementary route to conformal bioelectronic interfaces with soft and irregular biological tissues by enabling shape adaptation and stress accommodation through intrinsic deformation behavior. From a mechanics perspective, materials employed for conformal bioelectronic interfaces can be classified according to their constitutive deformation behavior into elastic, viscoelastic, and viscous regimes, each offering a distinct mode of conformal adaptation through reversible deformation, time-dependent stress relaxation, or flow.

Elastic materials (**Fig. 1-3a**), characterized by a dominant storage modulus (G') compared to the loss modulus (G''), store the majority of the mechanical energy induced by deformation in a recoverable elastic form and obey Hooke's law, in which deformation (ε) is linearly and instantaneously proportional to the applied stress (σ)[105]:

$$\varepsilon = \frac{\sigma}{E} \tag{1.8}$$

where E is the elastic modulus. As a result, sustaining stress is required to maintain conformal contact. Reducing elastic modulus lowers the stress needed to accommodate tissue curvature, thereby mitigating interfacial stress and facilitating the formation of conformal interfaces at soft and irregular tissue surfaces.

Viscoelastic materials (**Fig. 1-3b**), characterized by comparable storage and loss moduli ($G' \approx G''$), dissipate a significant fraction of the mechanical energy induced by deformation and exhibit time-dependent mechanical behavior. Notably, many soft biological tissues also display viscoelastic responses over physiologically relevant timescales[106]. Such behavior can be approximated by the Maxwell model[107]:

$$\frac{d\varepsilon}{dt} = \frac{1}{E}\frac{d\sigma}{dt} + \frac{\sigma}{\eta} \tag{1.9}$$

where ε is the strain, σ is the applied stress, E is the elastic modulus representing elastic energy storage, η is the viscosity associated with viscous dissipation, and t denotes time. Consequently, time-dependent deformation allows viscoelastic materials to gradually adapt to the substrate geometry, leading to partial relaxation of interfacial stress and stabilization of a conformal interface.

Viscous materials (**Fig. 1-3c**), characterized by a dominant loss modulus ($G'' \gg G'$), dissipate mechanical energy primarily through viscous flow and exhibit negligible elastic energy storage. Their deformation is governed by a constitutive relation of the form[108]:

$$\sigma = \eta\frac{d\varepsilon}{dt} \tag{1.10}$$

where σ is the applied stress, ε is the strain, η is the viscosity, and t denotes time. Viscous materials readily flow to conform to complex substrate geometries, such that conformal interfaces can be maintained with negligible interfacial stress. However, due to the lack of

elastic restoring forces, viscous materials have limited ability to maintain a stable shape, making them more suitable for short-term applications.

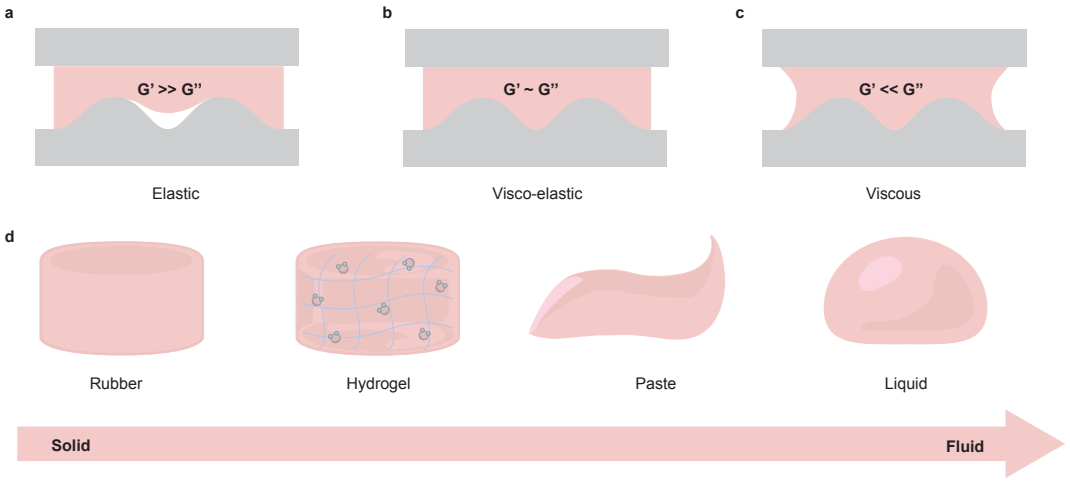

Fig. 1-3 Representative material development principles and material types. a, Elastic regime (G'≫G"). Reversible deformation with limited energy dissipation; reduced modulus lowers interfacial stress but requires sustained stress to maintain contact. b, Viscoelastic regime (G'≈G"). Time-dependent stress relaxation enables gradual surface adaptation and reduces residual interfacial stress. c, Viscous regime (G"≫G'). Flow-driven deformation enables near stress-free conformity but limits structural stability. d, Representative material classes. Elastomers, viscoelastic hydrogels, and paste-like or liquid materials span the continuum from solid-like to fluid-like behavior, balancing conformity and mechanical stability.

Elastomers, owing to their low elastic moduli and large reversible deformability, are widely used in bioelectronics to form conformal interfaces with soft tissues. Among these materials, silicone rubbers are one of the most extensively adopted elastomers due to their low Young's moduli (~10 kPa–1 MPa), which are comparable to those of many soft biological tissues, as well as their excellent chemical stability and established biocompatibility, enabling reliable long-term interfacial contact in implantable systems[92,109–111]. In addition to silicones, thermoplastic polyurethanes (TPU) and styrenic thermoplastic elastomers, such as

poly(styrene–ethylene–butylene–styrene) (SEBS), poly(styrene–butadiene–styrene) (SBS), and poly(styrene–isoprene–styrene) (SIS), are also commonly employed at biointerfaces. These materials provide improved mechanical durability, facile processability, and good compatibility with conductive fillers, making them particularly suitable for soft and stretchable bioelectronic interfaces[112–114].

Hydrogels represent a representative class of viscoelastic materials for conformal tissue interfacing, owing to their low effective moduli, high water content, and pronounced stress relaxation behavior. Unlike elastic elastomers, hydrogels undergo time-dependent deformation under sustained loading, allowing interfaces to gradually adapt to surface roughness and complex tissue geometries while partially releasing interfacial stress[115]. Their tissue-like mechanical properties and hydrated nature further promote intimate contact with biological surfaces. In addition, the viscoelastic response of hydrogels can be tuned through polymer composition, crosslinking density, and network architecture, enabling control over relaxation timescales and interfacial mechanics. These features make hydrogels particularly attractive for applications requiring long-term, stable conformal contact[32,38,74,116,117].

Paste-like and liquid materials occupy the fluid end of the interfacial material spectrum. Paste-like or gel-based materials, such as ultrasound gels and conductive paste, possess weak network structures that provide limited elastic resistance, allowing them to spread and conform to complex tissue geometries under applied pressure or shear, while retaining a degree of shape stability in the absence of sustained external forces[118–120]. Notably, such paste-like interfacial behavior is not limited to gel-based materials. Eutectic gallium–indium (EGaIn), although liquid at physiological temperatures, exhibits partial shape retention ability owing to the oxide layer, which imparts paste-like behavior and enables conformal bioelectronic interfaces for electrophysiological signals recording[121,122].

1.4 Fabrication strategies for bioelectronics interfaces

The intrinsic processing constraints of flexible and soft materials complicate the fabrication of bioelectronic interfaces, particularly due to their limited thermal, chemical, and

dimensional stability. These challenges become more pronounced when high geometric precision must be achieved alongside reliable electrical performance, particularly in applications that require personalized devices tailored to specific tissue geometries.[123,124]. Under such conditions, conventional fabrication strategies become insufficient, motivating the development of hybrid and multi-material fabrication approaches.

In this section, we review microfabrication approaches compatible with flexible substrates that enable improved patterning resolution, device reliability, and signal transmission stability at the tissue interface. We then highlight emerging printing-based strategies, including advanced three dimensional (3D) and in vivo printing approaches, and hybrid integration strategies that allow the construction of conformal, geometry-adaptive bioelectronic interfaces for complex biological environments.

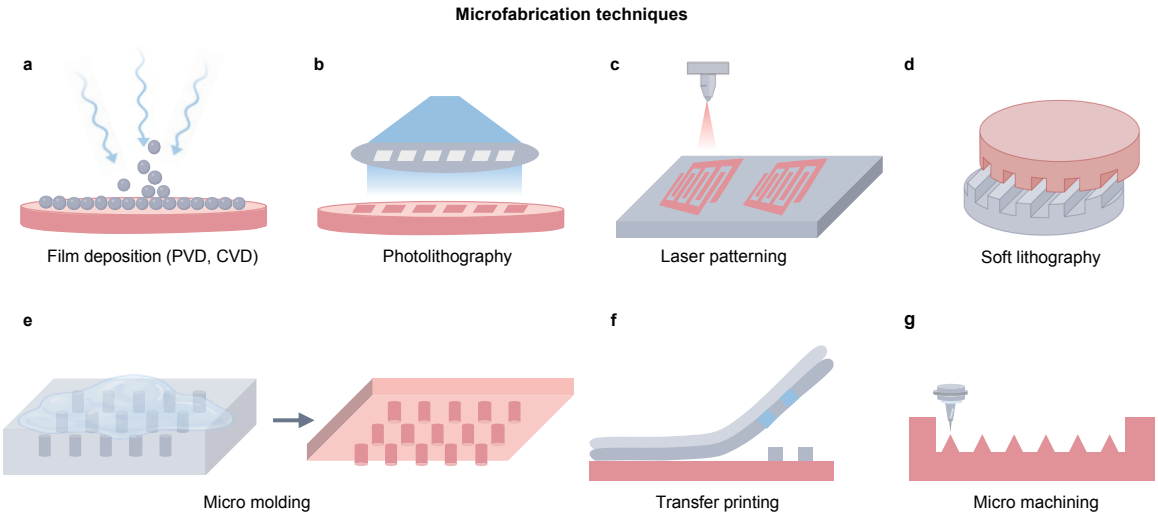

Fig. 1-4 Representative microfabrication strategies for flexible and in vivo bioelectronic interfaces. (a) Film deposition, CVD, chemical vapor deposition; PVD, physical vapor deposition; (b) Photolithography; (c) Laser patterning; (d) Soft lithography; (e) Micro molding; (f) Transfer printing; (g) Micro machining.

1.4.1 Microfabrication methods

Microfabrication methods form the foundation of many tissue–bioelectronics interfaces by enabling high-resolution patterning, dense interconnects, and well-controlled material stacks on flexible substrates. Although originally developed for rigid electronics, these techniques have been adapted to soft and stretchable materials through process modifications that balance geometric precision with mechanical compliance. In this subsection, we summarize representative microfabrication approaches and highlight their capabilities and limitations for constructing conformal bioelectronic interfaces.

Thin-film construction

Physical vapor deposition (PVD) is widely used to deposit the foundational thin-film layers for conformal tissue-bioelectronic interfaces (**Fig. 1-4a**). Its appeal lies in the precise control of film thickness, the ability to achieve uniform coatings over large areas, and the excellent electronic quality of the deposited films. A key limitation, however, is the thermal load associated with vacuum processing. Because many flexible substrates possess limited thermal tolerance, the allowable thermal budget often constraints materials choice and processing window.[124–126].

Chemical vapor deposition (CVD) provides an alternative route for thin-film formation and is frequently employed for stretchable dielectric layers. In this process, gaseous precursors are introduced into a reaction environment and undergo surface reactions on the substrate, resulting in the controlled growth of solid films (**Fig. 1-4a**). CVD enables the formation of nanoscale coatings with superior conformality and coverage, while preserving favorable mechanical, electrical, and chemical properties.[125,127].

Light-enabled patterning

Light-driven patterning methods define microstructures through photoinduced reactions and remain a central step in flexible electronics manufacturing. In conventional photolithography, light transmitted through a shadow mask induces localized chemical transformations in a

photosensitive material, such as photoinitiated crosslinking, while unexposed regions are removed during subsequent development (**Fig. 1-4b**). This approach is widely valued for its high resolution, scalability, and processing speed[112,128,129]. However, its limitations include mask-related constraints on achievable resolution and practical challenges in extending the workflow to very large-area substrates. In addition, many soft polymeric materials, such as hydrogels and elastomers, are sensitive to organic solvents and or prone to swelling, complicating lithographic patterning in soft or composite systems[130].

Laser patterning defines features through localized ablation using a focused beam that follows a programmed path (**Fig. 1-4c**). By adjusting laser power and scan speed, the cutting/engraving process can be precisely tuned[131,132]. Laser-based methods are attractive for maskless, rapid prototyping but are less suitable for materials that are transparent to the laser wavelength, resistant to thermal ablation, or rich in liquid. In such cases, additional ablation-stop layers or tightly controlled processing conditions may be necessary to ensure reproducibility[129,133,134].

Soft lithography and micromolding

Unlike conventional photolithography that relies on rigid masks, soft lithography employs elastomeric stamps, enabling repeatable, high-throughput pattern transfer onto compliant substrates (**Fig. 1-4d**). This approach is particularly attractive for curved, deformable, or hydrated surfaces, and is compatible with a wide range of hydrogels and elastomers[135,136].

Micromolding (mold casting) relies on a mold that defines the target geometry, into which a polymer precursor (e.g., a thermoplastic or UV-curable resin/photoresist) is introduced, cured, and subsequently demolded (**Fig. 1-4e**). Because fine features can be encoded directly into the mold, geometry definition and patterning occur simultaneously during casting[137,138]. Reusable molds replicated from a single master enables low-cost and scalable production of micro-/nano-scale patterns. Importantly, certain direct molding strategies can bypass traditional planar lithography and enable three-dimensional microstructures that would otherwise be difficult to realize[139,140].

Transfer printing

Transfer printing employs to deterministically relocate high-quality thin films from rigid donor substrates to flexible or stretchable receivers (**Fig. 1-4f**). Device yield is often limited by film fracture, misregistration, and incomplete transfer, making precise control of interfacial adhesion at each step essential for reliable pickup and placement[141–143]. Although transfer printing has enabled many hybrid bioelectronic systems, its application to elastomeric and hydrogel substrates remains challenging, as achieving robust and reversible adhesion on soft, hydrated materials is nontrivial[144,145].

Micromachining

Conventional micromachining uses high-speed rotating tools under miniature multi-axis CNC control to fabricate microscale geometries (**Fig. 1-4g**). This approach offers advantages in producing smooth surfaces, micrometre-scale sharp features, and strong repeatability, and can be scaled for batch manufacturing[140]. It is particularly compatible with rigid materials such as PMMA and stainless steel[146,147]. However, integrating rigid micromachined components with flexible substrates typically requires additional assembly steps, and achievable miniaturization and feature density are ultimately constrained by tool size and material machinability[147,148].

1.4.2 Printing methods

Printing-based approaches complement microfabrication by enabling additive, maskless construction of bioelectronic interfaces with complex geometries, material gradients, and three-dimensional architectures. These methods are particularly valuable for tailoring device form factors to irregular tissue surfaces and for integrating soft, multifunctional materials (**Fig. 1-5**).

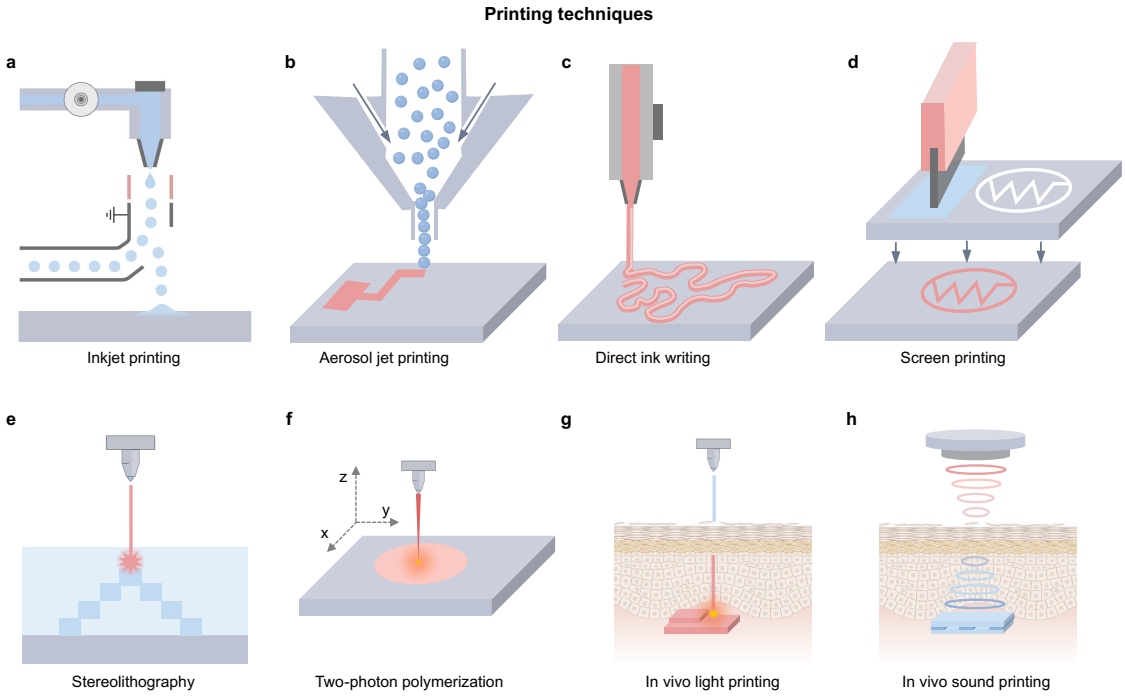

Fig. 1-5 Representative printing methods applicable to flexible interface fabrication. (a) Inkjet Printing; (b) Aerosol jet printing (AJP); (c) Direct ink writing (DIW); (d) Screen printing; (e) Stereolithography; (f) Two-photon polymerization (TPP); (g) In vivo light printing; (h) In vivo sound printing.

Inkjet printing

Inkjet printing ejects picolitre-scale droplets through a nozzle that is typically actuated either piezoelectrically or thermally. By tailoring ink properties, most importantly density, viscosity, and surface tension, droplet size and flight dynamics can be controlled, governing line width, feature uniformity, and deposition reliability[149,150] (**Fig. 1-5a**). As a maskless and non-contact technique, inkjet printing supports rapid patterning of a broad range of functional materials, including graphene-based inks, metals, dielectrics, and conducting polymers, and is inherently scalable. Practical limitations include nozzle clogging (particularly for particle-laden inks), a narrow rheological window for stable jetting, modest spatial resolution, and difficulty in constructing truly three-dimensional architectures via droplet-by-droplet deposition[151,152].

Aerosol jet printing

In aerosol jet printing, functional inks are atomized into fine droplets and transported by a carrier gas, then aerodynamically focused by a sheath gas to achieve feature sizes down to ~10 μm[153,154] (**Fig. 1-5b**). This approach enables relatively high-resolution deposition on demand and is well suited for thin, conformal layers on non-planar substrates. However, its low deposition rate limits throughput, constraining scalability for large-scale or high volume manufacturing[155].

Direct ink writing

Direct ink writing (DIW) builds 3D structures by extruding high-viscosity shear-thinning inks (~10^2–10^8 cP) in a layer-by-layer manner (**Fig. 1-5c**). The inks are typically formulated to be shear-thinning and to exhibit yield stress, enabling smooth extrusion while maintaining shape after deposition through rapid solidification. DIW is attractive for its materials flexibility: it can accommodate unconventional and sensitive components (e.g., enzymes) and readily supports multi-material printing to expand device functionality[156,157]. For conductive inks (notably carbon-based systems and MXenes), DIW can sometimes be implemented without binders/additives, helping preserve intrinsic electrical properties[158]. A key limitation is the difficulty of forming complex, self-supporting structures without compromising mechanical integrity or functional performance, which requires careful balancing of functional and support phases.

Screen printing

Screen printing remains widely valued owing to its low cost, simplicity, and suitability for large-area patterning. It relies on a predesigned mesh/stencil architecture through which a formulated ink is forced to form the desired pattern, and it can transfer inks onto a wide range of substrates (**Fig. 1-5d**). Mechanistically, the process proceeds in a reciprocating cycle: during the forward stroke, the squeegee drags ink across the screen and fills the open regions of the mesh; during the return stroke, a controlled pressure promotes ink release and transfer

onto the substrate surface[159,160]. By repeating the printing passes, multilayer accumulation becomes feasible, enabling the construction of raised, out-of-plane composite structures in a relatively simple manner. Owing to these advantages, screen printing has been broadly adopted in miniaturized and integrated electronics manufacturing, particularly where reducing the cost of large-batch production is a primary objective[161,162]. Its principal limitations include relatively coarse resolution and reduced pattern fidelity compared with lithographic methods.

Stereolithography (SLA)

Stereolithography (SLA) constructs 3D objects by sequentially solidifying patterned layers, typically by scanning a laser along a programmed path to cure liquid resin into the desired geometry. This layer-by-layer strategy can yield parts with fine details and smooth surface finishes[163] (**Fig. 1-5e**). A closely related route is to photopattern a thin film of precursor, then deposit an additional thin layer on top of the previous one and repeat the exposure—effectively building a 3D structure through stacked 2D photopatterning. To increase printing speed and improve manufacturing flexibility, digital micromirror devices (DMDs) can be employed. In DMD-based systems, an array of micromirrors modulates the illumination field to project predefined patterns, thereby generating a sequence of "virtual masks" without physically fabricating a mask set[164,165].

Despite these advantages, these approaches often require chemical development steps to remove unexposed regions, an issue that can become nontrivial for nanocomposites or solvent-sensitive formulations. More advanced variants, including digital light processing (DLP) and continuous liquid interface production (CLIP), further extend the throughput and process window of photopolymerization-based manufacturing[166–169]. Moreover, many photocurable resins are mechanically rigid compared with the soft materials preferred at tissue interfaces. Integrating elastomers, hydrogels, or shape-memory polymers into these high-throughput photopolymerization workflows—while ensuring mechanical durability and long-term stability—remains an important challenge for translating SLA-derived approaches for bioelectronic interfaces[170,171].

Two-photon polymerization

Two-photon polymerization (TPP) is a liquid-resin-based rapid prototyping method that has increasingly been used to fabricate miniaturized 3D medical structures directly from computer-aided designs. In TPP, a photosensitive resin undergoes near-simultaneous absorption of two photons within a highly confined focal volume, which initiates photochemistry between the photoinitiator and monomers only at the focal point[172,173] (**Fig. 1-5f**). Femtosecond-pulsed lasers are typically used to generate the required peak intensities, enabling three-dimensional structuring with feature sizes that can reach the nanoscale[173].

A wide range of photo-responsive materials can be processed by TPP, including acrylate-based polymers, organically modified ceramic systems, zirconia sol–gel formulations, and titanium-containing hybrid materials—many of which are accessible and cost-effective. However, the intrinsic trade-off between resolution, build volume, and printing speed limits throughput, motivating continued advances in optical design, materials chemistry, and process control for broader adoption in bioelectronics.

1.4.3 In vivo printing

With the rapid evolution of 3D printing technologies, in vivo bioprinting—also referred to as in situ, intraoperative, or living bioprinting—has emerged as an approach in which bioinks are deposited directly onto tissues under clinically relevant conditions, enabling immediate interaction with living systems[174]. A key distinction from conventional workflows is that in vivo printing effectively fuses “printing” and “implantation” into a single step with minimum invasive procedures. This integration allows real-time acquisition of local surface morphology, enabling the printing process to dynamically adapt to changes in the target geometry and evolving defect microenvironments. As a result, the printed construct can be shaped to closely conform to complex tissue geometries. Moreover, in situ crosslinking can reinforce adhesion between the printed construct and residual tissue, stabilizing tissue–interface integration while avoiding contamination or mechanical damage that fragile hydrogel scaffolds may experience during handling, transplantation, or suturing[174–176].

As in vivo printing forms 3D constructs inside the body, it imposes stricter constraints on bioinks than conventional ex vivo printing. Ideal bioinks should satisfy the following requirements: a) Fast crosslinking and reliable gelation in vivo under physiological temperature (~37 °C), a wet and mechanically dynamic interface, and potentially acidic local conditions; b) Tissue-matched mechanical compliance: flexible mechanical behavior resembling the native tissue targeted for repair; c) Biocompatibility with programmable biodegradation: supporting cell proliferation, migration, and infiltration as a temporary scaffold, followed by controlled degradation as the tissue matures; d) Strong wet-tissue adhesion: robust, long-term attachment to moist and potentially bleeding tissue surfaces in the defect region; e) One-step curing: avoiding post-processing during gelation to minimize disruption of local physiology[177].

Light-triggered in vivo printing

Light-based in vivo printing typically involves delivering a liquid bioink precursor to a defect site, followed by spatially selective illumination to localized gelation or polymerization. A central requirement is sufficient tissue penetration of the excitation light, which limits the utility of ultraviolet activation in many settings[163,178]. Accordingly, significant effort has been directed toward systems that respond to near-infrared (NIR) illumination, given its improved penetration in soft tissues (**Fig. 1-5g**).

For example, a nanoparticle-assisted initiating system was introduced to enable GelMA gelation under DMD-projected patterns[179]. The resulting subcutaneously printed hydrogel constructs were reported to maintain high cell viability and exhibit favorable tissue integration, suggesting therapeutic relevance for volumetric muscle loss[179]. Alternatively, approaches based on two-photon excitation of coumarin derivatives have enabled high-resolution in vivo printing without conventional photoinitiators[180]. In these systems, multiphoton microscopy can simultaneously image and guide the laser scanning, creating a closed-loop printing process with micrometer-scale spatial precision. With controllable optical power, minimally invasive in situ light-based printing has been demonstrated for generating complex architectures within mouse skin, muscle, and brain, without apparent

adverse effects on adjacent healthy tissue. Despite their minimal invasiveness and high resolution, light-based approaches remain constrained by penetration depth and printable volume.

Ultrasound-triggered in vivo printing

Ultrasound offers a complementary trigger for in vivo printing owing to its deep tissue penetration and compatibility with real-time imaging. High-frequency (>2 MHz) acoustic waves can propagate through heterogeneous tissues, and focused ultrasound can localize energy deposition at depths approaching tens of centimetres. These properties have motivated emerging approaches that use ultrasound as a trigger for in vivo 3D printing (**Fig. 1-5h**).

For example, an "acoustic ink"—a mixture of polymers, particles, and chemical initiators—was designed to absorb acoustic energy, rapidly form a gel to suppress flow, and simultaneously enable a thermally triggered acrylate polymerization reaction, thereby achieving localized material formation[181]. Building on this direction, an ultrasound-enabled 3D printing approach capable of creating complex structures beneath centimeter-thick tissue in vivo was developed. This strategy could be integrated with conventional ultrasound imaging to customize implant geometries based on real-time needs. Importantly, acoustic inks can be engineered with additional functions relevant to bioelectronics, such as electrical conductivity, local drug delivery, and wet adhesion. Incorporating conductive nanoparticles enables the printing of soft sensors and biopotential electrodes that can record electrical activity from living tissues, supporting proof-of-concept monitoring of physiological signals such as ECG and EMG[62].

Overall, these proof-of-concept demonstrations highlight the translational potential of ultrasound-triggered in vivo printing for creating customized bioelectronics interfaces that conform to target anatomy. This acoustically mediated strategy helps relax constraints associated with tissue depth and can be compatible with image-guided, precision placement.

Nonetheless, expanding the repertoire of in situ printable bioelectronic functions—beyond structural fabrication—remains a key step toward realistic clinical translation.

Extrusion-based and droplet-based in vivo printing

In addition to light- and ultrasound-triggered strategies, extrusion-based and droplet-based approaches have been explored for in situ printing, particularly on external or surface-accessible tissues. In extrusion bioprinting, bioinks rapidly responds to a prescribed stimulus applied at the nozzle (e.g., pressure-driven extrusion), forming a continuous, smooth filament that is well suited for macroscale deposition and can support its own weight[182]. The filaments are then deposited layer-by-layer onto the defect region to build three-dimensional constructs. A representative class of extrusion-printable inks is photo-crosslinkable gelatin methacryloyl (GelMA). To date, a substantial body of research has focused on extrusion-based in situ printing for applications such as skin wound closure and repair of superficial tissue defects, where geometric coverage and rapid scaffold formation are priorities. By contrast, droplet-based in situ bioprinting deposits bioinks as discrete droplets at predefined locations, enabling precise, non-contact placement[183]. Droplets are commonly generated at picoliter scales using thermal, piezoelectric, or laser-assisted actuation, which helps preserve cell viability while offering fast printing, relatively high spatial resolution, and flexible patterning[184].

1.4.4 Combination strategies

Soft bioelectronic systems are rarely built as single-function devices; instead, they typically comprise multiple functional modules assembled into an united platform. To realize closed-loop operation that couples diagnosis with therapy, a single system often needs to incorporate sensors, control system, Data analysis and storage, power supply, and stimulation units. A fundamental challenge is that these modules frequently rely on distinct material sets and fabrication requirements, making it highly nontrivial to manufacture every component directly on one fully stretchable substrate without sacrificing performance. To address this

gap, hybrid (mixed-mode) manufacturing has become an important route for electronics that must conform to complex biological surfaces.

In hybrid integration, rigid, high-performance electronic elements are combined with soft or flexible substrates, enabling a practical balance between long-term wearability/implantability and high-fidelity signal integrity. By decoupling mechanical compliance from electronic functionality, hybrid integration can preserve essential device performance while improving user comfort and chronic stability—representing a key enabling concept for advanced bioelectronic interfaces.

At the manufacturing level, combining micro/nanofabrication with multiple 3D-printing approaches and tissue-engineering techniques enables the constructionof 3D electronic architectures directly on or within biological tissues, with robust functionality and stable performance. Beyond process-level integration, system-level assembly is equally critical: multilayer stacking to form vertically integrated architectures[185–188], adhesive-based bonding of discrete components[185,189,190], and mechanical interlocking or co-assembly between different substrates[123] can all support efficient integration of multifunctional biointerfaces within a single platform.

Looking forward, a key translational challenge is scaling these combination strategies toward reproducible, batch-compatible manufacturing while preserving the mechanical compliance, interfacial stability, and long-term performance required for soft bioelectronics. Addressing this challenge will be critical for translating complex, multifunctional tissue–bioelectronics systems from laboratory demonstrations to widespread clinical use.

1.5 Applications in sensing and modulation

Bioelectronic devices interfaces with biological tissues have rapidly developed in recent years, encompassing wearable, implantable, and swallowable formats for monitoring a wide range of physiological signals and enabling multimodal therapeutic modulation[191]. These platforms provide expand the scope of personalized medicine by supporting continuous

sensing and targeted intervention. In this section, we categorize applications into two major areas: biosignal monitoring and therapeutic intervention. In this section, we will discuss approaches for sensing electrophysiological, biochemical, and biophysical signals, as well as strategies for therapeutic intervention, including drug delivery, electrotherapy, and stimulation-based therapies.

1.5.1 Physiological signal monitoring

Living tissue–interfaced sensing enables seamless integration of physiological monitoring with the human body and underpins continuous health management and disease prevention. Multiple sensing modalities, including electrophysiological[192], biochemical[193–195] and biophysical approaches[196,197], can be implemented through appropriately engineered tissue–device interfaces.

Electrophysiological signals

Electrophysiological sensors capture bioelectric potential variations from electrically active organs and tissues, most commonly the brain, heart, and skeletal muscle, yielding signals such as EEG, ECG, EMG, and EOG. In practice, these measurements typically require intimate electrode tissue contact to maximize coupling efficiency and sensitivity. Because the electrode tissue interface impedance directly shapes signal quality (noise floor, bandwidth, and motion artifacts), engineering a high-quality, conformal biointerface is often as important as the front-end electronics.

A representative example is an ultrathin, breathable elastic conductor built on a thin elastomeric substrate with a microcracked metal film, achieving a total thickness on the order of ~1.3 μm. Its low bending stiffness enables nearly seamless lamination onto skin and soft biological surfaces, supporting continuous acquisition of ECG and subtle mechanical signatures such as pulse-wave-related signals[192] (**Fig. 1-6a**). For neural recordings, an ultra-compliant and scalable cortical interface (NeuroGrid) illustrates how organic, highly conformal arrays can follow the brain's curved topology and deliver stable, high-SNR field-

potential recordings in clinical contexts such as epilepsy monitoring[198] (**Fig. 1-6b**). At the non-invasive end of the spectrum, a wrist-worn surface-EMG neuromotor interface demonstrates that robust motor-intent decoding can be achieved with wearable electrophysiology, balancing performance with usability for human-computer interaction[199] (**Fig. 1-6c**).

Biochemical biomarkers

Biochemical markers, such as pH, glucose, lactate, electrolytes, and hormones, provide critical information on physiological homeostasis and disease states. These targets can be sampled from multiple biofluids (blood, sweat, interstitial fluid, saliva, and gastrointestinal fluids), but continuous operation, sensing reliability, long-term stability, and user comfort remain persistent constraints for many biochemical biointerfaces.

A skin-interfaced wearable aptamer platform based on a target-triggered strand-displacement mechanism provides a concrete pathway toward non-invasive hormone tracking (e.g., estradiol) through in situ sweat analysis, supported by on-body microfluidics for time-resolved sampling[194] (**Fig. 1-6d**). Ingestible biointerfaces extend biochemical sensing to internal organs: the PillTrek capsule (~7 mm diameter, 25 mm length) integrates miniaturized wireless electrochemical instrumentation with interchangeable sensors to profile multiple gut parameters (e.g., pH, temperature, neurotransmitters, and metabolites), enabling longitudinal tracking of dynamic monitoring of diet- and health-related biochemical dynamics[195] (**Fig. 1-6e**). For higher-molecular-weight targets, microneedle-based interstitial fluid platforms combined with regenerable ("active-reset") protein sensors have demonstrated real-time tracking of protein biomarkers in vivo, representing an important step for translating biochemical sensing beyond small molecules[193] (**Fig. 1-6f**).

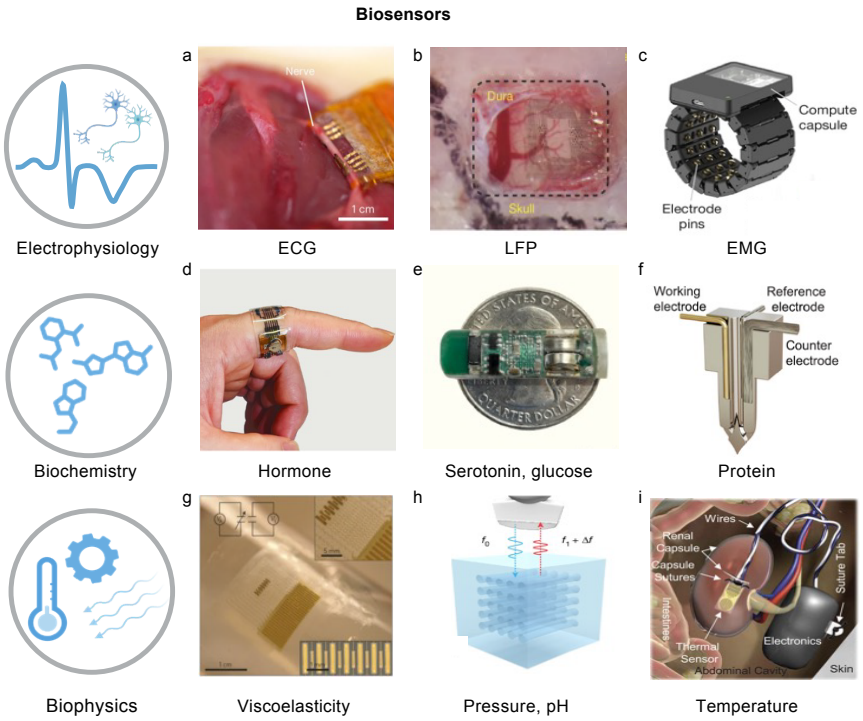

Fig. 1-6 Representative tissue-interfaced bioelectronic platforms for physiological monitoring. (a–c) Electrophysiological monitoring. a, Ultrathin elastic epidermal conductor enabling conformal ECG acquisition. b, Highly compliant cortical interface (NeuroGrid) for stable neural field-potential recording. c, Wearable surface-EMG neuromotor interface for motor-intent decoding. (d–f) Biochemical sensing. d, Skin-interfaced wearable aptamer sensor for hormone monitoring in sweat. e, Ingestible smart capsule for longitudinal gastrointestinal biochemical profiling. f, Microneedle/interstitial-fluid platform with regenerable protein sensors for continuous inflammation monitoring. (g–i) Biophysical sensing. g, Conformal piezoelectric actuator–sensor array for near-surface tissue viscoelasticity measurement. h, Injectable bioresorbable ultrasonic sensor for deep-tissue multiparameter monitoring. i, Implantable thermal and conductivity sensor for organ-level inflammatory assessment.

Biophysical signals

Bioelectronic interfaces increasingly target biophysical readouts, including mechanical forces, temperature, and optical or acoustic signatures. Strain and pressure sensors quantify tissue deformation and force transmission, respectively. A conformal piezoelectric actuator–sensor network built from ultrathin inorganic piezoelectric elements (e.g., PZT nanoribbons) enables rapid, quantitative assessment of near-surface tissue viscoelasticity with intimate contact to soft, textured biological surfaces[91] (**Fig. 1-6g**).

For deep-tissue monitoring, an injectable, bioresorbable metastructured hydrogel ("metagel") ultrasonic sensor demonstrates wireless multiparameter readout (including intracranial pressure, temperature, pH, and flow-related signals) by translating volumetric responses into ultrasound-detectable spectral shifts, with reported sensing at depth and degradation over weeks, highlighting a minimally invasive route to chronic monitoring without wired leads[196] (**Fig. 1-6h**). Temperature monitoring is also clinically meaningful because localized thermal changes can serve as early indicators of inflammation or infection. An implantable bioelectronic system that continuously tracks local organ temperature and thermal conductivity on the kidney surface illustrates how biophysical sensing can support early detection of inflammatory processes associated with transplant rejection in animal models[197] (**Fig. 1-6i**). Finally, bioacoustic/mechano-acoustic sensing has become increasingly attractive for non-invasive monitoring of deep or otherwise hard-to-access physiology. Many routine biological activities (e.g., valve motion, gastrointestinal peristalsis, vocal fold vibration) generate mechanical waves with rich spectral content; soft, skin-compatible acoustic sensors can capture these signatures for continuous health monitoring and human-machine interfacing[200–202].

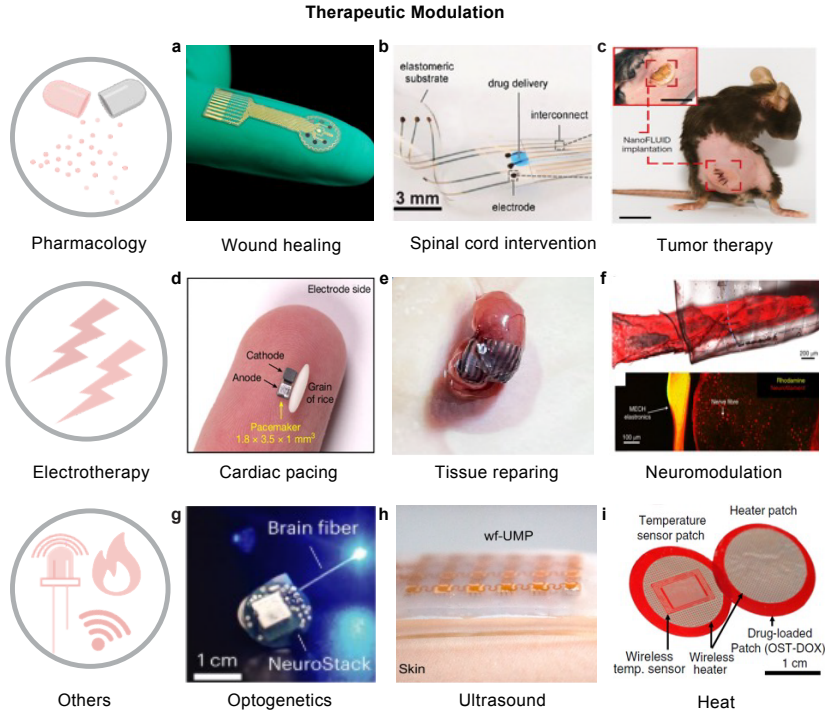

Fig. 1-7 Representative tissue-interfaced bioelectronic platforms for therapeutic intervention. (a–c) Drug-based and intracellular therapeutic platforms. a, Wireless wearable system integrating wound sensing with electrically triggered drug release and stimulation-assisted healing. b, Electronic dura mater ("e-dura") enabling localized pharmacological modulation and spinal neuromodulation. c, Flexible nanofluidic intracellular delivery patch for electroporation-assisted molecular transport within internal organs. (d–f) Electrical stimulation and electrotherapy. d, Millimetre-scale bioresorbable optoelectronic implant for temporary cardiac pacing. e, Self-powered biodegradable electronic bandage for accelerated intestinal wound repair. f, Conductive hydrogel-based elastic microelectronic array for low-voltage neuromodulation. (g–i) Optical, acoustic, and thermal modalities. g, Multifunctional microelectronic fiber for optogenetic modulation in deep-brain and gastrointestinal applications. h, Wearable flexible ultrasound microneedle patch (wf-UMP) for acoustic-enhanced cancer therapy. i, Flexible wireless thermal modulation system integrating heating and drug delivery for intracranial tumor treatment.

1.5.2 Multimodal disease management

Real-time disease intervention and management constitute another major application area of bioelectronics interfaces. In particular, the effective integration of strategies based on diverse stimuli, including pharmacological treatment[203], electrotherapy[204,205], photostimulation[206], thermal stimulation[207], and acoustic stimulation[208], with bioelectronics devices offers reliable, safe, and scalable possibilities for treating various diseases, especially chronic conditions. For vital organs such as the nervous system and heart, these devices are designed not only to meet therapeutic needs but also to reduce invasiveness, simplify surgical procedures, and improve long-term prognosis management.

Drug-based therapy and on-demand delivery

Soft bioelectronic interfaces provide platforms for localized drug delivery, enabling spatially confined and dose-controllable release at the target site. This localized paradigm can maximize drug exposure in the lesion region while minimizing off-target distribution and systemic side effects. Importantly, drug-delivery functionality can be coupled with in situ sensing of local physiological signals to create feedback-regulated therapeutic systems. For example, a fully integrated, wireless wearable system combines multimodal wound monitoring with electrically triggered release of anti-inflammatory/antimicrobial agents, alongside exogenous electrical stimulation to promote tissue regeneration[209] (**Fig. 1-7a**).

Implantable neural interfaces have similarly incorporated localized pharmacological actuation. The electronic dura mater ("e-dura") integrates electrophysiological recording, signal routing, and local delivery modules, enabling electrochemical neuromodulation of spinal circuits and supporting motor-function restoration after severe spinal cord injury[210] (**Fig. 1-7b**). In parallel, emerging intracellular delivery concepts further expand the scope of bioelectronic-tissue interactions. A battery-free and chipless flexible nanofluidic intracellular delivery patch (NanoFLUID) has been developed for efficient payload transport into cells

within internal organs; the nanopore–microchannel–microelectrode architecture enables safe electroporation-assisted transmembrane delivery, boosting transport kinetics by ~10^5 compared with passive diffusion, and illustrates the potential of stable, cell-level bioelectronic interfacing[203] (**Fig. 1-7c**).

Electrotherapy and electrical stimulation

Electrical stimulation is widely used to modulate neural and muscular activity for suppressing pathological excitability, relieving pain, or accelerating tissue repair. Flexible and soft stimulation platforms are particularly attractive because their compliant mechanics and conformal contact can reduce interfacial impedance and improve charge-injection efficiency, thereby supporting effective and potentially long-term interventions. A representative example is a millimetre-scale bioresorbable optoelectronic system that combines wireless power with optical control to deliver programmable stimulation, demonstrating a temporary pacing strategy while minimizing patient burden through fully resorbable materials and minimally invasive deployment[205] (**Fig. 1-7d**).

Soft and biodegradable electrotherapeutic devices have also shown substantial promise in regenerative medicine. A self-powered electronic bandage made from soft, bioresorbable materials has been reported to accelerate intestinal wound healing by integrating two complementary stimulation modes including pulsed stimulation to facilitate epithelial cell transfection and direct-current stimulation to enhance pro-healing factor secretion, thereby improving closure and regeneration in vivo[211] (**Fig. 1-7e**). In addition, conductive hydrogel-based elastic microelectronic arrays, with Young's modulus in the kPa range and thickness down to ~20 μm, further demonstrate stable in vivo electrical performance and therapeutically relevant current densities at low operating voltages, highlighting the advantages of tissue-like mechanics for efficient neuromodulation[212] (**Fig. 1-7f**).

Other stimulus modalities

Soft bioelectronics are increasingly integrated with light, acoustic, and thermal modalities to expand the therapeutic design space. Wireless, miniaturized, implantable optoelectronic probes enable cell-type-specific optogenetic modulation in neuroscience, supporting translational applications in neurological disease management. Multifunctional polymer-fiber bioelectronic interfaces that embed multiple solid-state microelectronic elements can access both deep-brain regions and the tortuous gastrointestinal tract. When paired with wireless control electronics, such interfaces can support programmable optogenetic stimulation of dopaminergic (DA) neurons to evoke reward-related behaviors, and intraluminal stimulation of vagal-afferent pathways to probe brain–viscera communication[206] (**Fig. 1-7g**).

Ultrasound-triggered interventions are also rapidly evolving. An integrated wearable flexible ultrasound microneedle patch combines a conformal lead-free transducer array with a dissolvable microneedle drug-delivery module; ultrasound activation promotes drug release and reactive oxygen species generation for effective tumor therapy, offering a portable and minimally invasive acoustic platform for cancer treatment[208] (**Fig. 1-7h**). Thermal modulation provides yet another route to spatiotemporally controlled therapy. A flexible, adhesive, biodegradable, and wirelessly controlled intracranial device has been reported to integrate a wireless heater, a temperature sensor, and a drug-loaded patch; radiofrequency magnetic-field activation enables mild thermal actuation that enhances drug release and penetration depth, yielding therapeutic benefit in a mouse glioblastoma model[207] (**Fig. 1-7i**).

1.5.3 Closed-loop strategies

Recent advances have enabled biointerfaces that integrate sensing, computation, and actuation into closed-loop systems, advancing the goal of personalized and adaptive therapy[213]. **Fig. 1-8** summarizes the key components and operating principles of closed-loop bioelectronic platforms.

In prosthetics, closed-loop concepts restore motor function by incorporating sensory feedback. A monolithically integrated, soft, low-voltage “electronic skin” (e-skin) platform

operates without rigid electronic components while reproducing several core features of biological somatosensation. This system integrates pressure and temperature sensors with neuromorphic circuitry capable of conditioning signals into spike-like pulse trains that directly drive closed-loop actuation, thereby emulating sensory–motor feedback pathways. By addressing long-standing challenges in system-level integration, this work provides a practical route toward e-skins with advanced tactile feedback capabilities[214].

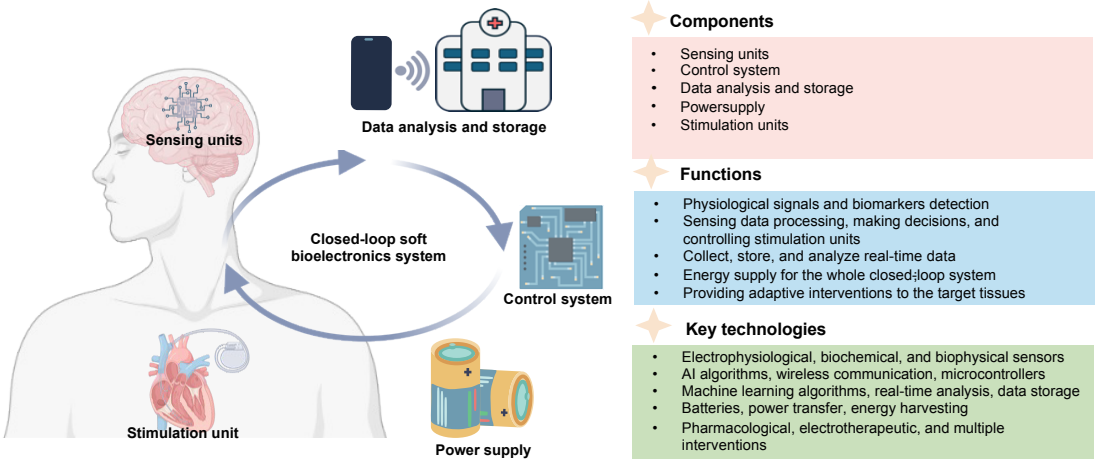

Fig. 1-8 Architecture of integrated closed-loop soft bioelectronic systems. Schematic representation of a closed-loop bioelectronic platform that integrates sensing, computation, power management, and therapeutic actuation. Physiological signals acquired by conformal sensing units are transmitted to embedded control electronics for signal processing, data storage, and decision-making. Based on predefined algorithms or adaptive models, stimulation or drug-delivery units are activated to provide targeted intervention. Wireless communication modules enable external data transfer and system monitoring, while power sources (for example, batteries or wireless energy transfer modules) support continuous operation.

Closed-loop operation has also been demonstrated in implantable optoelectronic biointerfaces. Miniaturized bio-optoelectronic implants based on microscale inorganic LEDs (μ-ILEDs) deliver optical stimulation to activate opsins. while flexible biophysical sensors continuously track organ function. Embedded control and data-analysis routines detect

pathological patterns and automatically trigger intervention. In a representative demonstration, algorithm-guided closed-loop optogenetic modulation of bladder sensory afferents restored normal bladder function[215].

1.6 Strategies for biocompatibility optimization

Interactions at the bioelectronic–tissue interface largely determine the biocompatibility, performance, and operational lifetime of bioelectronic devices. When interfaces with pronounced mechanical or chemical mismatches are chronically implanted, or maintained in long-term contact with target tissues, adverse events can arise across acute and chronic stages. In neural implantation, for instance, acute complications may include elevated intracranial pressure, hemorrhage, and disruption of the blood-brain barrier, followed by immune-driven recruitment and accumulation of nonfunctional glial cells and astrocytes that progressively compromise the brain-electrode coupling and signal reliability[216,217]. In vascular settings, bulky and stiff wire-type electrodes can intensify sustained abrasion against the compliant endothelial surface, promoting local injury that increases the risk of thrombus formation and vessel narrowing. Even in wearable platforms, prolonged use may cause user discomfort and inflammatory skin symptoms (e.g., dermatitis)[218], and in severe cases, persistent irritation and local inflammation can precipitate unintended device dislodgement or extrusion[219]. Importantly, even when interface materials are nominally non-cytotoxic and chemically stable, cyclic mechanical loading in harsh in vivo environments can still induce fatigue, degradation, or fracture. Such failure modes may release metal ions and particulate debris, or lead to secondary functional issues such as insulation breakdown and loss of electrode performance, thereby accelerating interface malfunction and indirectly amplifying immune activation[220]. Accordingly, this section highlights four complementary approaches to improve bioelectronic interface biocompatibility: mechanical adjustment, chemical modification, bioactive modification, and drug-releasing surfaces (**Fig. 1-9**).

1.6.1 Mechanical adjustment

Conventional electronics built on Si and other inorganic functional materials are typically orders of magnitude stiffer than soft tissues, and they also differ markedly in thickness, deformability, and overall geometry. Such physical mismatches amplify interfacial micromotion and local strain concentrations, which can cause repetitive micro-injury, compromise recording/stimulation fidelity, and exacerbate the foreign-body response (FBR). Immunology studies consistently indicate that large disparities in stiffness and device dimensions are associated with more severe chronic inflammation and encapsulation. Mechanically induced immune responses often originate from interfacial stress caused by mechanical mismatch. Consequently, reducing device rigidity to minimize interfacial stress has become a central design principle, similar to strategies used for achieving conformal interfaces. Broadly, these approaches can be categorized into structural engineering and materials development.

Structure engineering of established electronic materials to achieve effective softness. Instead of changing the functional materials, structural designs—such as macro-/micro-/nano-porosity and mesh-like architectures—reduce the effective flexural rigidity while maintaining electrical performance[103,221]. Open, mesh-based implants can minimize tissue trauma and scarring, decrease the total implant "footprint" and flexural rigidity, and facilitate tissue ingrowth and nutrient diffusion[103,222].

Development of intrinsically compliant electronic materials. A complementary route is to replace or hybridize conventional conductors and encapsulants with materials whose mechanical properties better match those of tissue. Hydrogels are particularly attractive because their low modulus and high water content can substantially mitigate stiffness-driven FBR in neural interfaces[223–225]. Viscoelastic alginate matrices combined with Ag flakes have enabled conductive hydrogel composites for skin-mounted neuromuscular stimulation electrodes[226] and Ag–polyacrylamide–alginate hydrogels have likewise been used to form conformal interfaces[227].

1.6.2 Chemical modification

Beyond mechanically driven interfacial trauma, the chemical nature of the electrode and encapsulation materials is also a key determinant of device usability and operational lifetime, because it governs how the interface interacts with the extracellular milieu and immune system. In practice, chemical compatibility is often evaluated along closely related dimensions, including intrinsic cytotoxicity and the propensity to trigger immune-mediated signaling at the material–tissue boundary[220,228,229]. Classical electronic materials—such as many implant-grade metals and silicon—have been widely adopted in neural electrodes over past decades, in part because they generally exhibit relatively low baseline toxicity in vivo. By contrast, newly developed polymeric systems (especially those that rely on reactive chemistries, initiators, plasticizers, or incomplete curing) can face additional scrutiny regarding material-intrinsic toxicity and the risk of residual monomers or other leachable species. Accordingly, before any implantable interface is advanced to in vivo testing, a comprehensive cytotoxicity and extractables/leachables assessment should be performed to minimize risks associated with material composition and potential unreacted or degradative byproducts[230,231].

In addition to material selection, surface chemical modification of polymer coatings on the device offers an effective route to mitigate FBR[232]. The central idea is to tune the interfacial chemistry such that immune-related signaling cascades are weakened—often by suppressing the earliest events that initiate downstream inflammation and fibrotic remodeling. Because protein adsorption and subsequent cell adhesion are common initiating steps for chronic immune activation, forming a stable, dense, and strongly hydrated antifouling layer at the interface can function as an anti-adhesion barrier. Such a hydration-rich layer reduces nonspecific adsorption of proteins, thereby lowering the likelihood of surface “conditioning” cellular contamination, and the subsequent amplification of immune cell recruitment and proliferation around the implant[236].

For bioelectronic interfaces, an additional constraint is that surface treatments should preserve electrical and ionic coupling between the device and tissue. Therefore, a primary design requirement is to minimize any adverse impact on signal transmission, for which

ultrathin antifouling coatings are particularly advantageous. Common antifouling chemistries include poly(ethylene glycol) (PEG) and, more recently, zwitterionic polymer coatings[234,235], both which leverage strong surface hydration to resist protein attachment and can reduce collagen deposition and biofouling for extended periods after implantation. For example, zwitterionic coatings on implanted glucose sensors maintained a low-fouling surface without dense collagenous encapsulation for at least three months, illustrating the potential of charge-balanced, superhydrophilic interfaces to sustain low-fouling conditions in vivo[236].

1.6.3 Bioactive modification

For certain applications—particularly neural interfaces—bioactive coatings can actively promote long-term compatibility by encouraging neurite ingrowth and supporting neuronal survival near the implant[77–79]. Incorporating extracellular-matrix (ECM) components, adhesion ligands, or growth-factor-related cues can modulate the local biological response, while cell-recognition elements (for example, selective antibodies) can enable preferential interactions with specific cell types. These strategies expand the functional scope of bioelectronic interfaces beyond passive toward more biologically integrated, potentially disease-modulating interventions.

ECM-derived bioactive coatings have been used to reduce glial scarring without compromising electrode operation. For instance, laminin coated microelectrode arrays (MEAs) exhibited a pronounced reduction in glial scar formation in a rat model over a one-month implantation period[237]. Similarly, astrocyte-derived ECM coatings of Si MEAs attenuated gliosis relative to clinically used, collagen-based formulations approved by the U.S. Food and Drug Administration (FDA)[79]. Hydrogels are particularly attractive bioactive coatings because their mechanical properties and chemical functionalities are tunable and they can provide a permissive 3D microenvironment that supports cell survival and outgrowth. This versatility enables “living” coatings that incorporate viable cells and exploit their paracrine signaling[224]. For example, hybrid microelectrodes seeded with live hippocampal neurons or astrocytes and subsequently protected by a biodegradable fibrin

hydrogel layer substantially reduced reactive astrocyte adsorption and weakened FBR-associated reactions while maintaining the electrode's electrical resistance[84].

A more targeted direction is to integrate cell-targeting bioactive layers that guide selective interactions with defined cell populations. In one design, SU-8 based mesh electronics were functionalized with antibodies (anti-EAAT2, anti-CD11b, and anti-D2DR) together with a laminin-1 derived synthetic peptide. Following implantation into the mouse hippocampus, chronic electrophysiological measurements and longitudinal histology demonstrated preferential targeting of distinct cell types (neurons, astrocytes, and microglia) and even neuronal subtypes, enabling cell-resolved interfacing that is difficult to achieve with non-functionalized probes[78].

1.6.4 Drug-releasing surfaces

A complementary strategy to attenuate foreign-body response (FBR) and subsequent scar formation is local immunomodulation, in which immunosuppressive or anti-inflammatory agents are incorporated at or within the bioelectronic–tissue interface. Representative examples include corticosteroids such as dexamethasone and anti-fibrotic compounds. Short-term local administration of these agents can temporarily suppress inflammatory-cell recruitment and, in some contexts, improve protein secretion from immune-isolated cell grafts by reducing immune-mediated isolation. However, many anti-inflammatory drugs are inherently pleiotropic, with broad biological effects and potential dose-limiting toxicities, which can introduce biocompatibility trade-offs beyond mechanics. This makes targeted immunomodulation preferable whenever feasible.

Beyond the four core approaches above, additional interfacial parameters can also shape tissue responses and long-term compatibility, including surface topography (hydrophobic/hydrophilic balance, roughness, and the arrangement/density), surface charge, wettability, and overall implant geometry[238,239]. For roughness, submicron features (<1 μm) appear to exert minimal influence on FBR, whereas features on the order of 1–4 μm can improve implant integration in some settings. Spatially confined architectures—where

characteristic dimensions are smaller than immune-cell size—may restrict the spreading and activation of pro-inflammatory cells on the material surface[240,241]. Importantly, while topographical tuning can be beneficial, it should not compromise the device's global mechanical integrity or its intended functional performance.

Surface charge is another key variable because it can regulate protein adsorption and shape immune-cell–material interactions across different phases of FBR. Adsorption behavior is often governed by net surface charge rather than by purely atomistic electrostatic interactions[242–244]. The interfacial charge state is determined by the relationship between the surface isoelectric point and the surrounding fluid pH: pH values below or above the isoelectric point typically yield net positive or negative surface charge, respectively[245]. Electrostatic interactions between negatively charged cells and charged material surfaces can then further modulate immune activation. In general, negatively charged surfaces are frequently associated with a milder response than positively charged surfaces, including thinner encapsulating layers and more limited neovascularization, whereas near-neutral surfaces can reduce protein adsorption and thereby markedly suppress FBR[246–248]. In practice, surface charge is commonly evaluated in conjunction with wettability, with protein adsorption serving as an experimentally tractable readout of combined interfacial effects. Finally, because tissue microenvironments vary substantially across implantation sites, biocompatibility should be evaluated in a site-specific manner[249].

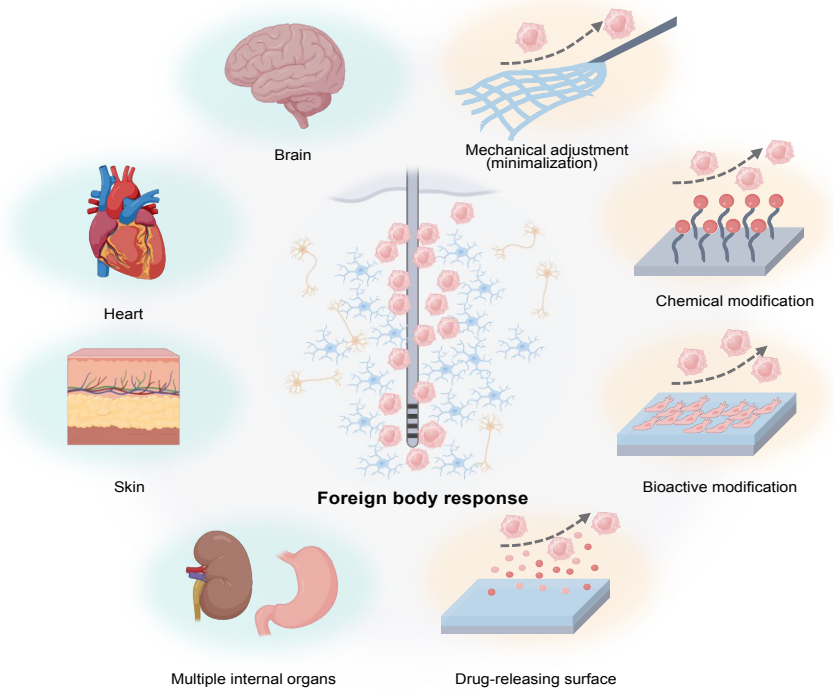

Fig. 1-9 Strategies for mitigating foreign-body responses at tissue–bioelectronic interfaces.

Bibliography of Chapter 1

1. Chen, C., Ding, S. & Wang, J. Digital health for aging populations. *Nat. Med.* **29**, 1623–1630 (2023).

2. Hajat, C. & Stein, E. The global burden of multiple chronic conditions: A narrative review. *Prev. Med. Rep.* **12**, 284–293 (2018).

3. Madhvapathy, S. R. *et al.* Implantable bioelectronics and wearable sensors for kidney health and disease. *Nat. Rev. Nephrol.* **21**, 443–463 (2025).

4. Brasier, N. *et al.* Applied body-fluid analysis by wearable devices. *Nature* **636**, 57–68 (2024).

5. Min, S. *et al.* Wearable blood pressure sensors for cardiovascular monitoring and machine learning algorithms for blood pressure estimation. *Nat. Rev. Cardiol.* **22**, 629–648 (2025).

6. Wang, C. *et al.* Wound management materials and technologies from bench to bedside and beyond. *Nat. Rev. Mater.* **9**, 550–566 (2024).

7. Perkins, B. A., Sherr, J. L. & Mathieu, C. Type 1 diabetes glycemic management: Insulin therapy, glucose monitoring, and automation. *Science* **373**, 522–527 (2021).

8. Chen, R., Canales, A. & Anikeeva, P. Neural recording and modulation technologies. *Nat. Rev. Mater.* **2**, 16093 (2017).

9. Barrese, J. C. *et al.* Failure mode analysis of silicon-based intracortical microelectrode arrays in non-human primates. *J. Neural Eng.* **10**, 066014 (2013).

10. Wynn, T. A. & Ramalingam, T. R. Mechanisms of fibrosis: therapeutic translation for fibrotic disease. *Nat. Med.* **18**, 1028–1040 (2012).

11. Tang, X., Shen, H., Zhao, S., Li, N. & Liu, J. Flexible brain–computer interfaces. *Nat. Electron.* **6**, 109–118 (2023).

12. Ni, Y. *et al.* Macrophages modulate stiffness-related foreign body responses through plasma membrane deformation. *Proc. Natl. Acad. Sci.* **120**, e2213837120 (2023).

13. Cogan, S. F. Neural Stimulation and Recording Electrodes. *Annu. Rev. Biomed. Eng.* **10**, 275–309 (2008).

14. Madhvapathy, S. R. *et al.* Implantable bioelectronic systems for early detection of kidney transplant rejection. *Science* **381**, 1105–1112 (2023).

15. Kim, D.-H. *et al.* Dissolvable films of silk fibroin for ultrathin conformal bio-integrated electronics. *Nat. Mater.* **9**, 511–517 (2010).

16. Song, E., Li, J., Won, S. M., Bai, W. & Rogers, J. A. Materials for flexible bioelectronic systems as chronic neural interfaces. *Nat. Mater.* **19**, 590–603 (2020).

17. Rogers, J. A., Someya, T. & Huang, Y. Materials and Mechanics for Stretchable Electronics. *Science* **327**, 1603–1607 (2010).

18. Nishio, Y. *et al.* Intrinsically stretchable transistors and integrated circuits. *Nat. Rev. Electr. Eng.* **2**, 715–735 (2025).

19. Zhao, X. *et al.* Soft Materials by Design: Unconventional Polymer Networks Give Extreme Properties. *Chem. Rev.* **121**, 4309–4372 (2021).

20. Vegas, A. J. *et al.* Combinatorial hydrogel library enables identification of materials that mitigate the foreign body response in primates. *Nat. Biotechnol.* **34**, 345–352 (2016).

21. Kim, D.-H. *et al.* Epidermal Electronics. *Science* **333**, 838–843 (2011).

22. Nam, S. & Mooney, D. Polymeric Tissue Adhesives. *Chem. Rev.* **121**, 11336–11384 (2021).

23. Boufidis, D., Garg, R., Angelopoulos, E., Cullen, D. K. & Vitale, F. Bio-inspired electronics: Soft, biohybrid, and "living" neural interfaces. *Nat. Commun.* **16**, 1861 (2025).

24. Wang, X. *et al.* Tough Wet Adhesion of Hydrogen-Bond-Based Hydrogel with On-Demand Debonding and Efficient Hemostasis. *ACS Appl. Mater. Interfaces* **14**, 36166–36177 (2022).

25. Kurokawa, T., Furukawa, H., Wang, W., Tanaka, Y. & Gong, J. P. Formation of a strong hydrogel–porous solid interface via the double-network principle. *Acta Biomater.* **6**, 1353–1359 (2010).

26. Reilly, A. & Tkatchenko, A. van der Waals dispersion interactions in molecular materials: beyond pairwise additivity. *Chem. Sci.* **6**, 3289–3301 (2015).

27. Yan, Z. *et al.* Highly stretchable van der Waals thin films for adaptable and breathable electronic membranes. *Science* **375**, 852–859 (2022).

28. Nie, B., Stutzman, J. & Xie, A. A Vibrational Spectral Maker for Probing the Hydrogen-Bonding Status of Protonated Asp and Glu Residues. *Biophys. J.* **88**, 2833–2847 (2005).

29. Chen, J. *et al.* An Adhesive Hydrogel with "Load-Sharing" Effect as Tissue Bandages for Drug and Cell Delivery. *Adv. Mater.* **32**, 2001628 (2020).

30. Yuk, H. *et al.* Dry double-sided tape for adhesion of wet tissues and devices. *Nature* **575**, 169–174 (2019).

31. Xue, B. *et al.* Hydrogel tapes for fault-tolerant strong wet adhesion. *Nat. Commun.* **12**, 7156 (2021).

32. Kim, J. *et al.* Soft Cardiac Patch Using a Bifacial Architecture of Adhesive/Low-Impedance Hydrogel Nanocomposites and Highly Conductive Elastomer Nanocomposites. *Adv. NanoBiomed Res.* **5**, 2400143 (2025).

33. Palacio, M. L. B. & Bhushan, B. Bioadhesion: a review of concepts and applications. *Philos. Trans. R. Soc. Math. Phys. Eng. Sci.* **370**, 2321–2347 (2012).

34. Rao, P. *et al.* Tough hydrogels with fast, strong, and reversible underwater adhesion based on a multiscale design. *Adv. Mater.* **30**, 1801884 (2018).

35. Roy, C. K. *et al.* Self-Adjustable Adhesion of Polyampholyte Hydrogels. *Adv. Mater.* **27**, 7344–7348 (2015).

36. Montazerian, H. *et al.* Stretchable and Bioadhesive Gelatin Methacryloyl-Based Hydrogels Enabled by in Situ Dopamine Polymerization. *ACS Appl. Mater. Interfaces* **13**, 40290–40301 (2021).

37. Li, J. *et al.* Tough adhesives for diverse wet surfaces. *Science* **357**, 378–381 (2017).

38. Yang, Q. *et al.* Photocurable bioresorbable adhesives as functional interfaces between flexible bioelectronic devices and soft biological tissues. *Nat. Mater.* **20**, 1559–1570 (2021).

39. Young, T. III. An essay on the cohesion of fluids. *Philos. Trans. R. Soc. Lond.* 65–87 (1805) doi:10.1098/rstl.1805.0005.

40. Delamarche, E. *et al.* Microfluidic Networks for Chemical Patterning of Substrates: Design and Application to Bioassays. *J. Am. Chem. Soc.* **120**, 500–508 (1998).

41. Wisniewski, D. J. *et al.* Spatial control of doping in conducting polymers enables complementary, conformable, implantable internal ion-gated organic electrochemical transistors. *Nat. Commun.* **16**, 517 (2025).

42. Boys, A. J. *et al.* Implantable bioelectronics for gut electrophysiology. *Nat. Commun.* **16**, 10240 (2025).

43. Xu, D. *et al.* Two-dimensional semiconductor-based active array for high-fidelity spatiotemporal monitoring of neural activities. *Nat. Mater.* 1–12 (2025) doi:10.1038/s41563-025-02430-4.

44. Park, H.-H. *et al.* Flexible and Shape-Reconfigurable Hydrogel Interlocking Adhesives for High Adhesion in Wet Environments Based on Anisotropic Swelling of Hydrogel Microstructures. *ACS Macro Lett.* **6**, 1325–1330 (2017).

45. Wang, Y., Kang, V., Arzt, E., Federle, W. & Hensel, R. Strong Wet and Dry Adhesion by Cupped Microstructures. *ACS Appl. Mater. Interfaces* **11**, 26483–26490 (2019).

46. Yang, J., Bai, R., Chen, B. & Suo, Z. Hydrogel Adhesion: A Supramolecular Synergy of Chemistry, Topology, and Mechanics. *Adv. Funct. Mater.* **30**, 1901693 (2020).

47. Samieipour, F., Dianat-Moghadam, H. & Khanahmad, H. Recent developments in bioconjugation: From strategies to design and clinical applications. *Biomed. Pharmacother.* **192**, 118593 (2025).

48. Yuk, H., Zhang, T., Lin, S., Parada, G. A. & Zhao, X. Tough bonding of hydrogels to diverse non-porous surfaces. *Nat. Mater.* **15**, 190–196 (2016).

49. Wallace, D. G. *et al.* A tissue sealant based on reactive multifunctional polyethylene glycol. *J. Biomed. Mater. Res.* **58**, 545–555 (2001).

50. Preul, M. C., Campbell, P. K., Bichard, W. D. & Spetzler, R. F. Application of a hydrogel sealant improves watertight closures of duraplasty onlay grafts in a canine craniotomy model. **107**, (2007).

51. Artzi, N., Shazly, T., Baker, A. B., Bon, A. & Edelman, E. R. Aldehyde-Amine Chemistry Enables Modulated Biosealants with Tissue-Specific Adhesion. *Adv. Mater. Deerfield Beach Fla* **21**, 3399–3403 (2009).

52. Lin, H. *et al.* Synthesis and characterization of a bio-aldehyde-based lignin adhesive with desirable water resistance. *Int. J. Biol. Macromol.* **264**, 130020 (2024).

53. Chao, H.-H. & Torchiana, D. F. BioGlue: Albumin/Glutaraldehyde Sealant in Cardiac Surgery. *J. Card. Surg.* **18**, 500–503 (2003).

54. Belowich, M. E. & Stoddart, J. F. Dynamic imine chemistry. *Chem. Soc. Rev.* **41**, 2003–2024 (2012).

55. M. Korde, J. & Kandasubramanian, B. Biocompatible alkyl cyanoacrylates and their derivatives as bio-adhesives. *Biomater. Sci.* **6**, 1691–1711 (2018).

56. Klemarczyk, P. The isolation of a zwitterionic initiating species for ethyl cyanoacrylate (ECA) polymerization and the identification of the reaction products between 1°, 2°, and 3° amines with ECA. *Polymer* **42**, 2837–2848 (2001).

57. Garcia-Roig, M., Gorin, M. A., Castellan, M. & Ciancio, G. OMNEX Surgical Sealant in the Extracorporeal Repair of Renal Artery Aneurysms. *Ann. Vasc. Surg.* **25**, 1141.e5-1141.e8 (2011).

58. Singer, A. J., Perry, L. C. & Allen Jr, R. L. In Vivo Study of Wound Bursting Strength and Compliance of Topical Skin Adhesives. *Acad. Emerg. Med.* **15**, 1290–1294 (2008).

59. Investigators, T. n-B. T. n-Butyl Cyanoacrylate Embolization of Cerebral Arteriovenous Malformations: Results of a Prospective, Randomized, Multi-center Trial. *Am. J. Neuroradiol.* **23**, 748–755 (2002).

60. Nair, L. S. & Laurencin, C. T. Biodegradable polymers as biomaterials. *Prog. Polym. Sci.* **32**, 762–798 (2007).

61. Hofman, A. H., van Hees, I. A., Yang, J. & Kamperman, M. Bioinspired Underwater Adhesives by Using the Supramolecular Toolbox. *Adv. Mater.* **30**, 1704640 (2018).

62. Davoodi, E. *et al.* Imaging-guided deep tissue in vivo sound printing. *Science* **388**, 616–623 (2025).

63. Yang, J., Stuart, M. A. C. & Kamperman, M. Jack of all trades: versatile catechol crosslinking mechanisms. **43**, 8271–8298 (2014).

64. Lee, H. A., Park, E. & Lee, H. Polydopamine and Its Derivative Surface Chemistry in Material Science: A Focused Review for Studies at KAIST. *Adv. Mater.* **32**, 1907505 (2020).

65. Hoang Thi, T. T., Lee, Y., Le Thi, P. & Park, K. D. Engineered horseradish peroxidase-catalyzed hydrogels with high tissue adhesiveness for biomedical applications. *J. Ind. Eng. Chem.* **78**, 34–52 (2019).

66. Ono, K. *et al.* Photocrosslinkable chitosan as a biological adhesive. *J. Biomed. Mater. Res.* **49**, 289–295 (2000).

67. Gilbert, T. W. *et al.* Lysine-Derived Urethane Surgical Adhesive Prevents Seroma Formation in a Canine Abdominoplasty Model. *Plast. Reconstr. Surg.* **122**, 95 (2008).

68. Anderson, J. M., Rodriguez, A. & Chang, D. T. Foreign body reaction to biomaterials. *Semin. Immunol.* **20**, 86–100 (2008).

69. Hong, G. & Lieber, C. M. Novel electrode technologies for neural recordings. *Nat. Rev. Neurosci.* **20**, 330–345 (2019).

70. Lecomte, A., Descamps, E. & Bergaud, C. A review on mechanical considerations for chronically-implanted neural probes. *J. Neural Eng.* **15**, 031001 (2018).

71. Fu, T.-M. *et al.* Stable long-term chronic brain mapping at the single-neuron level. *Nat. Methods* **13**, 875–882 (2016).

72. Luan, L. *et al.* Ultraflexible nanoelectronic probes form reliable, glial scar–free neural integration. *Sci. Adv.* **3**, e1601966 (2017).

73. Musk, E. & Neuralink. An Integrated Brain-Machine Interface Platform With Thousands of Channels. *J. Med. Internet Res.* **21**, e16194 (2019).

74. Zhou, T. *et al.* 3D printable high-performance conducting polymer hydrogel for all-hydrogel bioelectronic interfaces. *Nat. Mater.* **22**, 895–902 (2023).

75. Dai, Y. *et al.* Soft hydrogel semiconductors with augmented biointeractive functions. *Science* **386**, 431–439 (2024).

76. Dobashi, Y. *et al.* Piezoionic mechanoreceptors: Force-induced current generation in hydrogels. *Science* **376**, 502–507 (2022).

77. Zhu, B. *et al.* Large enhancement in neurite outgrowth on a cell membrane-mimicking conducting polymer. *Nat. Commun.* **5**, 4523 (2014).

78. Zhang, A., Zwang, T. J. & Lieber, C. M. Biochemically functionalized probes for cell-type–specific targeting and recording in the brain. *Sci. Adv.* **9**, eadk1050 (2023).

79. Oakes, R. S., Polei, M. D., Skousen, J. L. & Tresco, P. A. An astrocyte derived extracellular matrix coating reduces astrogliosis surrounding chronically implanted microelectrode arrays in rat cortex. *Biomaterials* **154**, 1–11 (2018).

80. He, W. & Bellamkonda, R. V. Nanoscale neuro-integrative coatings for neural implants. *Biomaterials* **26**, 2983–2990 (2005).

81. Gearing, M. & Kennedy, P. Histological Confirmation of Myelinated Neural Filaments Within the Tip of the Neurotrophic Electrode After a Decade of Neural Recordings. *Front. Hum. Neurosci.* **14**, (2020).

82. Kennedy, P. R. The cone electrode: a long-term electrode that records from neurites grown onto its recording surface. *J. Neurosci. Methods* **29**, 181–193 (1989).

83. Rochford, A. E. *et al.* Functional neurological restoration of amputated peripheral nerve using biohybrid regenerative bioelectronics. *Sci. Adv.* **9**, eadd8162 (2023).

84. De Faveri, S. *et al.* Bio-inspired hybrid microelectrodes: a hybrid solution to improve long-term performance of chronic intracortical implants. *Front. Neuroengineering* **7**, (2014).

85. Purcell, E. K., Seymour, J. P., Yandamuri, S. & Kipke, D. R. In vivo evaluation of a neural stem cell-seeded prosthesis. *J. Neural Eng.* **6**, 026005 (2009).

86. Miles, A. W. & Gheduzzi, S. Basic biomechanics and biomaterials. *Surg. Oxf.* **27**, 90–95 (2009).

87. Widlund, T., Yang, S., Hsu, Y.-Y. & Lu, N. Stretchability and compliance of freestanding serpentine-shaped ribbons. *Int. J. Solids Struct.* **51**, 4026–4037 (2014).

88. Zhang, Y. *et al.* Mechanics of ultra-stretchable self-similar serpentine interconnects. *Acta Mater.* **61**, 7816–7827 (2013).

89. Timoshenko, S. P. & Gere, J. M. *Theory of Elastic Stability*. (Courier Corporation, 2012).

90. Fan, Z. *et al.* A finite deformation model of planar serpentine interconnects for stretchable electronics. *Int. J. Solids Struct.* **91**, 46–54 (2016).

91. Dagdeviren, C. *et al.* Conformal piezoelectric systems for clinical and experimental characterization of soft tissue biomechanics. *Nat. Mater.* **14**, 728–736 (2015).

92. Kim, D.-H. *et al.* Stretchable and Foldable Silicon Integrated Circuits. *Science* **320**, 507–511 (2008).

93. Yang, D. *et al.* Double-Microcrack Coupling Stretchable Neural Electrode for Electrophysiological Communication. *Adv. Funct. Mater.* **33**, 2300412 (2023).

94. Nur, R. *et al.* A Highly Sensitive Capacitive-type Strain Sensor Using Wrinkled Ultrathin Gold Films. *Nano Lett.* **18**, 5610–5617 (2018).

95. Song, J. *et al.* An analytical study of two-dimensional buckling of thin films on compliant substrates. *J. Appl. Phys.* **103**, 014303 (2008).

96. Babaee, S. *et al.* Kirigami-inspired stents for sustained local delivery of therapeutics. *Nat. Mater.* **20**, 1085–1092 (2021).

97. Pradhan, S. *et al.* Biofunctional Silk Kirigami With Engineered Properties. *ACS Appl. Mater. Interfaces* **12**, 12436–12444 (2020).

98. Yu, Y. *et al.* All-printed soft human-machine interface for robotic physicochemical sensing. *Sci. Robot.* **7**, eabn0495 (2022).

99. Ko, H. C. *et al.* A hemispherical electronic eye camera based on compressible silicon optoelectronics. *Nature* **454**, 748–753 (2008).

100. Kim, D.-H. *et al.* Materials and noncoplanar mesh designs for integrated circuits with linear elastic responses to extreme mechanical deformations. *Proc. Natl. Acad. Sci.* **105**, 18675–18680 (2008).

101. Han, M. *et al.* Catheter-integrated soft multilayer electronic arrays for multiplexed sensing and actuation during cardiac surgery. *Nat. Biomed. Eng.* **4**, 997–1009 (2020).

102. Someya, T. *et al.* Conformable, flexible, large-area networks of pressure and thermal sensors with organic transistor active matrixes. *Proc. Natl. Acad. Sci.* **102**, 12321–12325 (2005).

103. Zhou, T. *et al.* Syringe-injectable mesh electronics integrate seamlessly with minimal chronic immune response in the brain. *Proc. Natl. Acad. Sci.* **114**, 5894–5899 (2017).

104. Zhang, A. *et al.* Ultraflexible endovascular probes for brain recording through micrometer-scale vasculature. *Science* **381**, 306–312 (2023).

105. Landau, L. D., Pitaevskii, L. P., Kosevich, A. M. & Lifshitz, E. M. *Theory of Elasticity: Volume 7*. (Elsevier, 2012).

106. Chaudhuri, O. *et al.* Extracellular matrix stiffness and composition jointly regulate the induction of malignant phenotypes in mammary epithelium. *Nat. Mater.* **13**, 970–978 (2014).

107. Ferry, J. D. & Myers, H. S. Viscoelastic Properties of Polymers. *J. Electrochem. Soc.* **108**, 142C (1961).

108. Kundu, P. K., Cohen, I. M., Dowling, D. R. & Capecelatro, J. *Fluid Mechanics*. (Elsevier, 2024).

109. Sun, H. *et al.* Liquid-based encapsulation for implantable bioelectronics across broad pH environments. *Nat. Commun.* **16**, 1019 (2025).

110. Ciatti, J. L. *et al.* An autonomous implantable device for the prevention of death from opioid overdose. *Sci. Adv.* (2024).

111. Kim, J. *et al.* A wireless, implantable bioelectronic system for monitoring urinary bladder function following surgical recovery. *Proc. Natl. Acad. Sci.* **121**, e2400868121 (2024).

112. Wang, S. *et al.* Skin electronics from scalable fabrication of an intrinsically stretchable transistor array. *Nature* **555**, 83–88 (2018).

113. Choi, S. *et al.* Highly conductive, stretchable and biocompatible Ag–Au core–sheath nanowire composite for wearable and implantable bioelectronics. *Nat. Nanotechnol.* **13**, 1048–1056 (2018).

114. Xu, Y. *et al.* Phase-separated porous nanocomposite with ultralow percolation threshold for wireless bioelectronics. *Nat. Nanotechnol.* **19**, 1158–1167 (2024).

115. Tringides, C. M. *et al.* Viscoelastic surface electrode arrays to interface with viscoelastic tissues. *Nat. Nanotechnol.* **16**, 1019–1029 (2021).

116. Deng, J. *et al.* Electrical bioadhesive interface for bioelectronics. *Nat. Mater.* **20**, 229–236 (2021).

117. Wang, C. *et al.* Bioadhesive ultrasound for long-term continuous imaging of diverse organs. *Science* **377**, 517–523 (2022).

118. Afzal, S. *et al.* Ultrasound Hydrogel: A Review on Materials and Method. *J. Mod. Polym. Chem. Mater.* **1(1)**, (2022).

119. Zhang, R., Wen, S., Zhao, Y. & Ji, S. Water-Removable Paste Electrode for Electrophysiological Monitoring on Hairy Skin. *ACS Appl. Electron. Mater.* **7**, 925–932 (2025).

120. Wang, X. *et al.* Towards Optimizing the Quality of Long-Term Physiological Signals Monitoring by Using Anhydrous Carbon Paste Electrode. *IEEE Trans. Biomed. Eng.* **70**, 423–435 (2023).

121. Yang, J., Cheng, W. & Kalantar-zadeh, K. Electronic Skins Based on Liquid Metals. *Proc. IEEE* **107**, 2168–2184 (2019).

122. Cole, T., Khoshmanesh, K. & Tang, S.-Y. Liquid Metal Enabled Biodevices. *Adv. Intell. Syst.* **3**, 2000275 (2021).

123. Kim, H. J., Koo, J. H., Lee, S., Hyeon, T. & Kim, D.-H. Materials design and integration strategies for soft bioelectronics in digital healthcare. *Nat. Rev. Mater.* **10**, 654–673 (2025).

124. Dai, Y., Hu, H., Wang, M., Xu, J. & Wang, S. Stretchable transistors and functional circuits for human-integrated electronics. *Nat. Electron.* **4**, 17–29 (2021).

125. Koo, J. H. *et al.* A vacuum-deposited polymer dielectric for wafer-scale stretchable electronics. *Nat. Electron.* **6**, 137–145 (2023).

126. Lee, Y. *et al.* Standalone real-time health monitoring patch based on a stretchable organic optoelectronic system. *Sci. Adv.* **7**, eabg9180 (2021).

127. Kang, J. *et al.* Ultrathin, solvent-resistant dielectric for monolithic fabrication of low-power, intrinsically stretchable active-matrix electronic skin. *Device* **2**, (2024).

128. Cui, N. *et al.* A photolithographic stretchable transparent electrode for an all-solution-processed fully transparent conformal organic transistor array. *J. Mater. Chem. C* **7**, 5385–5393 (2019).

129. Yang, J. C. *et al.* Electronic Skin: Recent Progress and Future Prospects for Skin-Attachable Devices for Health Monitoring, Robotics, and Prosthetics. *Adv. Mater.* **31**, 1904765 (2019).

130. Zhang, P. & Travas-Sejdic, J. Fabrication of conducting polymer microelectrodes and microstructures for bioelectronics. *J. Mater. Chem. C* **9**, 9730–9760 (2021).

131. Kim, M. *et al.* Nanowire-assisted freestanding liquid metal thin-film patterns for highly stretchable electrodes on 3D surfaces. *Npj Flex. Electron.* **6**, 99 (2022).

132. Xu, C., Ma, B., Yuan, S., Zhao, C. & Liu, H. High-Resolution Patterning of Liquid Metal on Hydrogel for Flexible, Stretchable, and Self-Healing Electronics. *Adv. Electron. Mater.* **6**, 1900721 (2020).

133. Kim, D. W. *et al.* Fabrication of practical deformable displays: advances and challenges. *Light Sci. Appl.* **12**, 61 (2023).

134. Sun, B. *et al.* Gas-Permeable, Multifunctional On-Skin Electronics Based on Laser-Induced Porous Graphene and Sugar-Templated Elastomer Sponges. *Adv. Mater.* **30**, 1804327 (2018).

135. Weibel, D. B., DiLuzio, W. R. & Whitesides, G. M. Microfabrication meets microbiology. *Nat. Rev. Microbiol.* **5**, 209–218 (2007).

136. Overholts, A. C., Granados Razo, W. & Robb, M. J. Mechanically gated formation of donor–acceptor Stenhouse adducts enabling mechanochemical multicolour soft lithography. *Nat. Chem.* **15**, 332–338 (2023).

137. Abe, Y. *et al.* Porous microneedle-based wearable device for monitoring of transepidermal potential. *Biomed. Eng. Adv.* **1**, 100004 (2021).

138. Lee, H. *et al.* Porous microneedles on a paper for screening test of prediabetes. *Med. DEVICES Sens.* **3**, e10109 (2020).

139. Zhu, Z. *et al.* Blue-ringed octopus-inspired microneedle patch for robust tissue surface adhesion and active injection drug delivery. *Sci. Adv.* **9**, eadh2213 (2023).

140. Sun, H., Zheng, Y., Shi, G., Haick, H. & Zhang, M. Wearable Clinic: From Microneedle-Based Sensors to Next-Generation Healthcare Platforms. *Small* **19**, 2207539 (2023).

141. Liu, C.-X. & Choi, J.-W. An embedded PDMS nanocomposite strain sensor toward biomedical applications. in *2009 Annual International Conference of the IEEE Engineering in Medicine and Biology Society* 6391–6394 (2009). doi:10.1109/IEMBS.2009.5333873.

142. Bhingardive, V., Menahem, L. & Schvartzman, M. Soft thermal nanoimprint lithography using a nanocomposite mold. *Nano Res.* **11**, 2705–2714 (2018).

143. Liu, C.-X. & Choi, J.-W. Patterning conductive PDMS nanocomposite in an elastomer using microcontact printing. *J. Micromechanics Microengineering* **19**, 085019 (2009).

144. Park, J.-E., Kang, H. S., Koo, M. & Park, C. Autonomous Surface Reconciliation of a Liquid-Metal Conductor Micropatterned on a Deformable Hydrogel. *Adv. Mater.* **32**, 2002178 (2020).

145. Zhang, S. *et al.* Hydrogel-Enabled Transfer-Printing of Conducting Polymer Films for Soft Organic Bioelectronics. *Adv. Funct. Mater.* **30**, 1906016 (2020).

146. Tehrani, F. *et al.* An integrated wearable microneedle array for the continuous monitoring of multiple biomarkers in interstitial fluid. *Nat. Biomed. Eng.* **6**, 1214–1224 (2022).

147. Yang, J. *et al.* Masticatory system–inspired microneedle theranostic platform for intelligent and precise diabetic management. *Sci. Adv.* **8**, eabo6900 (2022).

148. Lee, W. *et al.* Conformable microneedle pH sensors via the integration of two different siloxane polymers for mapping peripheral artery disease. *Sci. Adv.* **7**, eabi6290 (2021).

149. Liu, Y. *et al.* Recent advances in inkjet-printing technologies for flexible/wearable electronics. *Nanoscale* **15**, 6025–6051 (2023).

150. Du, X. *et al.* A review of inkjet printing technology for personalized-healthcare wearable devices. *J. Mater. Chem. C* **10**, 14091–14115 (2022).

151. Li, L. *et al.* All Inkjet-Printed Amperometric Multiplexed Biosensors Based on Nanostructured Conductive Hydrogel Electrodes. *Nano Lett.* **18**, 3322–3327 (2018).

152. Chi, K. *et al.* Freestanding Graphene Paper Supported Three-Dimensional Porous Graphene–Polyaniline Nanocomposite Synthesized by Inkjet Printing and in Flexible All-Solid-State Supercapacitor. *ACS Appl. Mater. Interfaces* **6**, 16312–16319 (2014).

153. Seiti, M., Degryse, O. & Ferraris, E. Aerosol Jet® printing 3D capabilities for metal and polymeric inks. *Mater. Today Proc.* **70**, 38–44 (2022).

154. Chen, X. *et al.* 3D-printed hierarchical pillar array electrodes for high-performance semi-artificial photosynthesis. *Nat. Mater.* **21**, 811–818 (2022).

155. Loh, J. M. *et al.* Design and fabrication of customizable microneedles enabled by 3D printing for biomedical applications. *Bioact. Mater.* **32**, 222–241 (2024).

156. Song, Y. *et al.* 3D-printed epifluidic electronic skin for machine learning–powered multimodal health surveillance. *Sci. Adv.* **9**, eadi6492 (2023).

157. Lacey, S. D. *et al.* Extrusion-Based 3D Printing of Hierarchically Porous Advanced Battery Electrodes. *Adv. Mater.* **30**, 1705651 (2018).

158. Wang, Y. *et al.* Supramolecular Liquid Crystal Carbon Dots for Solvent-Free Direct Ink Writing. *Adv. Mater.* **35**, 2303680 (2023).

159. Zhang, L., Wang, R., Wang, J., Wu, L. & Zhang, X. Mechanically robust nanocomposites from screen-printable polymer/graphene nanosheet pastes. *Nanoscale* **11**, 2343–2354 (2019).

160. Li, W., Yang, S. & Shamim, A. Screen printing of silver nanowires: balancing conductivity with transparency while maintaining flexibility and stretchability. *Npj Flex. Electron.* **3**, 13 (2019).

161. Somalu, M. R., Muchtar, A., Daud, W. R. W. & Brandon, N. P. Screen-printing inks for the fabrication of solid oxide fuel cell films: A review. *Renew. Sustain. Energy Rev.* **75**, 426–439 (2017).

162. Chen, C. *et al.* Screen-Printing Technology for Scale Manufacturing of Perovskite Solar Cells. *Adv. Sci.* **10**, 2303992 (2023).

163. Quan, H. *et al.* Photo-curing 3D printing technique and its challenges. *Bioact. Mater.* **5**, 110–115 (2020).

164. Shin, D. & Hyun, J. Silk fibroin microneedles fabricated by digital light processing 3D printing. *J. Ind. Eng. Chem.* **95**, 126–133 (2021).

165. Melchels, F. P. W., Feijen, J. & Grijpma, D. W. A review on stereolithography and its applications in biomedical engineering. *Biomaterials* **31**, 6121–6130 (2010).

166. Dong, Z. *et al.* 3D printing of inherently nanoporous polymers via polymerization-induced phase separation. *Nat. Commun.* **12**, 247 (2021).

167. Moore, D. G., Barbera, L., Masania, K. & Studart, A. R. Three-dimensional printing of multicomponent glasses using phase-separating resins. *Nat. Mater.* **19**, 212–217 (2020).

168. Cheng, J. *et al.* Centrifugal multimaterial 3D printing of multifunctional heterogeneous objects. *Nat. Commun.* **13**, 7931 (2022).

169. Yin, S. *et al.* Wearable and Implantable Soft Robots. *Chem. Rev.* **124**, 11585–11636 (2024).

170. Ge, Q. *et al.* 3D printing of highly stretchable hydrogel with diverse UV curable polymers. *Sci. Adv.* **7**, eaba4261 (2021).

171. Dhand, A. P. *et al.* Additive manufacturing of highly entangled polymer networks. *Science* **385**, 566–572 (2024).

172. Narayan, R. J., Doraiswamy, A., Chrisey, D. B. & Chichkov, B. N. Medical prototyping using two photon polymerization. *Mater. Today* **13**, 42–48 (2010).

173. Xing, J.-F., Zheng, M.-L. & Duan, X.-M. Two-photon polymerization microfabrication of hydrogels: an advanced 3D printing technology for tissue engineering and drug delivery. *Chem. Soc. Rev.* **44**, 5031–5039 (2015).

174. Singh, S., Choudhury, D., Yu, F., Mironov, V. & Naing, M. W. *In situ* bioprinting – Bioprinting from benchside to bedside? *Acta Biomater.* **101**, 14–25 (2020).

175. Albanna, M. *et al.* In Situ Bioprinting of Autologous Skin Cells Accelerates Wound Healing of Extensive Excisional Full-Thickness Wounds. *Sci. Rep.* **9**, 1856 (2019).

176. Kolan, K. C. R., Semon, J. A., Bromet, B., Day, D. E. & Leu, M. C. Bioprinting with human stem cell-laden alginate-gelatin bioink and bioactive glass for tissue engineering. *Int. J. Bioprinting* **5**, 204 (2019).

177. Zhao, W., Hu, C. & Xu, T. *In vivo* bioprinting: Broadening the therapeutic horizon for tissue injuries. *Bioact. Mater.* **25**, 201–222 (2023).

178. Ash, C., Dubec, M., Donne, K. & Bashford, T. Effect of wavelength and beam width on penetration in light-tissue interaction using computational methods. *Lasers Med. Sci.* **32**, 1909–1918 (2017).

179. Chen, Y. *et al.* Noninvasive in vivo 3D bioprinting. *Sci. Adv.* **6**, eaba7406 (2020).

180. Urciuolo, A. *et al.* Intravital three-dimensional bioprinting. *Nat. Biomed. Eng.* **4**, 901–915 (2020).

181. Kuang, X. *et al.* Self-enhancing sono-inks enable deep-penetration acoustic volumetric printing. *Science* **382**, 1148–1155 (2023).

182. Zhang, Y. S. *et al.* 3D extrusion bioprinting. *Nat. Rev. Methods Primer* **1**, 75 (2021).

183. Gudapati, H., Dey, M. & Ozbolat, I. A comprehensive review on droplet-based bioprinting: Past, present and future. *Biomaterials* **102**, 20–42 (2016).

184. Gupta, D., Derman, I. D., Xu, C., Huang, Y. & Ozbolat, I. T. Droplet-based bioprinting. *Nat. Rev. Methods Primer* **5**, 25 (2025).

185. Kim, M., Park, J. J., Cho, C. & Ko, S. H. Liquid Metal based Stretchable Room Temperature Soldering Sticker Patch for Stretchable Electronics Integration. *Adv. Funct. Mater.* **33**, 2303286 (2023).

186. Chung, H. U. *et al.* Skin-interfaced biosensors for advanced wireless physiological monitoring in neonatal and pediatric intensive-care units. *Nat. Med.* **26**, 418–429 (2020).

187. Zhou, S. *et al.* Transcranial volumetric imaging using a conformal ultrasound patch. *Nature* **629**, 810–818 (2024).

188. Li, J. *et al.* Vertically stacked skin-like active-matrix display with ultrahigh aperture ratio. *Light Sci. Appl.* **13**, 177 (2024).

189. Lopes, P. A., Santos, B. C., de Almeida, A. T. & Tavakoli, M. Reversible polymer-gel transition for ultra-stretchable chip-integrated circuits through self-soldering and self-coating and self-healing. *Nat. Commun.* **12**, 4666 (2021).

190. Zheng, S. *et al.* Pressure-stamped stretchable electronics using a nanofibre membrane containing semi-embedded liquid metal particles. *Nat. Electron.* **7**, 576–585 (2024).

191. Sunwoo, S.-H. *et al.* Soft bioelectronics for the management of cardiovascular diseases. *Nat. Rev. Bioeng.* **2**, 8–24 (2023).

192. Jiang, Z. *et al.* A 1.3-micrometre-thick elastic conductor for seamless on-skin and implantable sensors. *Nat. Electron.* **5**, 784–793 (2022).

193. Zargartalebi, H. *et al.* Active-reset protein sensors enable continuous in vivo monitoring of inflammation. *Science* **386**, 1146–1153 (2024).

194. Ye, C. *et al.* A wearable aptamer nanobiosensor for non-invasive female hormone monitoring. *Nat. Nanotechnol.* **19**, 330–337 (2024).

195. Min, J. *et al.* Continuous biochemical profiling of the gastrointestinal tract using an integrated smart capsule. *Nat. Electron.* **8**, 844–855 (2025).

196. Tang, H. *et al.* Injectable ultrasonic sensor for wireless monitoring of intracranial signals. *Nature* **630**, 84–90 (2024).

198. Khodagholy, D. *et al.* NeuroGrid: recording action potentials from the surface of the brain. *Nat. Neurosci.* **18**, 310–315 (2015).

199. Kaifosh, P. & Reardon, T. R. A generic non-invasive neuromotor interface for human-computer interaction. *Nature* **645**, 702–711 (2025).

200. Liu, Y. *et al.* Epidermal mechano-acoustic sensing electronics for cardiovascular diagnostics and human-machine interfaces. *Sci. Adv.* **2**, e1601185 (2016).

201. Lee, K. *et al.* Mechano-acoustic sensing of physiological processes and body motions via a soft wireless device placed at the suprasternal notch. *Nat. Biomed. Eng.* **4**, 148–158 (2020).

202. Cotur, Y. *et al.* Stretchable Composite Acoustic Transducer for Wearable Monitoring of Vital Signs. *Adv. Funct. Mater.* **30**, 1910288 (2020).

203. Yin, D. *et al.* A battery-free nanofluidic intracellular delivery patch for internal organs. *Nature* **642**, 1051–1061 (2025).

204. Liu, Y. *et al.* Soft and elastic hydrogel-based microelectronics for localized low-voltage neuromodulation. *Nat. Biomed. Eng.* **3**, 58–68 (2019).

205. Zhang, Y. *et al.* Millimetre-scale bioresorbable optoelectronic systems for electrotherapy. *Nature* **640**, 77–86 (2025).

206. Sahasrabudhe, A. *et al.* Multifunctional microelectronic fibers enable wireless modulation of gut and brain neural circuits. *Nat. Biotechnol.* **42**, 892–904 (2024).

207. Lee, J. *et al.* Flexible, sticky, and biodegradable wireless device for drug delivery to brain tumors. *Nat. Commun.* **10**, 5205 (2019).

208. Xue, H. *et al.* Wearable flexible ultrasound microneedle patch for cancer immunotherapy. *Nat. Commun.* **16**, 2650 (2025).

209. Shirzaei Sani, E. *et al.* A stretchable wireless wearable bioelectronic system for multiplexed monitoring and combination treatment of infected chronic wounds. *Sci. Adv.* **9**, eadf7388 (2023).

210. Minev, I. R. *et al.* Electronic dura mater for long-term multimodal neural interfaces. *Science* **347**, 159–163 (2015).

211. Wu, H. *et al.* Accelerated intestinal wound healing via dual electrostimulation from a soft and biodegradable electronic bandage. *Nat. Electron.* **7**, 299–312 (2024).

212. Hu, H. *et al.* Stretchable ultrasonic arrays for the three-dimensional mapping of the modulus of deep tissue. *Nat. Biomed. Eng.* **7**, 1321–1334 (2023).

213. Zheng, Z., Zhu, R., Peng, I., Xu, Z. & Jiang, Y. Wearable and implantable biosensors: mechanisms and applications in closed-loop therapeutic systems. *J. Mater. Chem. B* **12**, 8577–8604 (2024).

214. Wang, W. *et al.* Neuromorphic sensorimotor loop embodied by monolithically integrated, low-voltage, soft e-skin. *Science* **380**, 735–742 (2023).

215. Mickle, A. D. *et al.* A wireless closed-loop system for optogenetic peripheral neuromodulation. *Nature* **565**, 361–365 (2019).

216. Xu, C., Mao, G., Williamson, R. & Whiting, D. Delayed intracerebral hemorrhage: A rare complication of deep brain stimulation surgery. *Interdiscip. Neurosurg.* **14**, 135–138 (2018).

217. Feiner, R. & Dvir, T. Tissue–electronics interfaces: from implantable devices to engineered tissues. *Nat. Rev. Mater.* **3**, 17076 (2017).

218. Khatsenko, K., Khin, Y. & Maibach, H. Allergic Contact Dermatitis to Components of Wearable Adhesive Health Devices. *Dermatitis* **31**, 283–286 (2020).

219. Baek, J.-Y., An, J.-H., Choi, J.-M., Park, K.-S. & Lee, S.-H. Flexible polymeric dry electrodes for the long-term monitoring of ECG. *Sens. Actuators Phys.* **143**, 423–429 (2008).

220. Li, Y., Li, N., De Oliveira, N. & Wang, S. Implantable bioelectronics toward long-term stability and sustainability. *Matter* **4**, 1125–1141 (2021).

221. Liu, J. *et al.* Syringe-injectable electronics. *Nat. Nanotechnol.* **10**, 629–636 (2015).

222. Seymour, J. P. & Kipke, D. R. Neural probe design for reduced tissue encapsulation in CNS. *Biomaterials* **28**, 3594–3607 (2007).

223. Ho, T.-C. *et al.* Hydrogels: Properties and Applications in Biomedicine. *Molecules* **27**, 2902 (2022).

224. Hydrogels. in *Biomaterials Science* 153–166 (Academic Press, 2020). doi:10.1016/B978-0-12-816137-1.00014-3.

225. Yuk, H., Lu, B. & Zhao, X. Hydrogel bioelectronics. *Chem. Soc. Rev.* **48**, 1642–1667 (2019).

226. Hui, Y. *et al.* Three-dimensional printing of soft hydrogel electronics. *Nat. Electron.* **5**, 893–903 (2022).

227. Ohm, Y. *et al.* An electrically conductive silver–polyacrylamide–alginate hydrogel composite for soft electronics. *Nat. Electron.* **4**, 185–192 (2021).

228. Mariani, E., Lisignoli, G., Borzì, R. M. & Pulsatelli, L. Biomaterials: Foreign Bodies or Tuners for the Immune Response? *Int. J. Mol. Sci.* **20**, 636 (2019).

229. Veiseh, O. & Vegas, A. J. Domesticating the foreign body response: Recent advances and applications. *Adv. Drug Deliv. Rev.* **144**, 148–161 (2019).

230. Wang, M. O. *et al.* Evaluation of the In Vitro Cytotoxicity of Cross-Linked Biomaterials. *Biomacromolecules* **14**, 1321–1329 (2013).

231. Imlimthan, S. *et al.* Systematic in vitro biocompatibility studies of multimodal cellulose nanocrystal and lignin nanoparticles. *J. Biomed. Mater. Res. A* **108**, 770–783 (2020).

232. Witherel, C. E., Abebayehu, D., Barker, T. H. & Spiller, K. L. Macrophage and Fibroblast Interactions in Biomaterial-Mediated Fibrosis. *Adv. Healthc. Mater.* **8**, 1801451 (2019).

233. Kutner, N., Kunduru, K. R., Rizik, L. & Farah, S. Recent Advances for Improving Functionality, Biocompatibility, and Longevity of Implantable Medical Devices and Deliverable Drug Delivery Systems. *Adv. Funct. Mater.* **31**, 2010929 (2021).

234. Jiang, S. & Cao, Z. Ultralow-Fouling, Functionalizable, and Hydrolyzable Zwitterionic Materials and Their Derivatives for Biological Applications. *Adv. Mater.* **22**, 920–932 (2010).

235. Knop, K., Hoogenboom, R., Fischer, D. & Schubert, U. S. Poly(ethylene glycol) in Drug Delivery: Pros and Cons as Well as Potential Alternatives. *Angew. Chem. Int. Ed.* **49**, 6288–6308 (2010).

236. Xie, X. *et al.* Reduction of measurement noise in a continuous glucose monitor by coating the sensor with a zwitterionic polymer. *Nat. Biomed. Eng.* **2**, 894–906 (2018).

237. He, W., McConnell, G. C. & Bellamkonda, R. V. Nanoscale laminin coating modulates cortical scarring response around implanted silicon microelectrode arrays. *J. Neural Eng.* **3**, 316 (2006).

238. Zaveri, T. D. *et al.* Contributions of surface topography and cytotoxicity to the macrophage response to zinc oxide nanorods. *Biomaterials* **31**, 2999–3007 (2010).

239. Capuani, S., Malgir, G., Chua, C. Y. X. & Grattoni, A. Advanced strategies to thwart foreign body response to implantable devices. *Bioeng. Transl. Med.* **7**, e10300 (2022).

240. Robotti, F. *et al.* A micron-scale surface topography design reducing cell adhesion to implanted materials. *Sci. Rep.* **8**, 10887 (2018).

241. Booth, M. A. *et al.* Polycrystalline diamond coating on 3D printed titanium scaffolds: Surface characterisation and foreign body response. *Mater. Sci. Eng. C* **130**, 112467 (2021).

242. Shelton, R. M., Rasmussen, A. C. & Davies, J. E. Protein adsorption at the interface between charged polymer substrata and migrating osteoblasts. *Biomaterials* **9**, 24–29 (1988).

243. Proteins at Interfaces II, Copyright, 1995 Advisory Board, Foreword. in *Proteins at Interfaces II* vol. 602 i–iv (American Chemical Society, 1995).

244. Haynes, C. A. & Norde, W. Globular proteins at solid/liquid interfaces. *Colloids Surf. B Biointerfaces* **2**, 517–566 (1994).

245. Wilson, C. J., Clegg, R. E., Leavesley, D. I. & Pearcy, M. J. Mediation of Biomaterial–Cell Interactions by Adsorbed Proteins: A Review. *Tissue Eng.* **11**, 1–18 (2005).

246. Hunt, J. A., Flanagan, B. F., McLaughlin, P. J., Strickland, I. & Williams, D. F. Effect of biomaterial surface charge on the inflammatory reponse: Evaluation of cellular infiltration and TNFα production. *J. Biomed. Mater. Res.* **31**, 139–144 (1996).

247. Lopez-Silva, T. L. *et al.* Chemical functionality of multidomain peptide hydrogels governs early host immune response. *Biomaterials* **231**, 119667 (2020).

248. Zhang, J. *et al.* Novel Balanced Charged Alginate/PEI Polyelectrolyte Hydrogel that Resists Foreign-Body Reaction. *ACS Appl. Mater. Interfaces* **10**, 6879–6886 (2018).

249. Hernandez, J. L. *et al.* Effect of tissue microenvironment on fibrous capsule formation to biomaterial-coated implants. *Biomaterials* **273**, 120806 (2021).

Chapter 2

ALL-PRINTED SOFT HUMAN-MACHINE INTERFACE FOR ROBOTIC PHYSICOCHEMICAL SENSING

Materials from this chapter appear in "Yu, Y.; Li, J.; Solomon, S.; Min, J.; Tu, J.; Guo, W.; Xu, C.; Song, Y.; Gao, W. All-printed soft human-machine interface for robotic physiochemical sensing. *Science Robotics* **7** eabn0495(2022). https://doi.org/10.1126/scirobotics.abn0495"

2.1 Introduction

The development of advanced autonomous robotic systems that mimic and surpass human sensing capabilities is critical for environmental and agricultural protection as well as public health and security surveillance[1–4]. In particular, robotic tactile perception allows for successful task implementation while avoiding harm to the device, user, and environment[4–6]. In addition, autonomous trace-level threat detection prevents human exposure from toxic chemicals when operating in extreme and hazardous environments[7, 8]. Such field-deployable, on-the-spot detection tools can be applied for the rapid identification of minute concentrations of nitroaromatic explosives that pose a health and security threat if they are unchecked[9–11]. There are numerous toxic compounds that need to be tightly regulated in health and agriculture, such as organophosphates (OPs): pesticides or chemical warfare nerve agents that can cause neurological disorders, infertility, and even rapid death[12, 13]. Such tools can be extended to monitor pathogenic biohazards such as SARS-CoV-2 without direct human exposure, which could play a crucial role in combating infectious diseases, especially because the COVID-19 pandemic remains uncontrolled around the world[14–16]. These strong demands for autonomous sensitive hazard detection have motivated the development of a controllable human-machine interactive robotic system with both physical and chemical sensing capabilities for task performing and point-of-use analysis.

Because of its high flexibility and conformability, electronic skin (e-skin) presents itself as the ideal interface between electronics and the human/robot bodies. In literature, e-skin has demonstrated a wide range of physical and chemical sensing applications, ranging from consumer electronics, digital medicine, smart implants, to environmental surveillance[17–31]. Despite such promise, several challenges exist for e-skin–based multifunctional robotic systems. Because most rapid detection approaches for hazardous compounds require manual solution-based sample preparation steps, integrating chemical sensors for autonomous remote dry-phase analyte detection onto an e-skin–based robotic sensing platform is extremely challenging and substantially underdeveloped, hindering e-skin's capabilities for

robotic interaction and cognition of the external world[7, 32]. A robotic manipulator would require tactile, chemical, and temperature feedback to handle arbitrary objects, collect target samples, and carry out accurate chemical analysis in extreme environments[33]. Another problem for e-skin interfaces is that preparing high-performance sensors generally requires manual drop-casting modifications of nanomaterials, which can lead to large sensor variations[34]. Now, there is a lack of scalable low-cost manufacturing approaches to prepare thin, ultraflexible, multifunctional robotic physicochemical sensor patches. Despite these concerns, there is a strong need for an efficient human-machine interface that can reliably extract physiological features[35] as well as accurately control and receive real-time user-interactive feedback.

To address these challenges, we introduce here an artificial intelligence (AI)–powered human-machine interactive multimodal sensing robotic system (M-Bot) (**Fig. 2-1A**). The M-Bot is composed of two fully inkjet-printed stretchable e-skin patches, namely, e-skin-R and e-skin-H, which interface conformally with the robot and human skin, respectively. The e-skins with powerful physicochemical sensing capabilities are mass producible and reconfigurable and can be entirely prepared using a high-speed, low-cost, and scalable inkjet-printing technology with a series of custom-developed nanomaterial inks. Upon collecting physiological data, the machine learning model can decode the surface electromyography (sEMG) signals from muscular contractions (recorded by e-skin-H) for robotic hand control. Simultaneously, e-skin-R can perform proximity sensing and tactile and temperature perceptual mapping, alongside real-time hydrogel-assisted electrochemical on-site sampling and analysis of both solution-phase and dry-phase threat compounds including explosives [such as 2,4,6-trinitrotoluene (TNT)], pesticides (such as OPs), and biohazards (such as SARS-CoV-2 virus). Upon detection, real-time haptic and threat alarm feedback communications were achieved via electrical stimulation of the human body with e-skin-H. The threat sensing capabilities of the M-Bot could pave the way for automated chemical sensing, facilitating machine-mediated decisions for a wide range of practical robotic assistance applications.

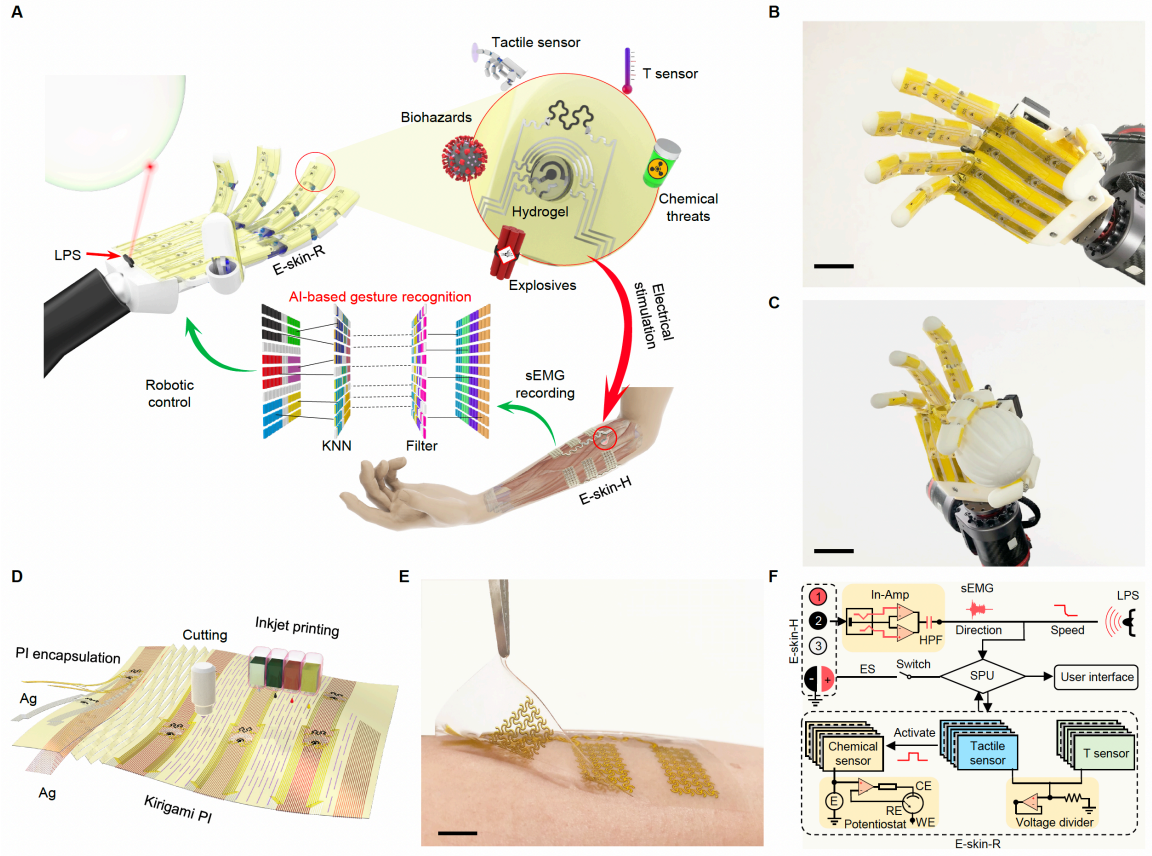

Fig. 2-1 Artificial intelligence (AI)-powered multimodal sensing robotic system (M-Bot) based on a fully-printed soft human-machine interface. (**A**) Schematic of the M-Bot that contains a pair of fully-printed soft electronic skins (e-skins): e-skin-H (interfacing with the human skin) and e-skin-R (interfacing with the robotic skin) for AI-powered robotic control and multimodal physicochemical sensing with user-interactive feedbacks. LPS, laser proximity sensor; sEMG, surface electromyography; T, temperature; KNN, K-nearest neighbors algorithm. (**B** and **C**) Photographs of the robotic skin-interfaced e-skin-R consisting of arrays of printed multimodal sensors. Scale bars, 3 cm. (**D**) Schematic illustration of rapid, scalable, and cost-effective prototyping of the kirigami soft e-skin-R using inkjet printing and automatic cutting. PI, polyimide. (**E**) Photograph of the human skin-interfaced soft e-skin-H with arrays of sEMG and feedback stimulation electrodes. Scale bar, 1 cm. (**F**) Schematic signal-flow diagram of the M-Bot. In-Amp, instrumentation amplifier; HPF, high-pass filter; E, applied voltage; ES, electrical stimulation; SPU, signal processing

unit. WE, CE, and RE represent working, counter, and reference electrodes of the printed chemical sensor, respectively.

2.2 Design of the human-machine interactive e-skins

E-skin-R is composed of high-performance–printed nanoengineered multimodal physicochemical sensor arrays that can be placed on the palm and fingers of the robotic hand (**Fig. 2-1, B** and **C**). The entire sensor patch can be rapidly manufactured in a large-scale and low-cost method via a powerful drop-on-demand inkjet printing technology (**Fig. 2-1D** and **Fig. A-1**). On top of e-skin-R are engraved kirigami structures that provide high stretchability without conductivity changes under a 100% strain, which is crucial for any robotic hand with high degrees of freedom in movement. E-skin-H consists of four sEMG electrode arrays (channels), alongside a pair of electrical stimulation electrodes, which can be fabricated similarly with inkjet printing followed by transfer printing onto a stretchable polydimethylsiloxane (PDMS) substrate (**Fig. 2-1E**). With assistance from AI, multimodal physicochemical sensing, and electrical stimulation–based feedback control, e-skin-R and e-skin-H form a closed-loop human-machine interactive robotic sensing system (**Fig. 2-1F**).

2.3 Fabrication and characterization of the fully inkjet-printed multimodal sensor arrays

The multimodal physicochemical sensor arrays on e-skin-R were fabricated via serial printing of silver (interconnects and reference electrode), carbon (counter electrode and temperature sensor), polyimide (PI) (encapsulation), and target-selective nanoengineered sensing films (tactile sensor and biochemical sensing electrodes) (**Fig. 2-2A**). Customized nanomaterial inks were developed to meet the viscosity, density, and surface tension requirement for inkjet printing and to achieve the desired analytical performance (**Figs. 2-2** and **2-3** and **Table A-1**). The chemical sensors were coated with a soft gelatin hydrogel that was loaded with an electrolyte or redox probe to facilitate target analyte sampling and analysis in situ (**Fig. A-4**). The inkjet-printed carbon electrodes (IPCEs) showed reproducible electroanalytical performance and rapid response for on-site detection of dry-phase analytes

(redox probe Fe3+/Fe2+ was used in the hydrogel as an example) (**Fig. A-5**). The detection area or resolution can be enhanced by increasing either hydrogel size (**Fig. A-6**) or electrode density (**Fig. A-7**).

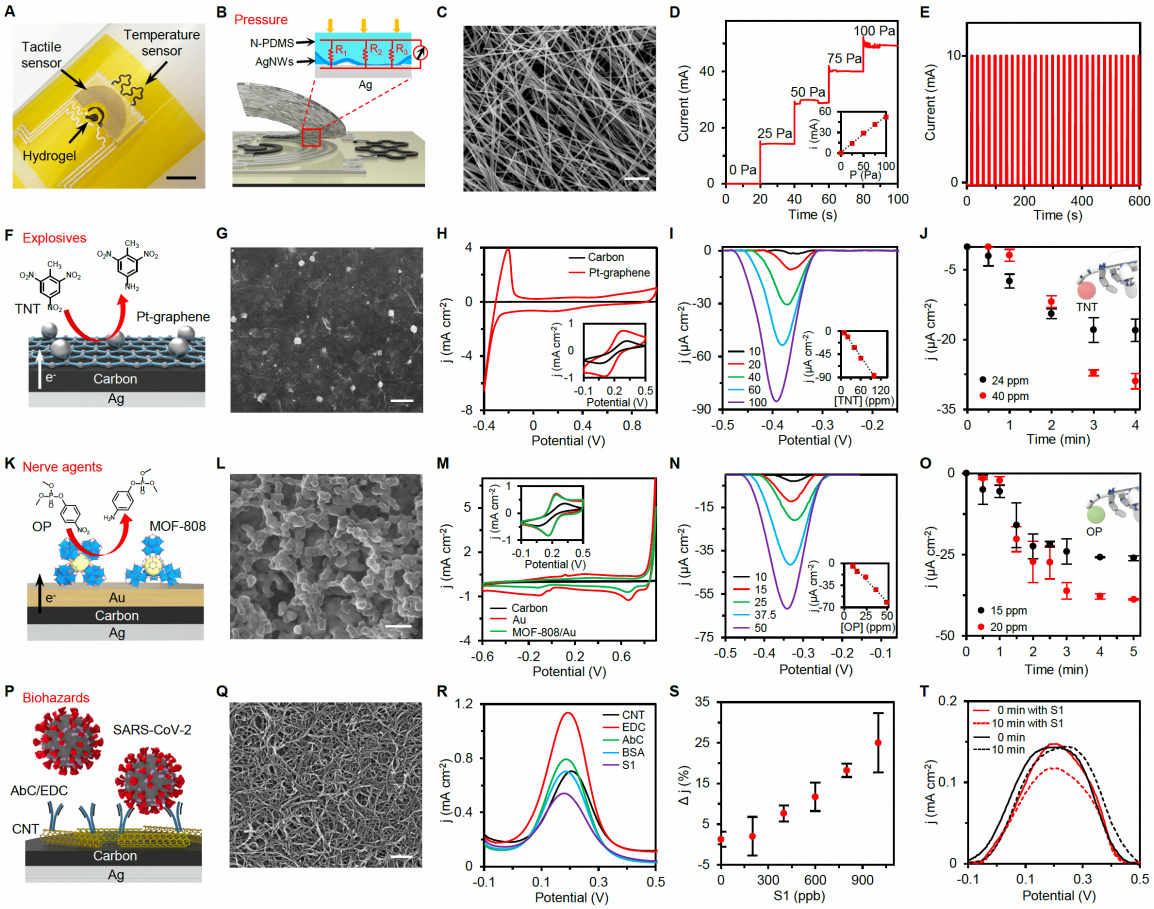

Fig. 2-2 Characterization of the fully inkjet-printed multimodal sensor arrays on the e-skin-R. (**A**) Photograph of a multimodal flexible sensor array printed with custom nanomaterial inks which consists of a temperature sensor, a tactile sensor, and an electrochemical sensor coated with a soft analyte-sampling hydrogel film. Scale bar, 5 mm. (**B** and **C**) Schematic (**B**) and scanning electron microscopy (SEM) image (**C**) of the printed AgNWs/N-PDMS tactile sensor. Scale bar, 1 μm. (**D** and **E**) Response of a tactile sensor under varied pressure loads (D) and repetitive pressure loading (E). (**F** and **G**) Schematic (F) and SEM (G) of the printed Pt-graphene electrode for TNT detection. Scale bar, 4 μm. (**H**) Cyclic voltammograms (CVs) of an IPCE and a printed Pt-graphene electrode in 0.5 M

H2SO4 and in 5 mM K3Fe(CN)6 (inset). j, current density. (**I**) nDPV voltammograms and the calibration plots (inset) of TNT detection using a Pt-graphene electrode. (**J**) Dynamics of robotic fingertip detection of dry-phase TNT using a Pt-graphene sensor. (**K** and **L**) Schematic (K) and SEM image (L) of the printed MOF-808/Au electrode for OP detection. Scale bar, 100 nm. (**M**) CVs of an IPCE, a Au electrode, and a MOF-808/Au electrode in McIlvaine buffer and in 5 mM K3Fe(CN)6 (inset). (**N**) nDPV voltammograms of the OP detection. Inset, the calibration plots. (**O**) Robotic fingertip detection of dry-phase OP using a MOF-808/Au sensor. (**P** and **Q**) Schematic (P) and SEM image (Q) of the printed CNT electrode for SARS-CoV-2 detection. Scale bar, 250 nm. (**R**) DPV voltammograms of a printed CNT electrode in 5 mM K3Fe(CN)6 after each surface immobilization step. EDC, 1-ethyl-3-(3-dimethylamonipropyl)carbodiimide; AbC, capture antibody; BSA, bovine serum albumin. (**S**) Calibration plots of the CNT-based sensor for S1 detection. Δj, percentage DPV peak current changes after target incubation. (**T**) Response of a CNT sensor in the presence and absence of dry-phase S1. All error bars represent the s.d. from 3 sensors.

To effectively manipulate objects and to avoid harming either the e-skin or the object, real-time tactile feedback was enabled by incorporating a piezoresistive pressure sensor based on a printed silver nanowires (AgNWs)/nanotextured PDMS (N-PDMS) sensing film (**Fig. 2-2, B** and **C**). Such tactile sensation provides the robot with the haptic capability to grasp and handle samples. The geometry changes of the AgNWs/N-PDMS in response to a pressure load change the sensor's conductance (**Fig. 2-2D** and **Fig. A-8**). The pressure sensor displayed stable performance under repetitive pressure loading (**Fig. 2-2E** and **Fig. A-8**).

To demonstrate the feasibility of using the printed biosensors for hazardous chemical detection, a standard chemical explosive (TNT), an OP nerve agent simulant (paraoxon-methyl), and a biohazard pathogenic protein from the SARS-CoV-2 virus were chosen. The detection of TNT was achieved using a Pt-nanoparticle–decorated graphene electrode, which was prepared by droplet inkjet printing of aqueous graphene oxide (GO), Pt ions, and propylene glycol and subsequently subjected to thermal reduction. The Pt-graphene showed superior electrocatalytic performance compared with classic carbon and graphene electrodes

(**Fig. 2-2, F** to **H**, and **Fig. A-9**). The reduction of p-NO2 to p-NH2 catalyzed by the Pt-graphene can be detected via negative differential pulse voltammetry (nDPV)[9, 36]. The obtained reduction peak amplitude in the nDPV voltammograms showed a linear relationship with the target TNT concentrations with a sensitivity of 0.95 μA cm−2 ppm−1 and a detection limit of 10.0 ppm (**Fig. 2-2I**). Note that a custom voltammogram analysis with an automatic peak extraction strategy was used by the robot to analyze the original nDPV curves as illustrated in **Fig. A-10**. When integrated onto a robotic hand, the hydrogel-coated Pt-graphene sensor could sample the dry-phase TNT efficiently and provide a stable current response within 3 min (**Fig. 2-2J**); the TNT sensor can be regenerated in situ through repetitive nDPV scans to deplete the sampled analyte molecules toward continuous robotic sensing (**Fig. A-11**). For OP analysis, Pt-graphene and carbon have low electrochemical activity, because Zr-based metal-organic framework (MOF-808) was reported to have strong interaction with OPs[37, 38]. Thus, the printed MOF-808–modified gold nanoparticle electrode (MOF-808/Au) was selected to achieve efficient nonenzymatic OP reduction at a relatively low voltage (**Fig. 2, K** to **M**, and **Fig. A-12**). In this way, the catalyzed reduction of paraoxon-methyl can be monitored via nDPV using the MOF-808/Au sensors with a sensitivity of 1.4 μA cm−2 ppm−1 and a detection limit of 4.9 ppm (**Fig. 2-2N**). In addition to high sensitivity, these printed sensors could also perform high-concentration threat analysis (**Fig. A-13**). Similar to TNT detection, a 3- to 4-min sampling time was found to be sufficient for stable robotic dry-phase OP analysis (**Fig. 2-2O**). The Pt-graphene TNT sensors and MOF-808/Au OP sensors showed high selectivity over other nitro compounds (**Figs. A14** and **A15**). Because of the excellent stability of the catalytic performance of Pt-graphene and MOF-808/Au, the printed sensors can perform continuous TNT and OP analysis (**Fig. A-16**).

Label-free SARS-CoV-2 virus detection was demonstrated from a printed multiwalled carbon nanotube (CNT) electrode that was functionalized with antibodies specific to SARS-CoV-2 spike 1 protein (S1) (**Fig. 2-2, P** and **Q**). The CNT layer had a high electroactive surface area for sensitive electrochemical sensing while providing rich carboxylic acid functional groups for amine-containing affinity probe immobilization to achieve versatile biohazard sensing[39–41]. The successful surface modification of the S1 sensor was confirmed

after each surface immobilization step (**Fig. 2-2R** and **Figs. A17** and **A18**). Parts-per-billion level S1 sensing was performed on the basis of the signal change of the electroactive redox probe (Fe3+/Fe2+) caused by the blockage of the electrode surface due to the S1 protein binding (**Fig. 2-2S**). The response variations of such S1 sensors can be further reduced in the future with an automatic surface modification process. The SARS-CoV-2 S1 sensor shows high selectivity over other viral proteins as illustrated in **Fig. A-19**. On-the-spot robotic S1 protein detection was successfully demonstrated using a collection and detection hydrogel containing the redox probe on the sensor that touched a surface containing a dry blot of the S1 protein (**Fig. 2-2T**). Although the nonspecific adsorption could potentially reduce the selectivity of the hydrogel detection process (**Fig. A-20**), the semiquantitative data conveniently and automatically obtained on site by the sensor could still provide the users rapid, real-time feedback and alert on the presence of biohazard.

To ensure accurate hazard detection in extreme operational environments, a printed carbon-based temperature sensor was designed for on-site temperature sensing and chemical sensor calibration during operation (**Fig. A-21**). All printed sensors maintained similar performance under and after repetitive mechanical bending tests, indicating their high mechanical stability (**Fig. A-22**). The freshly prepared hydrogels can be stored at 4°C in a moist chamber for more than 1 week and maintain similar sensing performance (**Fig. A-23**). To minimize the influence of the shearing and normal forces on the sensor performance, the AgNWs/N-PDMS pressure sensor was designed to form a protection microwell for each hydrogel-coated biosensor and to facilitate reliable chemical analyte sample collection (**Figs. A24** and **A25**); moreover, the tactile feedback from the AgNWs/N-PDMS pressure sensor could ensure stable electrochemical sensing performance (contact pressure was maintained between 0 and 500 Pa during operation).

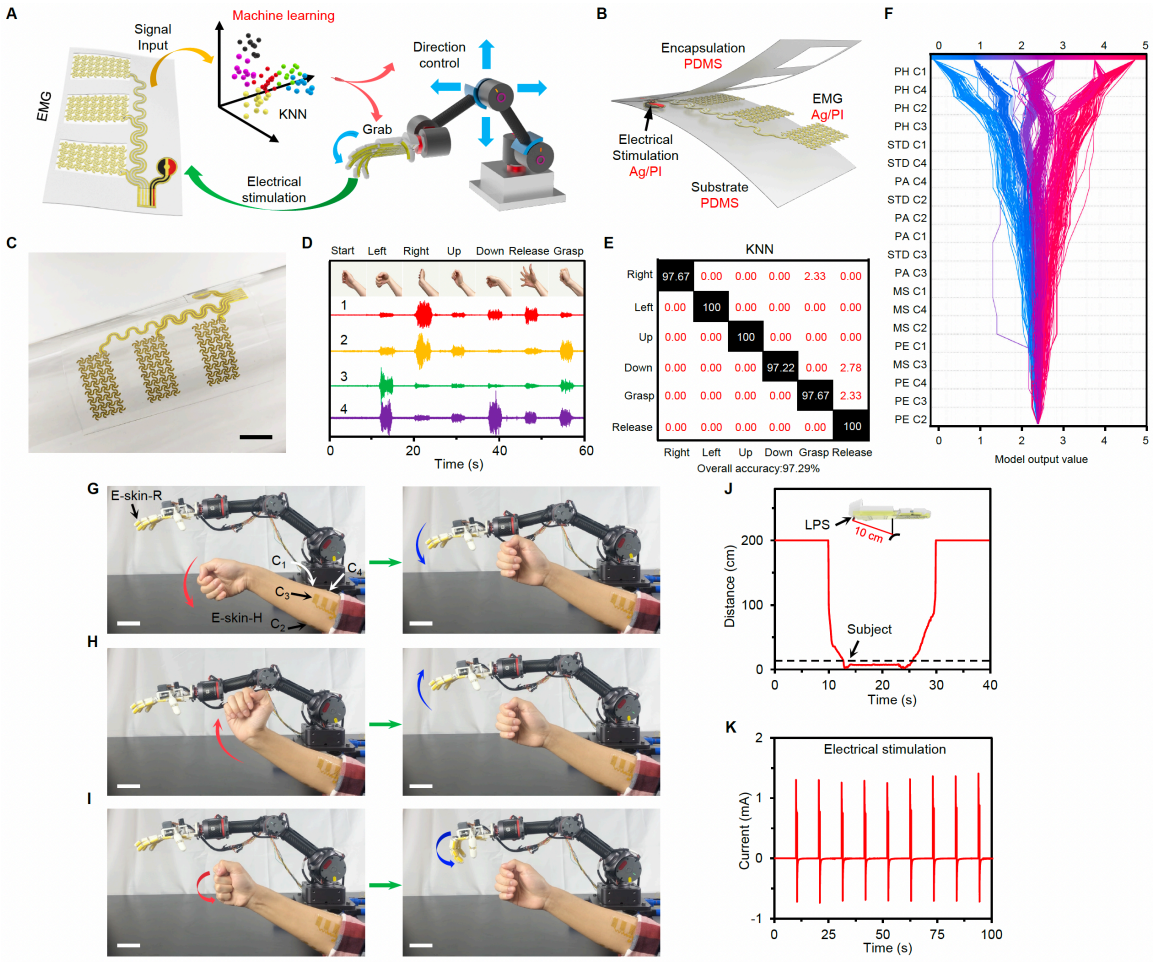

Fig. 2-3 Evaluation of the e-skin-H for AI-assisted human-machine interaction. (**A**) Schematic of machine learning-enabled human gesture recognition and robotic control. (**B** and **C**) Schematic (B) and photograph (C) of a PDMS encapsulated soft e-skin-H with sEMG and electrical stimulation electrodes for closed-loop human interactive robotic control. Scale bar, 1 cm. (**D**) sEMG data collected by the four-channel e-skin-H from 6 human gestures. (**E**) Classification confusion matrix using a KNN model based on real-time experimental data. White text values, percentages of correct predictions; red text values, percentages of incorrect predictions. (**F**) A SHAP decision plot explaining how a KNN model arrives at each final classification for every datapoint using all 5 features. Each decision line tracks the features contributions to every individual classification; each final classification is represented as serialized integers (that map to a hand movement). Dotted lines represent

misclassified points. (**G–I**) Time-lapse images of the AI-assisted human-interactive robotic control using the M-Bot. Scale bars, 5 cm. (**J**) Response of the LPS when the robot approaches and leaves an object. (**K**) Current applied on a subject's arm during the feedback stimulation.

2.4 Evaluation of e-skin-H for AI-assisted human-machine interaction

E-skin-H acts as a human-machine interface for autonomous robotic control and object manipulation (**Fig. 2-3A**). In particular, e-skin-H records neuromuscular activity, which provides an intuitive interface to perform hand gesture recognition, through its inkjet-printed, PDMS-encapsulated, four-channel, three-electrode sEMG arrays (**Fig. 2-3, B** and **C**, and **Fig. A-26, A** to **C**). Analyzing the interfacial contact with the skin, e-skin-H demonstrates high stretchability with good mechanical compliance during physical activities through its serpentine structure to provide reliable sEMG recordings (**Fig. A-26, D** to **I**).

Upon signal acquisition, various machine learning algorithms were evaluated for accurate gesture recognition including linear regression, random forest, artificial neural networks, support vector machines (kernels: radial, sigmoid, linear, and polynomial), and k-nearest neighbors (KNNs). Each algorithm was shown to extract motor intention from sEMG signals, acting as a bridge between conscious thought and prosthetic actuation. Of all the machine learning algorithms, the KNN model provided the highest prediction accuracy for all six hand gestures with an overall mean accuracy across 5000 randomly selected training data of 97.29 ± 1.11% based on real-time experimental results collected from a human participant (**Fig. 2-3, D** and **E**, and **Fig. A-27**). The next best model was the random forest classifier, which was found to have a similar average classification accuracy except with a higher variance. The KNN model was able to provide high-accuracy recognition of gestures with different angles when applying the e-skin-H to other body parts such as the neck, lower limb, and upper back—each time achieving an accuracy of greater than 90% (**Figs. A28** and **A29**).

For each gesture, five features were extracted from the associated peak in the root mean square (RMS)–filtered sEMG data (**Fig. A-30**): peak height (PH), peak standard deviation

(STD), maximum slope (MS), peak average (PA), and peak energy (PE) (Supplementary Methods). The relevance of each feature and channel in the prediction method was further evaluated using Shapley additive explanation (SHAP) values[42]. Through the SHAP values and the KNN accuracy, it was determined that PH was the most important feature for accurate gesture classification (**Fig. 2-3F** and **Fig. A-31**). When considered alongside PH, SD and PA both increased the classification accuracy, with SD being the most beneficial (**Figs. A31** and **A32**). In terms of channels, it was found that three EMG channels were sufficient to provide a high gesture accuracy of 96.31 ± 1.25%. Adding a fourth channel was beneficial but not statistically significant (**tables A2** and **A3**).

With the KNN algorithm, the robot can imitate the user's gesture in millisecond-level time for automatic object manipulation. The data acquisition and signal processing time delay to determine a gesture were around 200 ms, well below the required time for optimal real-time robotic control[43]. This was achieved using a sampling rate of 534 Hz and analyzing the data in batches of 100 points. The M-Bot's time delay was substantially reduced by training the KNN model on only half of any sEMG signal for gesture recognition. By reducing the required data needed to determine a gesture, the machine learning model was able to predict the movement almost immediately after the gesture was complete.

The AI-powered e-skin-H–enabled gesture recognition provides a framework for online multidirectional robotic control with high-accuracy remote object manipulation (as illustrated in **Fig. 2-3, G** to **I**). After object contact, recognition, and positive threat detection, tactile and alarm feedback can be activated to inform the user of any potential danger using a pulsed current load between the two stimulation electrodes (**Fig. 2-3J**). To facilitate safe robotic handling and to protect e-skin-R from uncontrolled collisions, a laser proximity sensor was integrated into the robotic hand to reduce the actuation speed as the hand approaches a barrier (<10 cm) (**Fig. 2-3K** and **Fig. A-33)**.

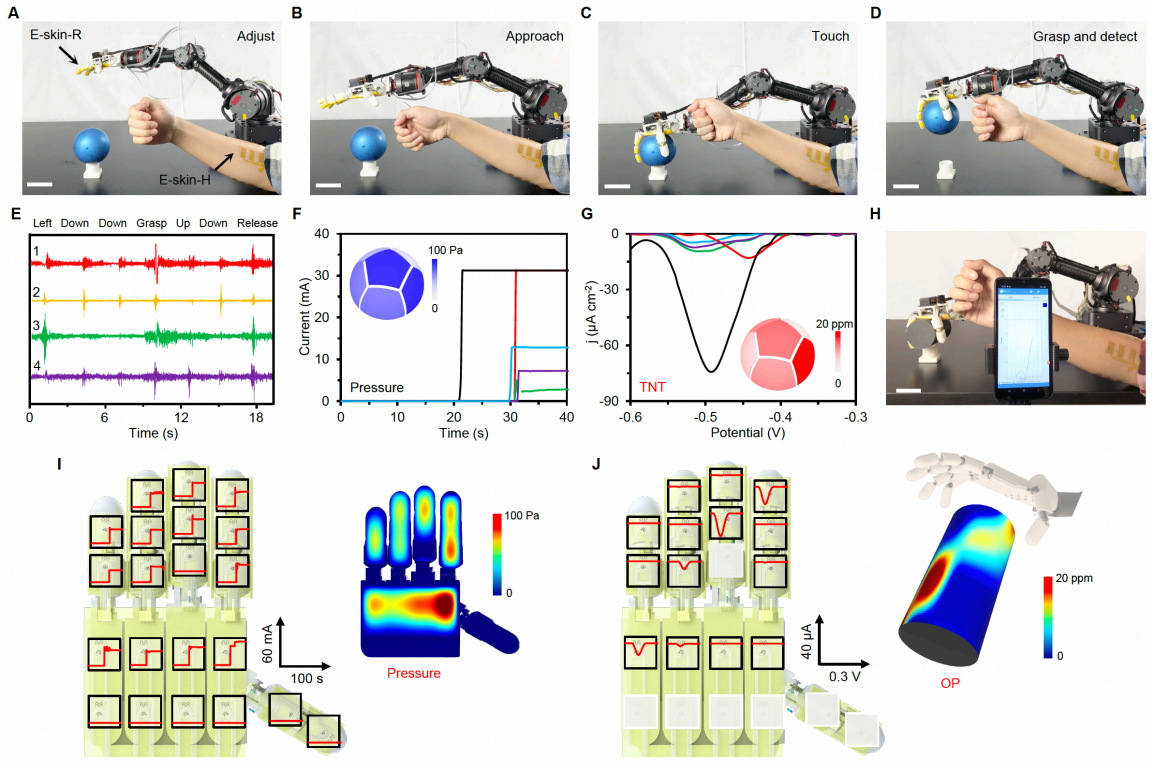

Fig. 2-4 Evaluation of the M-Bot in human-interactive robotic physicochemical sensing. (**A–D**) Time-lapse images of the human-interactive robotic control for object grasping and on-site TNT detection. Scale bars, 5 cm. (**E–G**) The sEMG data collected in real-time which allow the robotic hand to approach and grasp a spherical object (E) and the corresponding tactile (F) and TNT (G) sensor responses. Insets in F and G, colored mapping of pressure and TNT distributions on the object. (H–J) Photograph of the robotic OP sensing on a cylindrical object (**H**) and the corresponding responses of the tactile sensors (**I**) and OP sensors (**J**) on an e-skin-R. Insets in I and J represent the color mappings of pressure and OP distributions on the object. Scale bar, 5 cm.

2.5 Evaluation of the M-Bot in human-interactive robotic physicochemical sensing

With delicate and precise control, the human-machine interactive M-Bot was successfully evaluated for fingertip point-of-use robotic TNT detection (**Fig. A-34**). The multimodal sensor data could be captured in real time using a portable multichannel potentiostat, wirelessly transmitted to the mobile phone, and displayed on the cellphone app (**Fig. A-34**).

The M-Bot was also able to perform object grasping and multispot tactile and chemical sensing (**Fig. 2-4, A** to **D**). Multiplexed physicochemical data were simultaneously recorded and automatically processed without signal interferences (**Fig. A-35**). In an example demonstration, seven AI-assisted gesture-controlled steps were used in sequence to control the robotic hand as it approached, grasped, and released a spherical object (**Fig. 2-4E**, **Fig. A-36**). In parallel, five sensor arrays were activated, displaying multiplexed tactile readings and surface TNT levels (**Fig. 2-4, F** and **G**).

The use of the M-Bot for multiplexed physicochemical robotic sensing was further evaluated on an OP-contaminated cylindrical surface (**Fig. 2-4H**). During the experiment, 14 sensor arrays on e-skin-R were activated. The tactile and OP sensor responses from each sensor, along with the corresponding color mapping of their distributions across the three-dimensional (3D) surface, are displayed in **Fig. 2-4** (**I** and **J**, respectively) (detailed data are demonstrated in **Figs. A37** and **A38**). We anticipate that by further increasing the number and density of the multimodal sensor arrays, more accurate and informative data can be obtained from arbitrary objects and surfaces.

2.6 Evaluation of an e-skin-R–enabled M-Boat for autonomous source tracking

The multimodal robotic sensing platform was further generalized onto an autonomous robotic boat capable of tracking pollutants, explosives, chemical threats, and biological hazards for risk prevention and mitigation, which is an important topic in civil security[7, 44]. In this regard, our printed multimodal e-skin-R technology was adapted onto a multimodal sensing robotic boat (M-Boat) for real-time hazard detection and to autonomously locate the source of water-based chemical leakages (**Fig. 2-5A**). 3D printed from simple computer-aided designs, the M-Boat contains an inkjet-printed multimodal sensor array with one temperature and three chemical sensors, two electrical motors (for boat propulsion and steering), and a printed circuit board (PCB) for data collection, signal processing, and motor control (**Fig. 2-5, B** to **D**, and **Fig. A-39**). The propulsion of the M-Boat can be precisely controlled by adjusting the individual duty cycle of pulsed voltages supplied to each motor (**Fig. 2-5E** and **Fig. A-40**). For source detection, an A* search algorithm[45] was implemented

for autonomous decision-making while searching for the maximum concentration of the chemical leakage (**Fig. 2-5, F** and **G**, **Fig. A-41**, and Appendix A Methods). At each decision point, the sensors can detect small traces of the chemical leak in three equidistant locations around the boat. With this input, the algorithm calculates the optimal direction to travel using the gradient vector, indicating the direction of the highest concentration, and a heuristic estimate of the diffusion based on an interpolated map from previous points. By using the heuristic map in parallel with the gradient, the algorithm takes advantage of both the past and present results to precisely predict the spatial location of the source. The performance of the M-Boat was evaluated through simulations and experimentally in water tanks containing various chemical gradients induced by a low pH-corrosive fluid (**Fig. 2-5, H** and **I**, **Fig. A-42**) and OP leakage (**Fig. 2-5, J** and **K**). In the water tank, the M-Boat performed real-time detection of the surrounding analyte concentrations, automatically adjusting its trajectory based on the A* algorithm, to successfully identify the leakage source. The M-Boat was also able to perform continuous hazard analysis and autonomous leakage tracking in seawater (**Fig. A-43**). The surrounding pH and ionic strength of a real-world sample matrix (e.g., lake water or seawater) did not show substantial influence on the sensor performance (**Fig. A-44**). When necessary, more real-time calibration mechanisms for precise hazard analysis can be introduced by incorporating more related biosensors (e.g., pH and conductivity sensors) into the e-skin-R. With more advanced robotic control and sensing designs, the M-Boat platform could serve as an important basis for intelligent path planning and decision-making of autonomous vehicles.

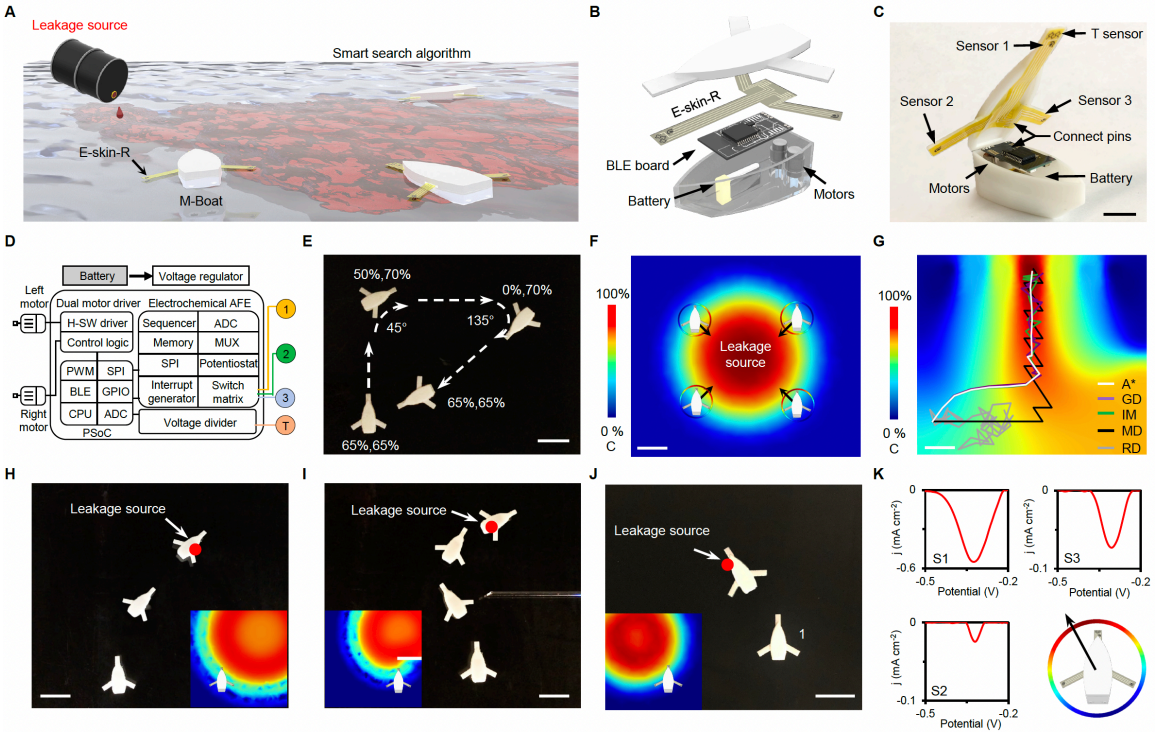

Fig. 2-5 Evaluation of the-skin-R in an autonomous multimodal sensing robotic boat (M-Boat). (**A**) Schematic of the intelligent M-Boat integrated with a printed multimodal e-skin-R sensor array that can perform temperature and multiplexed chemical sensing for autonomous source tracking. **(B** and **C**), Schematic (B) and photograph (C) illustrating the assembly of the M-Boat components. (**D**) System block diagram of the M-Boat for autonomous propulsion, sensing, and signal processing. ADC, analog-to-digital converter; AFE, analog front-end; BLE, Bluetooth low energy; CPU, central processing unit; GPIO, general-purpose input/output; H-SW, H-bridge software; MUA: multiplexer; PWM, pulse width modulation; SPI, serial peripheral interface. (**E**) Wireless control of the M-Boat. (**F**) Simulated distributions of a hazardous chemical (OP) leak and the algorithm used by the M-Boat for autonomous source tracking. C, concentration. (**G**) Simulation comparison of different search algorithms used by the M-Boat for intelligent source tracking. GD, gradient descent; IM, interpolated map; MD, max direction; RD, random direction. (**H** and **I**) Time lapse images showing example demonstrations of the M-Boat enabled autonomous source tracking. Insets, simulated target (proton from corrosive acid) distributions. Scale bars, 5 cm. (**J** and **K**) Time lapse images (J) and the nDPV voltammograms collected at location 1 (K)

for autonomous decision-making and chemical threat (OP) source tracking using an M-Boat. Insets, simulated OP distribution. Scale bar, 5 cm.

2.7 Discussion

Here, we have described a human-machine interactive e-skin–based robotic system (M-Bot) with multimodal physicochemical sensing capabilities. The mass-producible flexible sensor arrays allow for high-performance on-site monitoring of temperature, tactile pressure, and various hazardous chemicals (in both dry phase and liquid phase) such as explosives, OPs, and pathogenic proteins. The integration of such multimodal sensors onto a robotic e-skin platform provides autonomous systems with interactive cognitive capabilities and substantially broadens the range of tasks that robots can perform, such as combating infectious diseases like COVID-19.

Existing robotic sensing technologies are largely limited to monitoring physical parameters such as temperature and pressure. To achieve high-performance chemical sensing, nanomaterials are commonly used via manual drop-casting methods, which could lead to large sensor variations. Moreover, most electrochemical sensing strategies require detection in aqueous solutions, making them impractical for dry-phase robotic analysis. Now, there are no reported scalable low-cost manufacturing approaches to prepare robotic physicochemical sensors. In this work, we proposed a scale solution to fabricate flexible, multifunctional, and multimodal sensor arrays prepared entirely by high-speed inkjet printing. Custom-developed functional nanomaterial inks are designed and optimized to achieve highly sensitive and selective sensors for the specific hazardous target analytes. The hydrogel-coated printed nanobiosensors allow for efficient dry-phase chemical sampling and rapid on-site hazard analysis on a robotic platform.

Manufactured using the same approach, e-skin-H ensured stable contact with the soft human skin for reliable recording of neuromuscular activity to facilitate remote robotic sensing and control. To minimize the amount of data collected and analyzed for human-robotic interaction, AI and smart algorithms were applied to decode incoming information and

efficiently predict and control robotic movement. An in-depth analysis into each sEMG channel's individual contribution to the machine learning model was presented, allowing future researchers to optimize the number of electrodes needed for robotic control. Using the SHAP analysis, we further untangled the hidden overlapping information between each channel's features and categorized which features present the most nonoverlapping information for gesture prediction. For the M-Bot, machine learning gesture prediction via e-skin-H was further coupled with user-interactive tactile and threat alarm feedback that allow seamless human-machine interaction for the remote deployment of robotic technology in extreme or contaminated environments. To obtain such real-time results, the robotic platform's data acquisition, signal processing, feature extraction, and gesture prediction of the sEMG signals were performed with millisecond-level time after the gesture was complete. The M-Boat similarly used a smart A* algorithm for autonomous source detection, minimizing the boat's path, and subsequently, time and energy, in finding potentially hazardous chemical leaks. In these applications, the systems demonstrated real-time autonomous movement, all within a low-cost mass-producible system, lowering the barrier for real-time robotic perception.

This human-machine–interactive robotic sensing technology represents an attractive approach to develop advanced flexible and soft e-skins that can reliably collect vital data from the human body and the surrounding environments. Full system integration to achieve high-speed, wireless, and simultaneous multichannel physicochemical sensing is strongly desired for future field deployment and evaluation. Moreover, we envision that, by integrating a high density and new types of multimodal sensors, this technology could substantially enhance the perceptual capabilities of future intelligent robots and pave the way to numerous new practical wearable and robotic applications.

2.8 Materials and methods

Materials

Graphite flake was purchased from Alfa Aesar. Sodium nitrate, potassium permanganate, hydrogen peroxide, potassium hexacyanoferrate(III), citric acid, chloroplatinic acid, PDMS, zirconium(IV) chloride, aniline, gelatin, paraoxon-methyl, TNT solution, 4-nitrophenol, 2-nitrophenyl octyl ether, 2-nitroethanol, 2-nitropropane, 4-nitrotoluene, 2,4-dinitrotoluene, poly(pyromellitic dianhydride-co-4,4′ -oxydianiline) amic acid (PAA) solution [12.8 weight % (wt %)], 1-methyl-2-pyrrolidinone (NMP), N-hydroxysulfosuccinimide sodium salt (Sulfo-NHS), N-(3-dimethylaminopropyl)-N′ -ethyl carbodiimide hydrochloride (EDC), 2-(N-morpholino)ethanesulfonic acid hydrate (MES), potassium permanganate (KMnO4), bovine serum albumin (BSA), human immunoglobulin G (IgG), and lysozyme were purchased from Sigma-Aldrich. Sodium chloride, sulfuric acid, hydrochloric acid, disodium phosphate, 1,3,5-benzenetricarboxylic acid (H3BTC), formic acid, N,N′ -dimethylformamide (DMF), potassium ferricyanide, propylene glycol, isopropyl alcohol (IPA), and phosphate-buffered saline (PBS) were purchased from Thermo Fisher Scientific. His-tagged SARS-CoV-2 S1 (PNA002), anti–Spike-RBD human monoclonal antibody (IgG) (S1-IgG, AHA013), SARS-CoV S1 (40150-V08B1), SARS-CoV nucleocapsid protein (NP; 40143-V08B), and SARS-CoV-2 NP (40588-V08B) were purchased from Sanyou Biopharmaceuticals. AgNW suspension (20 mg ml−1 in IPA) was purchased from ACS Material LLC. Silver ink (25 wt %) and carbon ink (5 wt %) were purchased from NovaCentrix. Gold ink (10 wt %) was purchased from C-INK Co. Ltd. Carboxyl-functionalized multiwalled CNT ink (2 mg ml−1; Nink-1000) was purchased from NanoLab Inc. PI film (12.5 μm) was purchased from DuPont.

Preparation and characterizations of print inks

To prepare the Pt-graphene ink, GO was first prepared following a modified Hummer's method[46]. One gram of graphite flake was mixed with 23 ml of H2SO4 for more than 24 hours, and then 100 mg of NaNO3 was added inside. Subsequently, 3 g of KMnO4 was added below 5°C in an ice bath. After stirring at 40°C for another 30 min, 46 ml of H2O was added while the solution temperature was slowly increased to 80°C. In the end, 140 ml of H2O and 10 ml of H2O2 were introduced into the mixture to complete the reaction. The GO

was washed with 1 M HCl and filtered. After dried under vacuum at 60°C, a GO (2 mg ml−1) suspension was prepared followed by the addition of 5 mM chloroplatinic acid under sonication. Last, the suspension was mixed with propylene glycol (80:20, v/v) to form the Pt-graphene ink.

The MOF-808 was synthesized solvothermally. Briefly, H3BTC (0.236 mM) and ZrCl4 (1 mM) were mixed with 15.6 ml of the DMF and formic acid (1:0.56, v/v) solvent and sonicated for 20 min. Then, the mixture was transferred to a 25-ml Teflon-lined autoclave and kept at 120°C for 12 hours. After the reaction, the autoclave was naturally cooled to room temperature. The product was washed with DMF and methanol and then dried under vacuum at 60°C. Last, a MOF-808 suspension in deionized (DI) water was prepared and mixed with propylene glycol (80:20, v/v) to form the MOF-808 ink.

The AgNWs ink was prepared by diluting the AgNW suspension with IPA to 2 mg ml−1 and sonicating it for 10 min. The CNT ink was prepared by mixing the commercial CNT ink (2 mg ml−1) with propylene glycol (80:20, v/v). PAA ink was prepared by diluting the commercial PAA solution with NMP to 3 wt %. Commercial silver and carbon inks were used as received.

The dynamic viscosity (η), density (ρ), and surface tension (γ) for all inks were characterized before printing. Dynamic viscosity was characterized with an Anton Paar MCR302 rheometer. Surface tension was measured with a Ramé-Hart contact angle goniometer using the equation

$$\gamma = \frac{\Delta\rho g R_0^2}{\beta} \tag{2.1}$$

Here, $\Delta\rho$ is the density difference between air and inks, g is the gravitational acceleration, $R_0$is the radius of curvature at the drop apex, and β is the shape factor.

Fabrication and assembly of the soft inkjet-printed e-skin-R

The fabrication process of the inkjet-printed e-skin-R is illustrated in **Fig. A-1**. The PI substrate was cut with kirigami structures by automatic precision cutting (Silhouette Cameo 3). A 2-min O2 plasma surface treatment was performed with Plasma Etch PE-25 (10 to 20 cm3 min−1 O2, 100 W, 150 to 200 mtorr) to enhance the surface hydrophilicity of the PI substrate. The multimodal sensor arrays on e-skin-R were fabricated via serial printing of silver (interconnects and reference electrode), carbon (counter electrode and temperature sensor), PI (encapsulation), and target-selective nanoengineered sensing layers (e.g., AgNWs, Pt-graphene, Au, and MOF-808) using an inkjet printer (DMP-2850, Fujifilm). The ink composition, characterizations, and thermal annealing conditions are shown in table S1. Thirty layers of AgNWs were printed on an N-PDMS substrate (cured on a 1000-mesh sandpaper) to form the piezoresistive tactile sensors. While printing, the plate temperature was set to 40°C to ensure the rapid vaporization of the IPA solvent. The AgNWs/N-PDMS were cut to semicircle shape and set on the e-skin.

For preparing biohazard S1 protein sensor (**Fig. A-17**), a CNT film was printed on the IPCE first. The carboxylic groups of multiwall CNTs were activated to NHS esters, by drop-casting 10 μl of EDC (400 mM) and NHS (100 mM) in MES buffer (25 mM, pH 5) for 35 min. In the next step, 5 μl of anti–Spike-RBD antibody (250 μg ml−1) in PBS were dropped on the modified electrode and incubated for 2 hours. Next, 10 μl of 1% BSA in PBS were dropped and incubated for 1 hour to deactivate residual NHS esters. The modified sensors were stored in the refrigerator until use.

To assemble the robotic e-skin, the pins of the finger printed e-skin were connected with the bottom printed silver connections of palm part through a z axis conductive tape (3M), and then e-skin-R was set on a robotic hand printed with a 3D printer (Mars Pro, Elegoo Inc.).

Characterizations of the multimodal robotic sensing performance of e-skin-R

The printed biosensors were characterized with cyclic voltammetry (scan rate: 50 mV s−1, unless otherwise noted), DPV, and amperometric current (i)-time (t) through an electrochemical workstation (CHI 660E). McIlvaine buffer solutions (pH 6.0) were used to

prepare the analyte solutions. A commercial Ag/AgCl reference electrode (CHI111) was used for characterizing the printed sensing electrodes in the solution, whereas printed Ag solid-state electrodes were used for hydrogel-based sensor characterization (there was an ~0.1-V difference between these two types of reference electrodes in McIlvaine buffer). To quantify the electrochemical performance and the electrochemical surface areas, the print electrodes were tested in 5 mM K3Fe(CN)6 and 1 M KCl with scan rates of 5 mV s−1 from −0.1 to 0.5 V.

For TNT and OP sensors, the conditions of nDPV measurements include a scan range of −0.15 to −0.5 V, an incremental potential of 0.004 V, a pulse amplitude of 0.05 V, a pulse width of 0.05 s, and a pulse period of 0.5 s. The reduction peaks of nDPV curves were extracted using a custom-developed iterative baseline correction algorithm. To prepare the electrolyte-loaded hydrogel for analyte sampling and sensing, 0.250 g of gelatin powder, 0.075 g of KCl, 0.071 g of citric acid, and 0.179 g of disodium phosphate were mixed in 10 ml of DI water and stirred at 80°C for 15 min. The hydrogel was stored and aged overnight. The gelatin electrolyte-loaded hydrogel was coated on the printed biosensors for dry blot detection.

For S1 protein detection, the modified electrode was incubated with 10 µl of S1 protein in PBS for 10 min, and the DPV measurements ranged from −0.1 to 0.5 V. The electrochemical signal of the sensor before and after antigen binding was measured in 5 mM K3Fe(CN)6. The difference between the peak current densities (Δj) was obtained as sensor readout. A sampling hydrogel pad was prepared to demonstrate the feasibility for SAR-CoV-2 virus dry blot detection. To perform one-step detection, 10 µl of gelatin hydrogel [7.5 wt % gelatin, 10 mM K3Fe(CN)6, and 0.2 M phosphate buffer (pH 7.0)] was placed onto a dry S1 protein blot [from 10 µl of a SARS-CoV-2 S1 protein droplet (1 µg ml−1)]. Such amount of S1 protein could potentially be found in the saliva droplet of a patient with COVID-19[47]. For dry-phase sensing selectivity study, the dry protein blots were created with the same amount of interference proteins (10 µl, 1 µg ml−1). The electrochemical signal of the gel was recorded immediately and 10 min after joining the biosensor with the gel.

The temperature sensor characterization was performed on a ceramic hot plate (Thermo Fisher Scientific), and an amperometric method (with an applied voltage of 2 V) was used to detect the temperature response. The piezoresistive tactile sensor characterization was also applied with a constant voltage of 2 V to record the current response under various pressure loads.

The scanning electron microscopy (SEM) images of the electrodes were obtained by a field-emission SEM (FEI Nova 600 NanoLab). Energy-dispersive spectroscopy (EDS) mapping were obtained by an EDS spectrometer (Bruker Quantax EDS).

Fabrication and assembly of e-skin-H

The fabrication process of e-skin-H was illustrated in **Fig. A-26**. A 2-min O2 plasma surface treatment was performed with Plasma Etch PE-25 to enhance the surface hydrophilicity of the PI substrate. Silver interconnects were printed with DMP-2850. The PI substrate without the printed patterns were removed with laser cut using a 50-W CO2 laser cutter (Universal Laser Systems). The optimized laser cutter parameters were power of 10%, speed of 80%, and pixels per inch (PPI) of 1000 in vector mode. After cleaned with ethanol and dried, the remaining patterns were transferred onto a 70-μm-thick PDMS substrate and then encapsulated with another layer of PDMS film as well (with sEMG and electrical stimulation electrodes exposed). An adhesive electrode gel (Parker Laboratories Inc.) was spread onto the electrodes before placing on human participants.

Evaluation of the human-machine interactive multimodal sensing robot

To evaluate the performance of the M-Bot, the e-skin-R–interfaced 3D printed robotic hand was assembled onto a five-axis robotic arm (Innfos Ltd.). The e-skin-H was then set around a human participant's forearm after cleaning the skin with alcohol swabs. The sEMG data were acquired with four channels (three sEMG electrodes in each channel) through an open-source hardware shield (Olimex). The signals were sampled as integers between 0 and 1023 by a 10-bit analog-to-digital converter (ADC) and then processed through a serial (cluster

communication) port. Each channel was then scaled back into voltages between 0 and 5 V. Although the robotic arm control was performed in real time, data processing was performed asynchronously to signal acquisition. During processing, the data were first put through a high-pass filter with a cutoff frequency of 100 Hz. The points were subsequently downsized using an RMS filter (batch size: 400 points and step size: 10 points). The peaks detected after processing were used as features for the machine learning model. Overlapping peaks from each channel (peaks within a half-peak width away) were categorized as a single group. If multiple peaks were detected in a single channel's set, then the first peak was used. The KNN training model was built using 60 samples per each of the six gestures. The training and testing datasets were divided 2:1, respectively, and were randomly selected using an equal representation of each gesture. After the model was developed, it was further evaluated for accuracy using new data from each gesture. The laser proximity sensor (LPS) (TOF10120) was operated through a customized interactive control software in Python (Python 3.8). For dry blot threat detection, TNT and OP threat coatings were created by spraying analyte vapor onto the selected objects in a fume hood. Multimodal sensing data collected during robotic sensing operations were collected through a portable electrochemical workstation (PalmSens4) with a multiplexer.

The validation and evaluation of the M-Bot were performed using human participants in compliance with all the ethical regulations under protocols (ID 19-0895) that were approved by the Institutional Review Board at the California Institute of Technology. Three participates were recruited from the California Institute of Technology's campus and the neighboring communities through advertisement. All participants gave written informed consent before study participation.

Machine learning data analysis

For each gesture, all five features were extracted from the associated peak in the RMS-filtered EMG data: height, average area, SD, average energy (intensity), and maximum slope. The features extracted were calculated in reference against their baselines, which were determined via a binary search of the previous data in 50-ms intervals.

After feature extraction, SHAP values were used to evaluate the performance enhancement of each feature extracted and EMG channel used. In addition to SHAP values, the average testing accuracy across 5000 training sessions was taken for each permutation of features and EMG channels, which supplemented the SHAP values in providing further insight into which channels and features contained nonoverlapping beneficial information for gesture determination. For each of the 5000 trials, the testing points represented 33% of the dataset, with each gesture in the test set being proportionally represented in the full dataset. For the arm EMG dataset, this amounted to 387 movements split across six gestures; of those points, the KNN model was fit using 257 training points and scored on the remaining 128 testing points (testing and training were proportionally stratified across all six gestures).

Evaluation of the M-Boat

To evaluate the performance of the M-Boat, the e-skin-R was assembled onto a 3D printed boat with a four-layer PCB, as shown in **Fig. 2-5** (**B** and **C**). On the PCB, a Bluetooth low-energy (BLE) module (CYBLE-222014-01, Cypress Semiconductor) was used for controlling the electrochemical front end through a serial peripheral interface (SPI). This module was also used to control the motor driver through general purpose input/output (GPIO) pins and pulse width modulation (PWM) and to transmit data over BLE. An electrochemical front end (AD5941, Analog Devices) was set up via SPI to perform multiplexed electrochemical measurements with the sensor arrays and to send the acquired data to the BLE module for signal processing and BLE transmission. A BLE dongle (CY5677, Cypress Semiconductor) was used to establish a BLE connection with the M-Boat and to securely receive the sensor data via BLE indications. An A* algorithm was used to analyze the sensor data and compute the next M-Boat's movement path with the optimal motor speed. The calculated motor speed information was sent back to the BLE module in real time for the pulse width–modulated control of two motors (Q4SL2BQ280001) through a dual dc motor driver (TB6612FNG, Toshiba). The entire system was powered by a 3.7-V Li-ion battery (40 mAh).

For the OP chemical threat tracking experiment, a natural diffusion gradient was generated by 10 droppings of 20 μl of 0.1 M OP into a 0.1 M NaCl solution tank. The seawater studies were performed in seawater samples collected from the Pacific Ocean in Los Angeles. The M-Boat was set into the tank after 30 min. For the corrosive acidic threat tracking experiment, pH sensors were modified on e-skin-R instead. Briefly, a polyaniline pH-sensitive film was electropolymerized on the IPCE in a solution containing 0.1 M aniline and 0.1 M HCl using a CV from −0.2 to 1 V for 25 cycles at a scan rate of 50 mV s−1. Then, 100 μl of H2SO4 (2 M) as the leakage source was dropped into the middle of the water tank. Last, the M-Boat was set after 45/30 min with/without barriers in the tank, respectively.

Bibliography of Chapter 2

1. G.-Z. Yang, J. Bellingham, P. E. Dupont, P. Fischer, L. Floridi, R. Full, N. Jacobstein, V. Kumar, M. McNutt, R. Merrifield, B. J. Nelson, B. Scassellati, M. Taddeo, R. Taylor, M. Veloso, Z. L. Wang, R. Wood, The grand challenges of Science Robotics. *Sci. Robot.* **3**, eaar7650 (2018).
2. S. Sundaram, P. Kellnhofer, Y. Li, J.-Y. Zhu, A. Torralba, W. Matusik, Learning the signatures of the human grasp using a scalable tactile glove. *Nature*. **569**, 698–702 (2019).
3. M. Cianchetti, C. Laschi, A. Menciassi, P. Dario, Biomedical applications of soft robotics. *Nat. Rev. Mater.* **3**, 143–153 (2018).
4. A. Chortos, J. Liu, Z. Bao, Pursuing prosthetic electronic skin. *Nat. Mater.* **15**, 937–950 (2016).
5. C. M. Boutry, M. Negre, M. Jorda, O. Vardoulis, A. Chortos, O. Khatib, Z. Bao, A hierarchically patterned, bioinspired e-skin able to detect the direction of applied pressure for robotics. *Sci. Robot.* **3**, eaau6914 (2018).
6. J. Yin, R. Hinchet, H. Shea, C. Majidi, Wearable soft technologies for haptic sensing and feedback. *Adv. Funct. Mater.* **31**, 2007428 (2020).

7. H. Ishida, Y. Wada, H. Matsukura, Chemical sensing in robotic applications: A review. *IEEE Sens. J.* **12**, 3163–3173 (2012).

8. J. Trevelyan, W. R. Hamel, S.-C. Kang, in *Springer Handbook of Robotics*, B. Siciliano, O. Khatib, Eds. (Springer International Publishing, Cham, 2016), pp. 1521–1548.

9. J. Wang, Electrochemical sensing of explosives. *Electroanalysis*. **19**, 415–423 (2007).

10. S. Singh, Sensors—An effective approach for the detection of explosives. *J. Hazard. Mater.* **144**, 15–28 (2007).

11. A. Fainberg, Explosives detection for aviation security. *Science*. **255**, 1531–1537 (1992).

12. S. Vucinic, B. Antonijevic, A. M. Tsatsakis, L. Vassilopoulou, A. O. Docea, A. E. Nosyrev, B. N. Izotov, H. Thiermann, N. Drakoulis, D. Brkic, Environmental exposure to organophosphorus nerve agents. *Environ. Toxicol. Pharmacol.* **56**, 163–171 (2017).

13. J. Bajgar, Organophosphates/nerve agent poisoning: Mechanism of action, diagnosis, prophylaxis, and treatment. *Adv. Clin. Chem.* **38**, 151–216 (2004).

14. A. Gao, R. R. Murphy, W. Chen, G. Dagnino, P. Fischer, M. G. Gutierrez, D. Kundrat, B. J. Nelson, N. Shamsudhin, H. Su, J. Xia, A. Zemmar, D. Zhang, C. Wang, G.-Z. Yang, Progress in robotics for combating infectious diseases. *Sci. Robot.* **6**, eabf1462 (2021).

15. Y. Shen, D. Guo, F. Long, L. A. Mateos, H. Ding, Z. Xiu, R. B. Hellman, A. King, S. Chen, C. Zhang, H. Tan, Robots under COVID-19 pandemic: A comprehensive survey. *IEEE Access*. **9**, 1590–1615 (2021).

16. G.-Z. Yang, B. J. Nelson, R. R. Murphy, H. Choset, H. Christensen, S. H. Collins, P. Dario, K. Goldberg, K. Ikuta, N. Jacobstein, D. Kragic, R. H. Taylor, M. McNutt, Combating COVID-19—The role of robotics in managing public health and infectious diseases. *Sci. Robot.* **5**, eabb5589 (2020).

17. T. R. Ray, J. Choi, A. J. Bandodkar, S. Krishnan, P. Gutruf, L. Tian, R. Ghaffari, J. A. Rogers, Bio-integrated wearable systems: A comprehensive review. *Chem. Rev.* **119**, 5461–5533 (2019).

18. D. H. Kim, N. Lu, R. Ma, Y. S. Kim, R. H. Kim, S. Wang, J. Wu, S. M. Won, H. Tao, A. Islam, K. J. Yu, T. I. Kim, R. Chowdhury, M. Ying, L. Xu, M. Li, H. J. Chung, H. Keum, M. McCormick, P. Liu, Y. W. Zhang, F. G. Omenetto, Y. Huang, T. Coleman, J. A. Rogers, Epidermal electronics. *Science*. **333**, 838–43 (2011).

19. W. Gao, S. Emaminejad, H. Y. Y. Nyein, S. Challa, K. Chen, A. Peck, H. M. Fahad, H. Ota, H. Shiraki, D. Kiriya, D.-H. Lien, G. A. Brooks, R. W. Davis, A. Javey, Fully integrated wearable sensor arrays for multiplexed in situ perspiration analysis. *Nature*. **529**, 509–514 (2016).

20. Y. Yang, Y. Song, X. Bo, J. Min, O. S. Pak, L. Zhu, M. Wang, J. Tu, A. Kogan, H. Zhang, T. K. Hsiai, Z. Li, W. Gao, A laser-engraved wearable sensor for sensitive detection of uric acid and tyrosine in sweat. *Nat. Biotechnol.* **38**, 217–224 (2020).

21. B. Shih, D. Shah, J. Li, T. G. Thuruthel, Y.-L. Park, F. Iida, Z. Bao, R. Kramer-Bottiglio, M. T. Tolley, Electronic skins and machine learning for intelligent soft robots. *Sci. Robot.* **5**, eaaz9239 (2020).

22. Y. Yu, J. Nassar, C. Xu, J. Min, Y. Yang, A. Dai, R. Doshi, A. Huang, Y. Song, R. Gehlhar, A. D. Ames, W. Gao, Biofuel-powered soft electronic skin with multiplexed and wireless sensing for human-machine interfaces. *Sci. Robot.* **5**, eaaz7946 (2020).

23. T. Someya, Z. Bao, G. G. Malliaras, The rise of plastic bioelectronics. *Nature*. **540**, 379–385 (2016).

24. C. Wang, X. Li, H. Hu, L. Zhang, Z. Huang, M. Lin, Z. Zhang, Z. Yin, B. Huang, H. Gong, S. Bhaskaran, Y. Gu, M. Makihata, Y. Guo, Y. Lei, Y. Chen, C. Wang, Y. Li, T. Zhang, Z. Chen, A. P. Pisano, L. Zhang, Q. Zhou, S. Xu, Monitoring of the central blood pressure waveform via a conformal ultrasonic device. *Nat. Biomed. Eng.* **2**, 687–695 (2018).

25. J. Kim, A. S. Campbell, B. E.-F. de Ávila, J. Wang, Wearable biosensors for healthcare monitoring. *Nat. Biotechnol.* **37**, 389–406 (2019).

26. S. Choi, S. I. Han, D. Jung, H. J. Hwang, C. Lim, S. Bae, O. K. Park, C. M. Tschabrunn, M. Lee, S. Y. Bae, J. W. Yu, J. H. Ryu, S.-W. Lee, K. Park, P. M. Kang, W. B. Lee, R. Nezafat, T. Hyeon, D.-H. Kim, Highly conductive, stretchable and biocompatible Ag–Au core–sheath nanowire composite for wearable and implantable bioelectronics. *Nat. Nanotech.* **13**, 1048–1056 (2018).

27. K. Sim, F. Ershad, Y. Zhang, P. Yang, H. Shim, Z. Rao, Y. Lu, A. Thukral, A. Elgalad, Y. Xi, B. Tian, D. A. Taylor, C. Yu, An epicardial bioelectronic patch made from soft rubbery materials and capable of spatiotemporal mapping of electrophysiological activity. *Nat. Electron.* **3**, 775–784 (2020).

28. A. S. Almuslem, S. F. Shaikh, M. M. Hussain, Flexible and stretchable electronics for harsh-environmental applications. *Adv. Mater. Technol.* **4**, 1900145 (2019).

29. Y.-T. Kwon, Y.-S. Kim, S. Kwon, M. Mahmood, H.-R. Lim, S.-W. Park, S.-O. Kang, J. J. Choi, R. Herbert, Y. C. Jang, Y.-H. Choa, W.-H. Yeo, All-printed nanomembrane wireless bioelectronics using a biocompatible solderable graphene for multimodal human-machine interfaces. *Nat. Commun.* **11**, 3450 (2020).

30. A. J. Bandodkar, S. P. Lee, I. Huang, W. Li, S. Wang, C.-J. Su, W. J. Jeang, T. Hang, S. Mehta, N. Nyberg, P. Gutruf, J. Choi, J. Koo, J. T. Reeder, R. Tseng, R. Ghaffari, J. A. Rogers, Sweat-activated biocompatible batteries for epidermal electronic and microfluidic systems. *Nat. Electron.* **3**, 554–562 (2020).

31. Z. Zhou, K. Chen, X. Li, S. Zhang, Y. Wu, Y. Zhou, K. Meng, C. Sun, Q. He, W. Fan, E. Fan, Z. Lin, X. Tan, W. Deng, J. Yang, J. Chen, Sign-to-speech translation using machine-learning-assisted stretchable sensor arrays. *Nat. Electron.* **3**, 571–578 (2020).

32. E. Cesewski, B. N. Johnson, Electrochemical biosensors for pathogen detection. *Biosens. Bioelectron.* **159**, 112214 (2020).

33. M. Amit, R. K. Mishra, Q. Hoang, A. M. Galan, J. Wang, T. N. Ng, Point-of-use robotic sensors for simultaneous pressure detection and chemical analysis. *Mater. Horiz.* **6**, 604–611 (2019).

34. A. Kaliyaraj Selva Kumar, Y. Zhang, D. Li, R. G. Compton, A mini-review: How reliable is the drop casting technique? *Electrochem. Commun.* **121**, 106867 (2020).

35. A. Moin, A. Zhou, A. Rahimi, A. Menon, S. Benatti, G. Alexandrov, S. Tamakloe, J. Ting, N. Yamamoto, Y. Khan, F. Burghardt, L. Benini, A. C. Arias, J. M. Rabaey, A wearable biosensing system with in-sensor adaptive machine learning for hand gesture recognition. *Nat. Electron.* **4**, 54–63 (2021).

36. S. Guo, D. Wen, Y. Zhai, S. Dong, E. Wang, Platinum nanoparticle ensemble-on-graphene hybrid nanosheet: one-pot, rapid synthesis, and used as new electrode material for electrochemical sensing. *ACS Nano* **4**, 3959–3968 (2010).

37. D. Troya, Reaction mechanism of nerve-agent decomposition with Zr-based metal organic frameworks. *J. Phys. Chem. C*. **120**, 29312–29323 (2016).

38. M. C. de Koning, M. van Grol, T. Breijaert, Degradation of paraoxon and the chemical warfare agents VX, tabun, and soman by the metal–organic frameworks UiO-66-NH_2, MOF-808, NU-1000, and PCN-777. *Inorg. Chem.* **56**, 11804–11809 (2017).

39. J. Wang, Carbon-nanotube based electrochemical biosensors: A review. *Electroanalysis*. **17**, 7–14 (2005).

40. V. Schroeder, S. Savagatrup, M. He, S. Lin, T. M. Swager, Carbon nanotube chemical sensors. *Chem. Rev.* **119**, 599–663 (2019).

41. R. M. Torrente-Rodríguez, H. Lukas, J. Tu, J. Min, Y. Yang, C. Xu, H. B. Rossiter, W. Gao, SARS-CoV-2 RapidPlex: A graphene-based multiplexed telemedicine platform for rapid and low-cost COVID-19 diagnosis and monitoring. *Matter*. **3**, 1981–1998 (2020).

42. S. M. Lundberg, S.-I. Lee, A unified approach to interpreting model predictions. *Advances in neural information processing systems* **2017**, 4765–4774 (2017).

43. B. Hudgins, P. Parker, R. N. Scott, A new strategy for multifunction myoelectric control. *IEEE Trans. Biomed. Eng.* **40**, 82–94 (1993).

44. R. A. Russell, D. Thiel, R. Deveza, A. Mackay-Sim, in *IEEE Int. Conf. Robot. Autom.* (IEEE, Nagoya, Japan, 1995), vol. 1, pp. 556–561.

45. X. Liu, D. Gong, A comparative study of A-star algorithms for search and rescue in perfect maze. *International Conference on Electric Information and Control Engineering* **2011**, 24–27 (2011).

46. W. S. Hummers, R. E. Offeman, Preparation of graphitic oxide. *J. Am. Chem. Soc.* **80**, 1339–1339 (1958).

47. J. G. Yoon, J. Yoon, J. Y. Song, S.-Y. Yoon, C. S. Lim, H. Seong, J. Y. Noh, H. J. Cheong, W. J. Kim, Clinical significance of a high SARS-CoV-2 viral load in the saliva. *J. Korean Med. Sci.* **35**, e195 (2020).

A p p e n d i x A

SUPPLEMENTARY INFORMATION FOR CHAPTER 2

Materials from this chapter appear in "Yu, Y.; Li, J.; Solomon, S.; Min, J.; Tu, J.; Guo, W.; Xu, C.; Song, Y.; Gao, W. All-printed soft human-machine interface for robotic physiochemical sensing. *Science Robotics* **7** eabn0495(2022). https://doi.org/10.1126/scirobotics.abn0495"

Diffusion dynamics of dry-phase analyte through the hydrogel

The simulation of the mass transport process for the dry-phase analyte through the hydrogel to the sensor's surface was conducted using finite element analysis (FEA) on the commercial software COMSOL Multiphysics. Tetrahedral elements with refined meshes allowed modeling of the source's diffusion in 3D space with testified accuracy. The fluid flow is described by the Navier-Stoke equation for incompressible flow

$$\rho\left(\frac{\partial v}{\partial t} + (v \cdot \nabla)v\right) = -\nabla p + \mu\nabla^2 v$$

$$\nabla \cdot v = 0$$

And the convection diffusion is described by

$$\frac{\partial c}{\partial t} + v \cdot \nabla c = D\nabla^2 C$$

Where ρ, v, p and μ denote liquid density, flow velocity, pressure and viscosity respectively, whereas C and D denote the concentration and the diffusion coefficient. The diffusion coefficient of paraoxon, TNT, proton, sarin, and nitrogen mustard are 4.7×10^{-6} cm^2 s^{-1}, 6.7×10^{-6} cm^2 s^{-1}, 9.3×10^{-5} cm^2 s^{-1}, 8.6×10^{-6} cm^2 s^{-1} and 8.2×10^{-6} cm^2 s^{-1} respectively.

The source diffusion in the water tank was modeled using a chemical droplet hitting the water with an initial speed of 0.5 m s^{-1} perpendicular to the surface (with height of 0). A no-slip boundary condition was applied on all tank walls including the barriers.

For the dry phase detection simulation, hydrogels are modeled as liquids with no internal fluid flow. It is assumed that the target species (1 mM) completely dissolved into the hydrogels from the bottom and form a 20 μM concentrated solution layer at $t = 0$. The solute concentration detected by the electrode is tracked by computing the average concentration at the hydrogel's top surface (hydrogel-electrode interface). The simulated diffusion process is shown in **Fig. A-4**. The time request for complete diffusion will increase dramatically as the

hydrogel's thickness increases. Thus, a thinner hydrogel layer will be appreciated for rapid dry phase detection. Moreover, among all simulated chemical species, protons diffuse much faster than all other species. It takes less than 30 s for protons to completely diffuse through the 0.5 mm hydrogel layer, which suggest the possibility of dry-phase pH monitoring.

Feature engineering and channel selection

The following five features were extracted from each peak (serialized gesture) found in the root mean squared (RMS) filtered EMG data: height, average area, standard deviation, average energy, and maximum slope. During feature extraction, each peak was referenced against its baseline, which was determined via a binary search of the previous data in 50 ms intervals. By skipping points, the algorithm ignored minor fluctuations in the peak's rise to find the local minimum (baseline of the peak). To decrease the delay time in gesture recognition, only points between the baseline and the top of the peak were analyzed. The five features extracted are defined as follows:

$$Peak\ Height: RMS[peakIndex] - RMS[leftBaselineIndex]$$

$$Peak\ Average: \frac{\sum_{i=leftBaselineIndex}^{i=peakIndex}[RMS_i]}{N}$$

$$Peak\ Standard\ Deviation: \frac{\sqrt{\sum_{i=leftBaselineIndex}^{i=peakIndex}[RMS_i - \mu_{RMS}]^2}}{N-1}$$

$$Average\ Peak\ Energy: \frac{\sum_{i=leftBaselineIndex}^{i=peakIndex}[RMS_i]^2}{N}$$

$$Maximum\ Peak\ Slope: \max(gradient(RMS[peakIndex: leftBaselineIndex + 1]))$$

Where peakIndex and leftBaselineIndex represent the indices of the peak's maximum and left baseline in the RMS data respectively; μ_{RMS} is the peak average; and N is the number of RMS points between the peak and its baseline.

After data collection and feature extraction, the performance enhancement of each feature and channel for accurate gesture classification was evaluated using Shapley additive explanation (SHAP) values, which utilizes a game theory approach to explain a feature's individual and overall contribution to the final prediction. Effectively, the SHAP value of a feature represents the average marginal contribution of the feature across the entire dataset (all prediction instances). In addition to SHAP values, the average testing accuracy across 5000 trials was taken for each permutation of features and channels, which supplemented the SHAP values in providing further insight into which channels and features contained non-overlapping beneficial information for gesture determination. For each of the 5000 runs, the testing points represented 33% of the dataset, with each gesture in the test set being proportionally represented in the full dataset.

Notable feature permutations, with and without 1 channel removed, from the arm EMG dataset is displayed in **Table A-2.** As shown in the table, out of each feature, peak height and standard deviation classified the 6 gestures the best with the highest mean accuracy and lowest standard deviation (when evaluated by themselves). On the contrary, peak energy, which holds a good amount of gesture information with an 88.71% classification accuracy, is the least import feature, with the lowest mean accuracy and greatest standard deviation. The relatively high accuracy for each feature substantiates the assumption that each peak property contains useful information about motor intention, validating their use in the KNN model. Based solely on the table values, however, there appears to be no statistically significant feature pairing that improves the classification accuracy above using peak height or standard deviation alone. The table additionally shows that channel 1 appears to be the least important channel, while channels 2 and 3 seems to be the most important channels for accurate motor classification.

This information is expanded upon when looking at the SHAP analysis. Despite no statistically significant accuracy change in **Table A-2**, using both STD and PH together can alleviate the model's reliance on only one parameter. When only considering PH in **Fig. A-31A**, each channel's feature can drastically alter the final gesture prediction. Such volatility

can be contrasted when the STD feature is added in **Fig. A-31D**. With PH and STD, the decision tree spreads out more at the base, reducing the model's reliance on any one feature. The perceived advantage of adding another feature is further exemplified when analyzing each feature pairing with PH (**Fig. A-31B–E**). When pairing PE or MS with PH, the model does not effectively utilize the added feature (negligible SHAP values). However, STD and PA are both relevant even when paired with PH, as seen by the tree spreading early. Even though the final classification remains the same, when pairing PH with STD or PH with PA, the model is more certain on the endpoint with each step and thus reduces the effect of a bad feature. For this reason, we recommend using PH, STD, and PA together (**Fig. A-31F**), to add as much novel information to the model while reducing the reliance on any one parameter.

In addition to proper feature extraction, another component to consider in gesture classification is the number of channels collecting data. While one can obtain a higher accuracy from using more data channels, it is advantageous to reduce the amount of hardware present on the patient's body for comfort and affordability. The number of channels needed to maintain a high classification accuracy was evaluated in **Table A-3**. As shown in the table, with the highest classification accuracy of 87.37%, there is a 10% accuracy decrease when only 2 channels are considered. For two channels, the most important combinations are channels 3 and 4, 2 and 4, as well as 2 and 3. Channel 1 is the least significant channel (as previously seen in **Table A-2**). The reason that channel 1 may not hold much information is because it is activated in almost every gesture. Because of this, it provides the most overlapping points across all the hand movements (the hardest to segment into classification groups). Meanwhile channels 3 and 4 (which represent the highest mean and lowest standard deviation), contains the least amount of activation for any gesture. Therefore, these channels carry a lot of weight when activated.

Combining the analysis from **tables A2 and A3**, the optimal number of channels to use is three channels, with two channels reducing the accuracy by at least 10%. For the highest accuracy, adding a fourth channel does have a marginal benefit to the mean (though not

statistically significant). The authors decided to use four channels as the purpose of the experiment was to maximize the accuracy for remote robotic control. However, it can be appreciated that the same experiment could have been performed on 3 channels.

M-Boat searching algorithms

In choosing an efficient and intelligent search algorithm, 6 different algorithms were developed and compared against each other. The simplest model between them is the random direction (RD) algorithm, which acts as a baseline for searching the space with no intelligence. In this algorithm, the M-Boat chooses an arbitrary direction to move in at each point. If the potential movement would cause the M-Boat to go outside the tank, the angle is ignored, and another direction is randomly chosen. The algorithm with the next level of intelligence is the maximum direction (MD) model. At each step in this algorithm, the MD boat turns towards the sensor with the maximum recorded value. The M-Boat will therefore only move in three distinct directions, representing the three sensor angles on the M-Boat, as shown in **Fig. A-42.** Each direction is calculated from the center of the boat to the edge of the highest-value sensor. However, if all the sensors record the same value, the algorithm will want to stay in its current location. For this edge case, the algorithm will inform the M-Boat to continue moving in its current direction (go straight). This model is very similar to the next method – the weighted maximum direction (WMD) algorithm. However, instead of using the maximum sensor's direction, each direction is weighted based on the sensor's value. To understand the mathematical discrepancies, the formulas for the maximum direction and weighted maximum direction algorithms is provided below:

$$\mathrm{MD} = \max(\mathrm{S}_1, \mathrm{S}_2, \mathrm{S}_3)\,[0{:}\,2]$$

$$\mathrm{WMD} = \sum_{i=1}^{3} S_i[0{:}\,2] * S_i[2]$$

Where S_i is the i^{th} sensor on the M-Boat, which is represented as a tuple of coordinates. The first two indices in the tuple are the X and Y locations of the M-Boat in the tank respectively and the last index is the sensor's reading ($S = \langle X_{Loc}, Y_{Loc}, Sensor\ Value \rangle$).

Instead of relying solely on the three chemical sensors to make a movement decision, the final three models use more intelligent algorithms that attempt to reconstruct part of the concentration profile in the tank. The interpolated map (IM) algorithm achieves this by using the last three readings to estimate the immediate concentration gradient around the M-Boat. The decision to only use three previous results instead of every recording stems from factors altering the concentration profile such as natural diffusion and induced diffusion as the M-Boat propels itself forwards. In the model, the space is mapped using linear interpolation with the griddata function from SciPy (version 1.4.1). After estimating the concentration profile, the M-Boat will move to the direction with the highest interpolated concentration. If all the values are the same, then the M-Boat will continue moving straight.

The gradient descent method similarly tries to reconstruct the concentration curve but achieves this through calculating the gradient at the current boat's position. In calculus, the gradient is defined as the direction of maximum increase in the 2D contour plane. On a 3D curve, where the XY plane represents the water's surface and the Z-direction represents the chemical's concentration, the direction of maximum increase would be the direction the M-Boat should travel to find the chemical's source. We will define the concentration at any given XY location as C(x,y) and the M-Boat's current location as x_0, y_0. With this information, the 2D gradient in the contour plane can be defined as follows:

$$Gradient = \overrightarrow{\nabla C}(x_0, y_0) = \left[\frac{dC(x, y_0)}{dx}\Big|_{x=x_0}, \frac{dC(x_0, y)}{dy}\Big|_{y=y_0} \right]$$

While the full concentration curve, C(x,y), is not known during the search, at each step, the sensor will record three points in C(x,y) around x_0, y_0 (the M-Boat's current location). One can therefore still extrapolate key information about the concentration curve at the M-Boat's location using these points.

With the sensor values, one can calculate the tangent plane at $C(x_0, y_0)$. To evaluate the concentration around the M-Boat, we first create a 3D function to calculate the gradient: F(x,y,z) = C(x,y) – z. With this new form, the general equation of the tangent plane can be defined as follows:

$$\left.\frac{dF(x, y_0, z_0)}{dx}\right|_{x=x_0}(x - x_0) + \left.\frac{dF(x_0, y, z_0)}{dy}\right|_{y=y_0}(y - y_0) + \left.\frac{dF(x_0, y_0, z)}{dz}\right|_{z=z_0}(z - z_0) = 0$$

Rearranging the equation above, we get:

$$\left\langle \left.\frac{dF(x, y_0, z_0)}{dx}\right|_{x=x_0}, \left.\frac{dF(x_0, y, z_0)}{dy}\right|_{y=y_0}, \left.\frac{dF(x_0, y_0, z)}{dz}\right|_{z=z_0} \right\rangle \cdot \langle x - x_0, y - y_0, z - z_0 \rangle = 0$$

As X,Y,Z and x_0, y_0, z_0 are both in the plane, the second term defines any arbitrary vector that is confined to the plane. Therefore, the first term $\langle \left.\frac{dF(x,y_0,z_0)}{dx}\right|_{x=x_0}, \left.\frac{dF(x_0,y,z_0)}{dy}\right|_{y=y_0}, \left.\frac{dF(x_0,y_0,z)}{dz}\right|_{z=z_0} \rangle$ represents the set of all vectors that are perpendicular to the plane, commonly referred to as the normal direction of the plane. This perpendicular direction can be calculated through the cross product of any two coplanar vectors. By defining the location of one sensor as $\langle S_{1x}, S_{1y}, S_{1z} \rangle$, two coplanar vectors in the tangent plane can be calculated as follows:

$$\vec{A} = \langle \mathrm{S_{1x}} - S_{2x}, S_{1y} - S_{2y}, S_{1z} - S_{2z} \rangle \; and \; \vec{\mathrm{B}} = \langle \mathrm{S_{1x}} - S_{3x}, S_{1y} - S_{3y}, S_{1z} - S_{3z} \rangle$$

Where the cross product (the normal vector) is calculated as:

$$\vec{A} \; x \; \vec{\mathrm{B}} = \begin{vmatrix} \hat{\imath} & \hat{\jmath} & \hat{k} \\ \mathrm{S_{1x}} - S_{2x} & S_{1y} - S_{2y} & S_{1z} - S_{2z} \\ \mathrm{S_{1x}} - S_{3x} & S_{1y} - S_{3y} & S_{1z} - S_{3z} \end{vmatrix} = Normal\ Vector$$

Substituting F(x,y,z) = C(x,y) – z back, one gets:

$$Normal\ Vector = \langle \frac{dF(x, y_0, z_0)}{dx}\Big|_{x=x_0}, \frac{dF(x_0, y, z_0)}{dy}\Big|_{y=y_0}, \frac{dF(x_0, y_0, z)}{dz}\Big|_{z=z_0} \rangle$$

$$= \langle \frac{dC(x, y_0)}{dx}\Big|_{x=x_0}, \frac{dC(x_0, y)}{dy}\Big|_{y=y_0}, -1 \rangle$$

The projection of the normal vector onto the X-Y plane is shown to be the gradient, representing the direction with the highest local concentration. For the gradient descent method, the above algorithm is performed at every decision point. If the gradient is too small to consider, the M-Boat does not change directions (it moves straight).

While the gradient descent method approximates the direction of maximum increase, this algorithm does not take advantage of past information. Meanwhile, the IM algorithm utilizes past information to interpolate what to do in the future. The A* approach utilized both algorithms together with equal weight to make a well-informed decision on where the M-Boat should move next using past and present information.

These various source-locating algorithms were simulated on the M-Boat to find the location of any chemical spill optimally and reliably. The M-Boat was further evaluated in the case of multiple leaks. As shown in **Fig. A-41D** and **E**, for two leakage sources, the maximum direction and gradient descent algorithms will preferentially find the closest source to its current location. This is because these algorithms only rely on data calculated from its current position, moving in the direction of maximum increase (which is biased by the closest chemical spill). In contrast, the interpolated map, which is used as a heuristic in the A* algorithm, takes advantage of previous points to map the space around the boat. Hence, after multiple steps, the algorithm realizes (interpolates) that there are two sources ahead. Through the interpolation, the algorithm can further differentiate which one is larger. As shown in **Fig. A-41D**, initially, the four algorithms follow the same path. However, after a few steps, the interpolated map and A* algorithms diverge towards the maximum source. For each algorithm, the path to the source is not direct as the data at any location is a superposition of both sources, which causes a distortion in the map where the sources overlap (seen as the

saddle point). The degree to which the A* algorithm will diverge to either source was further evaluated in **Fig. A-41E**, where various start points were selected.

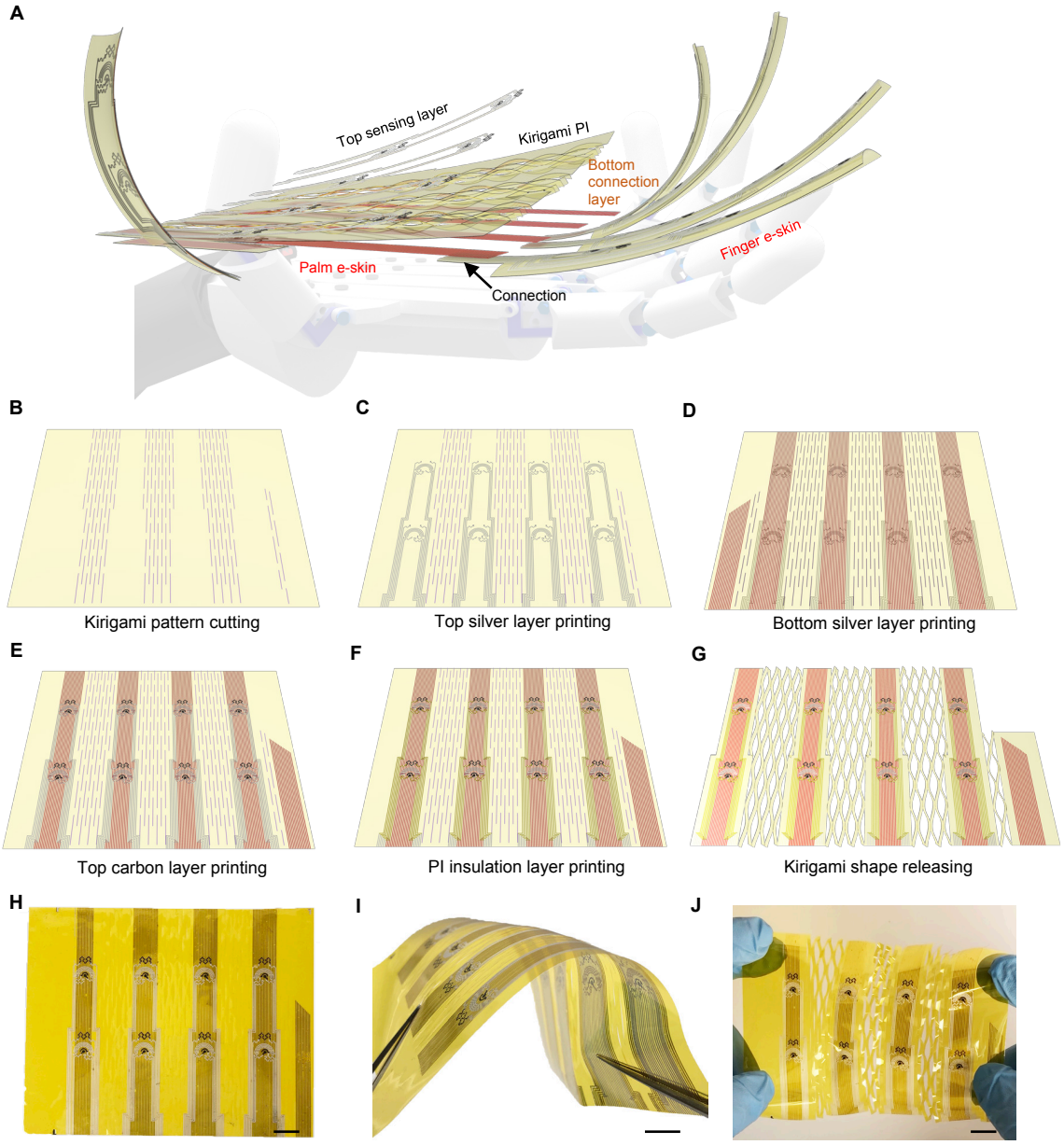

Fig. A-1. Schematic and fabrication procedure of e-skin-R. (**A**) Schematic of a robotic hand-interfaced soft kirigami e-skin-R patch. (**B–G**), Fabrication process of the soft e-skin with automatic kirigami cutting and inkjet printing. (**H–J**) Photographs of an e-skin-R under flat (**H**), bended (**I**), and stretched (**J**) conditions. Scale bars, 1 cm.

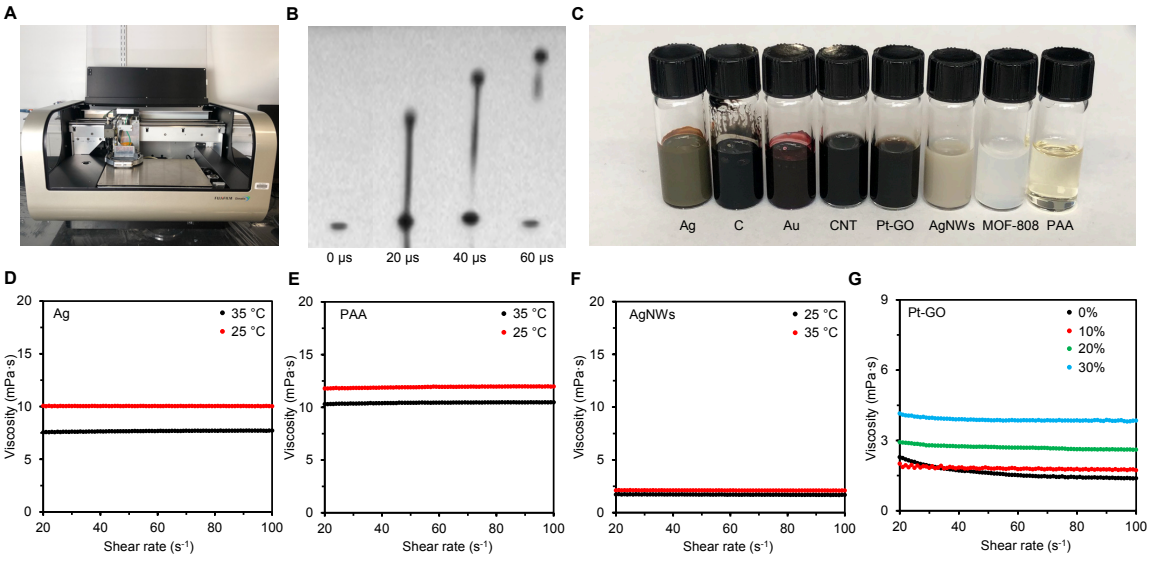

Fig. A-2. Characterization of drop-on-demand inkjet printing with custom-designed inks. (**A**) Photograph of the inkjet printer (Dimatix Materials Printer DMP-2850). (**B**) Time lapse images of a 10-pl ink droplet ejected from the printer head. Ink, PAA. (**C**) Photograph of the nanoengineered inks used to prepare the M-Bot. (**D–F**) The viscosities of Ag (**D**), PAA (**E**), and AgNWs (**F**) inks under 25 °C and 35 °C. (**G**) The viscosities of Pt-GO inks with propylene glycol ranging from 0% to 30% (v:v).

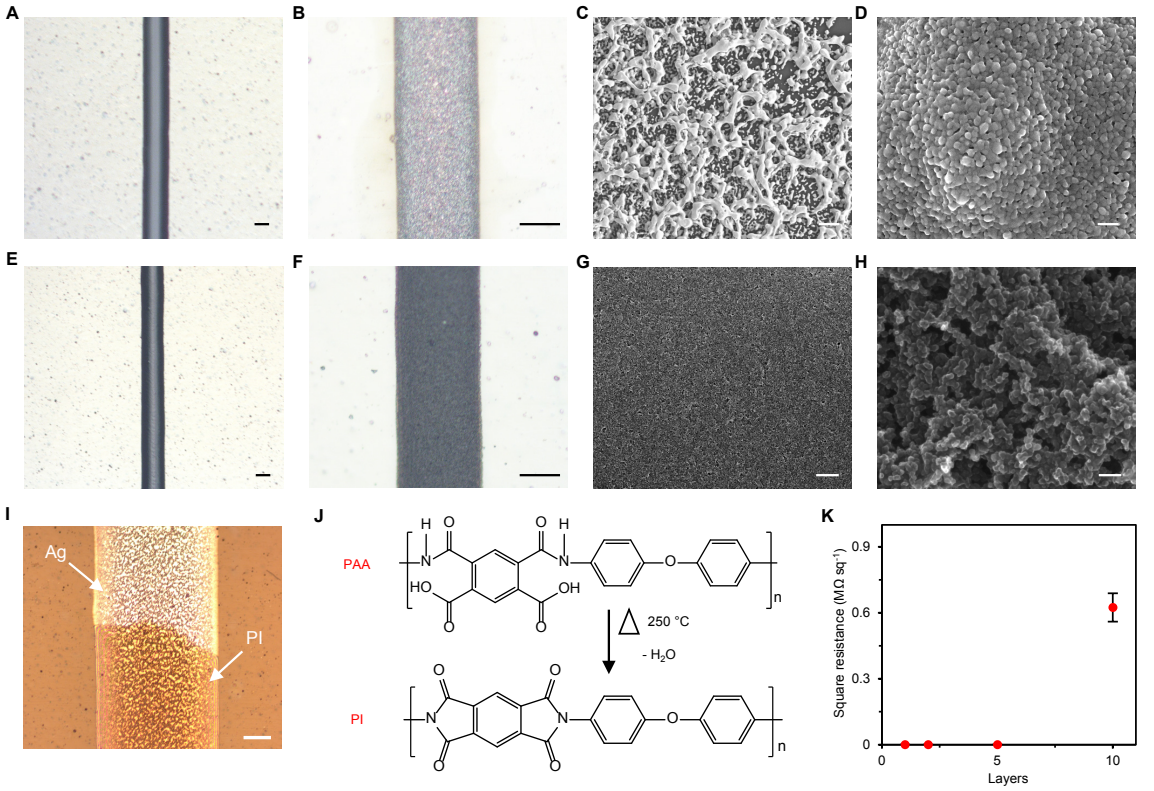

Fig. A-3. Characterizations of inkjet-printed nanostructured patterns for M-Bot. (A and B) Microscopic images of a printed silver interconnect before (**A**) and after (**B**) annealing. Scale bars, 10 µm. (**C** and **D**) SEM images of a printed silver interconnect after annealing. Scale bars, 10 µm and 100 nm, respectively. (**E** and **F**) Microscopic images of a printed carbon pattern before (**E**) and after (**F**) annealing. Scale bars, 10 µm. (**G** and **H**) SEM images of a printed carbon pattern after annealing. Scale bars, 5 µm and 100 nm, respectively. (**I**) Microscopic image of a partially PI insulated silver interconnect after annealing. Scale bar, 40 µm. (**J**) Thermal transformation of PAA ink to PI insulation layer during thermal annealing. (**K**) Square resistance of the PI insulation films printed with different layers. Error bars represent the s.d. from 3 measurements.

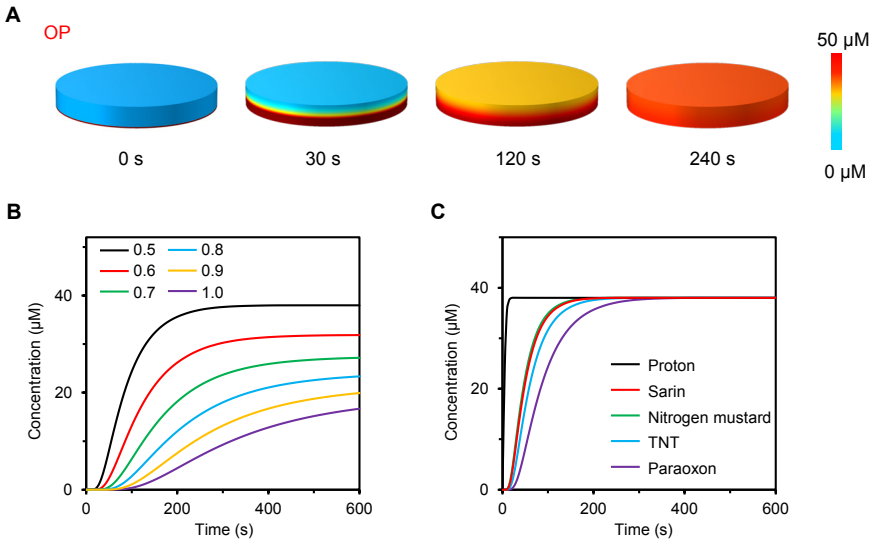

Fig. A-4. Simulation of the hydrogel-based solid-phase hazard analyte sampling and sensing. (**A**) Simulated diffusion dynamics of a hazard chemical (OP) though a 0.5-mm thick hydrogel. (**B**) Simulated time-dependent of OP concentrations at the electrode's surface coated with hydrogels of various thickness (0.5–1 mm). (**C** and **D**) Simulated time-dependent levels of hazard chemicals (proton, sarin, nitrogen mustard, TNT, paraoxon) at the sensor's surface coated with a 0.5-mm thick hydrogel.

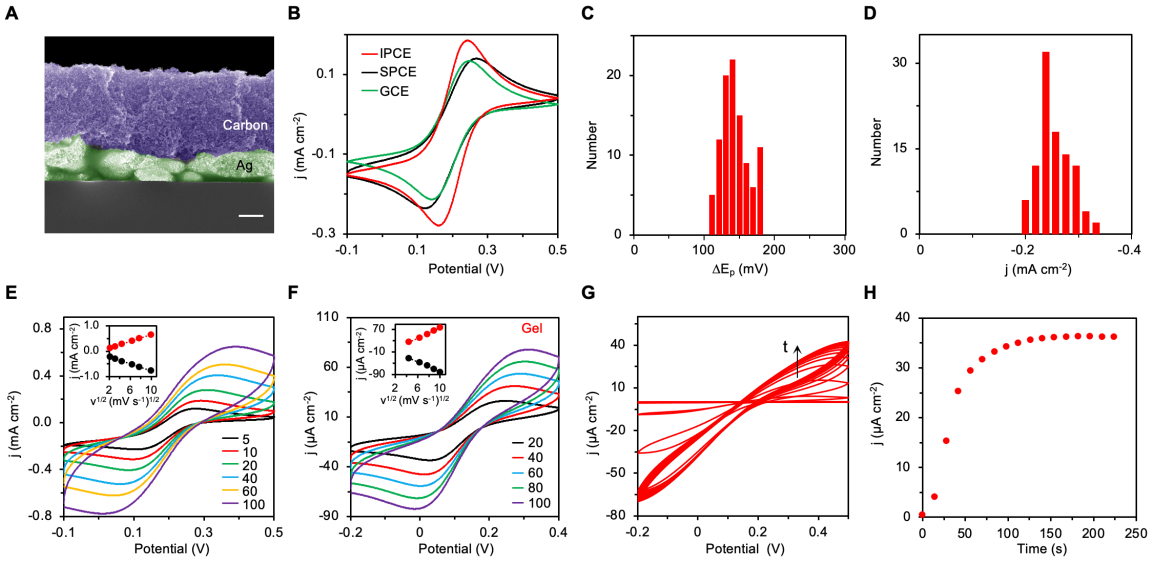

Fig. A-5. Characterizations of the IPCEs. (**A**) Cross-sectional scanning electron microscopy (SEM) image of an IPCE. Scale bar, 1 μm. (**B**) CVs of an IPCE, a screen print carbon electrode (SPCE), and a glassy carbon electrode (GCE) in 5 mM $K_3Fe(CN)_6$. Scan rate, 5 mV s^{-1}. (**C** and **D**) Distributions of redox peak potential differences (ΔE_p) (**C**) and reduction peak current densities (j) (**D**) in the cyclic voltammograms (CVs) of 100 IPCEs in 5 mM $K_3Fe(CN)_6$. Scan rates, 5 mV s^{-1}. (**E** and **F**) CVs of an IPCE in 5 mM $K_3Fe(CN)_6$ (**E**) and an IPCE coated with a hydrogel containing 2 mM $K_3Fe(CN)_6$ (**F**) under different scan rates. Insets, the corresponding current peak densities plotted against the square root of the scan rates ($v^{1/2}$). Scan rates, 5–100 mV s^{-1}. (**G** and **H**) The CVs (**G**) and the time-dependent oxidation peak current densities (**H**) obtained after adding 8 μg $K_3Fe(CN)_6$ onto a hydrogel-loaded IPCE (final equilibrium concentration is ~2 mM). Scan rates, 100 mV s^{-1}.

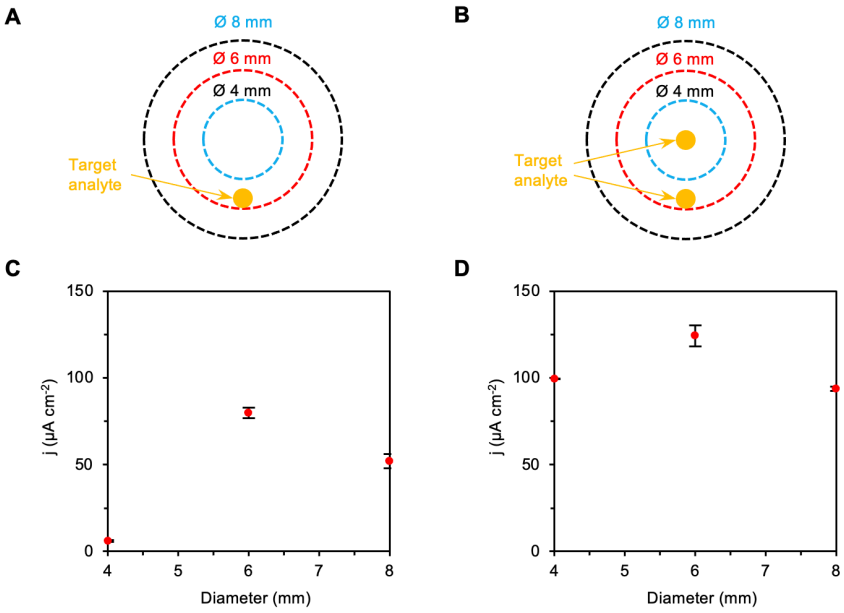

Fig. A-6. **Evaluation of the M-Bot chemical sensing using hydrogels with enlarged size.** (**A–D**) Illustrations of dry-phase target analyte detection using hydrogels with different sizes (**A** and **B**) and the corresponding current responses of the IPCEs (**C** and **D**). j, oxidation peak current density of the CVs of the IPCEs (scan rate, 50 mV s^{-1}). Dry-phase $K_3Fe(CN)_6$ (8 μg) was used as the target analyte. Error bars represent the s.d. from 3 sensors.

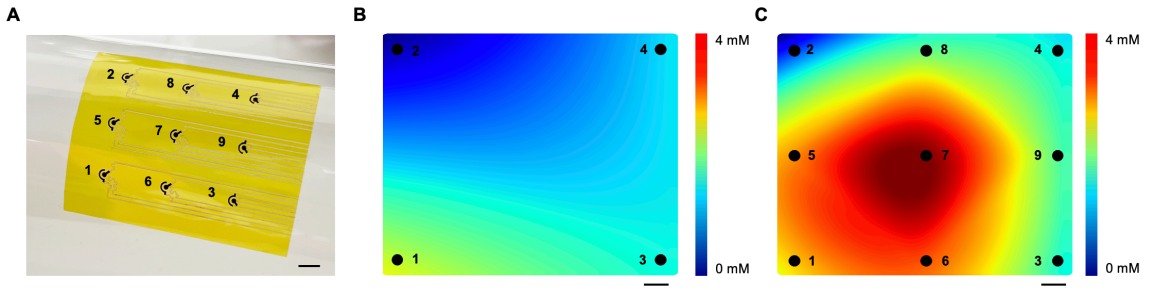

Fig. A-7. **Evaluation of the M-Bot chemical sensing with increased sensor density.** (**A**) Photograph of an IPCE sensor array with 9 chemical sensors. Scale bar, 5 mm. (**B** and **C**) The color mappings of target distributions generated by 4 sensors (**B**) and 9 sensors (**C**). Scale bars, 2 mm. The target analyte – $K_3Fe(CN)_6$ – was spray-coated around the center of the detection area.

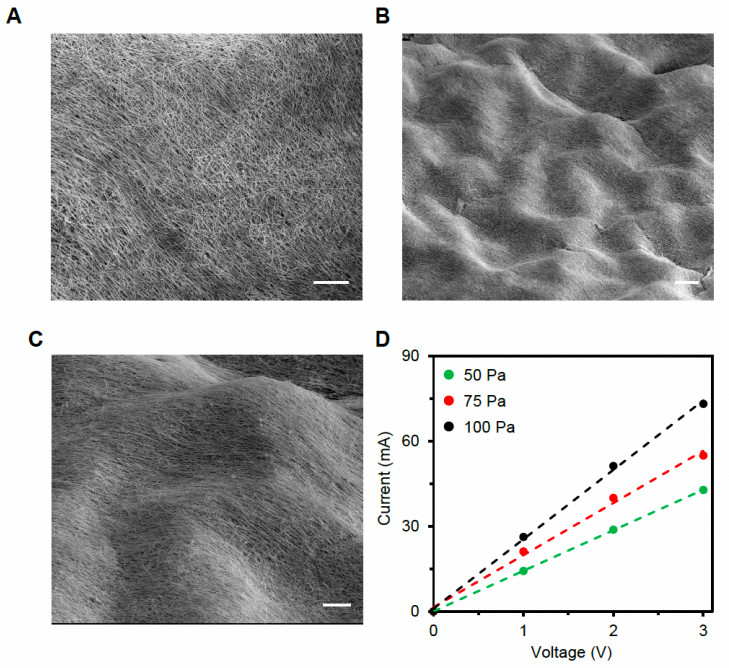

Fig. A-8. Characterization of the printed AgNWs/N-PDMS tactile sensors. (**A–C**) SEM images of inkjet-printed AgNWs on a nanotextured PDMS substrate. Images were taken with a substrate angle of 52°. Scale bars, 10, 20, and 10 μm, respectively. (**D**) Current response of a tactile sensor under varied pressure and voltage loads.

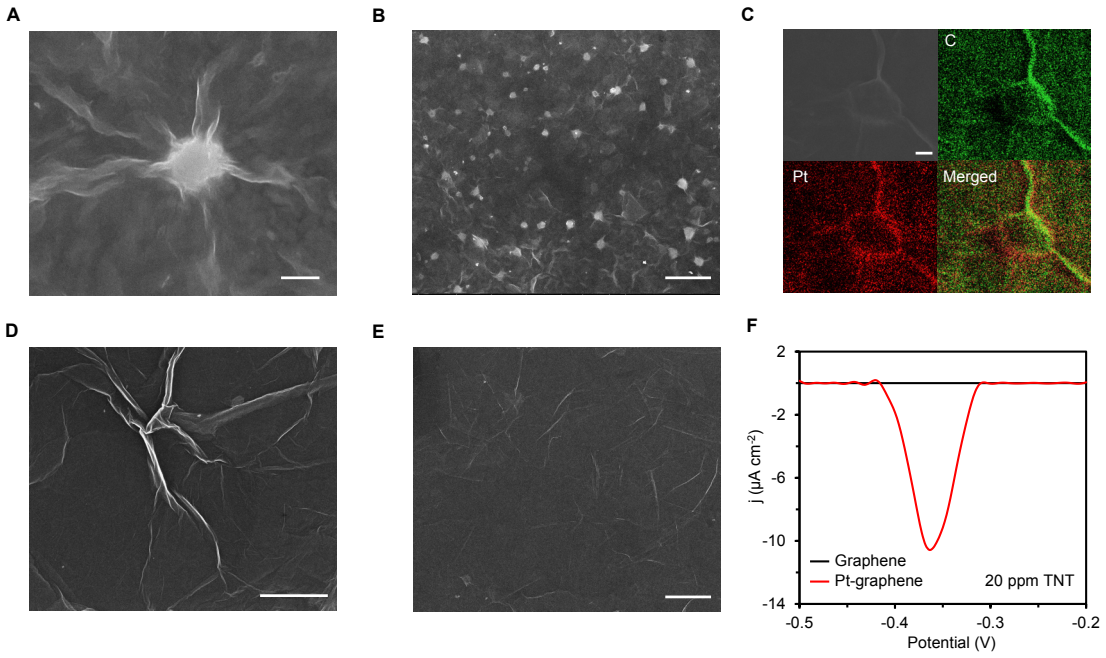

Fig. A-9. Characterization of printed Pt-graphene electrodes. (**A** and **B**) SEM images of an inkjet-printed Pt-graphene electrode. Scale bars, 1 and 5 μm, respectively. (**C**) Energy dispersive X-Ray analysis (EDX) of a printed Pt-graphene electrode. Scale bar, 1 μm. (**D** and **E**) SEM images of inkjet-printed graphene electrode. Scale bars, 1 and 3 μm, respectively. (**F**) nDPVs of a printed Pt-graphene electrode and a graphene electrode in 20 ppm TNT.

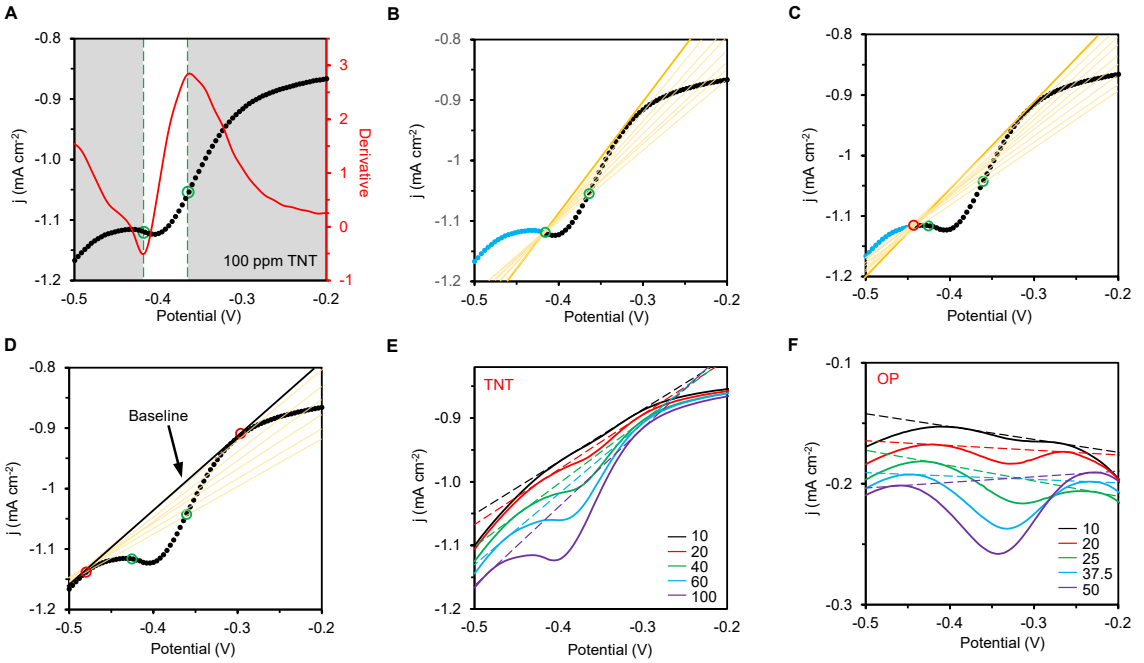

Fig. A-10. The algorithm used for automatic baseline correction of the DPV voltammograms. (**A**) DPV voltammograms of TNT detection (black) and its corresponding first derivative (red). The DPV curve can be divided into three segments by the inflection points (green), where the DPV peak will fall into the middle-highlighted region. (**B**) Beginning with the left inflection point, multiple lines (yellow) were extended to points in the right region through linear fitting to find the tangent line to the curve on the right hand side. The data points to the left (blue) were above all lines defined in this case. (**C**) Using the tangent point, and repeating the steps described in part **B**, the red point next to the left inflection point was chosen as the new center point. The procedure in part b was repeated with this new center point. If there exist data points that are above all lines defined in this case, the next point will be chosen as the center point and the same procedure will be applied again. (**D**) Eventually, one line above all data points (defined by the two data points shown in red) will be found, and this line will be taken as the baseline (thick black line) to the DPV curve. (**E**) DPV voltammograms of TNT detection and their baselines defined by this algorithm. (**F**) DPV voltammograms of OP detection and their baselines defined by this algorithm.

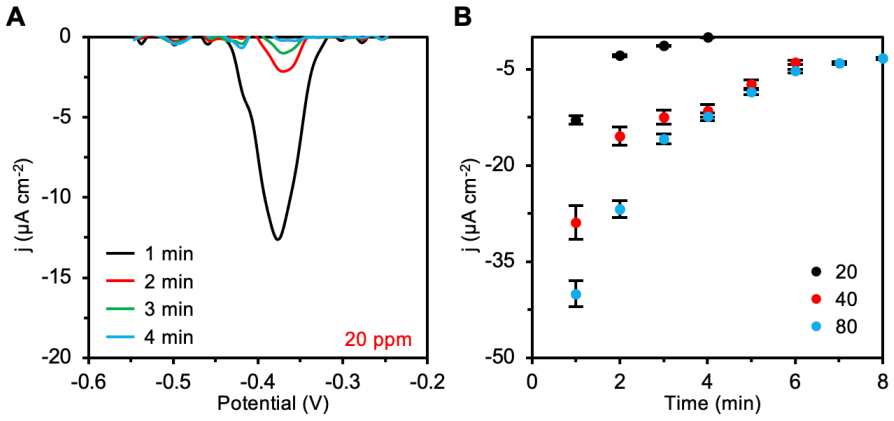

Fig. A-11. In situ regeneration of the hydrogel-loaded Pt-graphene TNT sensors. (**A**) nDPV voltammograms of the regeneration process for a Pt-graphene sensor coated with a hydrogel containing 20 ppm TNT. (**B**) Peak current densities of the nDPV voltammograms of the regeneration process for Pt-graphene sensors coated with hydrogels containing 20, 40, and 80 ppm TNT. Error bars represent the s.d. from 3 sensors.

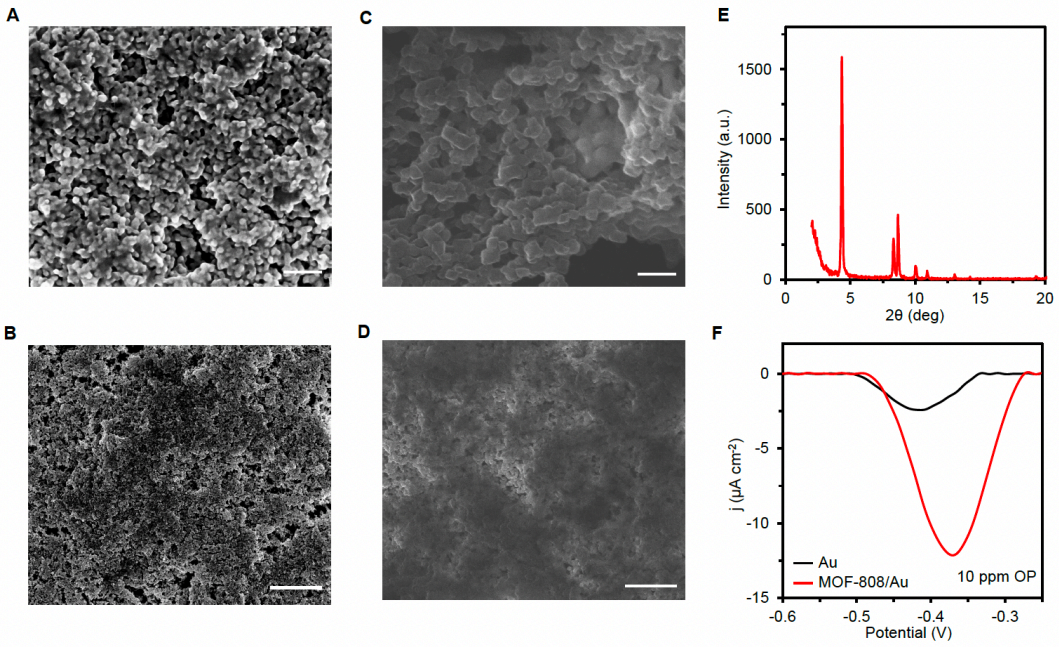

Fig. A-12. Characterization of the printed MOF-808/Au electrodes. (**A** and **B**) SEM image of inkjet-printed Au nanoparticles. Scale bars, 200 nm, and 2 μm. (**C** and **D**) SEM image of inkjet-printed MOF-808/Au. Scale bars, 100 nm, and 500 nm. (**E**) XRD curve of MOF-808. (**F**) DPV voltammograms of printed MOF-808-Au and Au electrodes in 10 ppm OP.

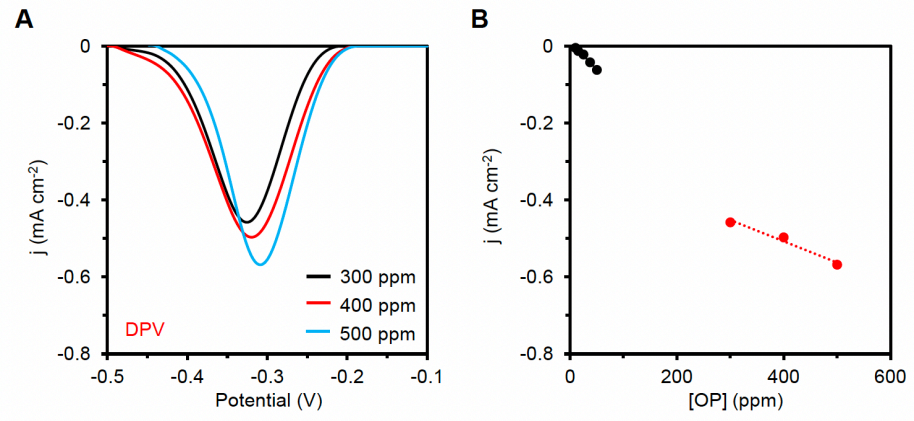

Fig. A-13. **Evaluation of the MOF-808/Au electrode for high-concentration OP analysis.** (**A** and **B**) nDPV voltammograms of a MOF-808/Au OP sensor in the presence of high-concentration OP (300–500 ppm) (**A**) and the corresponding calibration curve (**B**).

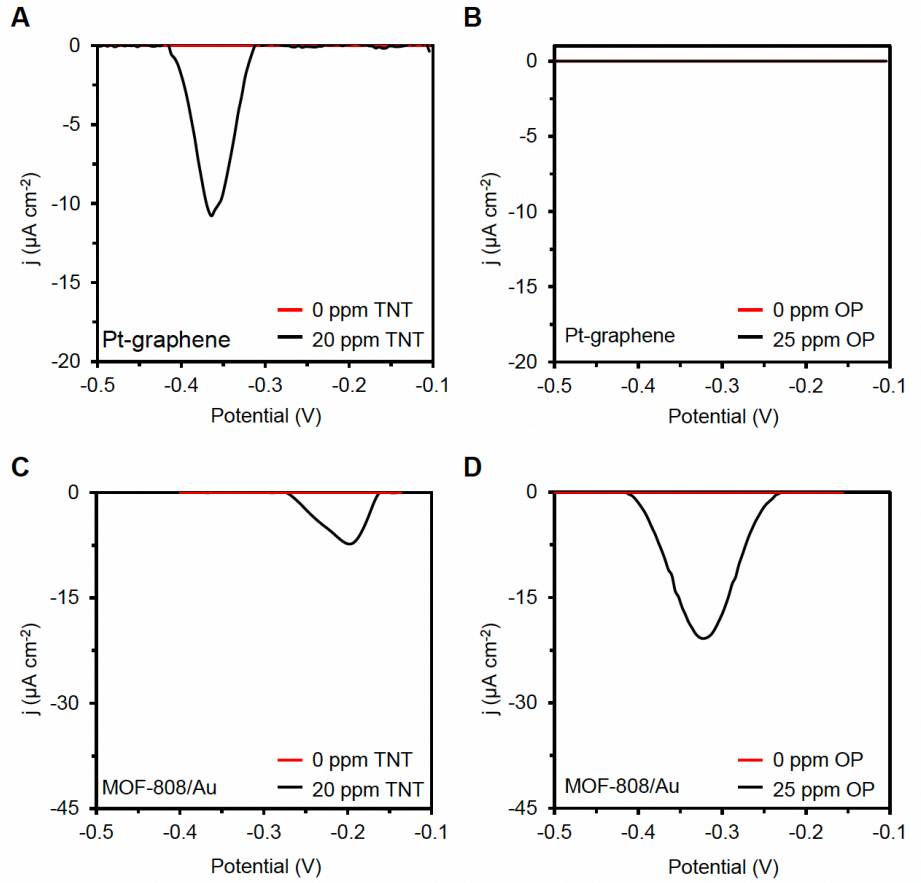

Fig. A-14. **The selectivity of Pt-graphene and MOF-808/Au electrodes over OP and TNT. (A–D)** nDPV voltammograms of a Pt-graphene sensor (**A** and **B**) and a MOF-808/Au sensor (**C** and **D**) in 20 ppm TNT and 25 ppm OP.

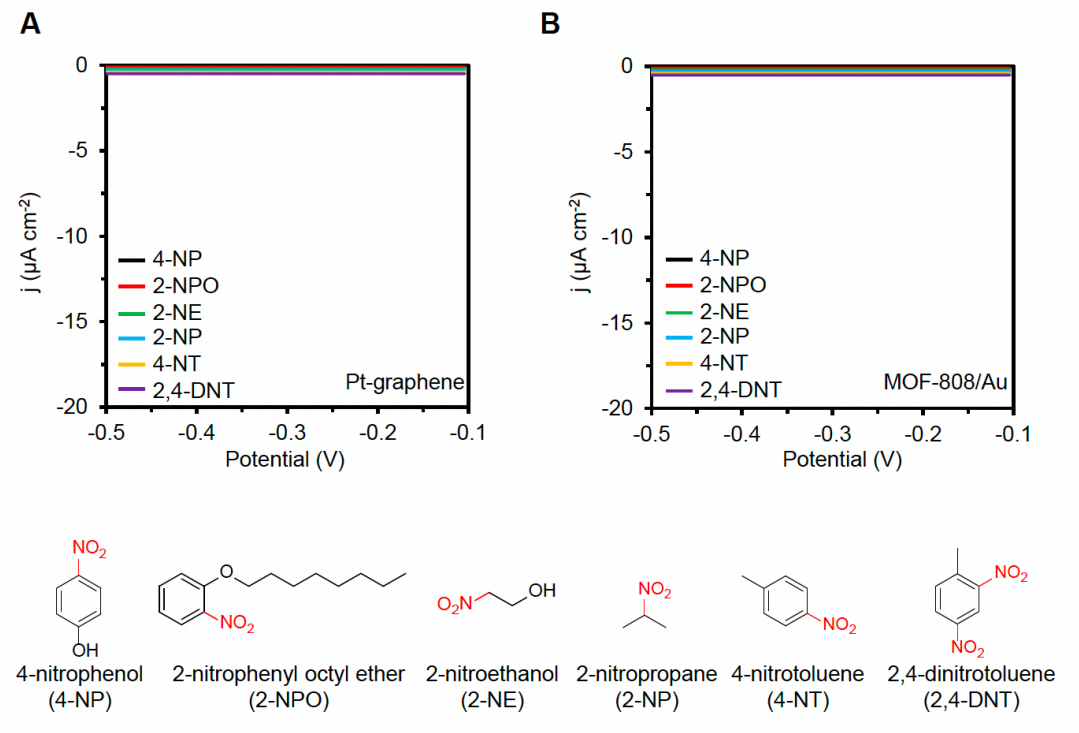

Fig. A-15. **The selectivity of TNT and OP sensors over other nitro compounds. (A** and **B)** nDPV voltammograms of a Pt-graphene TNT sensor (**A**) and a MOF-808/Au OP sensor (**B**) in 20 ppm six different types of nitro compounds.

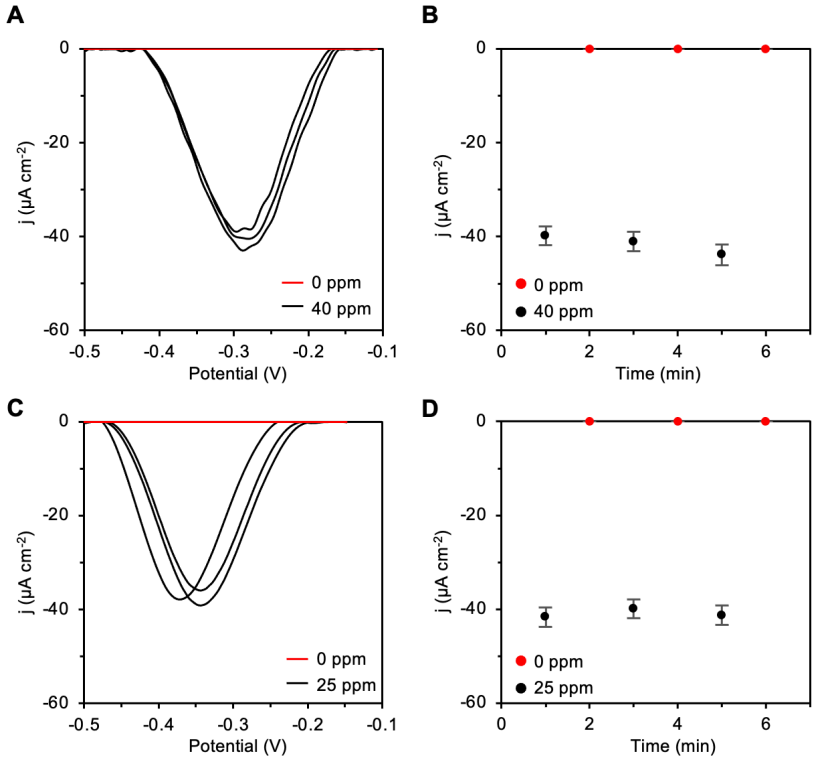

Fig. A-16. **The continuous and reversible TNT and OP sensing with the printed TNT and OP sensors.** (**A** and **B**) nDPV voltammograms of the Pt-graphene TNT sensors (**A**) and corresponding peak current heights (**B**) obtained continuously 0 and 40 ppm TNT. (**C** and **D**) nDPV voltammograms of the MOF-808/Au OP sensors (**A**) and corresponding peak current heights (**B**) obtained continuously in 0 and 25 ppm OP. Error bars represent the s.d. from 3 sensors.

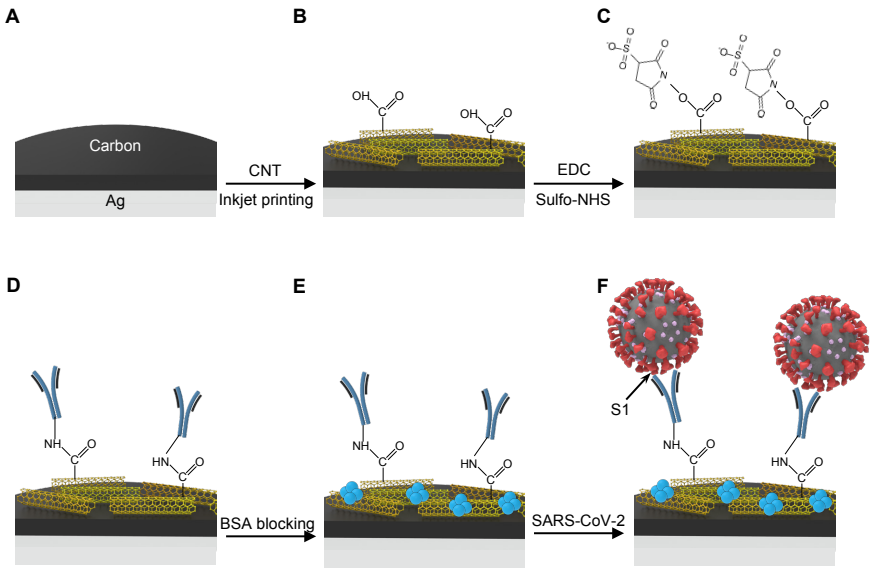

Fig. A-17. Schematic of the modification procedure of the printed CNT electrode for SARS-CoV-2 S1 sensing.

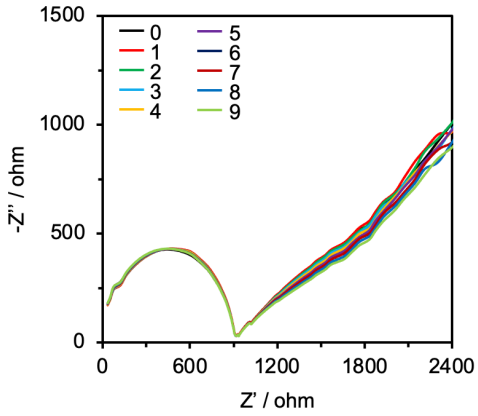

Fig. A-18. **Evaluation of the stability of antibody immobilization.** Nyquist plots of a CNT-based SARS-CoV-2 S1 sensor in 5 mM $K_3Fe(CN)_6$ before and after repetitive washing steps. Electrochemical impedance spectroscopy tests were performed at open circuit potentials with an AC amplitude 5 mV in the range of 0.1–10^6 Hz.

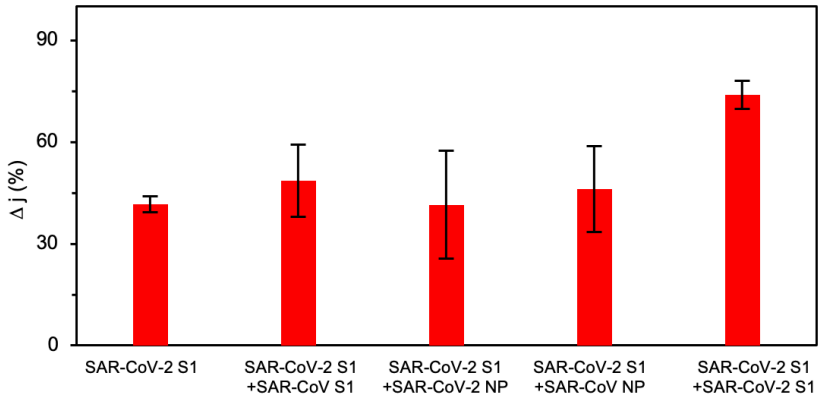

Fig. A-19. **Selectivity of the SARS-CoV-2 S1 sensor over other viral proteins.** Δj, percentage DPV peak current changes after target incubation. Error bars represent the s.d. from 3 sensors. 500 ppb interference proteins were added into 500 ppb SARS-CoV-2 S1. NP, nucleocapsid protein.

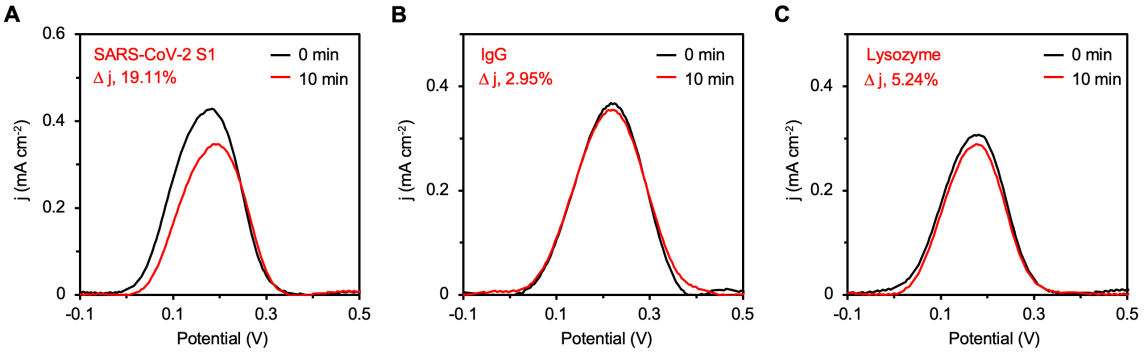

Fig. A-20. **Selectivity of the SARS-CoV-2 biosensor for dry-phase protein detection.** (**A**–**C**) DPV voltammograms of the SARS-CoV-2 S1 sensors before and after incubation with 10 ng dry-phase SARS-CoV-2 S1 (**A**), human immunoglobulin G (IgG) (**B**), and lysozyme (**C**). Inset values show percentage DPV peak current changes before and after incubation.

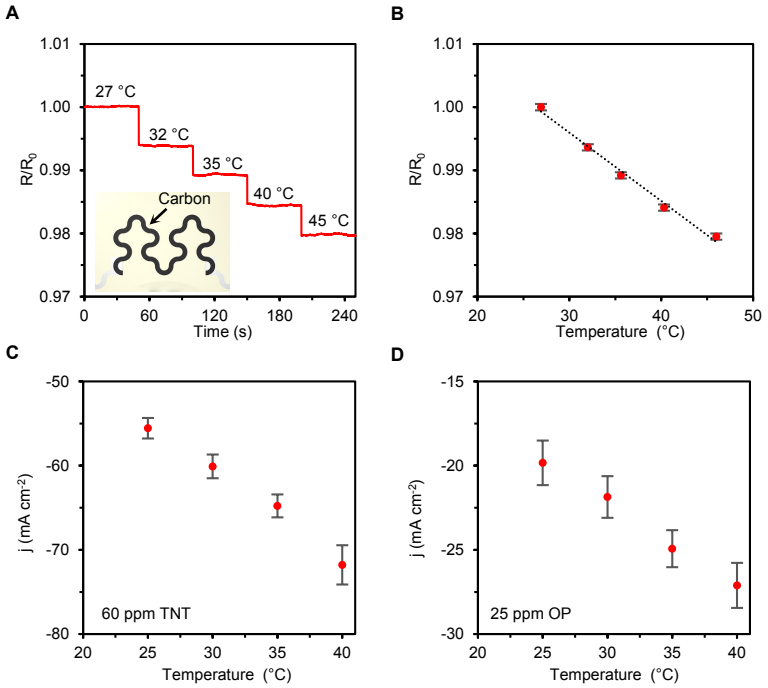

Fig. A-21. Characterization of printed carbon-based temperature sensor toward real-time temperature sensing and calibration. (**A** and **B**) Dynamic response (**A**) and calibration plot (**B**) of the inkjet-printed carbon based temperature sensor. Inset, schematic of the carbon temperature sensor. R and R_0 represent the resistive response of the sensors after and before bending, respectively. (**C** and **D**) The performance of a TNT sensor (**C**) and an OP sensor (**D**) under different temperatures in the presence of 60 ppm TNT and 100 μM OP, respectively. All error bars represent the s.d. from 3 sensors.

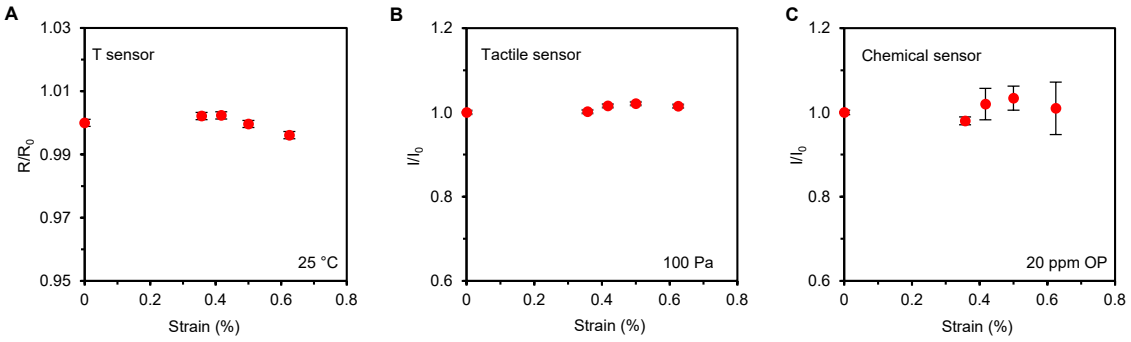

Fig. A-22. Performance of the printed sensor arrays under mechanical deformation. (**A**–**C**) The response of the inkjet-printed temperature sensors (**A**), tactile sensors (**B**), and OP sensors (**C**) under varied strain (0 to 0.625%). R and R_0 represent the resistive response of the sensors after and before bending, respectively. I and I_0 represent the current response of the sensors after and before bending, respectively. All error bars represent the s.d. from 3 sensors.

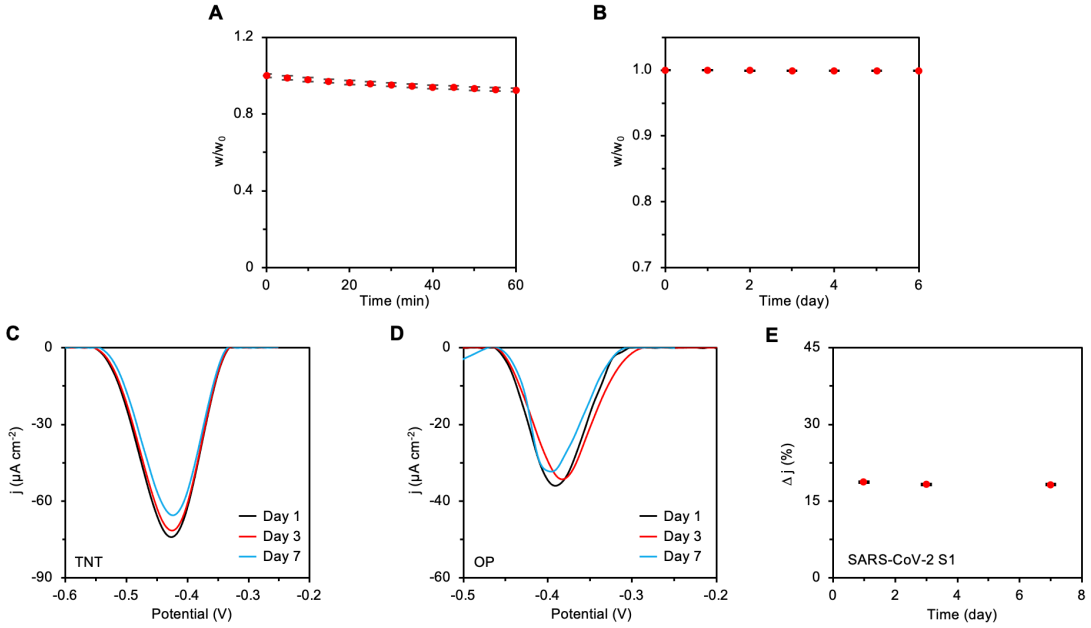

Fig. A-23. **Stability of the hydrogel.** (**A** and **B**) The weight of the hydrogel under operation condition (**A**) and 4°C storage condition (**B**). W and W_0 represent the measured weight during test and the weight before the storage, respectively. (**C** and **D**) nDPV voltammograms of the Pt-graphene sensors for detecting 60 ppm TNT (**C**) and MOF-808/Au sensors for detecting 25 ppm OP (**D**) with fresh, 2-day, and 6-day aged hydrogels. Error bars represent the s.d. from 3 units. (**E**) Percentage DPV peak current changes of the CNT-based SARS-CoV-2 S1 sensor after target incubation.

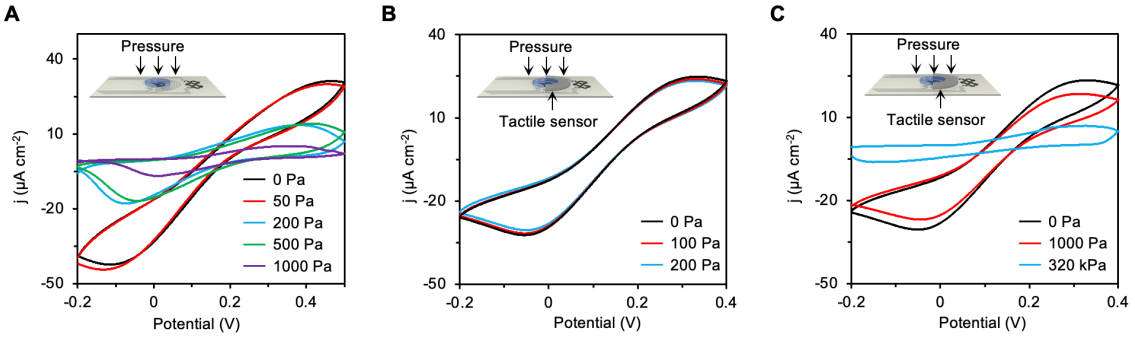

Fig. A-24. Influence of the contact pressure on the electrochemical sensor performance. (**A**) The CVs obtained under varying contact pressure on a hydrogel-loaded IPCE. (**B** and **C**) The CVs obtained under varying contact pressure on a PDMS microwell (tactile sensor) protected hydrogel-loaded IPCE. 2 mM $K_3Fe(CN)_6$ was used as the model target. Scan rates, 50 mV s^{-1}.

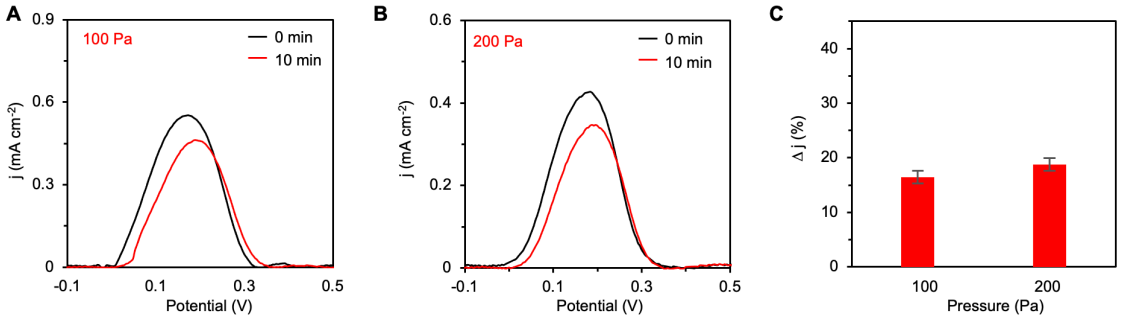

Fig. A-25. **Interference of the contact pressure on SARS-CoV-2 S1 sensor performance.** (**A**–**C**) DPV voltammograms (**A** and **B**) of the SARS-CoV-2 S1 sensors and percentage DPV peak current changes (**C**) before and after target incubation under varying applied normal pressure.

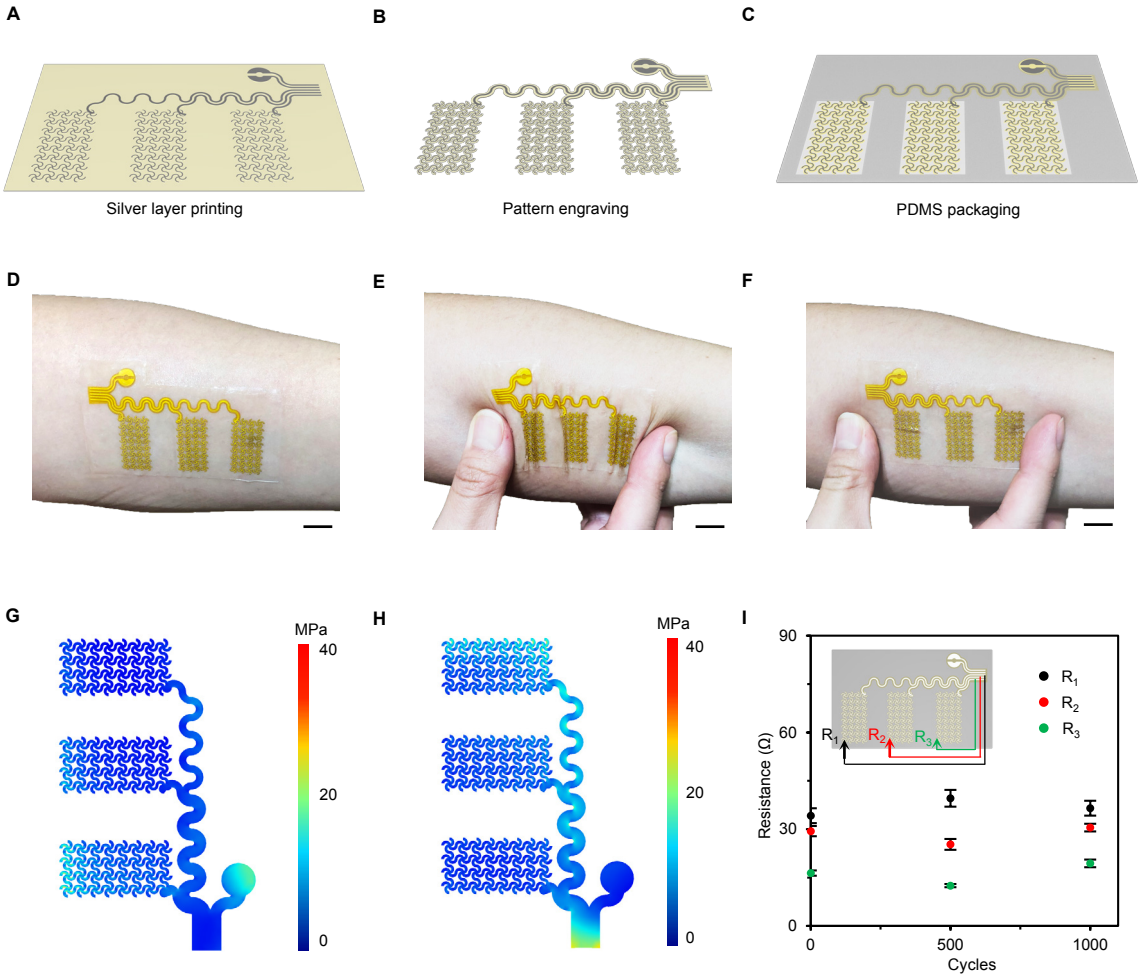

Fig. A-26. Fabrication and characterization of the soft and stretchable e-skin-H. (**A–C**) Schematic fabrication process of the inkjet-printed, PDMS encapsulated e-skin-H. (**D–F**) Photographs of an e-skin-H on a subject's arm. Scale bars, 5 mm. (**G** and **H**) Numerical simulation showing the pressure distributions of e-skin-H under 1% strain along the horizontal and vertical axis. (**I**) The resistance between the sEMG electrodes and their connection pins after bending (with a radius of bending curvature of 1.5 cm). All error bars represent the s.d. from 3 measurements.

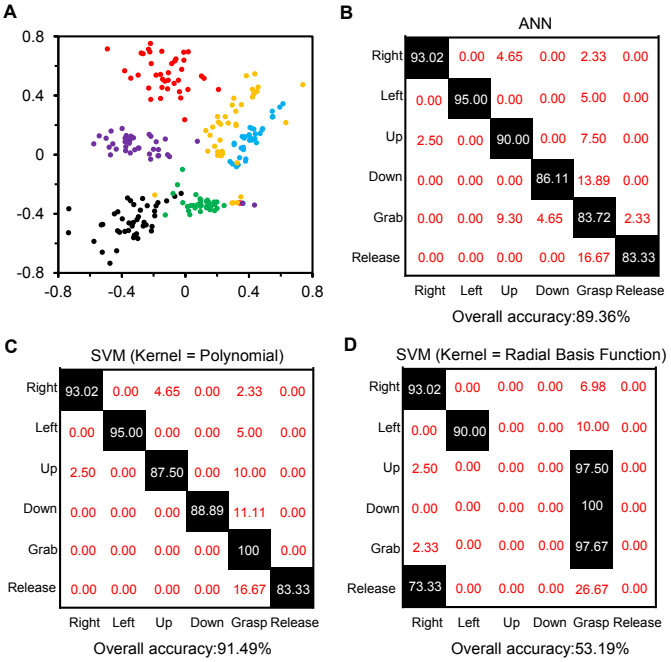

Fig. A-27. Gesture classification confusion matrix obtained with different machine learning algorithms. (**A**) A 2-dimensional representation of the 4-dimensional feature set extracted from the sEMG recording. The multidimensional scaling from 4 dimensions to 2 dimensions was performed using the scikit-learn MDS API (version 0.24.2). (**B–D**) The gesture accuracy breakdown for hand movement using the artificial neural network (ANN) (**B**), the support vector machine (SVM) (polynomial kernel) (**C**), and the SVM (radial kernel) (**D**). Each row represents a hand movement that was performed, while each column represents what gesture the model labeled the movement. The values in each cell represent the percentage of time the movement (in the row) was labeled as the respective columns gesture.

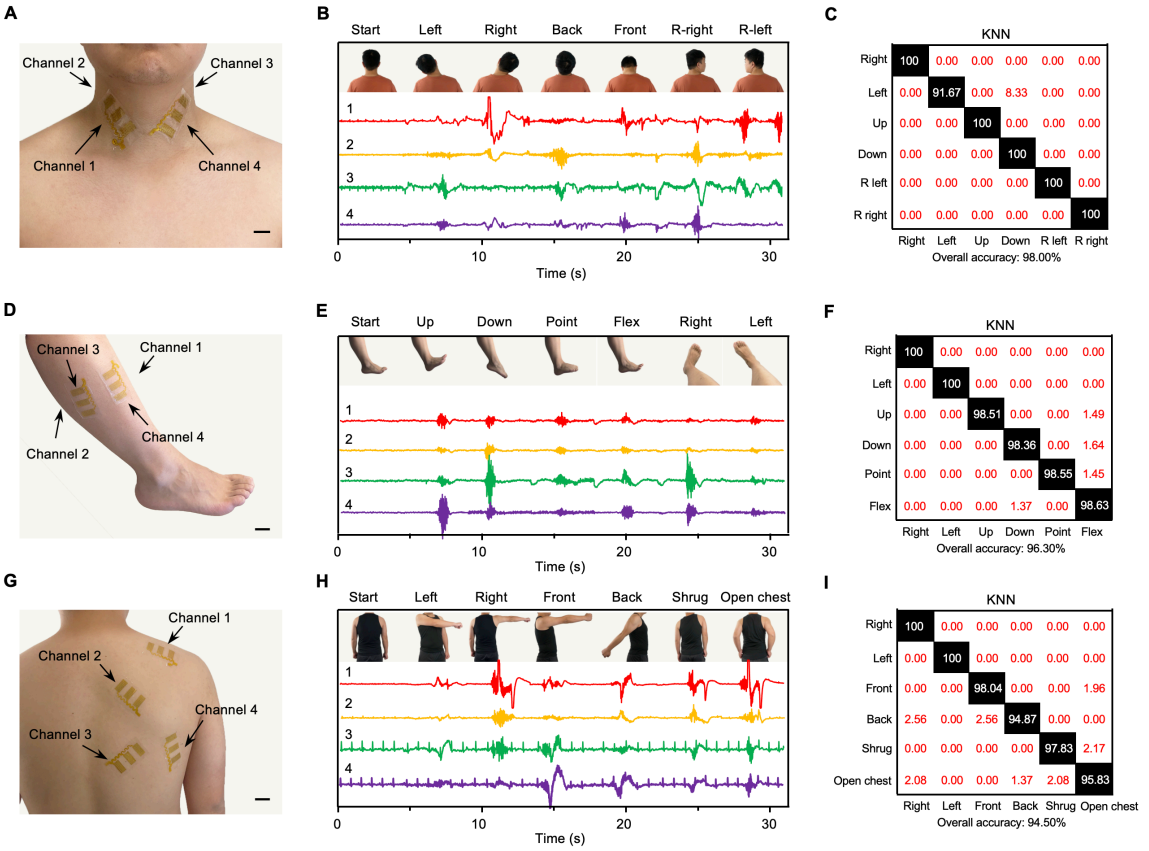

Fig. A-28. Evaluation of the e-skin-H on different body parts for AI-assisted human-machine interaction. (**A**) Photograph of the e-skin-H on the neck. (**B** and **C**) sEMG data (**B**) and the corresponding classification confusion matrix using a KNN model (**C**) from the e-skin-H on the neck. (**D**) Photograph of the e-skin-H on the lower limb. (**E** and **F**) sEMG data (**E**) and the corresponding classification confusion matrix using a KNN model (**F**) from the e-skin-H on the lower limb. (**G**) Photograph of the e-skin-H on the upper back. (**H** and **I**) sEMG data (**H**) and the corresponding classification confusion matrix using a KNN model (**I**) from the e-skin-H on the upper back. Scale bars, 2 cm.

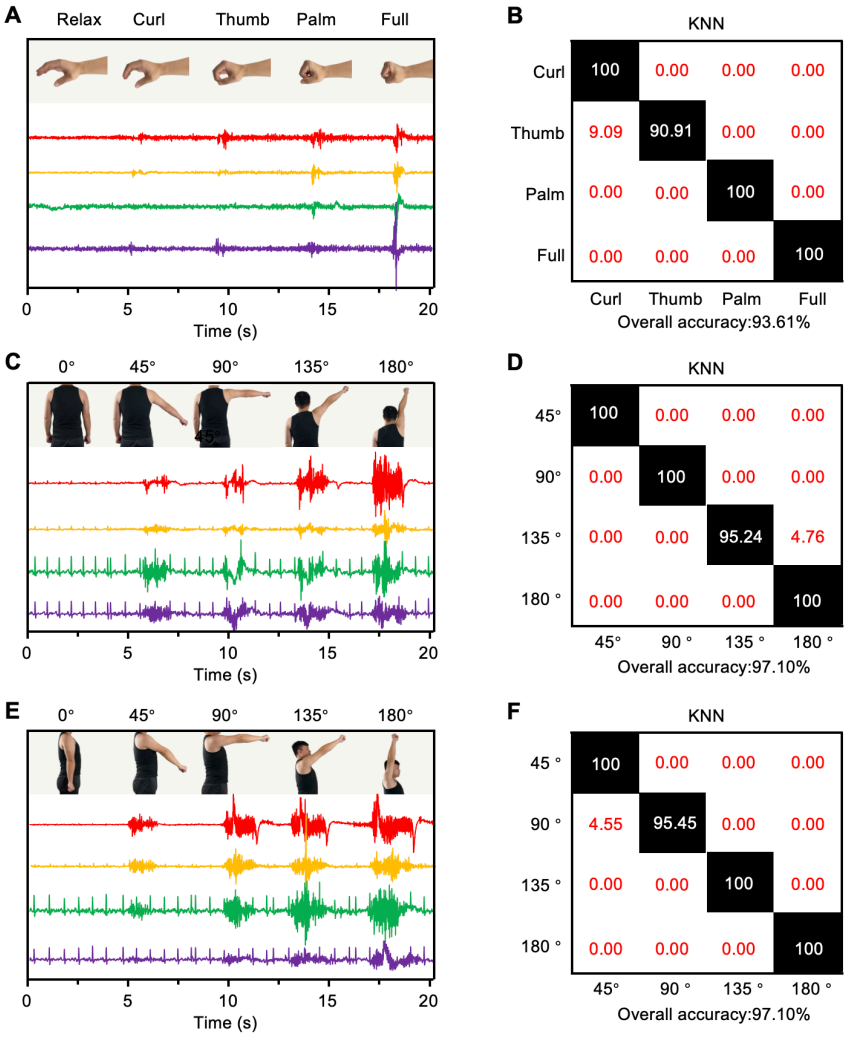

Fig. A-29. **Evaluation of the e-skin-H from gestures with different degrees.** (**A** and **B**) sEMG data collected by the e-skin-H on the arm from 4 grasp degrees (**A**) and the corresponding classification confusion matrix using a KNN model (**B**). (**C** and **D**) sEMG data collected by the e-skin-H on the upper back from 4 right gesture degrees (**C**) and the corresponding classification confusion matrix using a KNN model (**D**). (**E** and **F**) sEMG data collected by the e-skin-H on the upper back from 4 front gesture degrees (**E**) and the corresponding classification confusion matrix using a KNN model (**F**).

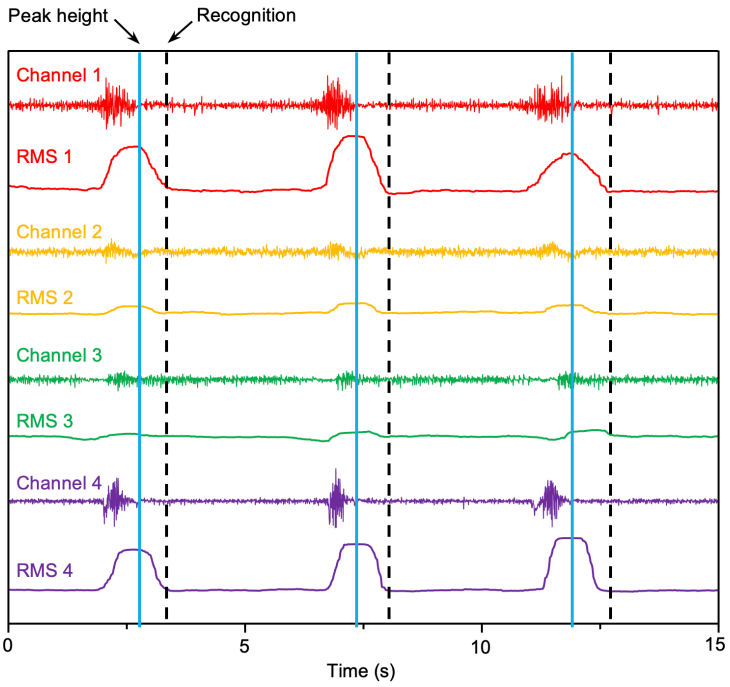

Fig. A-30. sEMG and root mean square (RMS) data process for robotic hand control.

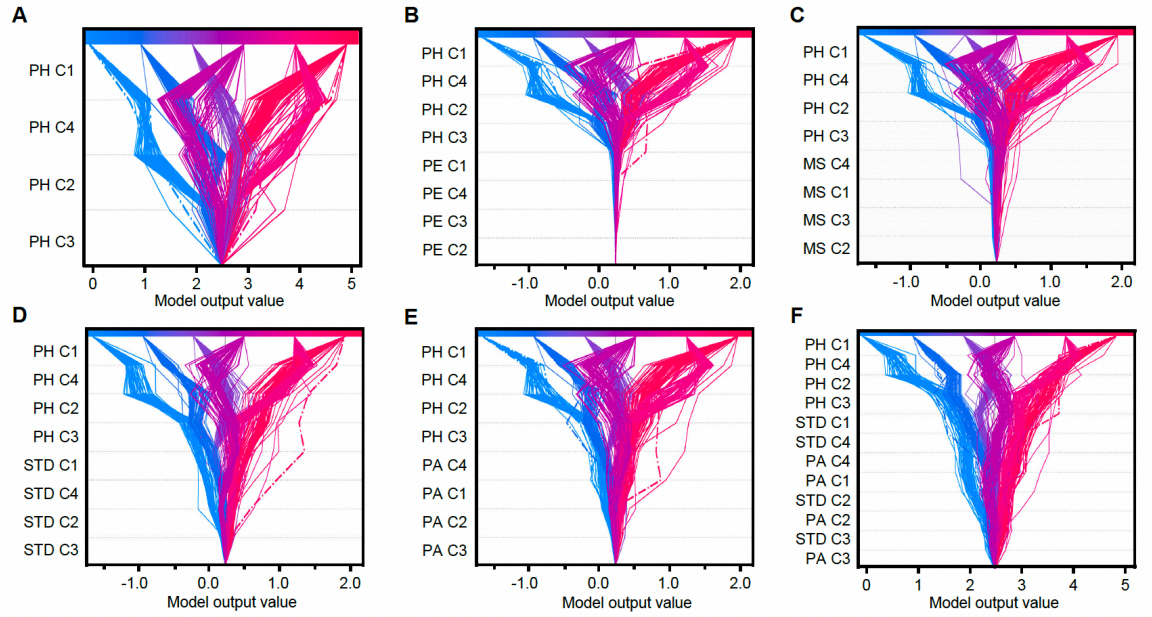

Fig. A-31. SHAP decision plots based on the arm sEMG dataset with respect to a KNN classification model. (A–F) SHAP decision plots displaying the SHAP contribution of feature(s) in a KNN classification model: PH only (**A**), PH+PE (**B**), PH+MS (**C**), PH+STD (**D**), PH+PA (**E**), and PH+STD+PA (**F**). Each decision line tracks the respective features' contributions to every individual classification, represented as serialized integer that maps to a hand movement. Dotted lines represent misclassified points.

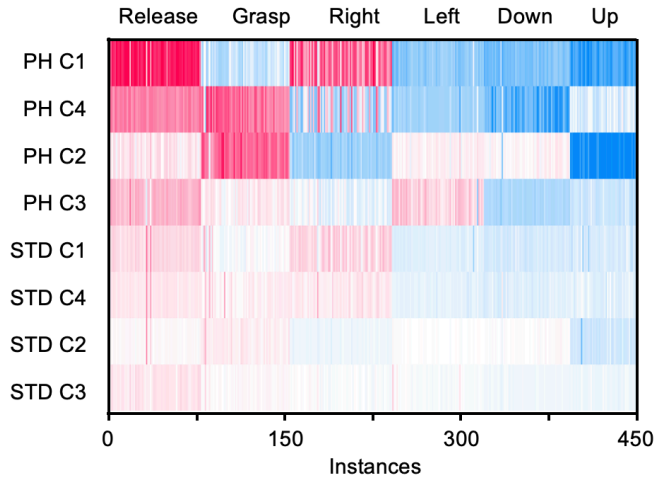

Fig. A-32. A SHAP heatmap that clusters each point's SHAP value by its respective gesture classification. The value (color) of each feature represents its SHAP value (prediction contribution) for a given gesture. The sign of the SHAP value represents its movement with respect to an arbitrary base value (average of all serialized classifications). Because of the arbitrary base value, each column in the heatmap should be evaluated within its respective gesture.

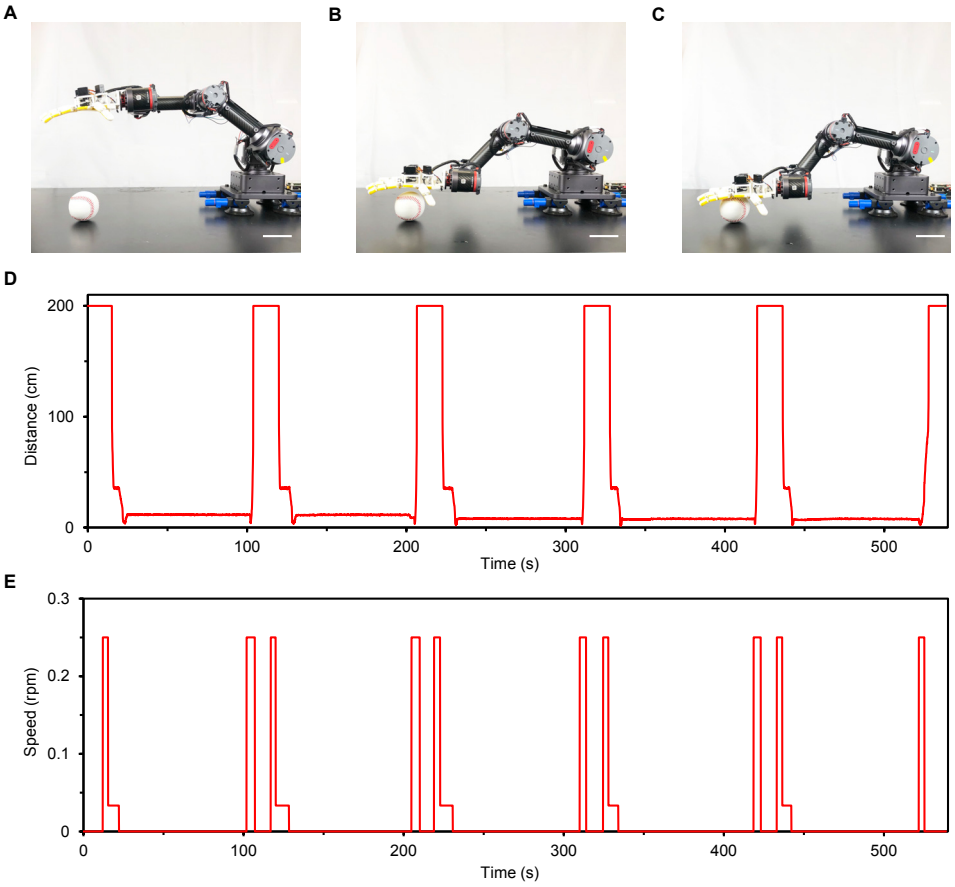

Fig. A-33. Evaluation of the laser proximity sensor in robotic operation. (**A–C**) Photographs of a robotic hand approaching and touching a spherical object. Scale bars, 7 cm. (**D** and **E**) The response of the laser proximity sensor (**D**) and the rotating speed of the robotic arm (**E**) during multiple operation cycles of object approaching and touching.

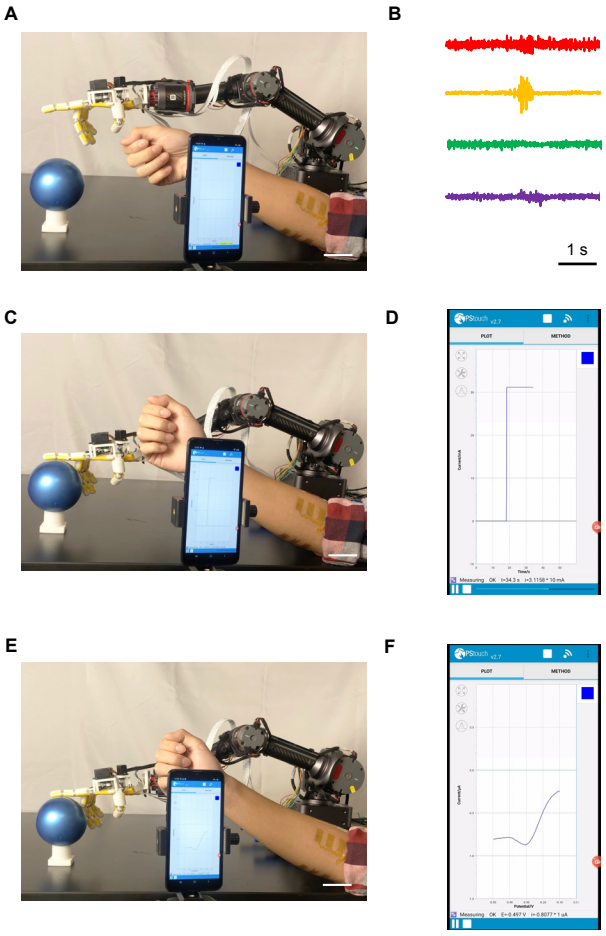

Fig. A-34. Human-interactive robotic control for object touching and on-site TNT detection. (**A** and **B**) Image (**A**) and sEMG data (**B**) for robotic hand control to approach the object. (**C** and **D**) Image of the robotic finger contact (**C**) and the corresponding tactile sensor response (**D**). (**E** and **F**) Image of the finger-tip on-site TNT detection (**E**) and the collected nDPV voltammogram using a mobile interface (**F**). Scale bars, 5 cm.

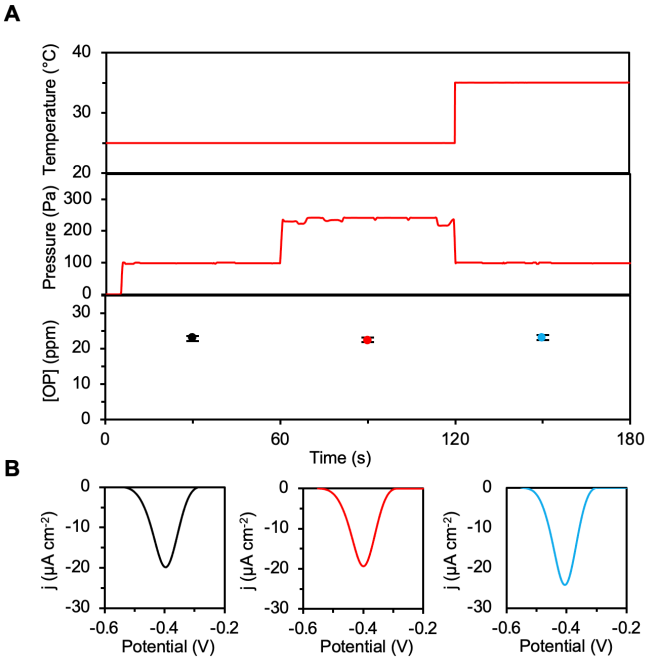

Fig. A-35. **Multiplexed simultaneous physicochemical sensor analysis using the printed sensor array. (A)** Dynamic responses of temperature, tactile, and OP sensors for single point OP analysis. OP, 25 ppm. Contact pressure and temperature were altered during the sensing to study the signal interferences; temperature induced OP sensor response change was automatically calibrated. (**B**) The nDPV voltammograms of the inkjet-printed MOF-808/Au sensor collected during the test.

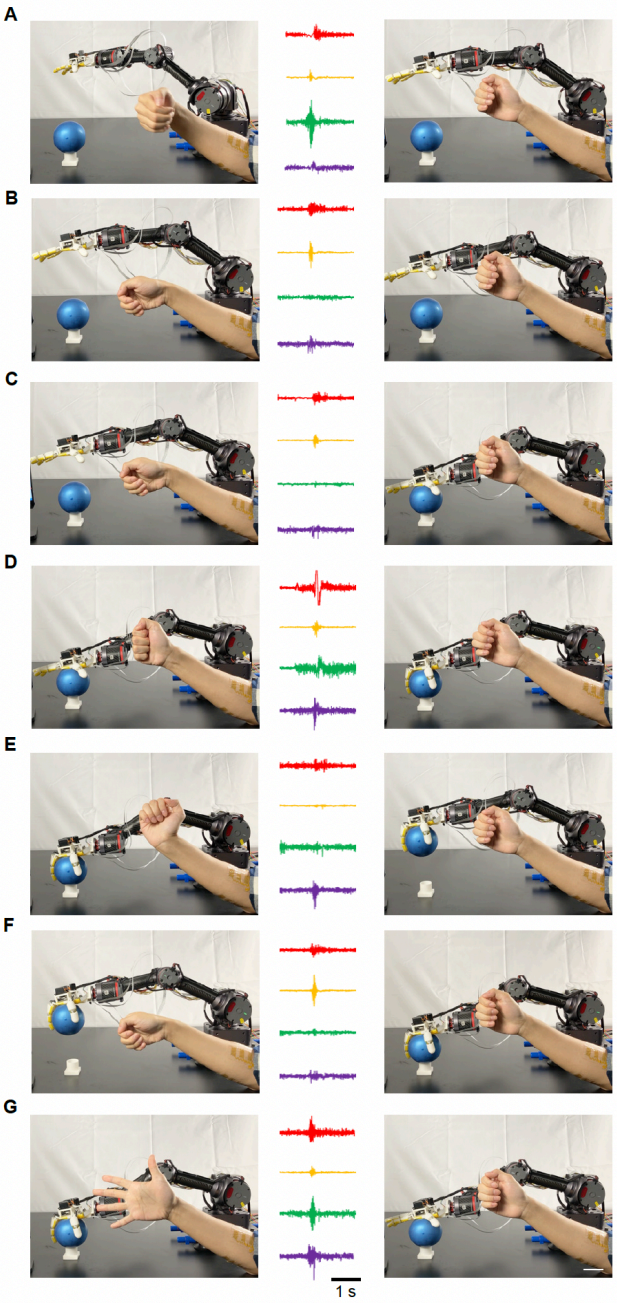

Fig. A-36. Human-machine interactive robotic operation for object grasping. (A–G) the robotic hand operation for object grasping based on sEMG data collected from 7 sequential gesture controlled steps. Left column, hand gesture; middle column, sEMG data collected from the gesture; right column, machine learning assisted robotic hand operation. Scale bar, 5 cm.

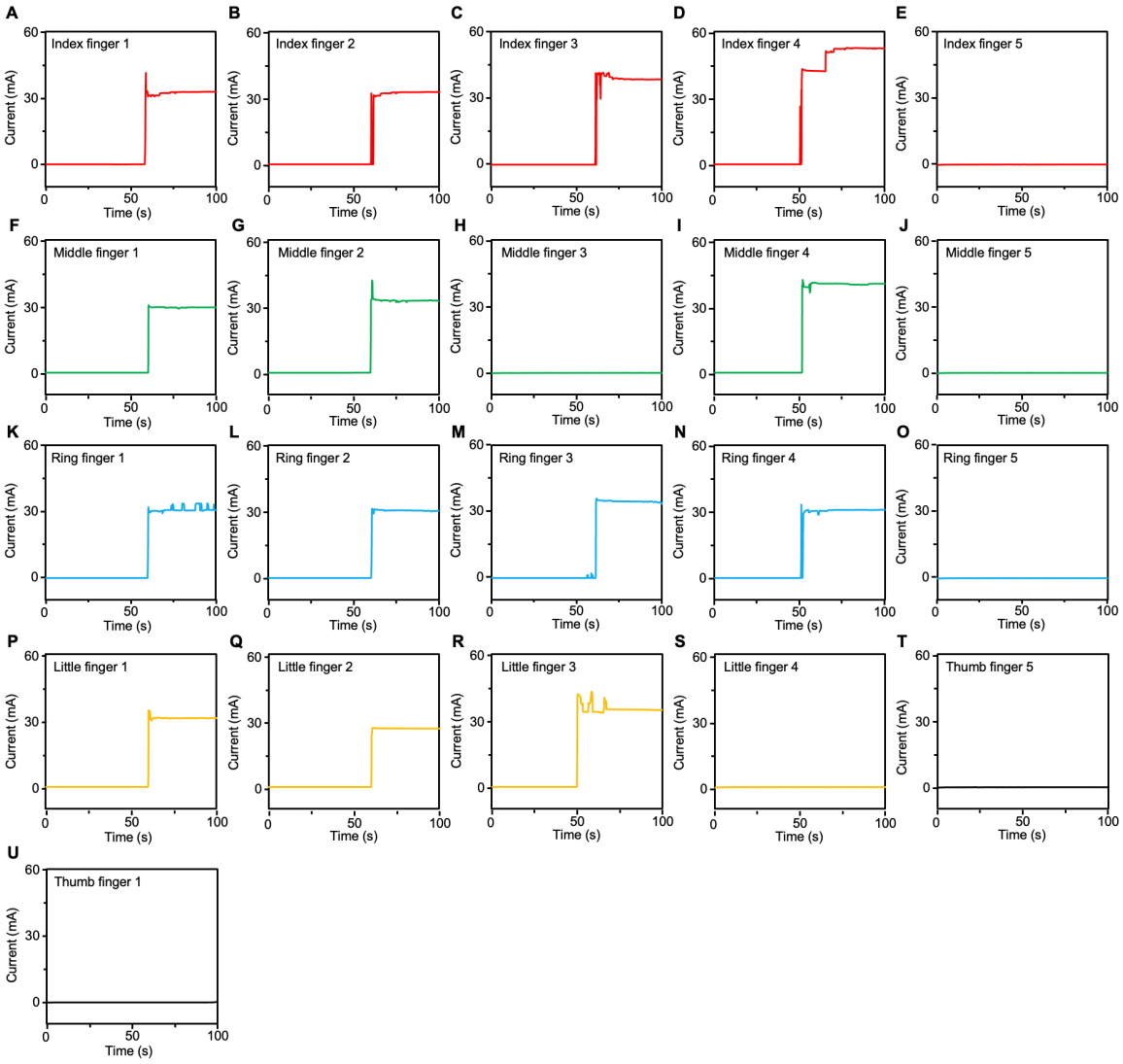

Fig. A-37. **The tactile responses of the e-skin-R on a cylindrical object.** (A-E) Response of the tactile sensors on the index finger (A-E), the middle finger (F-J), the ring finger (K-O), the little finger (P-S), and the thumb finger (T and U).

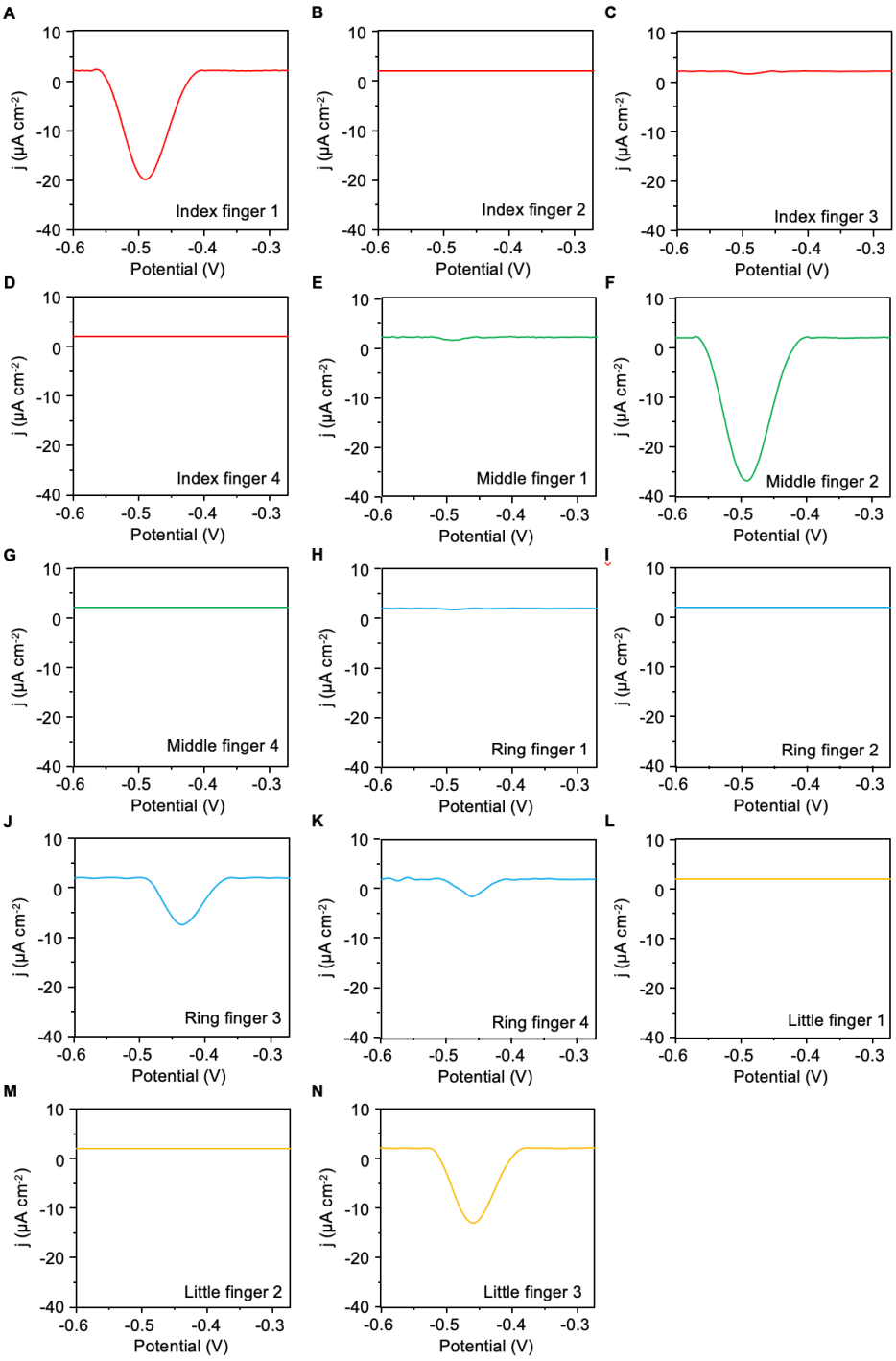

Fig. A-38. **The OP sensing responses of the e-skin-R on a cylindrical object. (A–N)** nDPV responses of the MOF-808/Au sensors on the index finger (A-D), the middle finger (E-G), the ring finger (H-K), and the little finger (L-N).

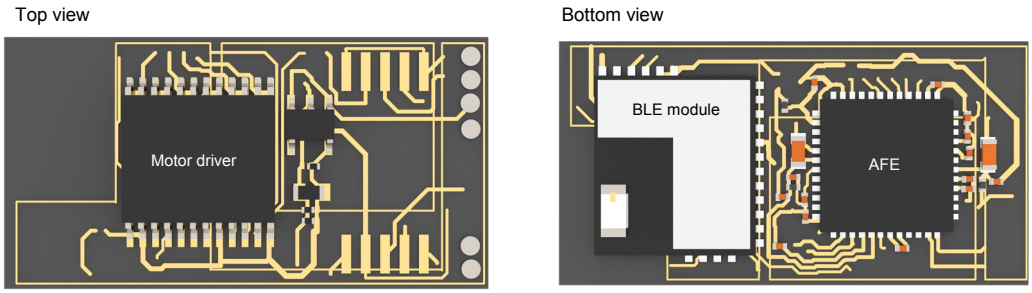

The list of components

Description	Value and series number	Number
BLE module	CYBLE-222014-01	1
Electrochemical front end	AD5941BCPZ	1
Motor driver	TB6612FNG	1
Voltage regulator	ADP162AUJZ-3.0-R7	1
Ferrite bead	BKP0603HS121-T	1
0201 Capacitor	220 pF	1
0201 Capacitor	0.1 μF	7
0201 Capacitor	0.47 μF	4
0201 Capacitor	1 μF	3
0201 Capacitor	4.7 μF	1
0402 Capacitor	10 μF	4
0201 Resistor	0 Ω	2
0201 Resistor	2.2 Ω	2
0201 Resistor	600 kΩ	1

Fig. A-39. Schematic illustration and component list of the electronic system of the M-Boat.

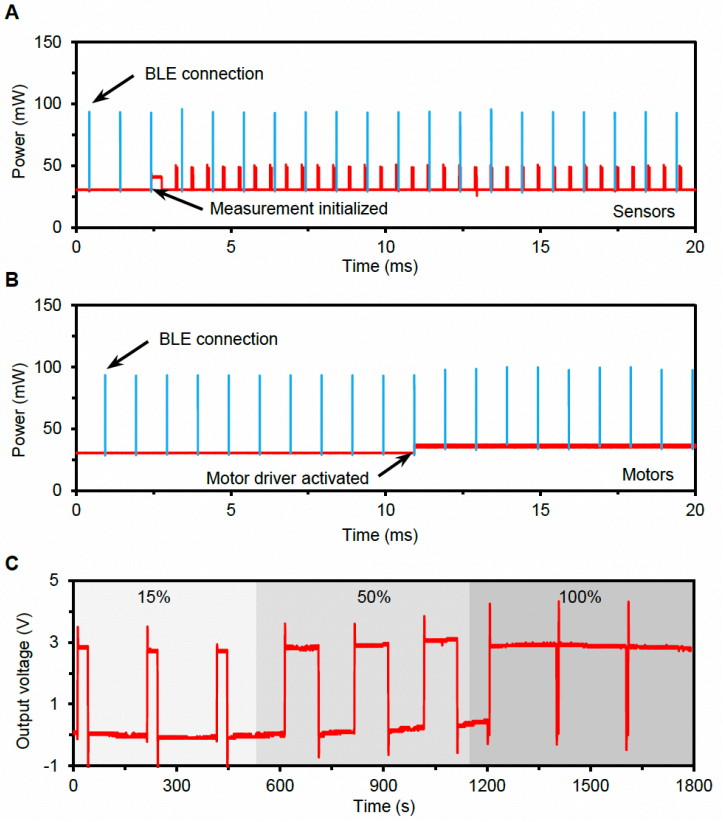

Fig. A-40. **Characterization of the operation of the M-Boat.** (**A**) Power consumption of the M-Boat during the sensing mode. (**B**) Power consumption of the M-Boat during the propulsion mode. (**C**) Voltage output of the motor driver at 15%, 50 %, and 100% load (motor control was achieved by pulse width modulation).

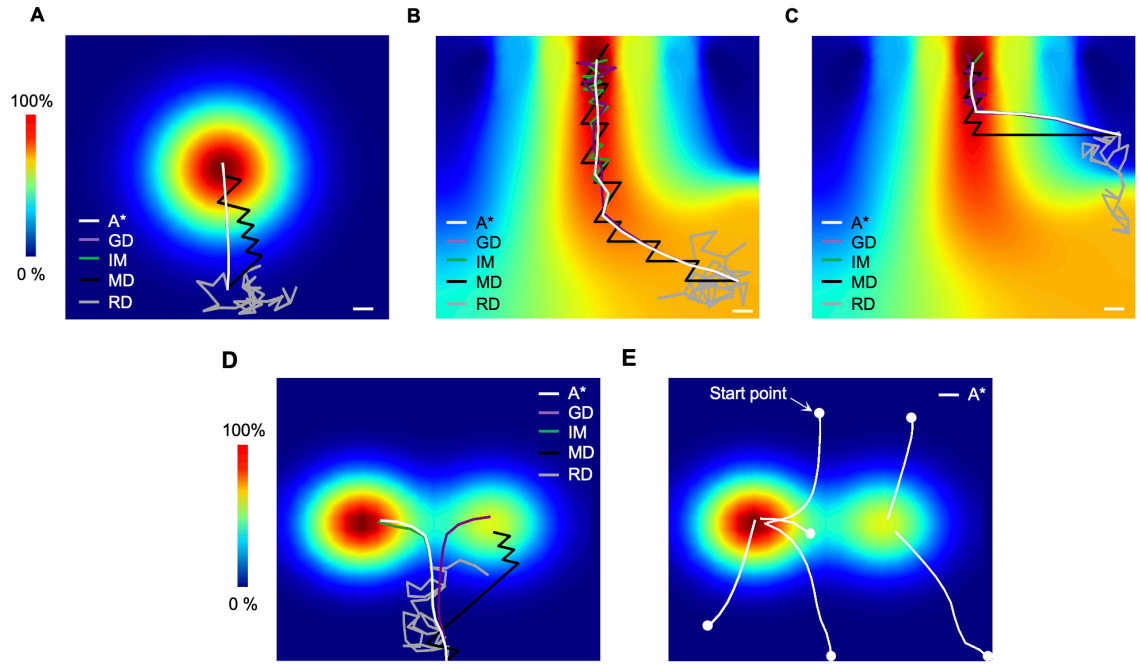

Fig. A-41. **Simulation comparison of the searching algorithms for M-Boat autonomous source locating.** (**A–C**) Simulation comparison of the searching algorithms for M-Boat autonomous source locating when one source is present. (**D** and **E**) Simulated paths the M-Boat would follow using different algorithms at the same starting location (**D**) and using A* algorithm at different starting locations (**E**) when two sources (unequal in magnitude) are present.

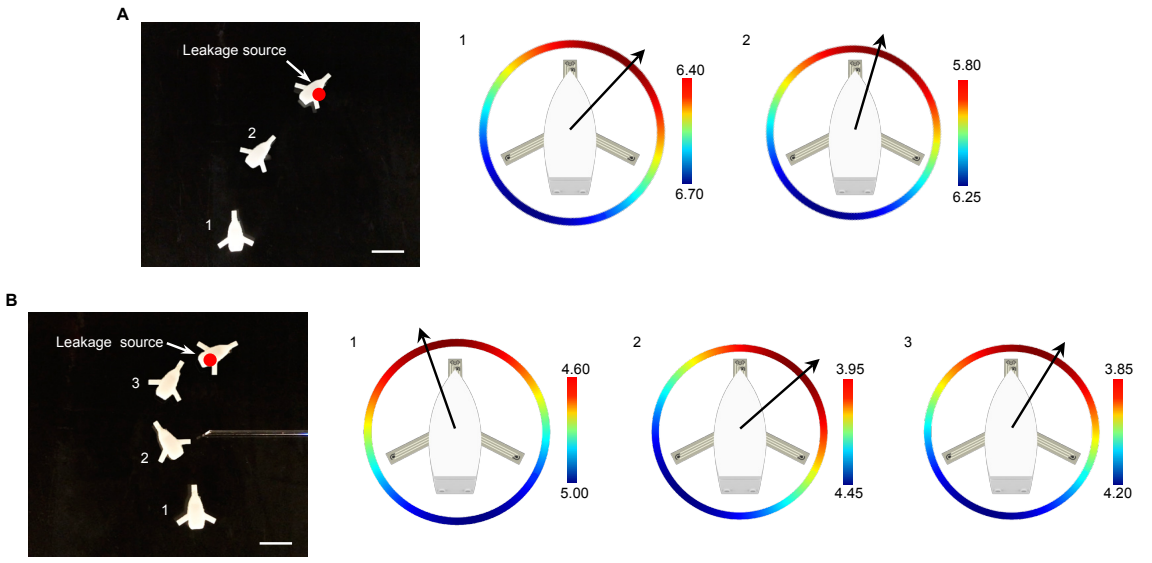

Fig. A-42. Evaluation of the M-Boat for autonomous source tracking. Time lapse images of the M-Boat-based source tracking and the data collected at each decision-making point (**A** and **B** represent data collected from two independent trials). Scale bars, 5 cm.

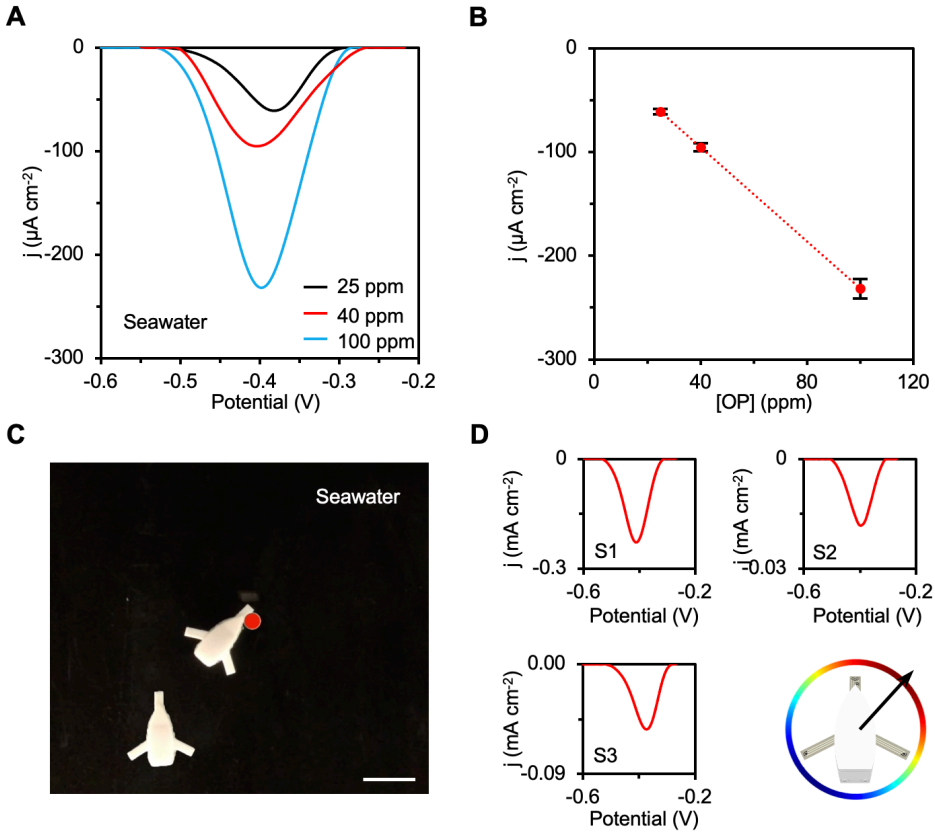

Fig. A-43. **Evaluation of the M-Boat in seawater.** (**A** and **B**) nDPV voltammograms of the inkjet-printed OP sensor in seawater with spiked OP (25–100 ppm) (**A**) and the corresponding calibration curves (**B**). (**C**) Time lapse images showing the operation of the M-Boat in seawater for autonomous OP source tracking. Scale bar, 5 cm. (**D**) nDPV voltammograms collected by the M-Boat's OP sensors in seawater and the resulted algorithm-driven decision-making for autonomous source tracking.

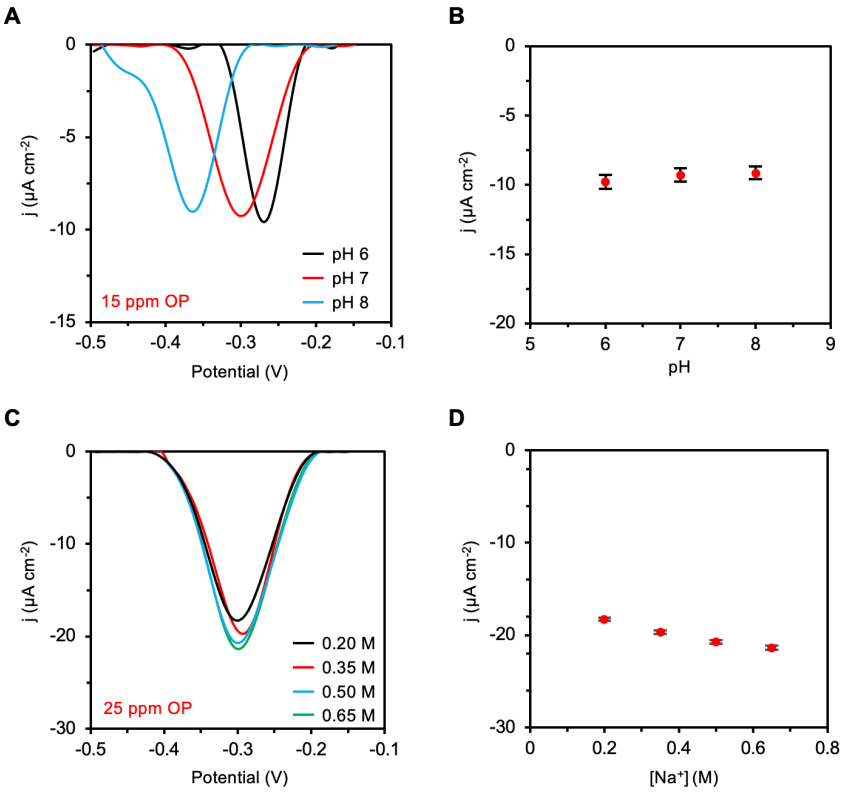

Fig. A-44. **Influence of ionic strength and pH on sensor performance.** (**A** and **B**) The nDPV voltammograms (**A**) and the corresponding calibration plot (**B**) of the OP sensors in solutions with 15 ppm OP and different pHs (6 to 8). (**C** and **D**) nDPV voltammograms (**C**) and the corresponding calibration plot (**D**) of the OP sensors in 25 ppm OP and varing sodium concentrations (from 0.20 M to 0.65 M). Error bars represent the s.d. from 3 sensors.

Table A-1. Ink composition and characterizations.

	Surface tension (mN m^{-1})	Viscosity (mPa*s)	Density (g ml^{-1})	Inverse Ohnesorge number	Thermal annealing (°C)
Ag (25 wt%)	31.0	8	1.3	3.6	240
Au (10 wt%)	30.0	10	1.1	2.6	180
C (5 wt%)	32.5	10	1.1	2.7	240
AgNWs (2 mg ml^{-1})	21.5	2	0.8	9.6	150
PAA (3 wt%)	42.8	11	1.1	2.8	250
GO (2 mg ml^{-1})	53.9	6	1.1	5.8	180
MOF-808 (2 mg ml^{-1})	56.6	3	1.0	11.7	180
CNT (2 mg ml^{-1})	55.5	7	1.0	4.9	120

Data measured at 25°C; inverse Ohnesorge number: $Z = \frac{\sqrt{\sigma \rho d}}{\eta}$; d (diameter of the nozzle) = 21 μm; σ, surface tension; ρ, density; η, viscosity.

Table A-2. Accuracy breakdown per feature with and without one channel removed. The values reported represent the mean accuracy ± the standard deviation of the KNN trained using the arm EMG dataset across 5000 trials. 3 features: PH, STD, and PA. 5 features: PH, STD, MS, PA, PE.

	5 features	3 fearures	PH	STD	MS	PA	PE
All channels	97.29±1.11	97.28±1.14	97.20±1.12	97.02±1.17	93.05±1.69	92.49±1.76	88.71±2.05
No channel1	96.31±1.25	96.45±1.25	96.65±1.15	96.04±1.28	90.44±1.85	90.55±1.86	87.47±2.16
No channel2	89.99±1.83	89.18±1.96	88.65±1.92	88.19±1.92	84.32±2.04	81.21±2.29	84.10±2.30
No channel3	92.63±1.83	91.96±1.86	90.23±1.91	90.64±1.81	84.31±2.25	79.39±2.77	76.94±2.71
No channel4	94.84±1.50	94.75±1.52	94.13±1.51	94.36±1.47	85.95±2.26	86.86±2.27	82.18±2.66

Table A-3. Accuracy breakdown based on five features with one and two channels.

The values reported represent the mean accuracy ± the standard deviation of the KNN trained using the arm EMG dataset across 5000 trials.

	Channel 1	Channel 2	Channel 3	Channel 4
Channel 1	52.53±3.12	80.05±2.55	79.44±2.32	76.74±2.57
Channel 2	80.05±2.55	56.32±3.09	85.81±2.45	86.05±2.25
Channel 3	79.44±2.32	85.81±2.45	68.42±3.41	87.37±1.88
Channel 4	76.74±2.57	86.05±2.25	87.37±1.88	65.35±2.72

Chapter 3

STRAIN-INSENSITIVE WET-TISSUE-ADHESIVE BIPHASIC BIOELECTRONICS FOR PHYSICOCHEMICAL MONITORING AND ADAPTIVE THERAPY

Materials from this chapter appear in "Li, J.; Fan, K.; Ma, X.; Wang, C.; Min, J.; Chen, Y.; Song, Y.; Xu, Y.; Gao, W. Strain-insensitive wet-tissue-adhesive biphasic bioelectronics for physicochemical monitoring and adaptive therapy. *Nature Materials*, Accepted"

3.1 Introduction

Implantable bioelectronics have become critical tools in modern medicine, enabling continuous physiological monitoring, precise diagnostics, and targeted therapeutic interventions[1-3]. Despite considerable advancements, current implants remain constrained by rigid form factors, mechanical mismatch with soft biological tissues, and limited functionality—often confined to electrical sensing or stimulation. These shortcomings can compromise signal fidelity, provoke adverse tissue responses, and ultimately result in premature device failure, especially in dynamic environments such as the beating heart or expanding gastrointestinal tract[4].

To address these challenges, recent efforts have explored flexible and stretchable systems based on structural engineering[5,6], stretchable polymer composites[7,8], and conductive hydrogels[9-11]. While these approaches enhance mechanical compatibility, they each face trade-offs: engineered structures often reduce device density, polymer composites may lose conductivity under strain[12-14], and hydrogels—though inherently soft—typically exhibit low conductivity (<0.5 S cm^{-1}) and present challenges in electronic system integration and durability[15-17].

Hybrid solutions combining conductive materials with hydrogel have demonstrated improved tissue compatibility and adhesion[18-22]. However, these approaches often involve complex fabrication procedures, post-fabrication processing or additional surgical steps. These complexities hinder scalability, limit spatial control over the device-tissue interface, and pose challenge for clinical translation. Many existing platforms still rely on sutures or surgical adhesives and fall short of offering a scalable, unified solution that supports both sensing and therapeutic functionalities.

A particularly underdeveloped area in implantable electronics is chemical sensing, which holds immense potential to enrich the functional scope of bioelectronic implants. Unlike electrical signals that reflect neuronal or muscular activity, chemical biomarkers offer more direct insights into dynamic physiological states at molecular levels[23-25]. Local biochemical

changes in specific organs or interstitial fluids—such as those associated with inflammation, metabolic dysregulation, or ischemia—often precede systemic symptoms and are not easily captured through conventional electrical modalities[26,27]. Seamlessly incorporating real-time chemical sensing into soft, tissue-conforming bioelectronic systems therefore represents a critical step toward multimodal, adaptive implants capable of richer physiological interrogation and closed-loop intervention.

In this work, we present, ElHyX, a soft, strain-insensitive elastomer–hydrogel biphasic cross-functional platform for implantable bioelectronics. ElHyX enables multimodal functionalities—including physical sensing, biochemical monitoring, and neural modulation—by integrating a conductive elastomer matrix with a tissue-adhesive hydrogel layer (**Fig. 3-1a** and **Fig. B-1**). Functional fillers such as eutectic gallium–indium (EGaIn) and graphite impart robust electrical and electrochemical performance, while the hydrogel component ensures conformal adhesion to dynamic, wet tissue surfaces without additional treatment. In contrast to conventional flexible devices (**Fig. 3-1b**) that require sutures and exhibit poor conformability to soft moving organs, ElHyX maintains stable performance under physiological deformation while gently interfacing with soft organs.

This biphasic platform enables fabrication of diverse device types—including bioelectrical sensors, biochemical sensors, and nerve cuffs—all of which can be readily adapted to conform and adhere to various internal organs for physiological sensing and metabolic regulation (**Fig. 3-1c**). Importantly, this platform is compatible with scalable manufacturing via direct ink writing (DIW) (**Fig. 3-1d, Fig. B-2**), enabled by a custom-developed set of printable inks optimized for both rheological printability and functional performance (**Fig. B-3** and **Table B-1**). The molecularly integrated elastomer–hydrogel interface provides robust mechanical compliance, strong wet-tissue adhesion, and reliable operation under dynamic strain (**Fig. 3-1e**).

We demonstrate the versatility of ElHyX across a series of in vivo applications, including electrocardiogram (ECG) monitoring on beating heart, real-time glucose sensing, and neural modulation (**Fig. 3-1c**). Furthermore, we integrate these functions seamlessly into a single

platform (**Fig. 3-1f**) to realize a closed-loop system for automated blood glucose regulation in a diabetic animal model. Compared with the state-of-the-art implantable bioelectronic platforms, ElHyX uniquely combines high stretchability, strain-invariant conductivity, wet-tissue adhesion, multimodal sensing, and therapeutic actuation—positioning it as a comprehensive and scalable solution for next-generation implantable bioelectronics[7,11,28-32] (**Fig. 3-1g** and **Tables B-2** and **B-3**).

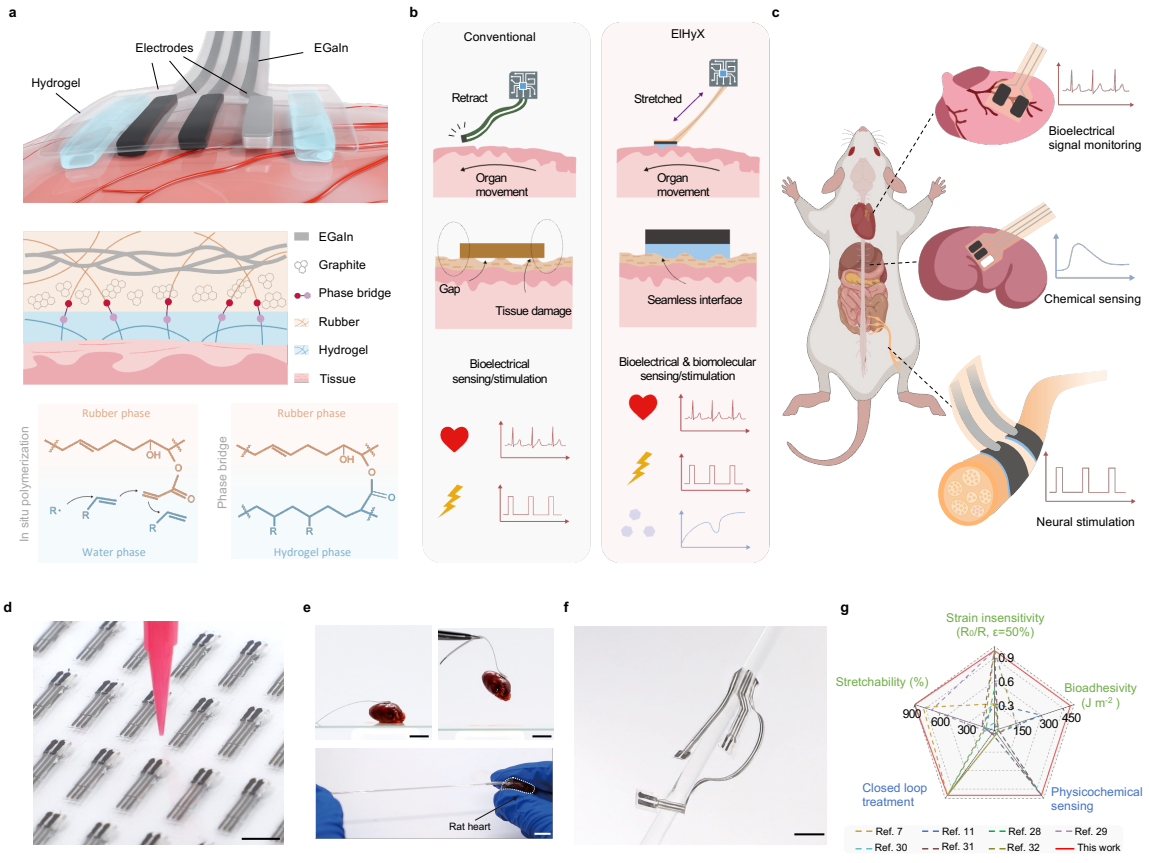

Fig. 3-1 Overview of the soft, strain-insensitive elastomer-hydrogel biphasic multifunctional platform (ElHyX) for multimodal implantable bioelectronics. a, Schematic illustration of the ElHyX architecture. The elastomer phase is chemically modified with vinyl groups that participate in hydrogel polymerization, enabling seamless molecular-level integration. Conductive fillers such as eutectic gallium–indium (EGaIn) and graphite provide strain-insensitive conductivity and an electrochemically stable interface. A bioadhesive hydrogel ensures robust adhesion to wet tissue. **b**, Compared to conventional

flexible electrodes, ElHyX eliminates the needs for sutures and enables secure, conformal integration onto soft, dynamic organs while supporting biomolecular sensing. **c**, Schematic of ElHyX implants applied to various organs for multimodal physiological monitoring and modulation. **d**, The ElHyX system can be manufactured rapidly at scale using direct ink writing (DIW). Scale bar, 1 cm. **e**, Demonstrations of ElHyX adhesion and functional stability under large deformation (100% strain) and on an isolated rat heart. Scale bars, 1 cm. **f**. Photo of an integrated ElHyX device combining electrophysiological sensing, biomolecular monitoring, and neural modulation for closed-loop disease management. Scale bar, 1 cm. **g**, Radar chart benchmarking ElHyX against other state-of-the-art implantable bioelectronic platforms across key materials and functionality metrics. ElHyX system uniquely combines high stretchability, strain-insensitive performance, wet-tissue adhesion, multimodal physicochemical sensing, and therapeutic feedback capabilities.

3.2 Mechanical and electromechanical characterizations of ElHyX

ElHyX is a biphasic platform that integrates conductive elastomers with a bioadhesive hydrogel, offering seamless molecular integration, tunable conductivity, and rapid strong adhesion to wet tissue surfaces for implantable bioelectronics. The architecture comprises a hydrogel phase covalently bonded to an elastomer composite, with eutectic gallium–indium (EGaIn) confined to the central elastomeric domain (**Fig. 3-2a**). Cross-sectional SEM imaging confirms this biphasic architecture, showing uniform hydrogel–elastomer integration and spatially localized EGaIn distribution (**Fig. 3-2b**).

Poly(styrene-butadiene-styrene) (SBS) was chosen as the elastomer backbone due to its excellent stretchability and mechanical durability. To enable seamless two-phase integration at molecular level, SBS was chemically modified to introduce vinyl side chains, producing acrylyl-opening epoxidized SBS (AESBS) via sequential epoxidation and acrylation (**Fig. 3-2c**). Fourier transform infrared (FTIR) spectra confirm successful functionalization, with characteristic peaks observed for SBS, epoxidized SBS (ESBS), and AESBS (**Fig. 3-2d**). These vinyl groups serve as active sites for radical polymerization, allowing molecular level integration between hydrogel and elastomer without the need for additional surface

treatments. This integration strategy allows the elastomer and hydrogel phases to form a chemically independent yet mechanically seamless interface (**Fig. B-4**), supporting robust adhesion and mechanical integrity while allowing independent optimization of elastomer properties through functional fillers and hydrogel formulation flexibility.

The hydrogel phase is built on a poly(acrylic acid) (PAAc) backbone that achieves stable wet-tissue adhesion through a high density of strong hydrogen bonding between carboxylic acid groups and biological surfaces[33,34]. To enhance mechanical robustness, we introduced sodium 4-vinylbenzenesulfonate and [2-(acryloyloxy)ethyl]trimethylammonium via copolymerization, to generate ionic crosslinks and form an ionically crosslinked hydrogel (i-Gel). These dynamic bonds can enhance energy dissipation and improve hydrogel toughness[35]. Following polymerization, a dry adhesive layer (DAL) is formed by dehydrating the hydrogel, enabling rapid rehydration and adhesion to moist tissue through water absorption and hydrogen bonding.

Leveraging this hydrogel design, ElHyX exhibits strong and stable adhesion to wet biological tissues (**Fig. 3-2e**). The incorporation of dynamic ionic crosslinks facilitates reversible bond exchange and enhanced energy dissipation during deformation, enhancing the hydrogel's mechanical integrity and preserving cohesive strength even after swelling[36]. In contrast, hydrogels lacking ionic crosslinking became compromised upon swelling, leading to rapid mechanical failure (**Fig. 3-2f**). This cohesive resilience is critical for maintaining reliable wet-tissue adhesion, as interfacial bonding can exceed the internal strength of swollen hydrogels. ElHyX incorporating ionically crosslinked i-Gel maintains robust adhesion across multiple tissue types after swelling, whereas versions lacking ionic reinforcement delaminate or disintegrate quickly (**Fig. 3-2g,h**). In addition, ElHyX-based bioelectronics can be detached from tissue on demand by applying a high concentration urea solution, which weakens the hydrogen bonds between i-Gel and tissue. This reversible adhesion mechanism provides a safe pathway for device retrieval. Owing to its high formulation flexibility, the ElHyX platform could also be extended toward biodegradable or bioresorbable designs using

bioresorbable polymer, degradable hydrogels and transient metals, enabling temporary, enabling temporary implantation scenarios with controlled functional lifetimes[22,37-41].

EGaIn was selected as the conductive filler for the elastomer phase due to its liquid nature, which ensures electrical continuity under deformation. When embedded within a SBS elastomer matrix, EGaIn remains confined, preventing leakage while preserving the composite's low modulus and high stretchability (**Fig. 3-2i** and **Figs. B5–7**). Initially non-conductive due to oxide shells surrounding EGaIn particles, the composite becomes conductive through mechanical activation—such as compression or stretching—that ruptures the shells and forms conductive pathways. In practice, the minor deformation that occurs naturally during peeling of the printed device from the substrate is sufficient to rupture the oxide shells surrounding the embedded EGaIn particles, thereby forming continuous conductive pathways. SEM imaging after stretching confirms the formation of continuous conductive networks via particle coalescence (**Fig. 3-2j**). Electrical measurements reveal a sharp conductivity increase from insulating to ~4×10^3 S·m^{-1} after 10% strain stretching cycle, and up to ~1×10^5 S·m^{-1} after 500% strain stretching cycle (**Fig. B-8**). Benefiting from the fluidic reconfigurability of EGaIn (**Fig. 3-2k**), the EGaIn-SBS composite maintains stable conductivity with minimal resistance change (~15%) even under 900% strain, and shows negligible hysteresis during cyclic loading. In contrast, conventional conductive elastomers that rely on solid conductive fillers experience major conductivity loss upon mechanical deformation (**Fig. 3-2l,m**). Moreover, the EGaIn-SBS system exhibits excellent durability and reliability, with no substantial resistance drift after 1000 cycles of 200% stretching. (**Fig. 3-2n**).

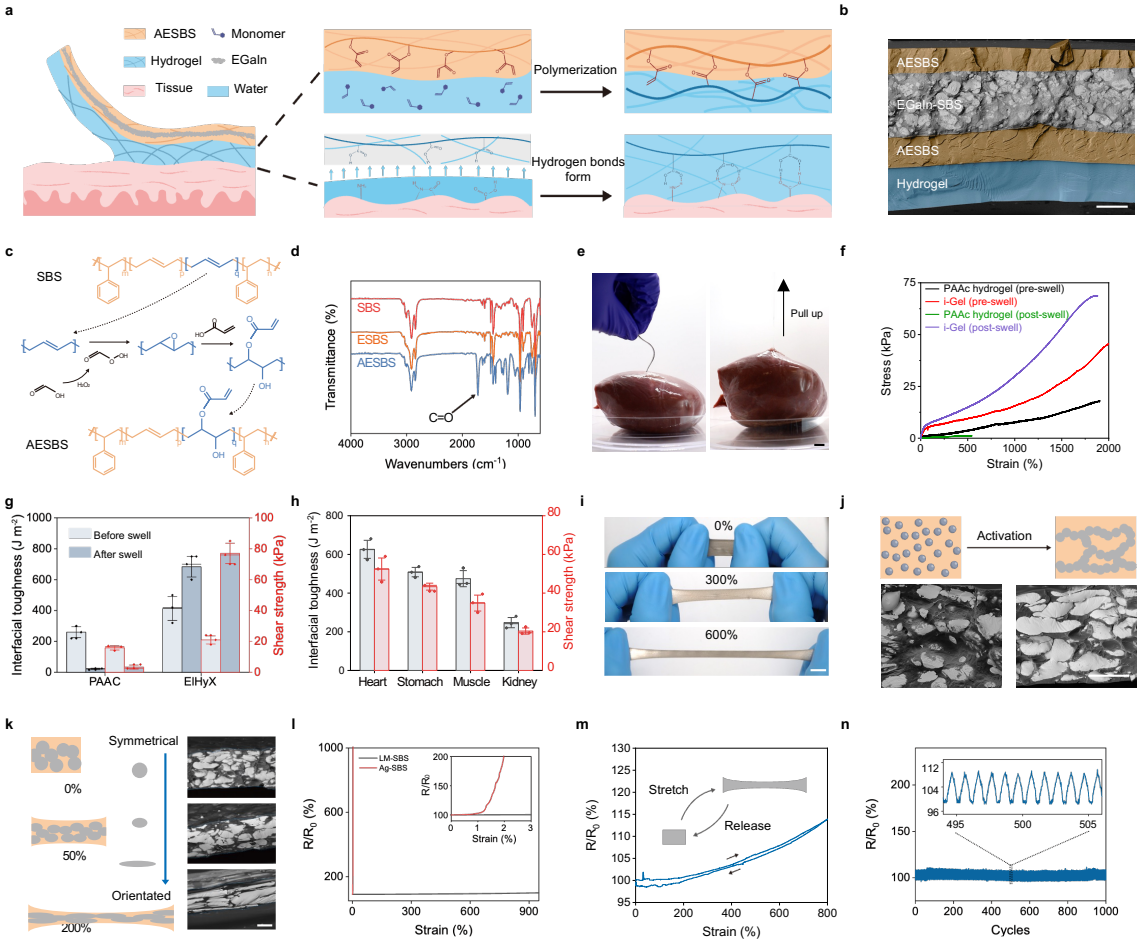

Fig. 3-2 Mechanical and electromechanical characterizations of ElHyX. a, Schematic of ElHyX formation via in situ hydrogel polymerization on a chemically modified elastomer. Water is removed from the hydrogel to form a dry adhesive layer (DAL) that rapidly absorbs interfacial moisture and forms hydrogen bonds with tissue. AESBS, acrylyl-opening epoxidized poly(styrene-butadiene-styrene). **b**, Cross-sectional scanning electron microscopy (SEM) image of ElHyX, showing seamless integration between elastomer, conductive filler and hydrogel. Scale bar, 100 μm. **c**, Synthesize process of AESBS through epoxidation and acrylation of poly(styrene-butadiene-styrene) (SBS). **d**, Fourier transform infrared spectroscopy (FTIR) spectra of SBS, epoxidized SBS (ESBS), and AESBS. **e**, Photograph of ElHyX conformally adhered to a porcine heart. Scale bar, 1 cm. **f**. Stress-Strain curves of hydrogels with and without ionic crosslinking. **g**, Comparison of adhesion performances of hydrogels with and without ionic crosslinks before and after swelling on

porcine skin. **h**, Tissue adhesion strength of the DAL on various biological tissues. **i**, Photographs of EGaIn-SBS under 0%, 300%, and 600% strain. Scale bar, 1 cm. **j**, Schematic and SEM images of EGaIn-SBS showing particle coalescence and activation of EGaIn-SBS after mechanical deformation. Scale bar, 50 μm. **k**, Schematic and cross-section SEM images of EGaIn-SBS under 0%, 50%, and 200% strain. Scale bar, 50 μm. **l**, Relative resistance changes (R/R_0) of EGaIn-SBS compared to silver-SBS composites under uniaxial strain. Inset, zoomed in to low-strain range. **m**, Relative resistance hysteresis of EGaIn-SBS over an 800% stretch-release cycle. **n**, Relative resistance changes of EGaIn-SBS over 1000 cycles at 200% strain.

3.3 Strain-insensitive bioelectrical and biomolecular sensors

Graphite was selected as the conductive filler for both bioelectrical and biomolecular sensing electrodes due to its excellent electrochemical stability. For the bioelectrical sensor, the bioadhesive hydrogel is directly polymerized onto the graphite-AESBS electrode, enabling a seamless tissue-device interface for stable signal acquisition. In contrast, biomolecular sensors feature hydrogel polymerized on AESBS substrate adjacent to the electrodes, preserving open diffusion paths for analytes and ensuring unobstructed molecular transport (**Fig. 3-3a**).

To enable enzymatic biomolecular sensing, Prussian blue (PB) is incorporated into the graphite-SBS composite to create graphite-PB-SBS electrodes capable of detecting hydrogen peroxide (H_2O_2)—a common byproduct in enzymatic reactions—at a low operation potential (0.0 V vs Ag/AgCl), thereby minimizing the interferences from other electroactive species. PB is uniformly blended into the ink formulation (**Fig. B-9**) and printed via DIW for reproducible electrode fabrication. Additional functional fillers such as polyaniline (PANI)—which exhibits high sensitivity and reversible electrochemical behavior—and carbon nanotubes (CNTs)—which provide superior electrical conductivity and strong electrocatalytic activity toward uric—were integrated to achieve high-performance pH and uric acid sensing, respectively. These functionalities were further validated in vivo (**Figs. B10** and **11**).

Cross-sectional SEM imaging of the printed electrode confirms the uniform dispersion of fillers within the elastomer phase and their cohesive integration with the bioadhesive hydrogel (**Fig. 3-3b**). The DIW process enables precise spatial patterning of all functional composites (**Fig. 3-3c** and **Figs. B12** and **13**), and the graphite-PB-SBS electrode exhibits a roughened surface morphology that enhances electrochemical sensitivity (**Fig. B-14**).

Owing to the seamless tissue–hydrogel interface, the ElHyX-based bioelectrical sensor exhibits substantially lower impedance compared to dry electrodes and performs on par with commercial gel electrodes (3M Red Dot™) of the same size (**Fig. 3-3d**). Robust wet-tissue adhesion and strain-insensitive signal acquisition are demonstrated in ECG and electromyography (EMG) recordings, which remains stable under 100% tensile strain (**Fig. 3-3e**,**f** and **Fig. B-15**). In contrast, electrodes based solely on conventional solid conductive fillers often suffer from cracking or conductivity loss under large deformation (**Fig. B-16**). We further demonstrated the advantages of ElHyX's bioadhesive and stretchable properties by mounting an ElHyX-based LED array onto an isolated porcine heart (**Fig. 3-3g**). The device functioned reliably with no signs of delamination during artificial heartbeats, indicating that ElHyX can maintain stable performance on dynamically moving organs.

Electrochemical characterization using the Fe^{3+}/Fe^{2+} redox system demonstrated excellent reproducibility **(Fig. 3-3h**,**i** and **Fig. B-17**) and stable performance under 100% strain, (**Fig. 3-3j** and **Fig. B-18**), underscoring the strain-insensitive nature of the ElHyX electrochemical sensors. Sensor sensitivity to H_2O_2 was tunable by adjusting PB concentration in the graphite-PB-SBS electrode (**Fig. 3-3k**). A glucose-sensing electrode was fabricated by printing an enzyme layer—comprising glucose oxidase and bovine serum albumin—followed by a polyurethane diffusion-limiting layer onto the graphite–PB–SBS electrode (**Fig. 3-3l**), achieving high sensitivity, linearity, selectivity, and stability at physiologically relevant glucose concentrations (**Fig. 3-3m** and **Fig. B-19**). Additionally, the sensor maintains consistent performance under mechanical deformation, confirming its strain-insensitive properties (**Fig. 3-3n** and **Fig. B-20**).

Finally, in vitro biocompatibility was confirmed using live/dead staining and PrestoBlue metabolic assays with human dermal fibroblasts (HDF) (**Fig. 3-3o**,**p**). High cell viability and metabolic activity over seven days validate the cytocompatibility of ElHyX for in vivo applications.

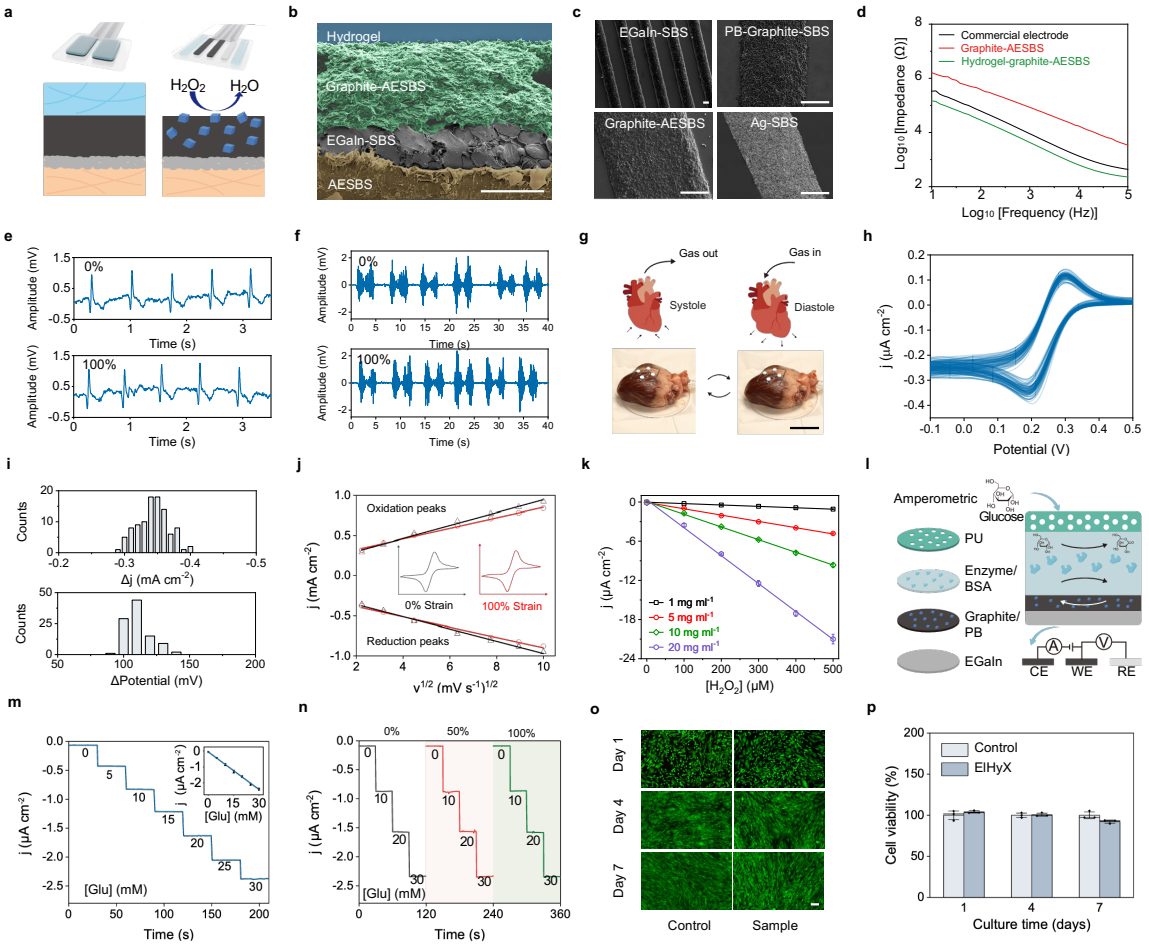

Fig. 3-3 Characterization of strain-insensitive ElHyX physical and chemical sensors. a, Schematic of ElHyX biophysical and biochemical sensors. **b**, Cross-sectional SEM image of ElHyX electrocardiogram (ECG) electrode structure. Scale bar, 100 μm. **c**, SEM image of printed elastomer composites used in sensor fabrication. Scale bars, 100 μm. **d**, Skin-electrode impedance comparison of graphite-AESBS electrodes with and without hydrogel, and commercial gel electrodes. **e**,**f**, ElHyX bioelectrical sensor under 0% and 100% strain for ECG (**e**) and electromyogram (EMG) (**f**) recording on human participants. **g**, In vitro

demonstration of ElHyX-based light-emitting diode (LED) array functioning on a beating porcine heart. Scale bar, 5 cm. **h**,**i**, Cyclic voltammograms (CVs) of 100 graphite-PB-SBS electrodes in 5 mM $K_3Fe(CN)_6$ (**h**) and statistic distribution of reduction peak current density and redox peak potential difference (**i**). **j**, Current peak densities of CVs of graphite-PB-SBS electrodes in 5 mM $K_3Fe(CN)_6$. under 0% (black) and 100% (red) strain, plotted against the square root of scan rates ($v^{1/2}$). **k**, Amperometric calibration of graphite-PB- electrodes with varying PB loadings in for H_2O_2 detection. Error bars represent the SD of the mean (n=3). **l**, Schematic of enzymatic glucose sensor immobilized on graphite-PB-SBS electrodes and overlaid with a polyurethane diffusion-limiting layer. **m**, Amperometric calibration of ElHyX-based glucose sensors. **n**, Strain-insensitive glucose detection under 0%, 50%, and 100% strain. **o**, Representative live(green)/dead (red) images of HDFs seeded

3.4 In vivo evaluation of ElHyX for physicochemical sensing and neural stimulation

We evaluated the ElHyX platform in vivo to demonstrate its multifunctional capabilities, including electrophysiological monitoring, biochemical sensing, and neural stimulation (**Fig. B-21**). For electrophysiological monitoring, ElHyX electrodes were placed directly onto the surface of a rat heart to acquire ECG signals. The ionically conductive hydrogel enabled immediate and robust adhesion to the beating myocardium, forming a conformal, low-impedance interface between the conductive graphite and wet tissue (**Fig. 3-4a**). This seamless integration facilitated efficient transmission of biopotentials, yielding high-fidelity ECG recordings (**Fig. 3-4b**). Importantly, the signal quality remained stable after 24 hours of implantation (**Fig. 3-4c**), highlighting the hydrogel's strong and durable adhesion in dynamic physiological environments.

To demonstrate the platform's real-time chemical sensing capability, glucose was selected as a representative biomarker. The ElHyX sensor was implanted onto the rib cage of a rat, targeting interstitial fluid (ISF) diffusion from surrounding tissues to simulate deep organ biochemical monitoring sites such as the liver, kidney, or gastrointestinal tract (**Fig. 3-4d** and **Fig. B-22**). Following retro-orbital (RO) injection of glucose (0.36 $g \cdot kg^{-1}$), the sensor detected a rapid and quantifiable increase in glucose levels, followed by a gradual decline to

baseline as glucose was metabolized (**Fig. 3-4e**). A repeated measurement 24 hours post-implantation produced a comparable response, confirming the device's stability and functional longevity in vivo (**Fig. 3-4f**). To further evaluate the in vivo stability and dynamic performance of physiological signal monitoring, we conducted continuous recordings for 6 hours (**Fig. B-23**) and multiple glucose elevation and clearance cycles (**Fig. B-24**). The results confirm the excellent stability, responsiveness, and signal fidelity of ElHyX-based sensors during prolonged physiological monitoring in vivo.

To improve long-term stability, we incorporated an additional polyurethane encapsulation layer printed around the original ElHyX structure (**Fig. B-25a–c**). Devices were implanted in rats and evaluated on Day 14 post-implantation through glucose sensing, ECG recording, and sciatic nerve stimulation. Clear signal recordings and consistent stimulation efficiency were observed (**Fig. B-25d–e**), demonstrating that the elastomer–hydrogel integration preserved strong tissue adhesion, electrical continuity, and mechanical integrity over time. These results establish the long-term robustness and biofunctional reliability of the ElHyX platform under physiologically dynamic conditions.

To assess ElHyX for bioelectronic therapy, we employed it as a neural stimulation interface. A soft, flexible ElHyX electrode strip was wrapped around the rat sciatic nerve without sutures to form a conformal, suture-free nerve cuff (**Fig. 3-4g** and **Fig. B-21**). the sciatic nerve was successfully activated, eliciting observable hindlimb movements. We quantified the stimulation-response relationship by delivering graded current amplitudes through the ElHyX nerve cuff. The degree of leg flexion increased with stimulation intensity, ultimately reaching a saturation point at higher currents (**Fig. 3-4h,i**), demonstrating effective and tunable neural modulation.

Finally, in vivo systemic biocompatibility of ElHyX was assessed through histological analysis. Hematoxylin and eosin (H&E) staining of the surrounding tissues and major organs—including the heart, liver, spleen, lungs, and kidneys—revealed no observable pathological abnormalities or inflammation (**Fig. 3-4j,k** and **Fig. B-26a,b**). In addition, immunofluorescence staining and quantitative analysis of subcutaneously implanted ElHyX

samples showed minimal presence of leukocytes (CD3, green) and macrophages (CD68, red) at 28 days post-implantation (**Fig. 3-4l** and **Fig. B-26c**), confirming the biosafety and long-term biocompatibility of ElHyX for chronic implantable applications.

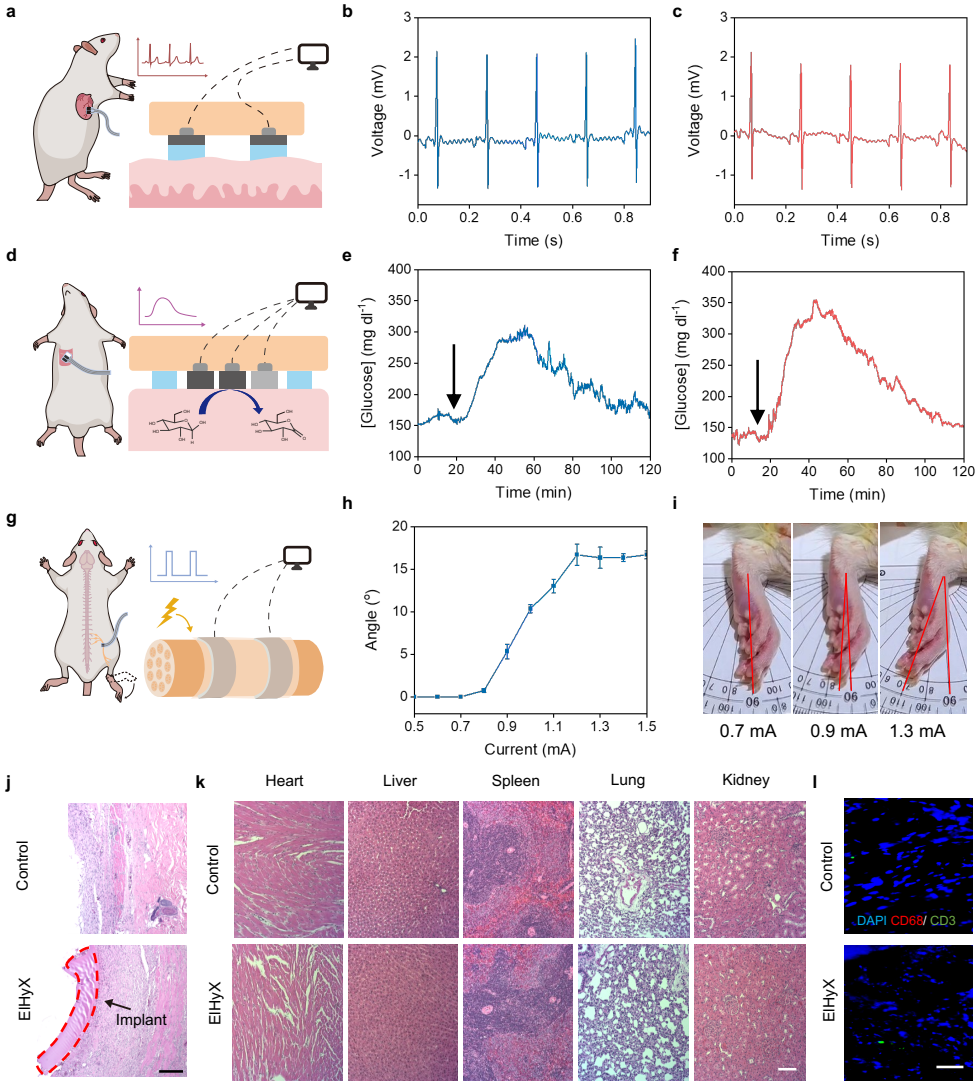

Fig. 3-4 In vivo characterization of ElHyX-based implantable electronics. a, Schematic illustrating the implantation of ElHyX-based ECG sensor on the surface of a rat heart. **b**,**c**, Representative ECG waveforms recorded at 0 hours and 24 hours post-implantation. **d**, Schematic of an ElHyX glucose sensor implanted on the outer surface of the rib cage of a rat to detect interstitial glucose. **e**,**f**, Real-time glucose monitoring using ElHyX electrode

immediately after implantation (**e**) and 24 hours post-implantation (**f**). A glucose dose (0.36 g kg^{-1}) was administered via retro-orbital injection at the time indicated by the arrow. **g**, Schematic of ElHyX electrode wrapping around the sciatic nerve for electrical stimulation and motor response. **h**, Quantitative analysis of leg flexion angles in response to different electrical stimulation currents, showing a dose-dependent motor response. **i**, Photographs of rat hindlimb flexion under stimulation currents of 0.7 mA, 0.9 mA, and 1.3 mA respectively. **j**,**k**, Histological evaluation of surrounding tissues (**j**) and main organs (**k**) via H&E staining after 28 days of implantation. Scale bars, 100 μm. **l**, Immunofluorescence staining of inflammatory markers in tissue surrounding the implant at days 28. Green, red and blue represent lymphocyte (CD3), macrophages (CD68) and cell nuclei, respectively. Scale bar, 50 μm.

3.5 Closed-loop blood glucose regulation in diabetic rat

To demonstrate the therapeutic potential of ElHyX, we established a closed-loop system for diabetes management integrating real-time sensing and neuromodulation (**Fig. 3-5a**). Following food intake, both heart rate and blood glucose levels increase. These physiological changes are concurrently monitored by implanted ElHyX sensors—an electrochemical glucose sensor and an ECG sensor. Once elevated glucose and heart rate levels are detected, targeted vagus nerve stimulation (VNS) is triggered to promote insulin secretion and facilitate glucose clearance[42].

To validate this concept, we fabricated a multifunctional implantable device based on ElHyX that supports simultaneous ECG recording, glucose monitoring, and VNS (**Fig. 3-5b**). The device was surgically implanted into diabetic rats, with individual modules positioned for optimal function: the ECG electrode on the heart, the glucose sensor on the rib cage, and the nerve cuff around the vagus nerve (**Fig. 3-5c** and **Fig. B-21**). This system can also be configured into a compact and wireless format for long-term, multimodal physiological monitoring and closed-loop regulation (**Figs. B27–29**).

Hyperglycemia was induced via intraperitoneal (IP) glucose injection (2 $g \cdot kg^{-1}$), which led to concurrent elevations in heart rate and blood glucose levels, peaking ~30 minutes post-injection (~550 $mg \cdot dl^{-1}$). A control injection of saline elicited no significant physiological changes (**Fig. B-30**), confirming the specificity of the glucose-induced response. In untreated diabetic rats, glucose levels remained elevated for an extended period (**Fig. 3-5d**). We subsequently applied bilateral VNS in response to the elevated glucose and heart rate, as defined by our dual-parameter closed-loop logic (**Fig. B-31**). However, despite stimulation (5 Hz, 3 mA, 0.5 ms pulse width), blood glucose levels remained elevated for an extended period (**Fig. 3-5e**). This inefficacy is likely due to the simultaneous activation of afferent and efferent vagal fibers, as afferent VNS has been shown to stimulate hepatic glucose release and suppress insulin secretion [43]. The stimulation parameters used in our study were selected based on previous reports of effective vagus nerve stimulation for metabolic modulation in rodent models[44]. To further evaluate their physiological effects, we performed in vivo optimization experiments in healthy rats while monitoring heart rate under different stimulation conditions. Heart rate decreased progressively with increasing stimulation current and reached a plateau once the current exceeded the effective threshold (**Fig. B-32a**). Within the low-frequency range (1–5 Hz), stimulation produced comparable effects on heart rate (**Fig. B-32b**). To circumvent this limitation, we implemented selective efferent VNS (eVNS) for targeted stimulation. This strategy minimizes off-target activation of afferent fibers and associated side effects, enabling more specific modulation of metabolic pathways. Following detection of elevated physiological markers, eVNS was applied using the same stimulation parameters. In contrast to bilateral VNS, eVNS significantly attenuated the glucose peak (~515 $mg \cdot dl^{-1}$) and accelerated glucose normalization, returning to baseline within 90 minutes (**Fig. 3-5f**). To further assess system-level reliability, multi-cycle closed-loop glucose regulation experiments were conducted over three consecutive days and up to one month in vivo (**Fig. B-33**). Consistent feedback-triggered glucose regulation and repeatable performance across sessions confirmed the stability and reproducibility of the ElHyX-based closed-loop system during extended operation. These results demonstrate sustained closed-loop neuromodulation and support the potential of ElHyX-enabled

automatic, responsive regulation of metabolic disorders under long-term physiological conditions.

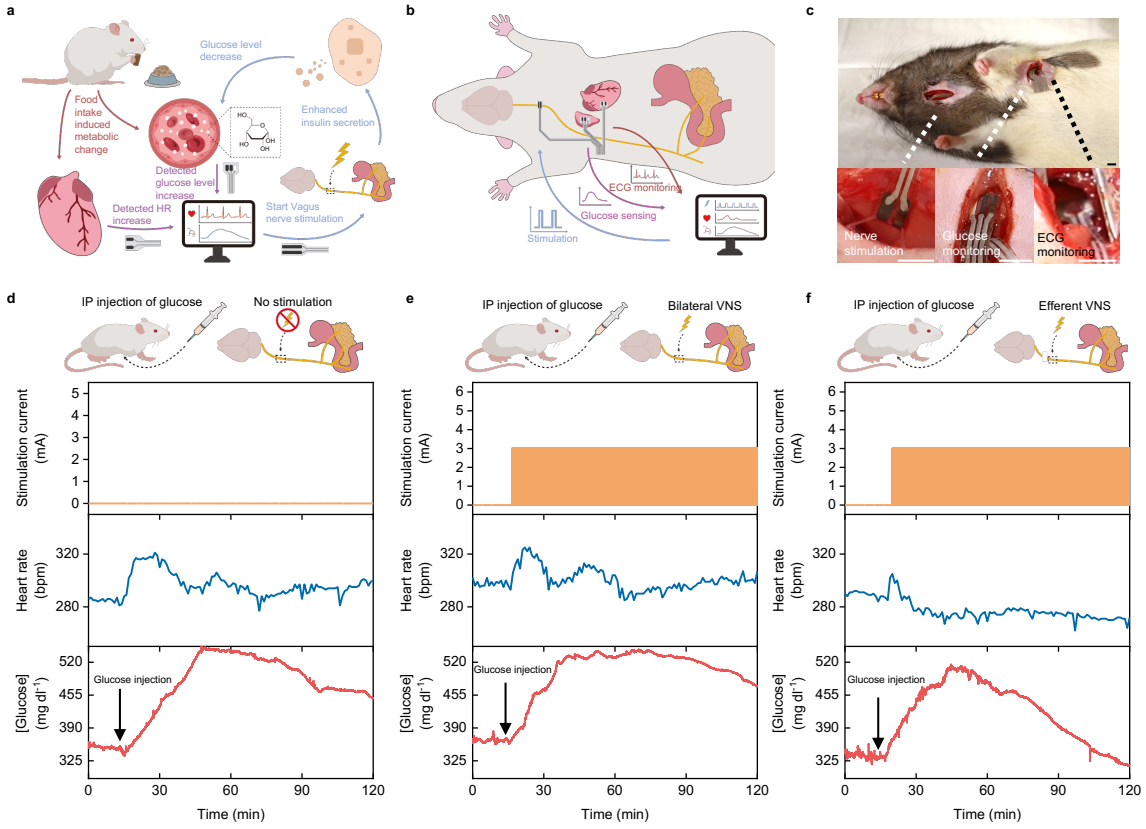

Fig. 3-5 In vivo evaluation of ElHyX-based closed-loop blood glucose regulation in diabetic rats. a, Schematic of the closed-loop blood glucose management concept: food intake triggers increases in blood glucose and heart rate, which are sensed in real-time and used to initiate vagus nerve stimulation (VNS) for insulin modulation. **b**,**c**, Schematic (**b**) and photograph (**c**) of the multifunctional ElHyX device implanted in a diabetic rat, showing the ECG sensor attached to the heart, the glucose sensor on the outer rib surface, and nerve cuff wrapped around the vagus nerve. Scale bars, 5 mm. **d,** In vivo monitoring of blood glucose levels and heart rate following intraperitoneal (IP) glucose injection without VNS. **e**, In vivo evaluation of blood glucose levels and heart rate following IP glucose injection with bilateral VNS. **f**, In vivo demonstration of closed-loop blood glucose management after IP glucose injection with selective efferent VNS (eVNS).

3.6 Conclusions

We present ElHyX, a stretchable, strain-insensitive, and wet tissue–adhesive elastomer–hydrogel biphasic platform that enables stable, multimodal sensing and stimulation for implantable bioelectronic applications. By molecularly integrating a conductive elastomer with a bioadhesive hydrogel, ElHyX forms a robust and seamless interface with dynamic, soft tissues while maintaining mechanical compliance and electrical continuity under deformation. Unlike previous adhesive or flexible electronic systems limited to single functionalities, ElHyX integrates real-time electrophysiological monitoring, biochemical sensing, and neuromodulation within a unified, customizable architecture compatible with direct ink writing (DIW) fabrication. In vivo demonstrations—including ECG recording, glucose monitoring, and targeted neural stimulation—highlight ElHyX's functional versatility, durability, and repeatability. As a proof of concept, we implemented a closed-loop system for diabetic management by coupling physiological sensing with responsive vagus nerve stimulation.

With its modular and tunable design, ElHyX can be readily adapted for a broad spectrum of biomarkers and therapeutic targets, enabling next-generation bioelectronic interfaces that combine multimodal sensing, adaptive actuation, and autonomous feedback control. ElHyX uniquely enables the stable co-integration of chemical biosensing, electrophysiological recording, and neuromodulation within a single soft, bioadhesive, and fully printed platform. This materials–systems strategy allows device functionality to be reconfigured through formulation-level tuning, rather than redesign of electrode geometries or multilayer assembly. As a result, ElHyX supports rapid adaptation across diverse sensing and therapeutic modalities while maintaining mechanical compliance, electrochemical stability, and scalable manufacturing—positioning it as a platform-level solution rather than a single application-specific sensor. Altogether, ElHyX represents a unified, scalable solution for continuous physiological monitoring and autonomous therapeutic intervention, bridging the gap between soft bioelectronics and translational medicine.

3.7 Methods

Materials and reagents

Poly(styrene-butadiene-styrene) (SBS), polyaniline (PANI), acrylic acid, hydroquinone, sodium 4-vinylbenzenesulfonate, [2-(Acryloyloxy)ethyl]trimethylammonium chloride solution (80 wt%), poly(ethylene glycol) diacrylate-575 (PEGDA-575), sodium chloride (NaCl), hydrogen peroxide (H2O2) [30% (w/v)], potassium ferricyanide (III) (K3Fe(CN)6), uric acid, bovine serum albumin (BSA), glucose oxidase, glutaraldehyde (50 wt%) and polyurethane (PU) were purchased from Sigma-Aldrich. Silver flake, graphite flake, EGaIn, poly(ethylene glycol)-600 (PEG-600, iron (III) chloride (FeCl3), tetrahydrofuran (THF), and L-lactic acid were purchased from Thermo Fisher Scientific. Toluene, methanol, ascorbic acid, dextrose (D-glucose), phosphate-buffered saline (PBS) solution and potassium chloride were purchased from Fisher Scientific. Prussian blue, formic acid and Butvar B-98 were purchased from Acros Organics. Multiwalled CNTs was purchased from Beijing Boyu Co. 2-oxoglutaric acid was purchased from Tokyo Chemical Industry. Polydimethylsiloxane (PDMS) (SYLGARD 184) was purchased from Dow Corning. Poly(vinyl alcohol) (PVA) (MW 125000, 88% hydrolyzed) was purchased from Polysciences Inc.

Preparation of customizable inks

SBS ink (25 wt%) was prepared by dissolving SBS in toluene under magnetic stirring. To formulate graphite-SBS, graphite-PANI-SBS, CNTs-SBS, Ag-SBS and EGaIn-SBS, a specified amount of the respective fillers was homogeneously mixed into the SBS ink using a planetary centrifugal mixer (THINKY, AR-100) for 5 minutes. To develop graphite-PB-SBS ink for the preparation of working and counter electrode for chemical sensors, PB powder was dispersed in toluene by probe sonication, followed by dissolving SBS (25 wt%) into the suspension. The resulted PB-SBS ink was then mixed with graphite through planetary centrifugal mixer for 5 min (**Fig. B-7**).

To synthesis AESBS, SBS was first epoxidized according to the method in the literature[45]. Briefly, 5 g SBS, 560 µl formic acid and 50 µl PEG-600 were dissolved in 50 ml toluene

with magnetic stir under 60 ºC. Then 1.5 ml H_2O_2 was dropped into the solution. The reaction was conducted at 60 ºC for 2 h, followed by precipitating and washing with methanol. The solid was dried under nitrogen flow overnight to give ESBS. To introduce vinyl side chains, ESBS was then acrylated according to the method in literature[46]. Briefly, 3.5 g ESBS, 19 ml acrylic acid and 17 mg hydroquinone was dissolved in 35 ml toluene with magnetic stir. The reaction was conducted at 60 ºC for 24 h, followed by precipitating and washing with methanol. The product was dried under nitrogen flow overnight to give AESBS.

AESBS ink (25 wt%) was prepared by dissolving AESBS in toluene by magnetic stirring. To formulate graphite-AESBS, 20 wt% graphite was homogeneously mixed into AESBS ink using planetary centrifugal mixer. To prepare glucose oxidase enzyme cocktail ink, glucose oxidase (0.1 mg ml^{-1}) and BSA (0.1 g ml^{-1}) were dissolved in PBS. To further stabilize the enzyme, the resulting solution was mixed with glutaraldehyde solution (1 wt%) at a volume ratio of 20:1. To prepare the diffusion-limiting membrane ink, PU (50 mg ml^{-1}) was dissolved in THF by magnetic stir. To prepare the ink for reference membrane that stabilize the reference electrode, Butvar (78 mg ml^{-1}) and NaCl (50 mg ml^{-1}) were dissolved in methanol followed by vigorous agitation in an ultrasonic bath for 30 min. To prepare the adhesive hydrogel ink, 1.5 ml acrylic acid, 0.3 ml [2-(Acryloyloxy)ethyl]trimethylammonium chloride solution (80 wt%), 250 mg sodium 4-vinylbenzenesulfonate, 0.2 ml PEGDA-575 solution (1.25 wt%) and 0.6 ml 2-oxogluaric acid solution (3.6 wt%) were mixed with 2.15 ml PVA solution (10 wt%) using magnetic stir in dark environment.

Fabrication of ElHyX-based bioelectronics

The ElHyX-based bioelectronics were fabricated through an all-printed process on PDMS coated glass slide (**Fig. B-2**). This involved the serial printing of multiple layers, including substrate (SBS/AESBS), interconnects (EGaIn-SBS), electrical sensing/stimulation electrodes (graphite-AESBS), electrochemical working/counter electrodes (graphite-PB-SBS, graphite-PANI-SBS or CNTs-SBS), reference electrodes (Ag-SBS), encapsulation

(SBS) and adhesive hydrogel using a three-axis robotic deposition stage (Aerotech). The printing paths were defined by G-code. The customized inks were loaded into 15 ml syringe barrels equipped with tapered tips ranging from 150 μm to 250 μm in diameter. The extrusion of ink was controlled by applying high pressure air through a benchtop fluid dispenser (EFD Nordson). The patch was then exposed to 360 nm UV light under nitrogen protection for 15 minutes to polymerize the hydrogel, followed by overnight drying under nitrogen flow to remove residual water from the hydrogel.

To prepare the glucose sensor, glucose oxidase enzyme cocktail was printed on the electrochemical working electrode (graphite-PB-SBS) and air-dried overnight under 4 ºC. PU diffusion-limiting layer was printed subsequently on the resulting electrode. To further stabilize the reference electrode, the Ag–SBS electrode was treated with 0.1 M $FeCl_3$ solution to form a surface AgCl layer. A reference membrane cocktail was then printed onto the electrode and air-dried overnight at room temperature (22 °C).

Rheology characterization

Rheological characterizations of the customized inks were conducted using a rheometer (Anton Paar, MCR 302) equipped with a parallel-plate measuring system with a 25 mm diameter. The tests were conducted with a 1 mm gap size.

Morphology characterization

The surface and cross-section structures of the printed ElHyX platform were studied by optical microscopy (ZEISS) and scanning electron microscopy (SEM; ZEISS 1550VP Field Emission SEM). Prior to SEM imaging, a ~10 nm layer of platinum was sputtered onto the sample surface. SEM imaging was performed at an acceleration voltage of 15 kV.

Mechanical characterization

Testing samples were printed into a rectangular shape with length/width of 20mm/5mm. Tensile and loading-unloading tests were performed using a motorized force tester (Mark-

10) at a deformation rate of 10 mm min^{-1} in air at room temperature. Cyclic stretching tests for fatigue were performed at a deformation rate of 100 mm min^{-1}.

For adhesion tests, all porcine tissues were purchased from local markets and were recovered to room temperature (22 °C) before use. The tissues and adhesive platforms were fixed to a PET substrate using medical tape before testing. Adhesive platforms were adhered to the tissue surface by gently pressing of ~5 kPa for 1 min.

The interfacial toughness was tested by 180° peel test (ATSM F2256) using a motorized force tester (Mark-10) at a deformation rate of 50 mm min^{-1}. The shear strength was tested by lap-shear test (ATSM F2255) with a mechanical test machine (Mark-10) at a deformation rate of 50 mm min^{-1}.

On body biopotential signals recording

ElHyX-based electrical sensing electrodes were used to record electrophysiological signals. For electrocardiogram (ECG) and electromyography (EMG) monitoring, the skin at the electrode placement site was pre-wetted with saline. For ECG monitoring, electrodes were positioned on the right and left arms (**Fig. B-15**), and the device was mechanically fixed to maintain the prescribed tensile strain during recording. For EMG monitoring, electrodes were placed at both ends of the biceps brachii muscle. Electrophysiological signals were captured using a PowerLab data acquisition system (ADInstruments) and processed through a 50 Hz low-pass filter in LabChart software. For impedance measurement, the ElHyX electrodes were attached to human forearm in a two-electrode configuration with a frequency range of 10 Hz–100 kHz under ambient conditions. Measurements were performed using an electrochemical workstation (CH Instruments).

Electrochemical characterization of biochemical sensors.

In vitro electrochemical analyses were conducted using CHI840D and CHI760 (CH Instruments) electrochemical workstations under ambient temperature. CV was used to assess the performance of the graphite-PB-SBS electrodes. For in vitro H_2O_2 and glucose

sensing characterization, amperometric measurements were conducted at a potential of 0 V in PBS (pH 7.4).

Electronic system design and characterization

An electronic system was integrated into a two-layer flexible PCB, crafted using Eagle CAD. The system's energy was harnessed from a 3.7V lithium battery. Power management within the system was administered through a voltage regulator (catalogue no. ADP162; Analog Devices), ensuring consistent and stable power output. ECG measurement is achieved by a heart rate monitor front end (catalogue no. AD8232; Analog Devices). Wireless communication and control processes were managed by an adept radio frequency module (catalogue no. nRF52832; Nordic), responsible for wireless data transmission, signal processing and overseeing the electrochemical instrumentation system, which operated principally through the AD5940 (Analog Devices). The electronic system supports continuous operation with an average power consumption of 0.52 mW during BLE communication and 67 mW during full operation, including sensing, electrical stimulation, and wireless data transmission via Bluetooth Low Energy (**Fig. B-28**). Power consumption was measured using a power profiler (catalogue no. PPK2; Nordic Semiconductor). The electronic components, including the circuit board and battery, were fully encapsulated with PDMS to prevent direct contact between tissues and electronic materials and to ensure electrical insulation and biocompatibility during implantation.

In vitro biocompatibility

Human dermal fibroblasts (HDFs) and the complete HDF cell culture media were acquired from ATCC. The incubator for cell culture was set at 37 °C and 5% CO_2. The tested samples were ~3 mm×3 mm in dimension, and were disinfected by washing with 70% ethanol and exposing them to ultraviolet light for 30 min. HDFs were first rejuvenated in a T25 flask before seeding to the 24-well microplate. 5×10^4 cells were seeded in each well on Day 0. 0.6 ml of cell culture media was added to each well, with a 0.1 ml addition to the transwell (Corning Costar). The sterilized samples were placed into the transwells.

The cell viability was tested on Day 1, 4 and 7. PrestoBlue (Thermo Fisher Scientific) mixed with the culture media (10%:90%, v/v) was added to each well at a volume of 0.3 ml after the removal of the transwells. After 45 min of co-culture with HDF cells in the incubator, 0.1 ml of the solution was transferred to a 96-well microplate for plate reading (540 nm excitation/590 nm emission, BioTek Instruments).

On Day 7, after the PrestoBlue cell viability test, the live/dead cell imaging and viability tests were conducted using the LIVE/DEADTM Viability/Cytotoxicity Kit (Invitrogen). For cell staining, 0.5 μl ml^{-1} of calcein AM and 2 μl ml^{-1} of ethidium homodimer-1 in Dulbecco's phosphate-buffered saline (DPBS) were added to each well, followed by the incubation in the incubator for 45 min. Live cells were labeled green, while dead cells were labeled red. After washing the cells twice with DPBS, the stained cells were imaged using an Axio Observer inverted microscope (ZEISS). The green image was captured using the fluorescein isothiocyanate (FITC) filter, while the red image was captured using the Cyanine-3 (Cy3) filter. The images were overlaid by the software ImageJ.

In vivo evaluation of ElHyX-based bioelectronics

The animal studies in this work were performed in accordance with the protocol approved by Caltech Institutional Animal Care and Use Committee. Experiments were performed in 12-week-old male healthy rats (Sprague Dawley, Charles River Laboratories) and 12-week-old male diabetic rats (ZDF obese fa/fa, Charles River Laboratories).

To evaluate the performance of ElHyX-based ECG sensors, healthy rats were connected to a mechanical ventilator (RoVent, KentScientific) and were anaesthetized and administered analgesia using 1.5-2.5% (v/v) isoflurane, ketoprofen (5 mg kg^{-1}), Ethiqa XR (3.25 mg kg^{-1}) and bupivacaine (1 mg kg^{-1}), a 1-cm incision between the 3^{rd} and 4^{th} ribs was made to expose the thoracic cavity. Then the ElHyX-based ECG sensor was adhered to the heart surface. The incision was closed with 5-0 Prolene (for ribcage and muscles) and 4-0 Nylon (for skin) sutures. The animals were ventilated with 100% oxygen until autonomous breathing was regained. On day 0 and day 1 post-implantation, the animals were anaesthetized using 1.5–

2.5% (v/v) isoflurane. The output end of the implanted ElHyX-based ECG sensor was connected to PowerLab for signal recording.

To evaluate the performance of ElHyX-based glucose sensors, healthy rats were anaesthetized and administered analgesia using 1.5-2.5% (v/v) isoflurane, ketoprofen (5 mg kg^{-1}), Ethiqa XR (3.25 mg kg^{-1}) and bupivacaine (1 mg kg^{-1}), a 1-cm incision was made to expose the rib cage. Then the ElHyX-based glucose sensor was adhered to the outer surface of rib cage. The incision was closed with 5-0 Prolene (for muscles) and 4-0 Nylon (for skin) sutures. The output end of the implanted ElHyX-based ECG sensor was connected to CHI760 for signal recording. Retro-orbital glucose (0.36 g kg^{-1}) injection was performed during the test.

To evaluate the performance of ElHyX-based nerve cuff, healthy rats were anaesthetized and administered analgesia using 1.5–2.5% (v/v) isoflurane, ketoprofen (5 mg kg^{-1}), Ethiqa XR (3.25 mg kg^{-1}) and bupivacaine (1 mg kg^{-1}), a 2-cm incision was made to expose the sciatic nerve. Then the ElHyX-based nerve cuff was adhered and wrapped around the nerve. The input end of the nerve cuff was connected to PowerLab equipped with stimulus isolator to apply electrical stimulation.

To evaluate the performance of ElHyX-based closed-loop blood glucose regulation system, diabetic rats were anaesthetized and administered analgesia using 1.5–2.5% (v/v) isoflurane, ketoprofen (5 mg kg^{-1}), Ethiqa XR (3.25 mg kg^{-1}) and bupivacaine (1 mg kg^{-1}). ECG sensing electrode and glucose sensing electrode were secured by methods mentioned above. To secure the vagus nerve cuff, a 2-cm incision was made along the midline of the neck to expose the vagus nerve. Then, the nerve cuff was adhered and wrapped around the nerve. In the case of selective efferent vagus nerve stimulation, the nerve was sectioned proximal form the electrode. Unless otherwise specified, the input and output terminals of the system were connected to PowerLab (with stimulus isolator) and CHI760 for signal recording and vagus nerve stimulation.

In vivo biocompatibility

Implantation studies were performed in accordance with a modified intradermal induction protocol based on FDA guidelines and approved by the Institutional Animal Care and Use Committee at the California Institute of Technology. 12-week-old male healthy rats (Sprague Dawley, Charles River Laboratories) were anesthetized with 2.5% (v/v) isoflurane and administered analgesics, including Ethiqa XR (3.25 mg kg^{-1}), ketoprofen (5 mg kg^{-1}), and bupivacaine (1 mg kg^{-1}). A 1-cm incision was made on the dorsal skin of each animal to create a subcutaneous pocket, into which the test samples were implanted. After 28 days, animals were humanely euthanized, main organs and the surrounding tissues were collected. The specimens were then preserved in 4% paraformaldehyde at 4 °C overnight, followed by thorough washing with DPBS repeated five times and then incubated in 30% sucrose overnight (4 °C). Samples were mounted in optimal cutting temperature compound (Thermo Fisher Scientific) followed by flash freezing and cryosectioning (50-μm sections). The sections were embedded in paraffin, fixed on the microscope slides, and stained with H&E staining. To remove the paraffin, cryosections were immersed in xylene for two cycles with each cycle lasting 10 mins, followed by two rounds of 5-min hydration using 100% ethanol. The sections were then briefly immersed in 95% and 70% ethanol for 1 min each, followed by rinsing in DI water. Next, the sections were submerged in filtered Harris Hematoxylin for 10 s. The rack containing the sections was transferred to a beaker which was exchanging water to dilute the dye. The sections were submerged in eosin stain for approximately 30 s and then transferred to the beaker with fresh water for rinsing. Two cycles of 5-min 100% ethanol immersion were performed to dehydrate the sections. Additionally, two cycles of 5-min xylene immersion were conducted to clear the sections. Lastly, the sections were fixed using resin-based mounting medium. For immunohistochemistry test, sections were incubated with the primary antibody anti-CD3 [SP7] (ab16669), followed by a secondary Alexa Fluor® 488-conjugated goat anti-rabbit IgG H&L antibody. Macrophages were identified using anti-CD68 [FA-11] (25-0681-82) directly conjugated with PE-Cyanine7 (Invitrogen). Nuclei were counterstained with DAPI. Slides were mounted using ProLong™ Diamond Antifade Mountant (Invitrogen) and imaged with a ZEISS LSM 800 confocal laser scanning microscope.

Bibliography of Chapter 3

1 Al-Khatib, S. M. Cardiac Implantable Electronic Devices. *N. Engl. J. Med.* **390**, 442-454 (2024).

2 Krauss, J. K. *et al.* Technology of deep brain stimulation: current status and future directions. *Nat. Rev. Mater.* **17**, 75-87 (2021).

3 Carlson, M. L. Cochlear Implantation in Adults. *N. Engl. J. Med.* **382**, 1531-1542 (2020).

4 Barrese, J. C. *et al.* Failure mode analysis of silicon-based intracortical microelectrode arrays in non-human primates. *J. Neural Eng.* **10**, 066014 (2013).

5 Park, S. I. *et al.* Soft, stretchable, fully implantable miniaturized optoelectronic systems for wireless optogenetics. *Nat. Biotechnol.* **33**, 1280-1286 (2015).

6 Jin, P. *et al.* A flexible, stretchable system for simultaneous acoustic energy transfer and communication. *Sci. Adv.* **7**, eabg2507 (2021).

7 Choi, S. *et al.* Highly conductive, stretchable and biocompatible Ag–Au core–sheath nanowire composite for wearable and implantable bioelectronics. *Nat. Nanotechnol.* **13**, 1048-1056 (2018).

8 Zhong, D. *et al.* High-speed and large-scale intrinsically stretchable integrated circuits. *Nature* **627**, 313-320 (2024).

9 Liu, Y. *et al.* Soft and elastic hydrogel-based microelectronics for localized low-voltage neuromodulation. *Nat. Biomed. Eng.* **3**, 58-68 (2019).

10 Tringides, C. M. *et al.* Viscoelastic surface electrode arrays to interface with viscoelastic tissues. *Nat. Nanotechnol.* **16**, 1019-1029 (2021).

11 Zhou, T. *et al.* 3D printable high-performance conducting polymer hydrogel for all-hydrogel bioelectronic interfaces. *Nat. Mater.* **22**, 895-902 (2023).

12 Sempionatto, J. R. *et al.* An epidermal patch for the simultaneous monitoring of haemodynamic and metabolic biomarkers. *Nat. Biomed. Eng.* **5**, 737-748 (2021).

13 Zhou, W. *et al.* Gas-Permeable, Ultrathin, Stretchable Epidermal Electronics with Porous Electrodes. *ACS Nano* **14**, 5798-5805 (2020).

14 Stoyanov, H., Kollosche, M., Risse, S., Waché, R. & Kofod, G. Soft Conductive

Elastomer Materials for Stretchable Electronics and Voltage Controlled Artificial Muscles. *Adv. Mater.* **25**, 578-583 (2013).

15 Wei, H. *et al.* Orthogonal photochemistry-assisted printing of 3D tough and stretchable conductive hydrogels. *Nat. Commun.* **12**, 2082 (2021).

16 Naficy, S., Oveissi, F., Patrick, B., Schindeler, A. & Dehghani, F. Printed, Flexible pH Sensor Hydrogels for Wet Environments. *Adv. Mater. Technol.* **3**, 1800137 (2018).

17 Pan, L. *et al.* An ultra-sensitive resistive pressure sensor based on hollow-sphere microstructure induced elasticity in conducting polymer film. *Nat. Commun.* **5**, 3002 (2014).

18 Shin, Y. *et al.* Low-impedance tissue-device interface using homogeneously conductive hydrogels chemically bonded to stretchable bioelectronics. *Sci. Adv.* **10**, eadi7724 (2024).

19 Lim, C. *et al.* Highly Conductive and Stretchable Hydrogel Nanocomposite Using Whiskered Gold Nanosheets for Soft Bioelectronics. *Adv. Mater.* **36**, 2407931 (2024).

20 Li, N. *et al.* Bioadhesive polymer semiconductors and transistors for intimate biointerfaces. *Science* **381**, 686-693 (2023).

21 Li, J. *et al.* Tough adhesives for diverse wet surfaces. *Science* **357**, 378-381 (2017).

22 Yang, Q. *et al.* Photocurable bioresorbable adhesives as functional interfaces between flexible bioelectronic devices and soft biological tissues. *Nat. Mater.* **20**, 1559-1570 (2021).

23 Sempionatto, J. R., Lasalde-Ramírez, J. A., Mahato, K., Wang, J. & Gao, W. Wearable chemical sensors for biomarker discovery in the omics era. *Nat. Rev. Chem.* **6**, 899-915 (2022).

24 Yang, Y. & Gao, W. Wearable and flexible electronics for continuous molecular monitoring. *Chem. Soc. Rev.* **48**, 1465-1491 (2019).

25 Ronkainen, N. J., Halsall, H. B. & Heineman, W. R. Electrochemical biosensors. *Chem. Soc. Rev.* **39**, 1747-1763 (2010).

26 Martin, W. R. W., Wieler, M. & Gee, M. Midbrain iron content in early Parkinson disease. *Neurology* **70**, 1411-1417 (2008).

27 Serkova, N., Klawitter, J. & Niemann, C. U. Organ-specific response to inhibition of mitochondrial metabolism by cyclosporine in the rat. *Transpl. Int.* **16**, 748-755 (2003).

28 Sunwoo, S.-H. *et al.* Ventricular tachyarrhythmia treatment and prevention by subthreshold stimulation with stretchable epicardial multichannel electrode array. *Sci. Adv.* **9**, eadf6856 (2023).

29 Xu, Y. *et al.* Phase-separated porous nanocomposite with ultralow percolation threshold for wireless bioelectronics. *Nat. Nanotechnol.* **19**, 1158-1167 (2024).

30 Li, R. *et al.* A flexible and physically transient electrochemical sensor for real-time wireless nitric oxide monitoring. *Nat. Commun.* **11**, 3207 (2020).

31 Zhao, Y. *et al.* Soft strain-insensitive bioelectronics featuring brittle materials. *Science* **378**, 1222-1227 (2022).

32 Lee, S. *et al.* A shape-morphing cortex-adhesive sensor for closed-loop transcranial ultrasound neurostimulation. *Nat. Electron* **7**, 800-814 (2024).

33 Nie, B., Stutzman, J. & Xie, A. A vibrational spectral maker for probing the hydrogen-bonding status of protonated Asp and Glu residues. *Biophys. J.* **88**, 2833-2847 (2005).

34 Chen, J. *et al.* An Adhesive Hydrogel with "Load-Sharing" Effect as Tissue Bandages for Drug and Cell Delivery. *Adv. Mater.* **32**, 2001628 (2020).

35 Rao, P. *et al.* Tough hydrogels with fast, strong, and reversible underwater adhesion based on a multiscale design. *Adv. Mater.* **30**, 1801884 (2018).

36 Sun, T. L. *et al.* Physical hydrogels composed of polyampholytes demonstrate high toughness and viscoelasticity. *Nat. Mater.* **12**, 932-937 (2013).

37 Freedman, B. R. *et al.* Degradable and Removable Tough Adhesive Hydrogels. *Adv. Mater.* **33**, 2008553 (2021).

38 Choi, Y. S. *et al.* A transient, closed-loop network of wireless, body-integrated devices for autonomous electrotherapy. *Science* **376**, 1006-1012 (2022).

39 Khan, A. *et al.* Highly Elastic, Biodegradable Polyester-Based Citrate Rubber for

3D Printing in Regenerative Engineering. *ACS Biomaterials Science & Engineering* **11**, 1571-1582 (2025).

40 Guo, J. *et al.* Recent Advances in Gelatin Methacryloyl Hydrogels for Bone Regeneration. *ACS Applied Nano Materials* **7**, 17193-17213 (2024).

41 Kang, S.-K., Koo, J., Lee, Y. K. & Rogers, J. A. Advanced Materials and Devices for Bioresorbable Electronics. *Acc. Chem. Res.* **51**, 988-998 (2018).

42 Kawana, Y. *et al.* Optogenetic stimulation of vagal nerves for enhanced glucose-stimulated insulin secretion and β cell proliferation. *Nat. Biomed. Eng.* **8**, 808-822 (2024).

43 Meyers, E. E., Kronemberger, A., Lira, V., Rahmouni, K. & Stauss, H. M. Contrasting effects of afferent and efferent vagal nerve stimulation on insulin secretion and blood glucose regulation. *Physiological Reports* **4**, e12718 (2016).

44 Yin, J., Ji, F., Gharibani, P. & Chen, J. D. Z. Vagal Nerve Stimulation for Glycemic Control in a Rodent Model of Type 2 Diabetes. *Obes. Surg.* **29**, 2869-2877 (2019).

45 Pandit, R. *et al.* Effect of Epoxidation of Diene Component of SBS Block Copolymer on Morphology and Mechanical Properties. *Macromol. Symp.* **315**, 152-159 (2012).

46 He, J. & Zhang, L. Chemical adhesion of a hydrogel on an elastomer surface enabling directionally-bendable actuators. *J. Mater. Chem. C* **10**, 2938-2944 (2022).

Appendix B

SUPPLEMENTARY INFORMATION FOR CHAPTER 3

Materials from this chapter appear in "Li, J.; Fan, K.; Ma, X.; Wang, C.; Min, J.; Chen, Y.; Song, Y.; Xu, Y.; Gao, W. Strain-insensitive wet-tissue-adhesive biphasic bioelectronics for physicochemical monitoring and adaptive therapy. *Nature Materials*, Under Revision"

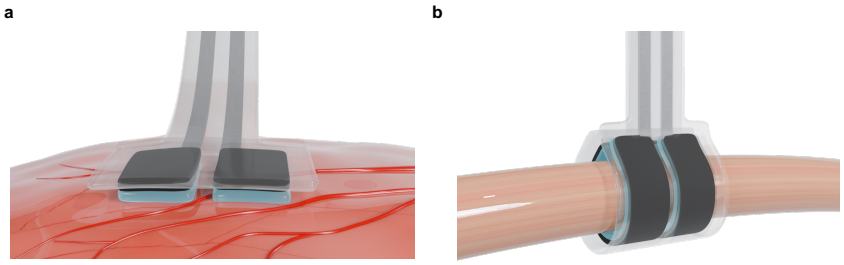

Fig. B-1. Schematic of ElHyX electrodes. a, Electrophysiological sensor. **b**, Nerve cuff.

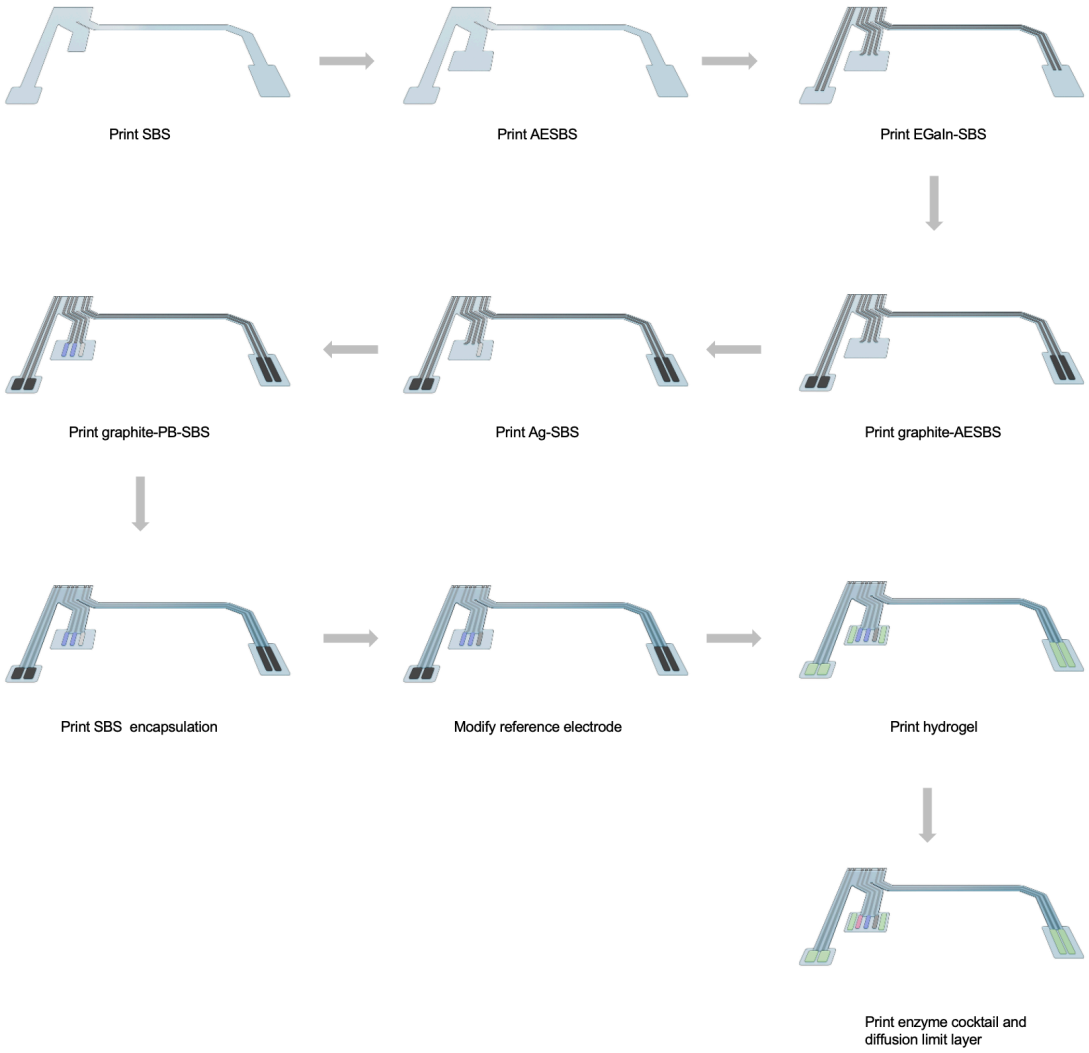

Fig. B-2. Fabrication process of ElHyX-based device. Schematic illustration of the sequential printing process of ElHyX-based device consisting of an ECG sensor, a glucose sensor and a nerve cuff.

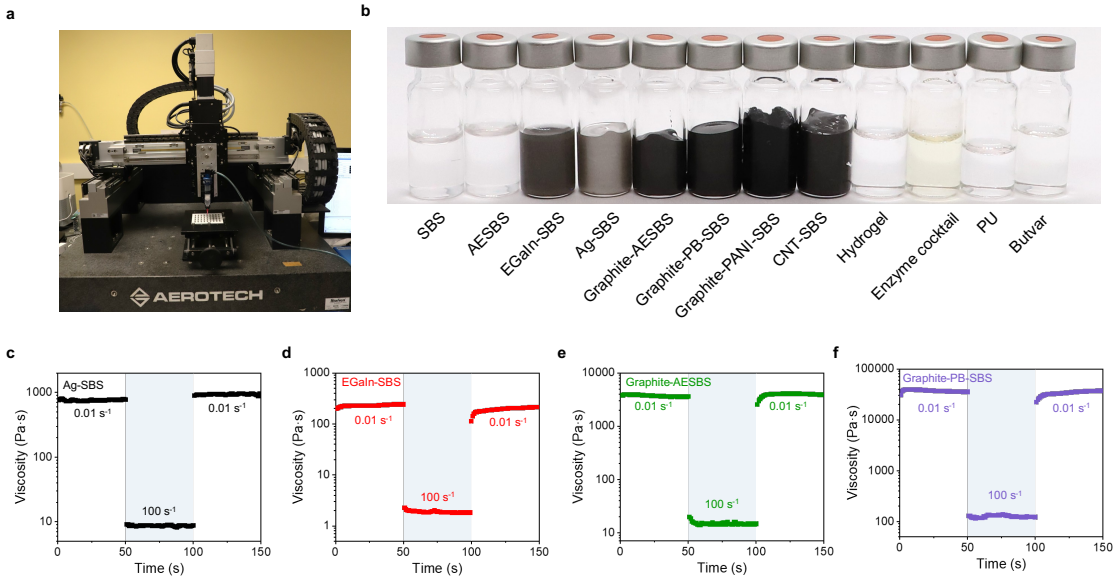

Fig. B-3. Direck ink writing using customized inks. a, Photograph of the direct ink writing system. **b**, Photograph of the customized inks used to print ElHyX devices. **c–f,** Viscosity of Ag-SBS (**c**), EGaIn-SBS (**d**), graphite-AESBS (**e**) and graphite-PB-SBS (**f**) under alternating shear rates between 0.01 s^{-1} and 100 s^{-1}.

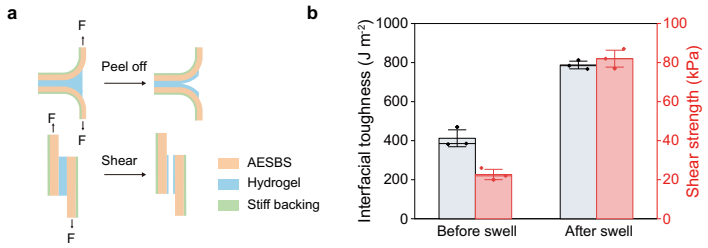

Fig. B-4. Quantitative evaluation of interfacial adhesion between the elastomer and hydrogel layers of the ElHyX platform. a, Schematic illustration of the experimental set up for peel-off and shear testing. In both test modes, failure occurred within the bulk hydrogel rather than at the interface. **b**, Measured adhesion strength between hydrogel and elastomer under pristine and swollen conditions.

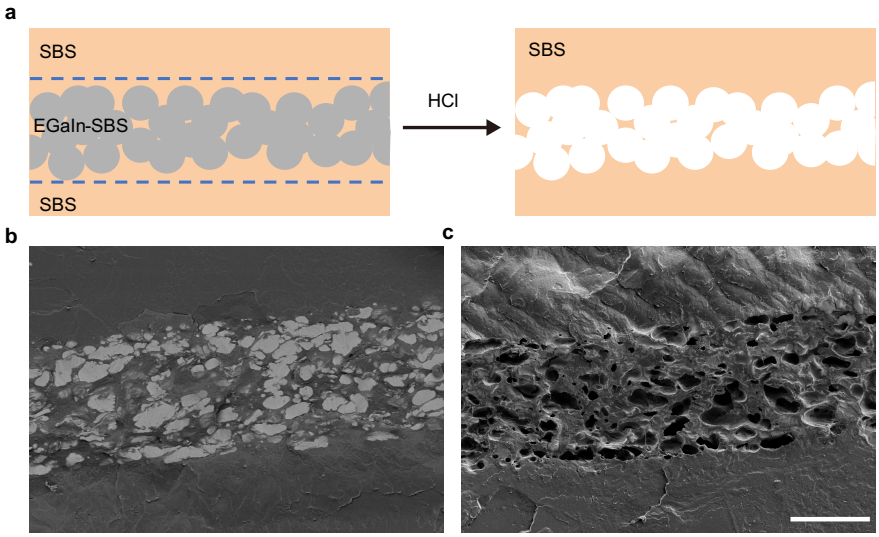

Fig. B-5. Schematic and SEM image of SBS-(EGaIn/SBS)-SBS trilayer structure. a-c, Schematic (**a**) and cross-section SEM image of a trilayer structure consisting of an SBS/EGaIn composite layer embedded between two pure SBS layers before (**b**) and after (**c**) EGaIn was selectively removed using HCl. The SEM image reveals no distinct boundary between the SBS domains of the middle and outer layers, indicating that SBS from the composite layer merges into the surrounding SBS layers, forming a strongly integrated, continuous interface. Scale bar, 100 μm.

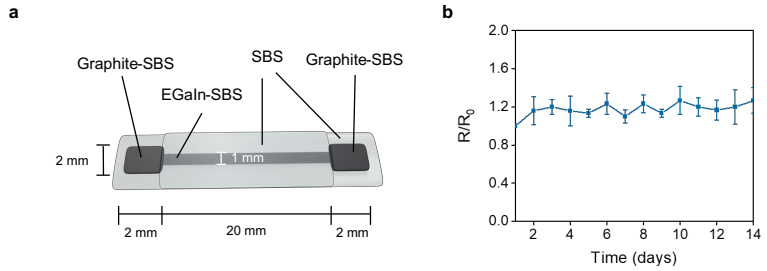

Fig. B-6. Electrical stability of encapsulated EGaIn–SBS composite under physiological conditions. a, Schematic of the testing structure mimicking the ElHyX-based electrode configuration. **b,** Electrical resistance of the encapsulated composite during a 14-day incubation in PBS at 37 °C.

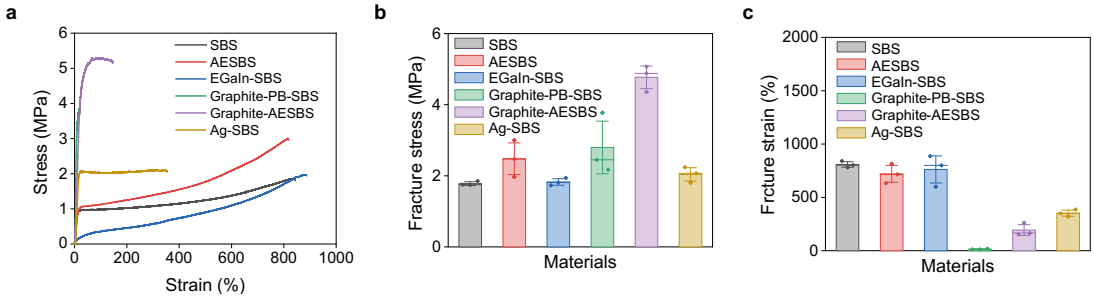

Fig. B-7. Mechanical properties of ElHyX components. a, Stress-strain curves of all printed materials for ElHyX fabrication. **b**,**c**, Fracture stress (**b**) and fracture strain (**c**) of each material.

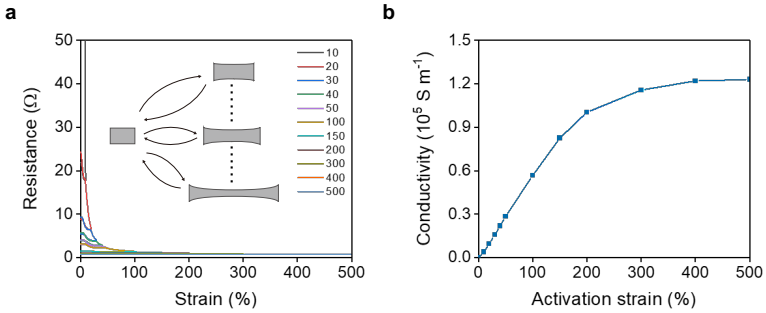

Fig. B-8. Activation of EGaIn-SBS. a, Resistance changes of an EGaIn–SBS sample (10 mm length, 0.12 mm thickness, 1 mm width) during cyclic uniaxial stretching at various strain levels. **b**, Extracted conductivity values of the composite after being activated under different strains.

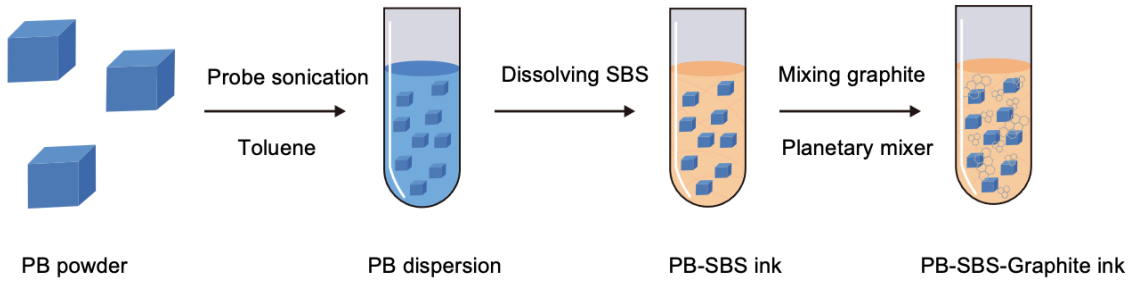

Fig. B-9. Fabrication process of Graphite-PB-SBS ink. The fabrication of graphite-PB-SBS ink includes disperse PB powder into toluene through probe sonication, followed by dissolving SBS into the PB toluene suspension. The resulted PB-SBS ink was subsequently mixed with graphite powder using planetary mixer to produce Graphite-PB-SBS ink.

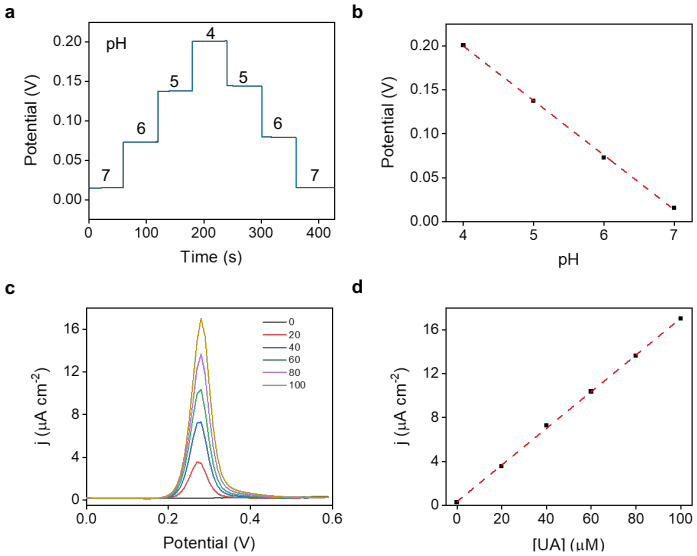

Fig. B-10. Demonstration of additional chemical sensing capabilities using functional fillers. a,**b**, Potentiometric response (**a**) and the corresponding calibration plot (**b**) of printed graphite-PANI-SBS electrode under different pHs. **c**,**d**, Differential pulse voltammetry response (**d**) of printed CNTs-SBS uric acid (UA) sensor and the corresponding calibration plot (**d**)

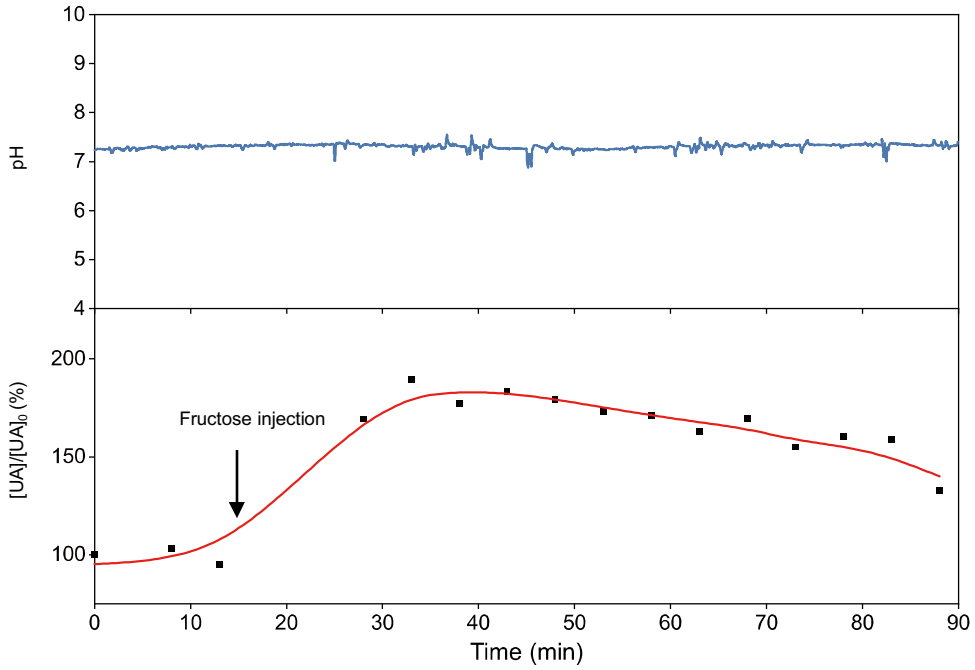

Fig. B-11. In vivo validation of ElHyX-based pH and uric acid sensors. A fructose dose of 7.5 g kg^{-1} was administered via intraperitoneal (IP) injection at the time indicated by the arrow. Potassium oxonate (250 mg kg^{-1}) was administered one hour before the experiment to reduce uricase activity.

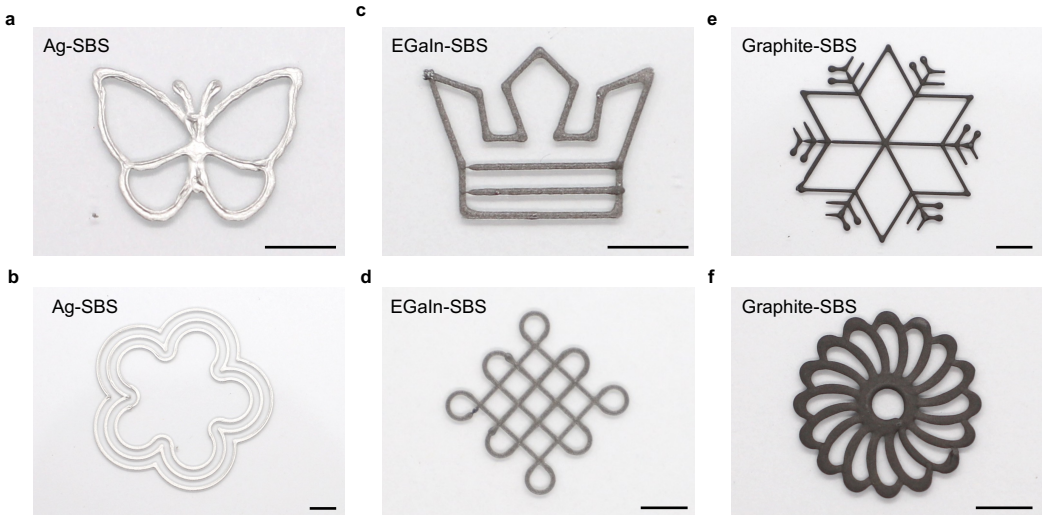

Fig. B-12. DIW patterned functional composites. a-f, Photograph of DIW patterned butterfly (A), flower (B), crown (C) Chinese knot (D), snow (E) and Archimedean spiral (F). Scale bars, 5 mm.

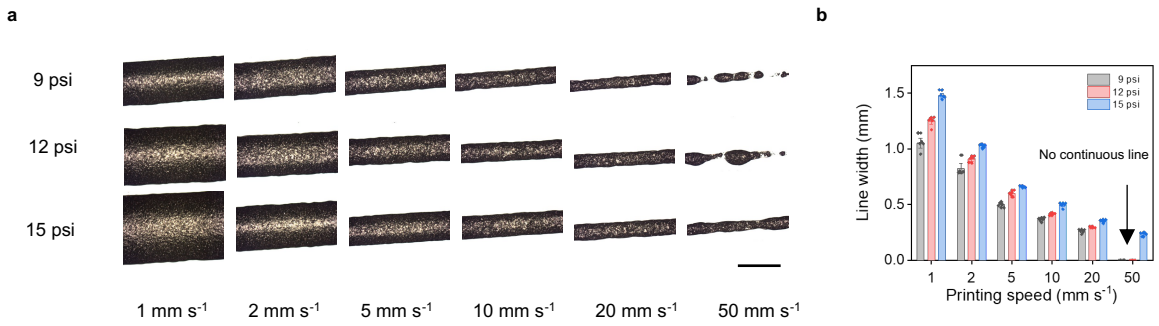

Fig. B-13. Printing resolution of EGaIn-SBS composite ink. a, Photograph of EGaIn–SBS lines printed under various combinations of extrusion pressure and printing speed. Scale bar, 1 mm. **b**, Line width of EGaIn-SBS printed under different pressure and speed. psi: pound per square inch.

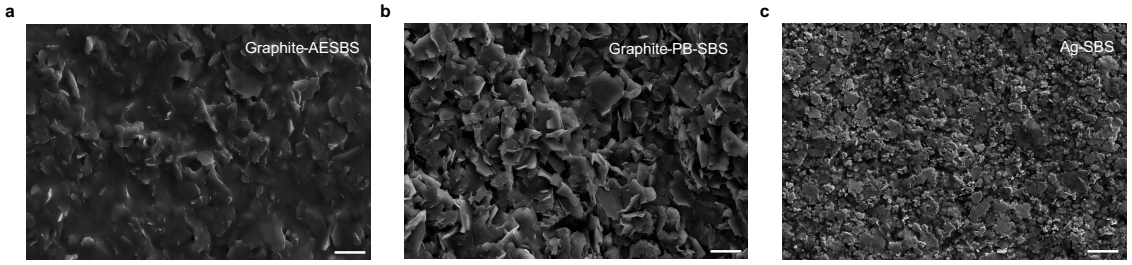

Fig. B-14. SEM characterization of electrode materials. a-c, SEM images of printed graphite-AESBS (**a**), graphite-PB-SBS (**b**) and Ag-SBS electrodes (**c**). Scale bars, 10 μm.

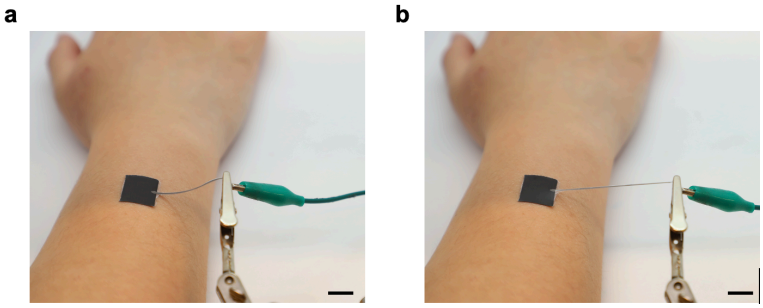

Fig. B-15. On-body ECG measurement under tensile strain. a,b, Photographs of on-body ECG measurements at 0% (**a**) and 100% (**b**) tensile strain. The ElHyX device was mechanically fixed at the prescribed extension during data acquisition to maintain constant strain. Scale bars, 1 cm.

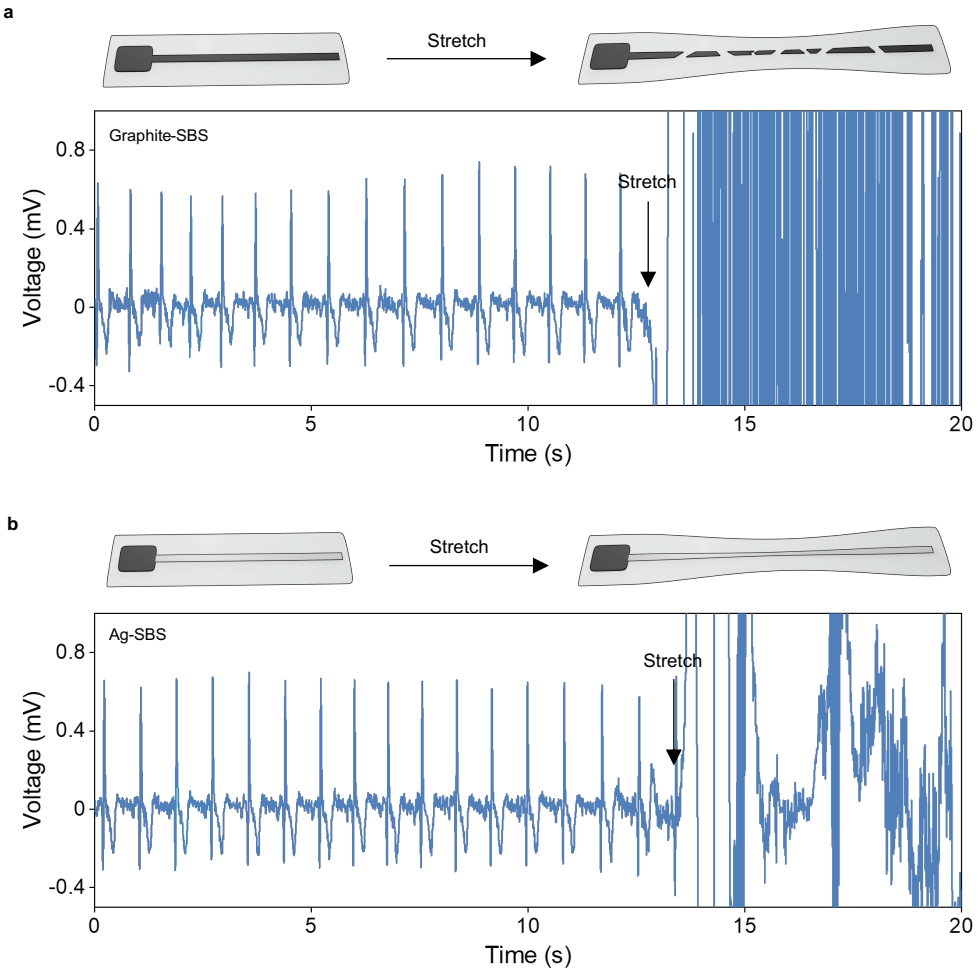

Fig. B-16. On-body ECG monitoring using conventional conductive composites. a, ECG recording using graphite-SBS as the conductor. **b,** ECG recording using Ag-SBS as the conductor. Both electrodes were subjected to 100% uniaxial strain at the time indicated by the arrow.

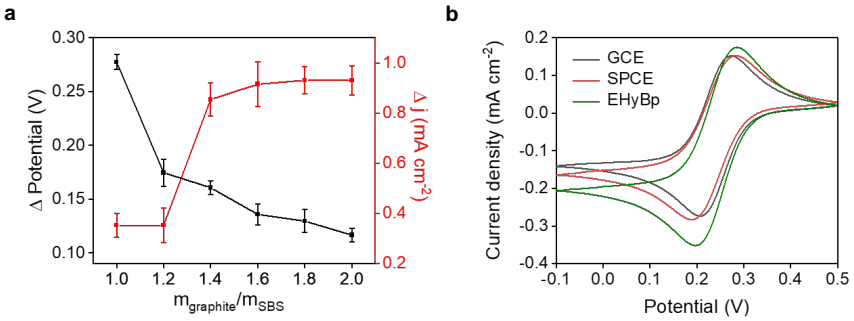

Fig. B-17. Optimization and evaluation of the electrochemical performance of the composite electrode. a, CV oxidation peak current density and redox peak potential difference of electrodes with different graphite to SBS ratio. **b**, CVs of ElHyX electrochemical working electrode ($m_{graphite}/m_{SBS}$ = 2), glassy carbon electrode (GCE) and screen-printed electrode (SPCE). Redox couple: 5 mM $K_3Fe(CN)_6$. Scan rate: 5 mV s^{-1}.

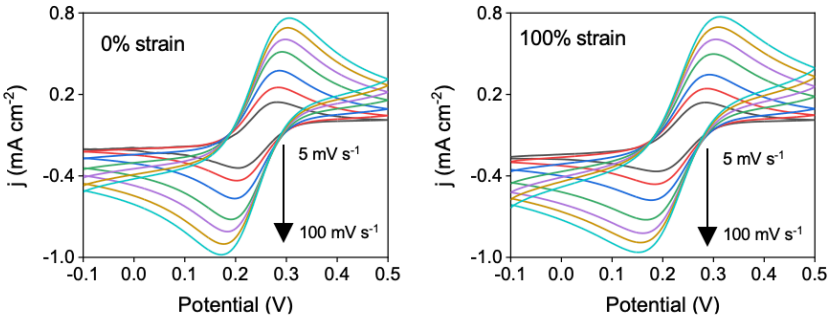

Fig. B-18. Evaluation of strain-insensitive electrochemical performance. CVs of an ElHyX electrochemical working electrode in 5 mM $K_3Fe(CN)_6$ solution under 0 strain (left) and 100% strain (right). Scan rates: 5, 10, 20, 40, 60, 80, and 100 mV s^{-1}.

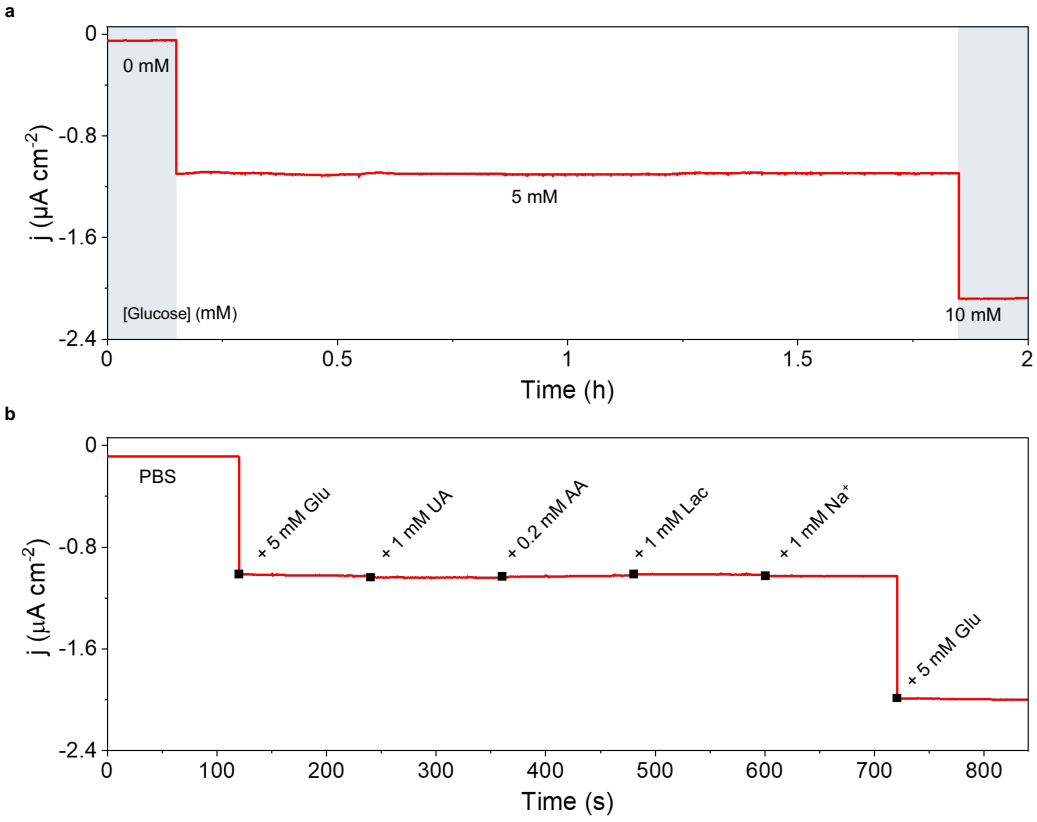

Fig. B-19. Evaluation of the stability and selectivity of ElHyX-based glucose sensor. (**A**) Amperometric response of glucose sensor tested in phosphate-buffered saline (PBS) solutions. (**B**) Selectivity of glucose sensor against other metabolites and electrolytes in PBS solution. Glu, glucose; UA, uric acid; AA, ascorbic acid; Lac, lactate.

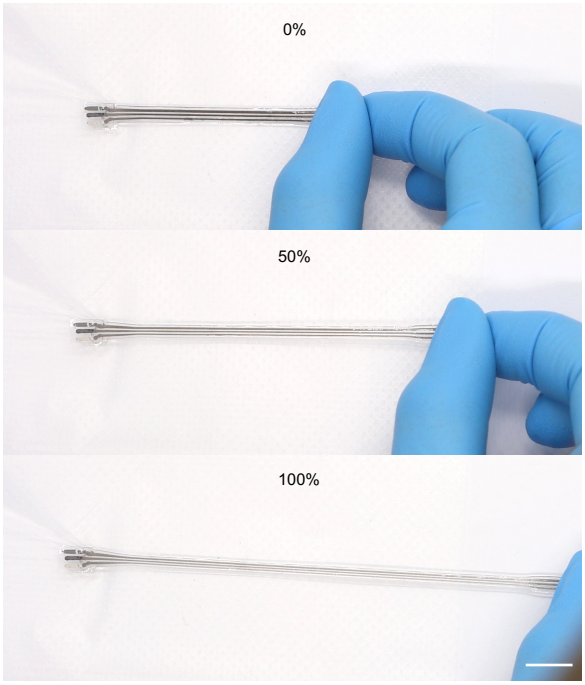

Fig. B-20. In vitro demonstration of adhesion on collagen sheet and stretchability of ElHyX-based electrochemical sensor. Scale bar, 1 cm.

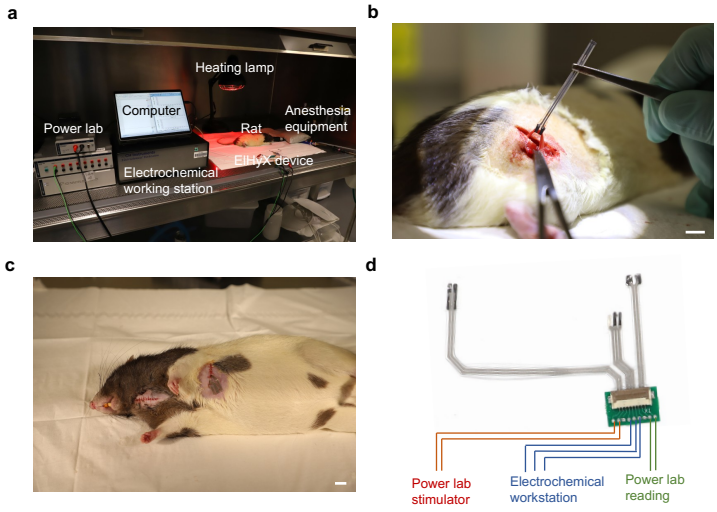

Fig. B-21. Photograph of in vivo animal tests. a, Photograph of the animal experiment set up. **b**, Pulling the nerve cuff wrapped around the rat's sciatic nerve. Scale bar, 1 cm. **c**, ElHyX-based closed-loop blood regulation system implanted in a diabetic rat with input/output end exposed externally through the skin. Scale bar, 1 cm. **d,** ElHyX-based closed-loop system connected via an FPC interface to external equipment for stimulation, sensing, and signal recording.

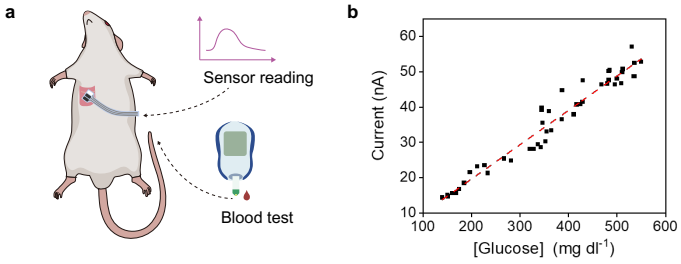

Fig. B-22. In vivo glucose sensor calibration. a, Schematic of the calibration setup. Blood samples were collected via tail-tip bleeding and analyzed using a commercial blood glucose meter. **b**, Calibration plot comparing sensor output with blood glucose concentrations measured by the commercial meter.

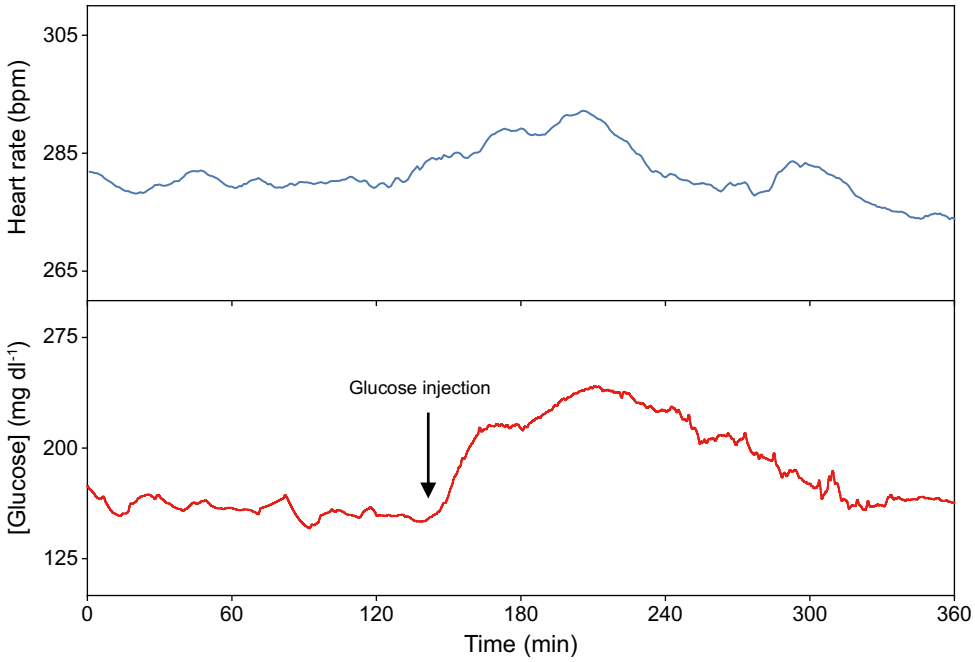

Fig. B-23. 6-hour continuous monitoring of heart rate and glucose levels using ElHyX electrode. A glucose dose of 2 g kg^{-1} was administered via IP injection at the time indicated by the arrow.

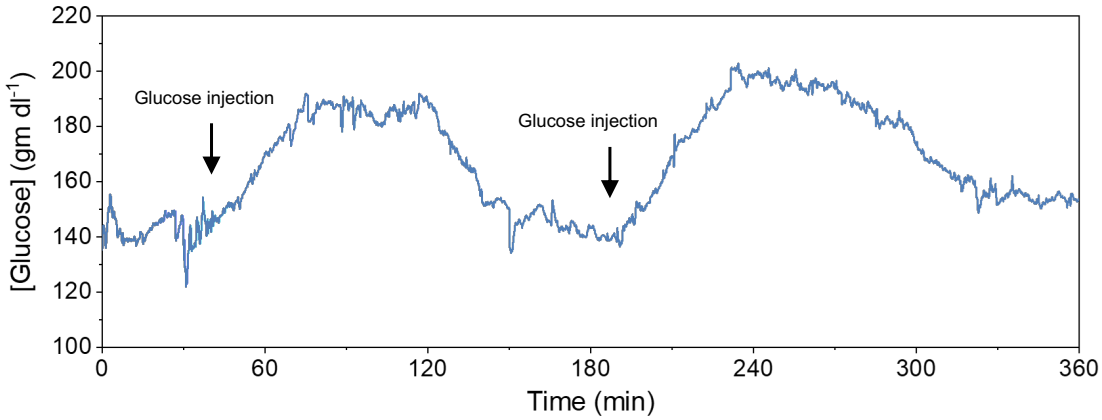

Fig. B-24. In vivo multi-cycle dynamic glucose sensing using ElHyX-based sensor. Consecutive glucose doses (1 g kg^{-1} each) were administered via intraperitoneal injection at the times indicated by arrows.

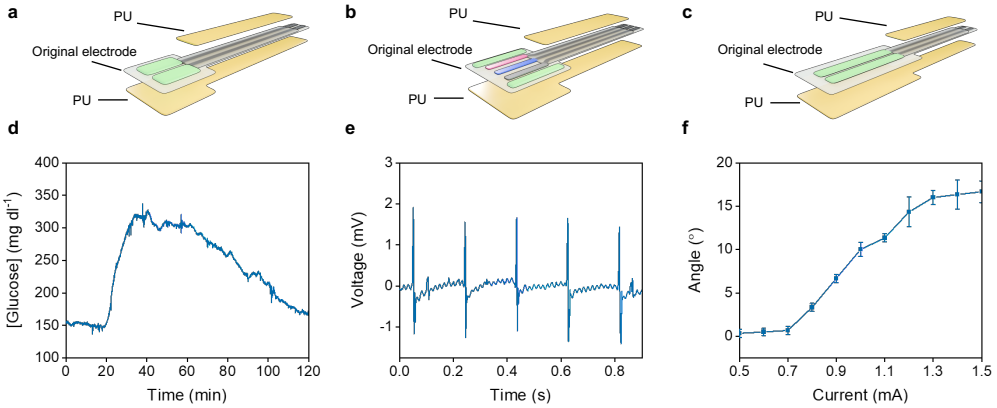

Fig. 25. Long-term stability of PU-encapsulated ElHyX devices. **a–c**, Schematics of ElHyX-based devices with polyurethane encapsulation, including glucose sensor (**a**), ECG electrode (**b**), and nerve cuff (**c**). **d–f**, Representative recordings from Day 14 post-implantation showing stable glucose sensing (**d**), ECG monitoring (**e**), and sciatic nerve stimulation (**f**), confirming long-term durability and preserved tissue integration.

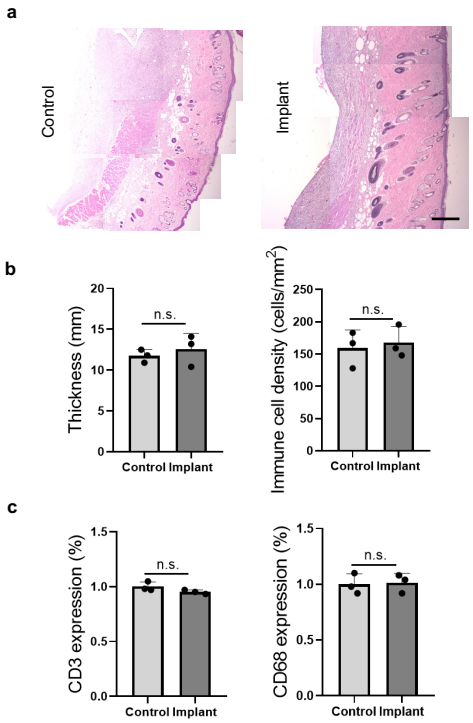

Fig. B-26. Histological and immunological evaluation of tissue response to implanted ElHyX device. a, Stitched high-resolution H&E-stained images of skin tissue sections from the control and implant groups after 28 days. Scale bar, 200 μm. **b,** Quantification of dermal tissue thickness and immune-cell infiltration based on H&E-stained sections. n.s., no significant difference. **c,** Quantitative analysis of CD3 and CD68 expression levels across regions of interest.

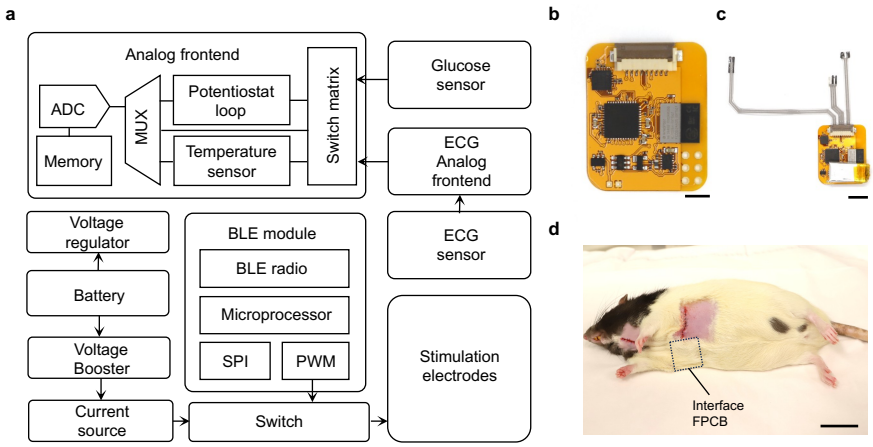

Fig. B-27. System integration of a fully implantable wireless ElHyX-based bioelectronic platform. a, System-level block diagram of the wireless platform. MPU, microprocessor unit; ADC, analogue to digital converter; SPI, serial peripheral interface; PWM, pulse-width modulation. **b,** Photograph of the flexible circuitry. Scale bar, 5 mm. **c,** Photograph of the fully assembled, fully implantable wireless ElHyX-based bioelectronic platform. Scale bar, 1 cm **d,** Photograph of a diabetic rat implanted with the wireless ElHyX system. Scale bar, 5 cm. FPCB, flexible printed circuit board.

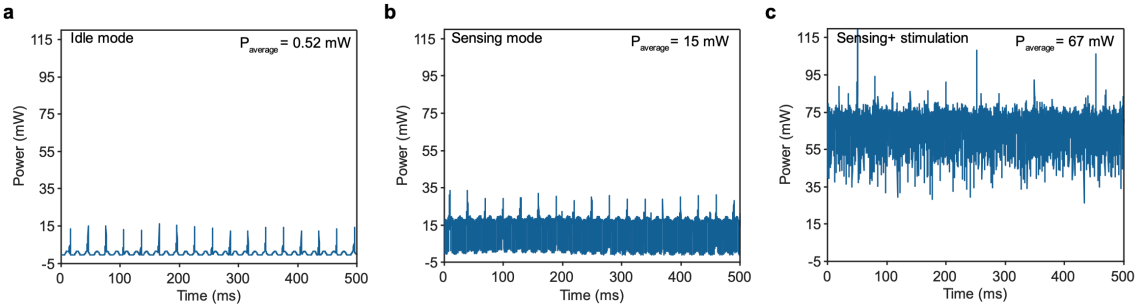

Fig. B-28. Power consumption of the wireless ElHyX system. a, Power consumption under idle mode. **b**, Power consumption under sensing mode. **c**, Power consumption under sensing and stimulation mode.

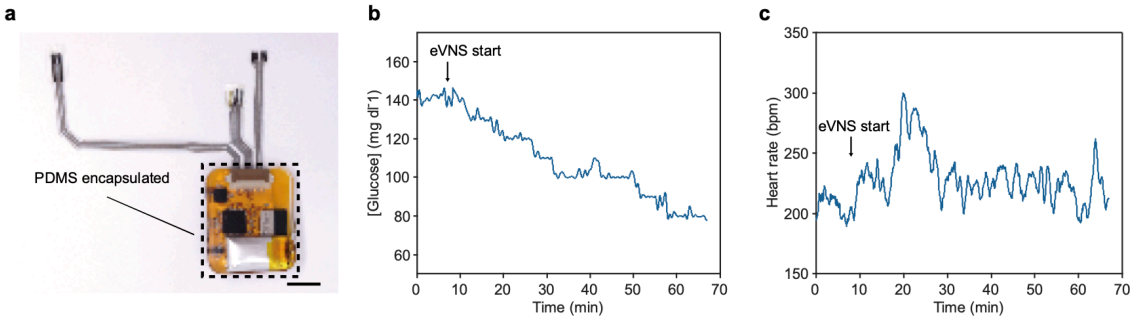

Fig. B-29. In vivo evaluation of wireless ElHyX system. a, Photograph of the wireless ElHyX system with the circuit board fully encapsulated in PDMS for in vivo implantation. Scale bar, 1 cm. **b**,**c**, In vivo demonstration of glucose monitoring (**b**) and heart rate (**c**) monitoring on healthy rat using the wireless ElHyX system. eVNS was applied to the animal at the time indicated by the arrows using the wireless ElHyX system.

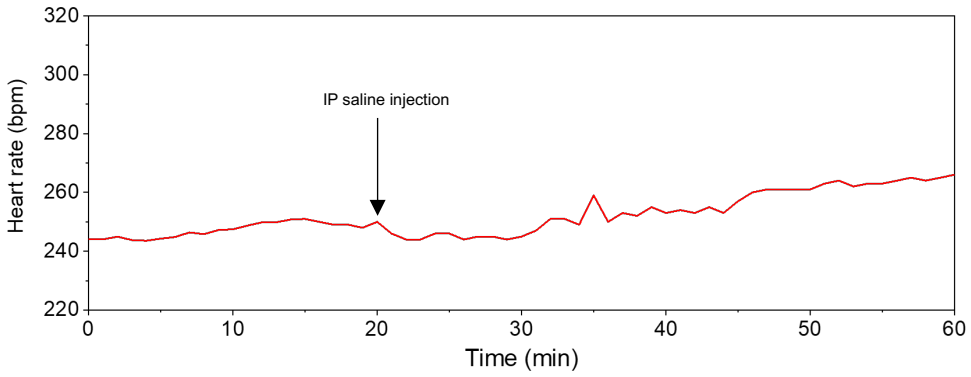

Fig. B-30. Heart rate response of a diabetic rat to IP saline injection. Heart rate was monitored to evaluate physiological response to a control injection (saline, 1 ml kg^{-1}), confirming that saline does not induce significant heart rate changes in diabetic rats.

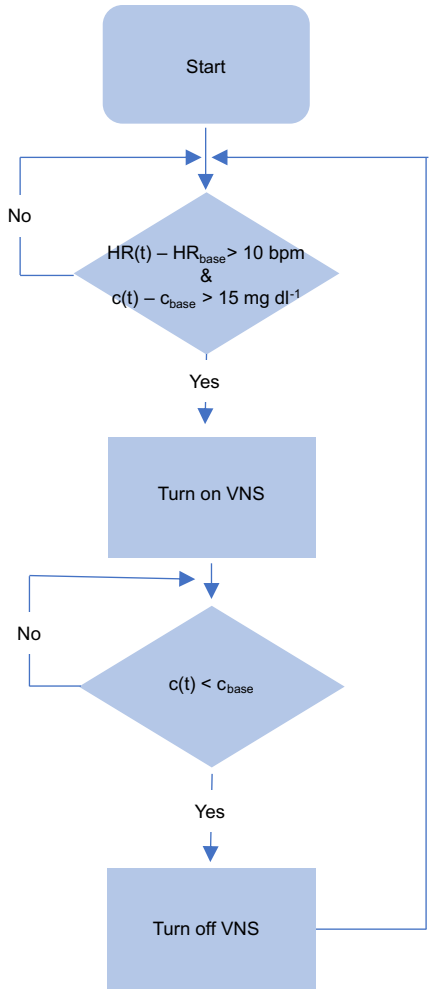

Fig. B-31. Closed-loop control logic for glucose regulation based on dual-parameter feedback. Flowchart illustrating the algorithm governing autonomous glucose regulation using the ElHyX-based bioelectronic system. Glucose concentration and heart rate are continuously monitored. When both parameters rise—heart rate increasing by >10 bpm and glucose level by more than 15 mg dL^{-1} compared to baseline—the system initiates vagus-nerve stimulation (VNS). Stimulation continues until glucose concentration falls to or below the baseline, after which passive monitoring resumes until the next concurrent increase is detected.

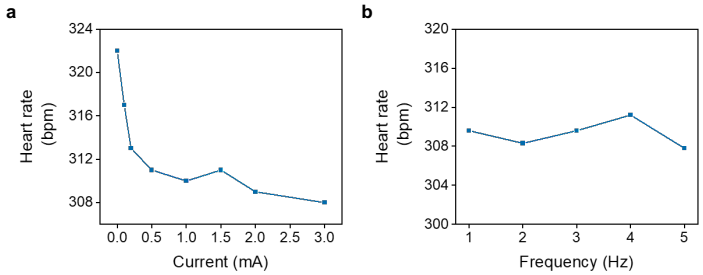

Fig. B-32. In vivo optimization of VNS parameters. a, HR changes as a function of stimulation current at a fixed pulse width and frequency. **b**, HR change as a function of stimulation frequency at a fixed current. Each stimulation epoch lasted 60 s, followed by a 60 s recovery period to re-establish baseline heart rate.

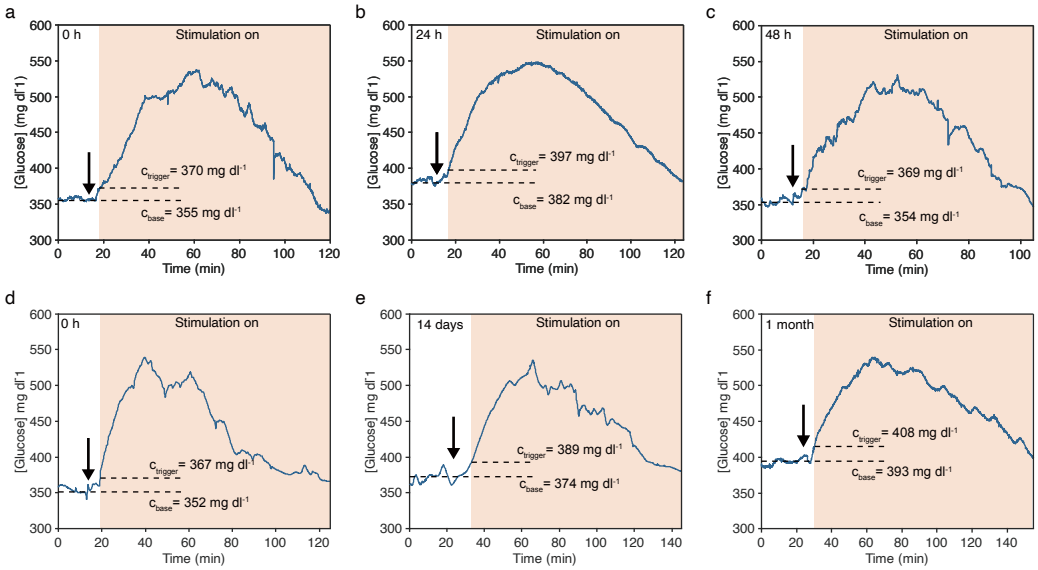

Fig. B-33. In vivo demonstration of closed-loop glucose regulation in diabetic rats using the ElHyX-based system. a–c, In vivo demonstration of closed-loop blood glucose management in diabetic rat on three consecutive days with selective efferent VNS at 0 h (**a**), 24 h (**b**), and 48 h (**c**) post-implantation. **d–f,** Chronic in vivo demonstration of closed-loop blood glucose management in diabetic rat with selective efferent VNS at 0 h (**d**), 14 days (**e**), and 1 month (**f**) post-implantation. A glucose dose of 2 g kg^{-1} was administered via IP injection at the times indicated by arrows. The shaded region indicates the periods during which selective eVNS was applied. Baseline glucose level was defined as the average glucose concentration measured during the 10 min prior to glucose injection. VNS stimulation was triggered when the glucose level exceeded the baseline by 15 mg/dL.

Table B-1. Composition and characterization of SBS composite inks.

Name	Ink composition	Conductivity	Function
EGaIn-SBS	SBS (0.5 g), toluene (1.5 g), EGaIn (6 g)	1.09×10^5 S m^{-1}	Strain insensitive conductor.
Ag-SBS	SBS (0.5 g), toluene (1.5 g), silver flake (3.5 g)	3.58×10^4 S m^{-1}	Reference for electrochemical sensing.
Graphite-AESBS	AESBS (0.5 g), toluene (1.5 g), graphite (0.5g)	9.22×10^1 S m^{-1}	Bioelectrical sensing/stimulation electrodes capable of integration with adhesive hydrogel.
Graphite-PB-SBS	SBS (0.5 g), toluene (1.5 g), graphite (1 g), PB (35 mg)	6.17×10^2 S m^{-1}	Working/counter electrodes for H_2O_2 sensing and enzymatic sensers.
Graphite-PANI-SBS	SBS (0.5 g), toluene (1.5 g), graphite (1 g), PANI (40 mg)	6.09×10^2 S m^{-1}	Working electrodes for pH sensing.
CNTs-SBS	SBS (0.5 g), toluene (2.3 g), CNTs (0.2 g)	3.86×10^2 S m^{-1}	Working electrodes for uric acid sensing.

Table B-2. Key materials and functionality metrics of the state-of-the-art implantable bioelectronic platforms.

Name	Stretchability	Strain insensitivity (R_0/R @ 100% strain)	Bioadhesivity	Physical sensing capability	Chemical sensing capability	Cloose loop treatment	Ref.
Our work	900%	~1	500 J m^{-2}	Yes	Yes	Yes	
Phase-separated conductive polymer	100%	0.3	300 J m^{-2}	Yes	No	No	[1]
Serpentine conductive elastomer composite	~50%	0.5	No	Yes	No	Yes	[2]
Phase-separated porous elastomer-AgNW composite	~700%	~1	No	Yes	No	No	[3]
Phase separated elastomer-nanowires composite	840%	0.3	No	Yes	No	Yes	[4]
Ultra-thin wavy gold	~50%	0.05	No	No	Yes	No	[5]
Cracked Au with supporting AgNW	150%	~1	No	Yes	Yes	No	[6]
Rolling coated liquid metal	400%	0.33	No	Yes	No	No	[7]
Serpentine conductive hydrogel	40%	N/A	No	Yes	No	Yes	[8]
Au nanomesh	20%	0.5 at 20%	30 J m^{-2}	Yes	No	No	[9]
Silk fibroin ion gel	30%–50%	N/A	180 J m^{-2}	Yes	No	No	[10]
Conductive hydrogel with interpenetr	430%	N/A	No	Yes	No	Yes	[11]

ating network							
Serpentine Cu	~50%	N/A	No	Yes	No	Yes	[12]
Structure engineered Mo	~40%	N/A	No	Yes	No	Yes	[13]
Reduced graphene oxide-adhesive hydrogel composite	200%	0.8 at 30%	420 J m^{-2}	Yes	No	No	[14]
PDMS composite with catechol-based adhesion	660%	N/A	7.2 kPa (shear strength)	Yes	No	Yes	[15]
Serpentine Au/Ti	70%	~1 at 70%	17.4 kPa (shear strength)	Yes	No	Yes	[16]
Twisted serpentine copper	~40%	N/A	No	Yes	No	Yes	[17]
Intrinsically stretchable conductive polymer	50%	N/A	0.6 kPa	Yes	No	No	[18]
PDMS encapsulated Liquid metal	~100%	N/A	No	Yes	No	No	[19]

Table B-3. Comparison of representative hydrogel–device and hydrogel–tissue integration strategies.

Name	Hydrogel-device integration mechanism	Hydrogel-tissue integration mechanism	Tissue adhesion mode	Fabrication complexity & note	Ref.
Our work	Covalent bonds	Hydrogen bonds	Tape-type	Fully printed, easy for mass production High materials and formulation flexibility, suitable for wide range of application	
Benzophenone enabled grafting	Covalent bonds	Hydrogen bonds	Tape-type	Complexed surface treatment and manual assembly required, difficult for mass manufacturing	20
Cyanoacrylate enabled integration	Covalent bonds	Covalent bonds	Glue-type	Manual assembly is required, difficult for patterning and mass manufacturing. Cyanoacrylate based interface lacks flexibility and may cause toxicity.	21
Tannic acid-based integration	Hydrogen bonds & Van der Waal force	Hydrogen bonds	Tape-type	Complexed multistep manual fabrication process, limited long-term adhesive strength in wet condition.	22
Silane condensation-based integration	Covalent bonds	N/A	N/A	Manual assembly required, limited materials selection.	23
Gold nanoparticle-silk fibroin integration	Electrostatic interaction & Van der Waal force	Hydrogen bonds	Tape-type	Complexed multistep manual fabrication process, limited materials selection.	10
Amino functionalized surface with NHS ester grafted hydrogel	Covalent bonds & hydrogen bonds	Covalent bonds & hydrogen bonds	Tape-type	Complexed multistep manual fabrication process, surface treatment required, limited materials selection.	14
Metal - catechol-conjugated hydrogel integration	Covalent bonds & hydrogen bonds	Covalent bonds & hydrogen bonds	Tape-type	Complexed multistep manual fabrication process, surface treatment required, limited materials selection. Catechol groups suffer from light and oxidation stability issue.	15
Ultra-thin elastomer integration	Van der Waal force	Van der Waal force	Tape-type	Clean room process required. Relatively weak adhesion strength.	18
Photocurable glue-based integration	Covalent bonds	Covalent bonds & polymer chain entanglement	Glue-type	Manual assembly and surface treatment required. Can be applied to various implantable devices but extra operations, including glue apply and uv exposure, are needed during surgery.	24

Bibliography of Appendix B

1 Zhou, T. *et al.* 3D printable high-performance conducting polymer hydrogel for all-hydrogel bioelectronic interfaces. *Nat. Mater.* **22**, 895-902 (2023).

2 Sunwoo, S.-H. *et al.* Ventricular tachyarrhythmia treatment and prevention by subthreshold stimulation with stretchable epicardial multichannel electrode array. *Sci. Adv.* **9**, eadf6856 (2023).

3 Xu, Y. *et al.* Phase-separated porous nanocomposite with ultralow percolation threshold for wireless bioelectronics. *Nat. Nanotechnol.* **19**, 1158-1167 (2024).

4 Choi, S. *et al.* Highly conductive, stretchable and biocompatible Ag–Au core–sheath nanowire composite for wearable and implantable bioelectronics. *Nat. Nanotechnol.* **13**, 1048-1056 (2018).

5 Li, R. *et al.* A flexible and physically transient electrochemical sensor for real-time wireless nitric oxide monitoring. *Nat. Commun.* **11**, 3207 (2020).

6 Zhao, Y. *et al.* Soft strain-insensitive bioelectronics featuring brittle materials. *Science* **378**, 1222-1227 (2022).

7 Wang, S. *et al.* Intrinsically stretchable electronics with ultrahigh deformability to monitor dynamically moving organs. *Sci. Adv.* **8**, eabl5511 (2022).

8 Rahman, M. S. *et al.* Soft, stretchable conductive hydrogels for high-performance electronic implants. *Sci. Adv.* **11**, eads4415 (2025).

9 Rao, Z. *et al.* Ultrathin rubbery bio-optoelectronic stimulators for untethered cardiac stimulation. *Sci. Adv.* **10**, eadq5061 (2024).

10 Jiang, C. *et al.* Self-Reinforcing Ionogel Bioadhesive Interface for Robust Integration and Monitoring of Bioelectronic Devices with Hard Tissues. *Adv. Mater.* **37**, 2413028 (2025).

11 Qu, J. *et al.* Multifunctional hydrogel electronics for closed-loop antiepileptic treatment. *Sci. Adv.* **10**, eadq9207 (2024).

12 Ausra, J. *et al.* Wireless, fully implantable cardiac stimulation and recording with

on-device computation for closed-loop pacing and defibrillation. *Sci. Adv.* **8**, eabq7469 (2022).

13 Choi, Y. S. *et al.* A transient, closed-loop network of wireless, body-integrated devices for autonomous electrotherapy. *Science* **376**, 1006-1012 (2022).

14 Deng, J. *et al.* Electrical bioadhesive interface for bioelectronics. *Nat. Mater.* **20**, 229-236 (2021).

15 Choi, H. *et al.* Adhesive bioelectronics for sutureless epicardial interfacing. *Nat. electron.* **6**, 779-789 (2023).

16 Lee, S. *et al.* A shape-morphing cortex-adhesive sensor for closed-loop transcranial ultrasound neurostimulation. *Nat. Electron* **7**, 800-814 (2024).

17 Ouyang, W. *et al.* A wireless and battery-less implant for multimodal closed-loop neuromodulation in small animals. *Nat. Biomed. Eng.* **7**, 1252-1269 (2023).

18 Liu, J. *et al.* Intrinsically stretchable electrode array enabled in vivo electrophysiological mapping of atrial fibrillation at cellular resolution. *Proc. Natl. Acad. Sci.* **117**, 14769-14778 (2020).

19 Wen, X. *et al.* Flexible, multifunctional neural probe with liquid metal enabled, ultra-large tunable stiffness for deep-brain chemical sensing and agent delivery. *Biosens. Bioelectron.* **131**, 37-45 (2019).

20 Tang, K. W. K. *et al.* Bioadhesive hydrogel-coupled and miniaturized ultrasound transducer system for long-term, wearable neuromodulation. *Nat. Commun.* **16**, 4940 (2025).

21 Wirthl, D. *et al.* Instant tough bonding of hydrogels for soft machines and electronics. *Sci. Adv.* **3**, e1700053 (2017).

22 Jo, Y. *et al.* Universal hydrogel adhesives with robust chain entanglement for bridging soft electronic materials. *npj Flex. Electron.* **8**, 39 (2024).

23 Liu, Q., Nian, G., Yang, C., Qu, S. & Suo, Z. Bonding dissimilar polymer networks in various manufacturing processes. *Nat. Commun.* **9**, 846 (2018).

24 Yang, Q. *et al.* Photocurable bioresorbable adhesives as functional interfaces between flexible bioelectronic devices and soft biological tissues. *Nat. Mater.* **20**, 1559-1570 (2021).

Chapter 4

OUTLOOK AND CONCLUSION

Materials from this chapter appear in "Li, J.; Qu, J.; Gao, W. Tissue-bioelectronics interfaces. *Chemical Society Reviews*, Under Revision"

Future progress in multimodal implantable bioelectronics will rely on the convergence of advances in materials science, device engineering, and biological understanding. Over the past decade, significant efforts have enabled the development of soft and conformal bioelectronic systems capable of interfacing with complex physiological environments. These technologies have demonstrated the potential to continuously monitor biochemical, electrophysiological, and mechanical signals in vivo while also enabling therapeutic interventions through electrical or chemical modulation. Despite these advances, achieving long-term stability, high sensing fidelity, and reliable therapeutic control within the dynamic and heterogeneous tissue microenvironment remains a major challenge.

One key direction for future research lies in the development of advanced materials that enable stable and durable implantable interfaces. Biological tissues exhibit continuous motion, biochemical activity, and immune responses that can gradually degrade device performance. While soft materials help reduce mechanical mismatch between devices and tissues, long-term stability also requires improved strategies for interfacial adhesion, encapsulation, and resistance to biofouling. Emerging materials such as dynamic polymer networks, self-healing elastomers, and bioadhesive hydrogels may help maintain stable tissue–device interfaces during extended implantation. In addition, biohybrid materials that incorporate biomimetic surface chemistries or immunomodulatory functionalities may promote long-term integration with surrounding tissues rather than passive tolerance.

Beyond interface stability, expanding the capabilities of multimodal physiological sensing represents another major opportunity for implantable bioelectronics. Physiological regulation involves complex interactions among biochemical, electrical, and mechanical signals. Implantable systems capable of simultaneously monitoring multiple classes of biomarkers could provide a more comprehensive understanding of physiological states and disease progression. Advances in nanomaterials, electrochemical sensing strategies, and flexible electronics may enable the detection of diverse biomarkers including metabolites, neurotransmitters, inflammatory molecules, and electrophysiological signals. Integrating

these sensing modalities into compact and energy-efficient implantable platforms will be essential for enabling continuous and long-term physiological monitoring.

Another promising direction is the development of intelligent closed-loop bioelectronic systems that combine sensing and therapeutic actuation. Continuous monitoring of physiological signals provides valuable diagnostic information, but the full potential of implantable bioelectronics may be realized when sensing capabilities are coupled with responsive therapeutic interventions. Closed-loop systems that integrate multimodal sensing, real-time signal processing, and targeted stimulation could enable adaptive therapies that dynamically respond to physiological changes. For example, metabolic signals, neural activity, or inflammatory markers could be continuously monitored to trigger electrical stimulation, neuromodulation, or localized drug delivery. Advances in low-power electronics, wireless communication, and embedded data processing will be critical for enabling autonomous operation of such implantable therapeutic systems.

In parallel with advances in materials and electronics, new fabrication and deployment strategies may significantly expand the design space of implantable bioelectronic devices. Conventional microfabrication methods have enabled remarkable progress in flexible electronics, but many biological tissues exhibit complex three-dimensional geometries that are difficult to interface with using planar device architectures. Emerging technologies such as three-dimensional printing, additive manufacturing, and in vivo fabrication may enable the creation of bioelectronic structures that conform more naturally to complex anatomical environments. In particular, in vivo printing strategies that fabricate functional materials directly within biological tissues may provide a new pathway for minimally invasive device deployment while achieving intimate integration with surrounding tissues.

Minimally invasive implantation approaches will also be critical for translating implantable bioelectronics toward clinical applications. Implantation procedures that require extensive surgical intervention may limit the adoption of otherwise promising technologies. Future implantable devices may therefore benefit from delivery strategies such as injectable electronics, catheter-based deployment, or self-expanding soft devices that can be inserted

through small incisions. Combining soft materials, compact electronics, and innovative deployment mechanisms may enable bioelectronic systems that can be implanted with reduced surgical burden while maintaining reliable long-term functionality.

Finally, the integration of computational design tools and data-driven approaches may further accelerate the development of multimodal implantable bioelectronics. The interactions between materials, device architectures, and biological environments are inherently complex and often difficult to optimize using empirical approaches alone. Multiphysics simulations that capture mechanical deformation, transport phenomena, and electrochemical processes may enable predictive design of implantable devices under realistic physiological conditions. In addition, machine learning techniques applied to large physiological datasets may help identify new biomarkers, optimize sensing strategies, and improve closed-loop therapeutic algorithms.

Collectively, these emerging directions point toward a new generation of implantable bioelectronic systems that are more adaptive, intelligent, and seamlessly integrated with biological systems. By combining multimodal sensing, advanced materials, minimally invasive deployment strategies, and autonomous therapeutic control, future bioelectronic technologies may enable continuous monitoring of complex physiological processes and personalized therapeutic interventions. Ultimately, the continued convergence of materials science, electronics, and biomedical engineering will drive the development of bioelectronic systems capable of transforming healthcare from reactive treatment toward predictive, preventive, and personalized medicine.